A Measurement of the Transverse Asymmetry in Forward-Angle Electron-Carbon Scattering Using the Q_{weak} Apparatus

by Martin James McHugh III

B.A. Physics, May 2010, St. Mary's College of Maryland

A Dissertation submitted to

The Faculty of
The Columbian College of Arts and Sciences
of The George Washington University
in partial fulfillment of the requirements
for the degree of Doctor of Philosophy

January 31, 2017

Dissertation directed by

Allena K. Opper
Professor of Physics

The Columbian College of Arts and Sciences of The George Washington University certifies that Martin James McHugh III has passed the Final Examination for the degree of Doctor of Philosophy as of November 16, 2016. This is the final and approved form of the dissertation.

A Measurement of the Transverse Asymmetry in Forward-Angle Electron-Carbon Scattering Using the Q_{weak} Apparatus

Martin James McHugh III

Dissertation Research Committee:

Allena K. Opper, Professor of Physics, Dissertation Director

Harald W. Griesshammer, Associate Professor of Physics, Committee Member

Gerald Feldman, Professor of Physics, Committee Member

Dedicated to Isabel. Thanks for hanging in there.

Acknowledgments

I would like to take this opportunity to thank my advisor, Allena Opper. I also would like to thank all of the Q_{weak} collaboration. Particularly, (in no particular order), Marks Pitt and Dalton, David Armstrong, Wouter Deconink, Greg Smith, Paul King, Kent Paschke, Dave Mack, and all the other collaborators who helped guide my education these past years. I'd also like to thank my fellow student collaborators. Those who have already graduated, John Leacock, John Leckey, Emmanouil Kargiantoulakis, Adesh Subedi, Amrendra Narayan, Katherine Myers-Mesick, Rakitha Beminiwattha, Buddhini Wadiyawansa, Peiquing Wang, Nuruzzzman, Don Jones, Josh Magee, Josh Hoskins, Scott MacEwan, Juan Carlos Cornejo, and any I may have forgotten. It was easier for all of your hard work. To my colleagues still working towards their degrees: Wade Duvall, Anna Lee, Valerie Gray, Kurtis Bartlett, and those who slipped my mind, I could not have completed this work without you to bounce ideas off of.

My time at JLab was greatly improved by my work with the Mott group, Joe Grames, Riad Suleiman, Matt Poelker, Charlie Sinclair, Tim Gay, Dan Moser, Marcy Stutzman, and Sam Rhodes. It was a pleasure to work with all of you.

Abstract

A Measurement of the Transverse Asymmetry in Forward-Angle Electron-Carbon Scattering Using the Q_{weak} Apparatus

The Q_{weak} experiment at Jefferson Lab aims to achieve a 4% measurement of the proton's weak charge by measuring the parity-violating asymmetry in elastic electron-proton scattering at low momentum-transfer squared, $Q^2 = 0.025$ (GeV/c)^2. The measurement utilized Jefferson Lab's high-quality beam of 89% longitudinally polarized electrons at currents up to 180 μA. A measurement of this parity-violating asymmetry will result in a precise 0.3% measurement of $\sin^2\theta_W$. The Standard Model makes a firm prediction of this quantity, making the high-precision Q_{weak} measurement sensitive to new physics at the TeV scale. The Q_{weak} apparatus was also used to measure the transverse asymmetry of electron-carbon scattering. This quantity is an observable of the imaginary component of the two-photon exchange process. My contributions to these two projects included data taking, analysis work, quantifying background contributions, and GEANT4 simulations of the apparatus. As an additional part of my graduate training, I was part of the team that updated the CEBAF Injector MeV Mott Polarimeter.

Table of Contents

Physical Constants

- Plank's constant: $\hbar = 4.135\ 667\ 662(25) \times 10^{-15}$ eV s
- Speed of light: $c = 299{,}792{,}458$ m/s
- Conversion constant: $\hbar c = 197.326\ 9788(12)$ MeV fm
- Mass of electron: $m_e = 0.510\ 998\ 9461(31)$ MeV/c^2
- Mass of proton: $m_p = 938.272\ 0813(58)$ MeV/c^2
- Mass of carbon-12 nucleus: $m_c = 11.178$ GeV/c^2
- Charge of proton: $e = 1.602\ 176\ 6208(98)\ \times 10^{-19}$ C
- Permittivity of space: $\varepsilon_0 = 8.854\ 187\ 817...\ \times 10^{-}12$ F/m
- Fine structure constant: $\alpha = \frac{e^2}{4\pi\varepsilon_0 \hbar c} = 1/137.035\ 999\ 139(31)$
- Fermi coupling constant: $G_F/(\hbar c)^3 = 1.166\ 3787(6)\ \times 10^{-}5$ GeV$^{-}2$

Abreviations

- **APV** - Atomic Parity Violation
- **BB** - Beamline Background
- **BCM** - Beam Current Monitor
- **BNSSA** - Beam Normal Single Spin Asymmetry
- **BPM** - Beam Position Monitor
- **CEBAF** - Continuous Electron Beam Accelerator Facility
- **CODA** - CEBAF Online Data Acquisition
- **DAQ** - Data Acquisition
- **DIS** - Deep Inelastic Scattering
- **EM** - Electromagnetic
- **EW** - Electroweak
- **FFB** - Fast Feedback
- **GDR** - Giant Dipole Resonance
- **HC** - Helicity Correlated
- **HDC** - Horizontal Drift Chambers
- **HCBA** - Helicity-Correlated Beam Asymmetry
- **IHWP** - Insertable Half-Wave Plate
- **JLab** - Thomas Jefferson National Accelerator Facility
- **LH_2** - Liquid Hydrogen
- **LHC** - Large Hadron Collider

- **MD** - Main Detector
- **MPS** - Macropulse Sync
- **OPE** - One-Photon Exchange
- **PDF** - Probability Density Function
- **PMT** - Photo-Multiplier Tube
- **ppm** - part(s)-per-million
- **ppb** - part(s)-per-billion
- **PV** - Parity-Violating
- **PVES** - Parity-Violating Electron Scattering
- **QED** - Quantum Electrodynamics
- **QTCNB** - QTor Transport Channel Neutral Background
- **QTor** - Q_{weak} Toroidal Spectrometer Magnet
- **ROC** - Readout Controller
- **SLAC** - Stanford Linear Accelerator
- **SM** - Standard Model
- **SRF** - Superconducting Radio Frequency
- **SUSY** - Super-Symmetry
- **TPE** - Two-Photon Exchange
- **TS** - Trigger Scintillator
- **UV** - Ultraviolet
- **VDC** - Vertical Drift Chamber

Chapter 1

Introduction

The *Standard Model* (SM) of particles and interactions is one of the most successful physical models ever tested. It successfully describes the interactions between matter due to three fundamental forces of nature: electromagnetism, the weak nuclear force, and the strong nuclear force. Its predictions for the electromagnetic (EM) interaction, the theory of *quantum electrodynamics* (QED), have been found to be in agreement with experiment at precisions of one part in ten billion [1], among the most precise measurements ever made. Recently, the discovery of the Higgs boson [2, 3] provided yet another confirmation of SM predictions. However, the SM is incomplete. It does not incorporate the fourth fundamental force, gravity. The discovery of neutrino oscillations [4], implying that neutrinos are in fact massive, requires a new understanding of the weak interaction. Additionally, cosmological questions, such as the matter-antimatter asymmetry and the existence of both dark matter and dark energy, are not addressed by the SM.

Our goal as nuclear physicists is to test the SM in myriad ways until we find out where it fails; potentially revealing a more general theory that the SM approximates well in most cases. These searches for physics beyond the SM can typically be placed into one of two broad categories: high-energy direct searches and high-precision indirect measurements. These two types of experiments, employing different tools and techniques, focus on the problem in complementary ways, allowing for a multi-faceted approach to finding signs of new physics.

High energy experiments, such as those carried out at the Large Hadron Collider (LHC), seek to find physics beyond the SM through direct observation of novel particles. High

precision tests of the SM cover a wide range of diverse experimental methods. Typically, precision measurements search for either extremely rare processes or very small deviations from the SM predictions of a particular quantity. In general, precision measurements require very high intensities and a very sensitive apparatus.

This dissertation includes both preliminary and published results from the Q_{weak} experiment at the Thomas Jefferson National Accelerator Facility (colloquially, Jefferson Lab or JLab) a precision test of the SM. Jefferson Lab is a Department of Energy research laboratory located in Newport News, VA. The Q_{weak} experiment used the highly polarized ($P \approx 89\%$), high intensity ($I \approx 180$ μA) electron beam from the JLab Continuous Electron Beam Accelerator Facility (CEBAF) to measure a *parity-violating electron scattering* (PVES) asymmetry from a 35 cm long liquid hydrogen (LH_2) target. The parity-violating asymmetry is proportional to the vector weak charge of the proton, Q_W^p, the neutral weak current analog of the proton's electric charge, e. This weak charge is directly related to the *weak mixing angle*, $\sin^2\theta_W$, of the electroweak interaction. The SM makes firm predictions about value of $\sin^2\theta_W$, which the Q_{weak} experiment will measure to a relative precision of 0.3 %.

The Q_{weak} apparatus was also used to make measurements of parity-conserving transverse asymmetries on hydrogen, aluminum, and carbon. This dissertation covers results of the transverse asymmetry from electron-carbon scattering. In this measurement, the beam polarization was changed to a transverse orientation and the beam was scattered from a thin, highly pure ^{12}C target. This scattering process directly probes the two-photon exchange interaction and gathers information useful to theorists and for further precision measurements.

1.1 Standard Model

Within the SM, all interactions of matter, represented by spin $s = \frac{1}{2}$ fermion fields, are mediated by the exchange of virtual particles known as intermediate vector bosons with integer spin, $s = 0, 1$. The photon (γ) and 8 gluons mediate the interactions of the EM and strong force, respectively, and are assumed to be massless. The weak nuclear force is mediated by three bosons: the charged W^+ and W^- with mass $m_{W^\pm} = [80.385 \pm 0.015]$

GeV/c^2 and the neutral Z with mass $m_Z = [91.1876 \pm 0.0021]$ GeV/c^2 [5]. In addition to these force-carriers, there exists the recently confirmed Higgs boson, with mass $m_H = [125.09 \pm 0.24]$ GeV/c^2 [3]. This boson is the signature of the scalar field that is responsible for the spontaneous symmetry breaking in the electroweak force as well as the generation of masses for the $W^{\pm}$ and Z and the masses of the elementary fermions.

The elementary fermions are split into two distinct groups called leptons and quarks. Quarks carry "color" charge that can take three values, known as red, green and blue. With this color charge, quarks experience the strong force mediated by gluons. However, there has never been an observation of a particle with a bare color charge, a principle known as "color-neutrality." The experimentally observed bound quark states are typically described as mesons (a quark-antiquark pair) or baryons (a color-neutral quark triplet). While quarks experience all four fundamental forces, leptons do not, as they have no color charge. Charged leptons interact through the EM, weak force and gravity, while neutrinos experience only the weak force and gravity. The known families are organized into three "generations" of particles grouped by increasing mass (which are assumed in the case of neutrinos). The fermions, gauge bosons, Higgs boson and their associated antiparticles are the elements that make up all directly detected matter and radiation in the universe. The particle content of the SM can be seen in Figure 1.1.

1.1.1 Electroweak Unification

A central accomplishment of the SM has been the unification of the EM and weak forces into a single electroweak (EW) interaction [7]. In this theory, both observed forces are simply low-energy expressions of one "primordial" force. The unification revolves around requiring invariance under general $SU(2)_L \otimes U(1)$ gauge transformations. The unified fields are represented by $W_\mu^{1,2,3}$ and B_μ, each associated with the $SU(2)_L$ and $U(1)$ transformations

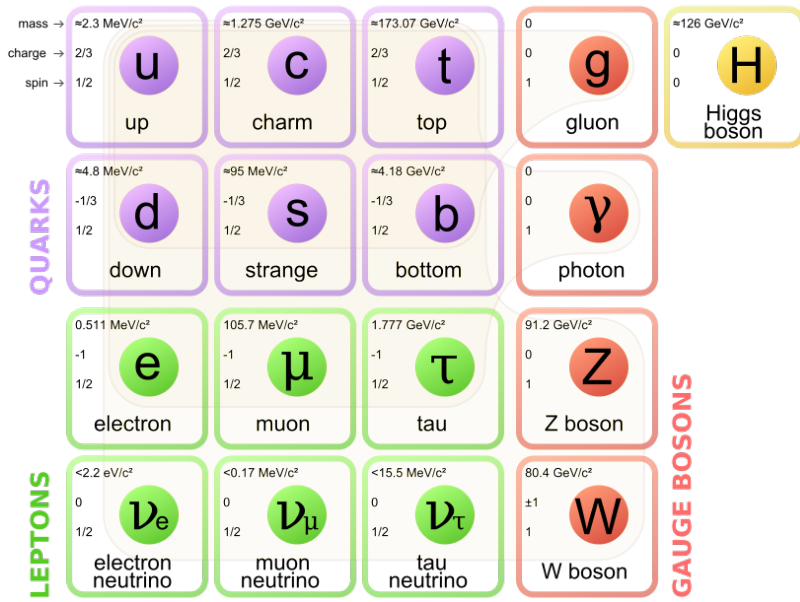

Figure 1.1: The elementary particles of the SM. The twelve fermions are organized by charge into the families of quarks (purple) and leptons (green) and by mass into three generations. The force-carrying gauge bosons (red) mediate interactions between fermions and bosons with the appropriate "charge." Note that not all masses are current. Reproduced from [6].

respectively. The physically observed fields are admixtures of these primordial fields [7]:

$$W_\mu^\pm = \left(W_\mu^1 \mp iW_\mu^2\right)/2 \tag{1.1}$$

$$Z_\mu = W_\mu^3 \cos\theta_W - B_\mu \sin\theta_W \tag{1.2}$$

$$A_\mu = W_\mu^3 \sin\theta_W + B_\mu \cos\theta_W \tag{1.3}$$

The massive $W^\pm$ and Z bosons are the quanta of the fields in eqs. (1.1) and (1.2) while the photon is the quantum of the A_μ field. The term θ_W, often referred to as the Weinberg angle, is the central parameter determining the level to which the primordial fields are mixed together to create the physically observed fields. This parameter is not predicted directly by the theory. However, it can be defined in terms of its relation,

$$\sin^2\theta_W = \frac{g'^2}{g^2 + g'^2}, \tag{1.4}$$

to the $SU(2)_L$ and $U(1)$ gauge couplings, g and g' respectively. Since this value is not predicted directly from first principles, one must measure the couplings in order to determine

its strength. However, it is observed that the Higgs mechanism provides masses to the weak bosons based on their coupling strength. Thus, at leading order, one finds:

$$\sin^2\theta_W = 1 - \frac{m_W^2}{m_Z^2}. \tag{1.5}$$

This SM parameter, $\sin^2\theta_W$, is what the Q_{weak} experiment was designed to measure. The weak mixing angle in relation to the Q_{weak} measurement will be discussed in greater detail in Section 2.3.1.

1.2 Transverse Scattering Asymmetries

In addition to testing the SM through PVES, the Q_{weak} apparatus was used to examine other interesting electron scattering phenomena. Electron scattering from nuclei, known as Mott scattering, has been an essential technique for gathering information about the properties of nuclei. Traditionally, the cross section in Mott scattering is calculated using the Born approximation, where the EM interaction is mediated by *one-photon exchange* (OPE). Higher-order processes are treated as small radiative corrections [8] altering the scattering cross section by less than 2%. While this precision was perfectly acceptable in previous decades, many modern electron scattering experiments such as Q_{weak} look for asymmetries that are on the order of parts-per-million (ppm). For measurements this precise, a clear accounting of higher-order processes is necessary.

In particular, the *two-photon exchange* (TPE) process has proven indispensable for the reconciliation of two types of lepton scattering experiments on the proton. At high momentum-transfer ($Q^2 > 2$ GeV/c^2), there was an observed discrepancy between the proton's electric/magnetic form-factor ratio when measured using the polarization transfer method [9, 10] as opposed to the Rosenbluth separation method [11]. It has been shown that including corrections for TPE processes brings the two measurements into agreement [12, 13]. However, the theoretical calculations of the TPE currently have large uncertainties arising from the treatment of intermediate-state excitations in the proton target. Measurements of observables related to TPE scattering are therefore of great interest.

One such observable is the *beam normal single spin asymmetry* (BNSSA), generated by the scattering of transversely polarized electrons from an unpolarized target. This observable, arising from the imaginary portion of the TPE amplitude, is a parity-conserving spatial scattering asymmetry that, at Q_{weak} kinematics, is on the order of several ppm. As a practical concern, the Q_{weak} experiment and other precision PVES measurements must take care to ensure that there is no leakage of this asymmetry into the PV asymmetry.

The Q_{weak} experiment undertook a transverse asymmetry measurement plan that included measurements using the LH_2 target, a solid aluminum target, and a solid carbon target. Measurements were made on all of these targets at kinematics that accessed elastic scattering and, separately, $\Delta(1232)$ resonance production. This dissertation focuses on the work done by the author to measure the BNSSA from the carbon target. The relevant scattering theory is discussed in greater detail in Section 2.4.

1.3 Dissertation Outline

The body of this dissertation is devoted to the methods and preliminary results of measurements made with the Q_{weak} apparatus. Chapter 2 contains a discussion of the theory required for interpreting the results of the Q_{weak} experiment in terms of the weak mixing angle as well as the implications of this result for physics beyond the SM. That chapter also covers the scattering theory for the results of the transverse carbon measurement. Chapter 3 describes the apparatus used to make the measurements. Chapter 4 describes the blinded analysis of the PVES asymmetry for the Run II Q_{weak} data set, including systematic effects. Chapter 5 performs the same function for the case of the unblinded BNSSA from carbon. The final chapter, Chapter 6, summarizes the physics results covered in the previous chapters.

In addition to the work done as part of the Q_{weak} Collaboration, the Ph.D. training of the author included a significant portion of time devoted to upgrading the CEBAF Injector MeV Mott Polarimeter. This included several hardware updates including the installation of a new beam dump, improved handling of backgrounds using updated analysis techniques, and a new Monte Carlo modeling effort using `GEANT4` [14] to understand systematic effects

that limit the potential precision of the polarimeter. This work was all done with the goal of reaching a final absolute precision of $< 1\%$. The description of the Mott Polarimeter and its upgrade can be found in Appendix A.

Chapter 2

Theory and Motivation

The Q_{weak} experiment used parity-violating electron scattering from protons to measure the proton's weak charge, Q_w^p. From this charge, one could extract the weak mixing angle, $\sin^2\theta_W$. In addition to this, the experimental apparatus was used to measure the transverse scattering asymmetry from ^{1}H, ^{12}C, and ^{27}Al. This section provides the theoretical framework for discussing these measurements. The motivations for these experiments are also covered.

2.1 Scattering Kinematics

In a two-body scattering process in the lab frame (initially stationary target), the incident particle with energy, E, and momentum, $\mathbf{k}$, scatters from the target with new energy, $E^{'}$. and momentum, $\mathbf{k}^{'}$, at the scattering angle, θ. The energy transferred to the target is defined as $\nu = E - E^{'}$, while the momentum transfer is given by $\mathbf{q} = \mathbf{k} - \mathbf{k}^{'}$. This allows us to define the four-momentum transfer,

$$Q^2 \equiv -q^2 = -(\nu^2 - \mathbf{k}^2) \geq 0. \tag{2.1}$$

Following energy and momentum conservation in the case of elastic scattering, the outgoing energy is strictly determined by the initial energy and scattering angle:

$$E^{'} = \frac{E}{1 - 2(E/M)\sin^2\theta/2}, \tag{2.2}$$

Where M is the mass of the target particle. Similarly, the four-momentum transfer for elastic scattering is also function of E and θ:

$$Q^2 = \frac{4E^2 \sin^2 \theta/2}{1 - 2(E/M)\sin^2 \theta/2}. \tag{2.3}$$

2.2 Elastic Electron-Proton Scattering and the Proton's Weak Charge

We move on to discuss the specific case of elastic scattering of electrons from protons:

$$e(k) + p(k_p) \rightarrow e(k') + p(k'_p) \tag{2.4}$$

where $k(k')$ is the incoming(outgoing) electron's four-momentum and $k_p(k'_p)$ is the initial(recoiling) proton's four-momentum. At leading order, the elastic scattering of an electron from a proton can be mediated by either a photon or a Z-boson as shown in Figure 2.1. The corresponding amplitudes are [15]:

$$\mathcal{M}_\gamma = \frac{-e^2}{Q^2} j^\mu_\gamma J^\gamma_\mu, \tag{2.5}$$

$$\mathcal{M}_Z = \frac{-G_F}{2\sqrt{2}} j^\mu_Z J^Z_\mu. \tag{2.6}$$

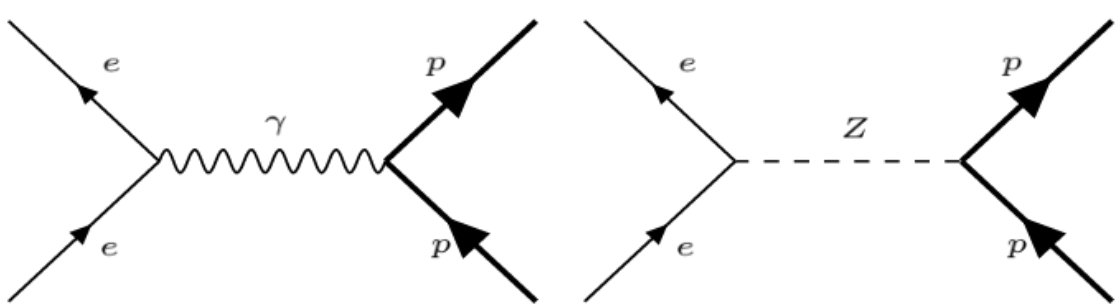

Figure 2.1: First-order diagrams for elastic, electron-proton scattering. Left(right) represents the amplitude $\mathcal{M}_\gamma(\mathcal{M}_Z)$.

Looking at each amplitude, one will see Dirac currents associated with the leptonic

vertex, j^μ, in each diagram, described by [15]:

$$j^\mu_\gamma = -e\bar{u}_e\gamma^\mu u_e, \tag{2.7}$$

$$j^\mu_Z = \bar{u}_e\gamma^\mu(g^e_V + g^e_A\gamma^5)u_e. \tag{2.8}$$

In the above equations, $u_e(\bar{u}_e)$ is the Dirac spinor for the incoming(outgoing) electron, γ^μ are the Dirac matrices, and $\gamma^5 = i\gamma^0\gamma^1\gamma^2\gamma^3$. The vector and axial-vector neutral-current coupling constants for the electron, g^e_V and g^e_A, respectively, have known values predicted by the electroweak theory of the SM. These values for the electron and other elementary fermions can be seen in Table 2.1.

Particle (f)	Q^f	g^f_V	g^f_A
e, μ, τ	-1	$-1 + 4\sin^2\theta_W$	1
ν_e, ν_μ, ν_τ	0	$-1 + 4\sin^2\theta_W$	1
u, c, t	+2/3	$1 - \frac{8}{3}\sin^2\theta_W$	-1
d, s, b	-1/3	$-1 + \frac{4}{3}\sin^2\theta_W$	1

Table 2.1: Standard model values for the electromagnetic charge (Q^f) and neutral current couplings (g^f_V, g^f_A) of the elementary fermions.

The currents from the hadronic vertex are more complex due to the proton's internal structure and are written in terms of the Pauli, Dirac and axial form factors, $F_1(Q^2)$, $F_2(Q^2)$ and $G_A(Q^2)$, respectively [15]:

$$J^\mu_{p,\gamma} = \bar{\psi}_p\left[F^\gamma_1(Q^2)\gamma^\mu + F^\gamma_2(Q^2)\frac{i\sigma^{\mu\nu}q_\nu}{2m_p}\right]\psi_p, \tag{2.9}$$

$$J^\mu_{p,Z} = \bar{\psi}_p\left[F^Z_1(Q^2)\gamma^\mu + F^Z_2(Q^2)\frac{i\sigma^{\mu\nu}q_\nu}{2m_p} + G^Z_A(Q^2)\gamma^\mu\gamma^5\right]\psi_p, \tag{2.10}$$

where ψ_p is the proton's spinor. One may re-write eqs. (2.9 - 2.10) in terms of the Sachs form factors [16]:

$$G^{\gamma,Z}_E = F^{\gamma,Z}_1(Q^2) - \tau F^{\gamma,Z}_2(Q^2). \tag{2.11}$$

$$G^{\gamma,Z}_M = F^{\gamma,Z}_1(Q^2) + F^{\gamma,Z}_2(Q^2). \tag{2.12}$$

with $\tau \equiv |Q^2|/4m^2_p$. The electric, G^γ_E, and magnetic, G^γ_M, Sachs form factors have a clear

physical interpretation. In the case of zero energy transfer, $\nu \to 0$, the Fourier transform of each gives the spatial charge and magnetization distribution of the proton [16]. In the case where $Q^2 \to 0$, the form factors give the appropriate charge or intrinsic magnetic moment of the proton [16]. We observe for the electric-like form factors that the leading order assumption - the proton is composed of two up quarks and one down quark - is borne out [16]:

$$G_E^{\gamma}(Q^2 \to 0) = Q = 2Q^u + Q^d = 1, \tag{2.13}$$

$$G_E^{Z}(Q^2 \to 0) = Q_W^p = 2g_V^u + g_V^d = 1 - 4\sin^2\theta_W. \tag{2.14}$$

The proton's weak charge, defined in eq. (2.14), is the quantity that the Q_{weak} experiment was designed to measure.

2.2.1 The Parity-Violating $\vec{e}p$ Scattering Asymmetry

The leading-order approximation of the elastic ep scattering cross section is proportional to the quadrature sum of the scattering amplitudes given in eqs. (2.5) and (2.6):

$$\sigma \propto |\mathcal{M}_\gamma + \mathcal{M}_Z|^2 = |\mathcal{M}_\gamma|^2 + |\mathcal{M}_Z|^2 + 2\Re\left(\mathcal{M}_\gamma^* \mathcal{M}_Z\right). \tag{2.15}$$

In the case of low momentum transfer, $Q^2 \ll m_Z^2$, the strength of the weak interaction is known to be roughly 10^{-5} smaller than the EM strength, allowing us to ignore its contribution. If we look specifically at the scattering of ultra-relativistic, longitudinally polarized electrons (where the electrons are eigenstates of the parity operator), they have the property that the axial-vector coupling in eq. (2.8) changes sign depending upon the electron's handedness. Thus we can write a parity-violating asymmetry for electron-proton scattering:

$$A_{ep} = \frac{\sigma_+ - \sigma_-}{\sigma_+ + \sigma_-} = \frac{2\mathcal{M}_\gamma^* \mathcal{M}_Z^{PV}}{|\mathcal{M}_\gamma|^2 + \left|\mathcal{M}_Z^{PV}\right|^2} \approx \frac{2\mathcal{M}_\gamma^* \mathcal{M}_Z^{PV}}{|\mathcal{M}_\gamma|^2}. \tag{2.16}$$

where $+(-)$ subscripts denote right(left)-handed electrons and $\mathcal{M}_Z^{PV}$ represents the parity-violating portion of the amplitude in eq. (2.6). It is exactly this parity-violating electron

scattering (PVES) asymmetry that the Q_{weak} experiment was designed to measure.

Using the formalism of Section 2.2, we write the asymmetry in terms of the proton's Sachs form factors [15]:

$$A_{ep} = \frac{-G_F Q^2}{4\pi\alpha\sqrt{2}} \left[\frac{g_A^e \left(\epsilon G_E^{p,\gamma} G_E^{p,Z} + \tau G_M^{p,\gamma} G_M^{p,Z} \right) + g_V^e \epsilon' G_M^{p,\gamma} G_A^{p,Z}}{\epsilon \left(G_E^{p,\gamma} \right)^2 + \tau \left(G_M^{p,\gamma} \right)^2} \right], \tag{2.17}$$

where

$$\epsilon = \left[1 + 2\left(1+\tau\right)\tan^2\frac{\theta}{2} \right]^{-1}, \tag{2.18}$$

$$\epsilon' = \sqrt{\tau(1+\tau)(1-\epsilon^2)}, \tag{2.19}$$

are kinematic factors. One sees two contributions to the parity-violating asymmetry: a term proportional to the axial-vector electron current coupling with the vector quark current, and a term proportional to the axial-vector quark current coupling to the vector electron current.

Measuring the parity-violating asymmetry at Q_{weak} kinematics (low Q^2, forward angles) allows one to further simplify eq. (2.17) [15]:

$$A_{ep} \approx -\frac{G_F Q^2}{4\pi\alpha\sqrt{2}} [Q_W^p + Q^2 B(Q^2, \theta)], \tag{2.20}$$

where $B(Q^2, \theta)$ is now an effective form factor representing the contributions from the proton's internal structure. This formula allows straightforward extraction of the proton's weak charge simply by measuring the parity-violating asymmetry at a known, low Q^2 and constraining the effects of $B(Q^2, \theta)$ with previous experimental results. Such an approach involves defining a reduced asymmetry:

$$\overline{A_{ep}} = \frac{A_{ep}}{A_0} = Q_W^p + Q^2 B(\theta, Q^2), \tag{2.21}$$

where $A_0 \equiv -(G_F Q^2 / 4\pi\alpha\sqrt{2})$.

The preliminary extraction of this reduced asymmetry is shown in Figure 2.2. The extraction utilized PVES data from a number of previous experiments [17, 18, 19, 20] and

the published Q_{weak} asymmetry from the commissioning data set [21]. All data included in this figure are from proton targets and are rotated to the forward-angle limit. The $Q^2 = 0$ intercept of the fit is the first determination of the proton's weak charge,

$$Q_W^p(\text{PVES}) = 0.064 \pm 0.012, \tag{2.22}$$

which agrees with the SM prediction [5] (indicated in the figure by the arrow on the y-axis),

$$Q_W^p(\text{SM}) = 0.0712 \pm 0.0009. \tag{2.23}$$

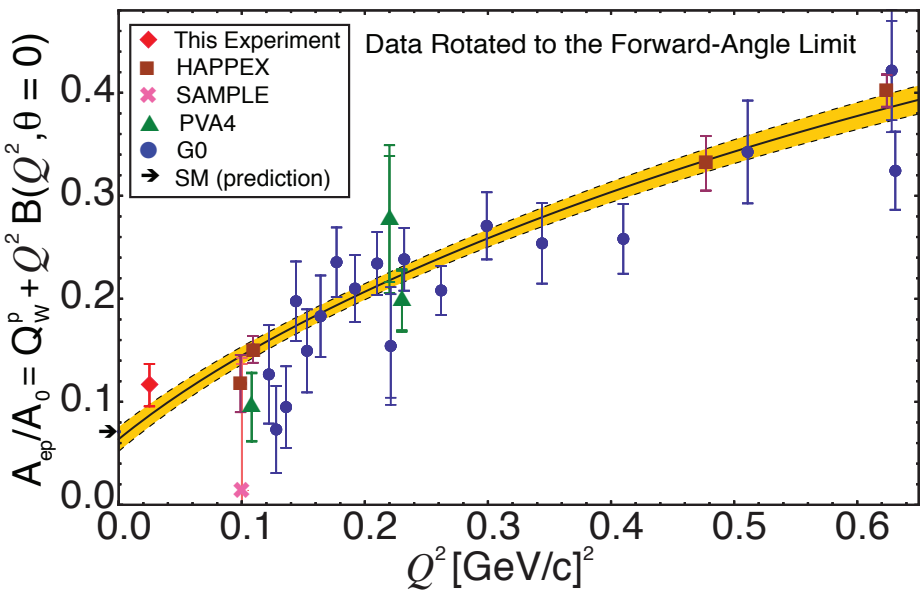

Figure 2.2: World data fit of the reduced asymmetry as a function of Q^2. The preliminary result of the Q_{weak} experiment, about 4% of the total data set, is included in this figure. This result is in good agreement with the SM prediction (indicated by an arrow on the y-axis). Reproduced from [21].

2.2.2 Quark Coupling Constants

At leading-order the proton's weak charge is a simple linear combination of the weak vector quark couplings C_{1u}, and C_{1d}. In general, the vector and axial-vector couplings, C_{1f} and

C_{2f} for quark flavor f, are defined in terms of the constants found in Table 2.1:

$$C_{1f} = -\frac{1}{2} g_V^f \tag{2.24}$$

$$C_{2f} = -\frac{1}{2}\left(1 - 4\sin^2\theta_W\right) g_A^f. \tag{2.25}$$

In particular, the proton's weak charge is equivalent to

$$Q_w^p(\mathrm{SM}) = -2\left(2C_{1u} + C_{1d}\right). \tag{2.26}$$

While this particular linear combination doesn't constrain the individual coupling constants, the results from atomic parity violation (APV) experiments[22] measure a nearly orthogonal combination of the vector weak quark couplings. Figure 2.3 shows the joint limits that are placed on the parameter space, resulting in $C_{1u} = -0.1835 \pm 0.0054$ and $C_{1d} = 0.3344 \pm 0.0050$ [21]. These results are in fair agreement with the SM predicted weak vector coupling coefficients for the up and down quarks, $C_{1u}(\mathrm{SM}) = -0.1885 \pm 0.0002$ and $C_{1d}(\mathrm{SM}) = 0.3414 \pm 0.0002$ respectively [5], indicated on the figure as a black dot at $\sin^2\theta_W(m_Z) = 0.231$.

2.3 Motivation for $\mathbf{Q_{weak}}$

The data displayed in Figure 2.2 indicate the importance of the Q_{weak} measurement. Aside from the Q_{weak} experiment, the data with the lowest Q^2 is at 0.1 (GeV/c)^2. Being located at the lowest momentum transfer to date, $\langle Q^2 \rangle = 0.025$ (GeV/c)^2, allows Q_{weak} to strongly influence the determination of Q_W^p. This makes Q_{weak} the first "direct" measurement of the proton's weak charge. The proton's weak charge is directly related to the weak mixing angle, a quantity of primary importance in the EW theory, as shown in eq. (2.14). The full data set for Q_{weak} should provide a 4% relative measurement of Q_W^p, which corresponds to a 0.3% relative measurement of $\sin^2\theta_W$. Q_{weak} will then be the most precise measurement of the weak mixing angle away from the Z pole. This allows the Q_{weak} experiment to measure the "running" of the weak mixing angle.

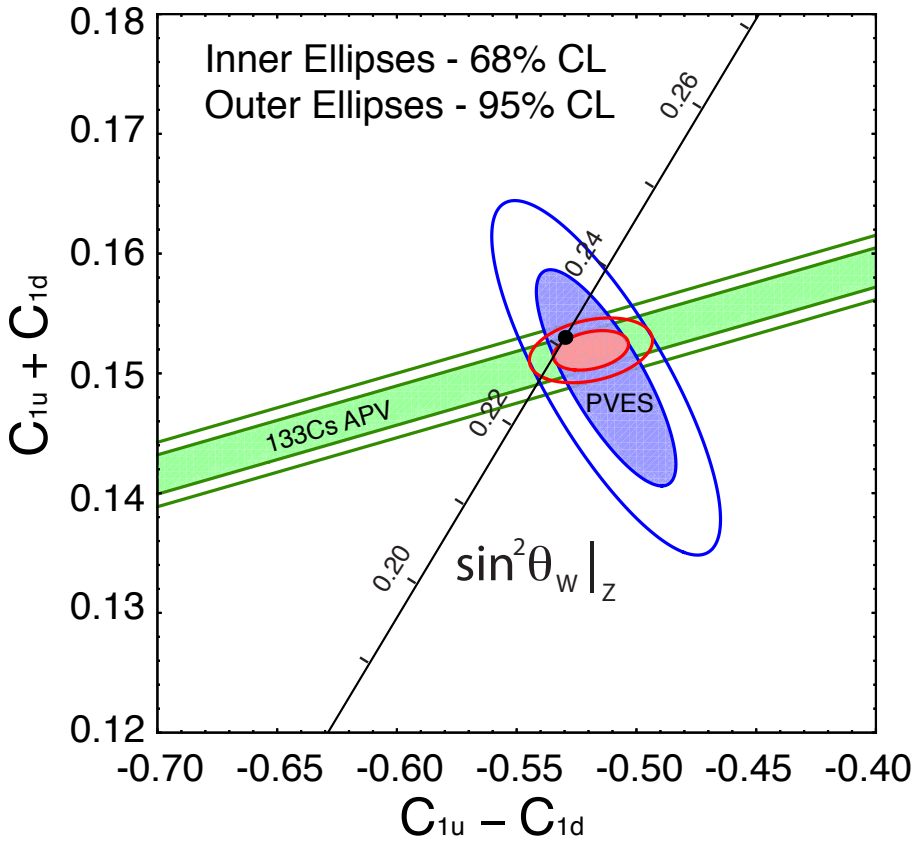

Figure 2.3: The constraints on the neutral-weak vector quark coupling constants. The x and y axes indicate the isovector and isoscalar combinations, respectively. The green band represents constraints from APV measurements [22]. The blue ellipse represents the combined PVES measurements, including the Q_{weak} experiment's preliminary result (roughly 4% of the total data). The small ellipse at the intersection shows the combined bounds put on the quark coupling constants. Reproduced from [21].

2.3.1 Running of the Weak Mixing Angle

It is well known that the EM fine structure constant, α, varies with momentum transfer. In the low Q^2 limit, one observes the well known value $\alpha \approx 1/137$, while at the scale of the Z mass, one observes $\alpha \approx 1/129$ [23]. It is predicted that the weak mixing angle, $\sin^2\theta_W$, has an analogous dependence upon Q^2, which is reffered to as the "running" of the weak mixing angle. Measurements at the Z pole, $\sqrt{Q^2} \approx 100GeV$, have constrained the weak mixing angle at that mass scale [5]. However, measurements at many different values of Q^2 with sufficiently small uncertainties are required to reasonably constrain the running. Accurately predicting this running is a non-trivial test of the validity of renormalization in EW quantum field theory. Currently, there are four results at low momentum transfer

($Q^2 \ll m_Z^2$): one from atomic parity-violation in cesium [22], a second from high-energy neutrino scattering from iron nuclei [24], a measurement of PV deep inelastic scattering [25] and one from PV Møller scattering at low momentum transfer [26].

Figure 2.4 shows the measurements of the weak mixing angle as a function of $Q = \sqrt{Q^2}$ from the above experiments as well as the result of the Q_{weak} commissioning data. The measurements at the Z pole fix the overall scale of the weak mixing angle using eq. (1.5). However, this is known to be accurate only to leading order since the masses of the weak bosons have a finite width. The curve in Figure 2.4 is from calculations [27] done in the modified Minimal Subtraction ($\overline{\text{MS}}$) renormalization scheme [28], which utilizes the coupling definition of $\sin^2\theta_W$ in eq. (1.4). The horizontal axis of Figure 2.4 is the renormalization scale, chosen to be identical to Q. The various discontinuities occur at particle masses that can appear in loops leading to γZ admixture. The weak mixing angle increases by roughly 3% as $Q \to 0$ from the Z pole.

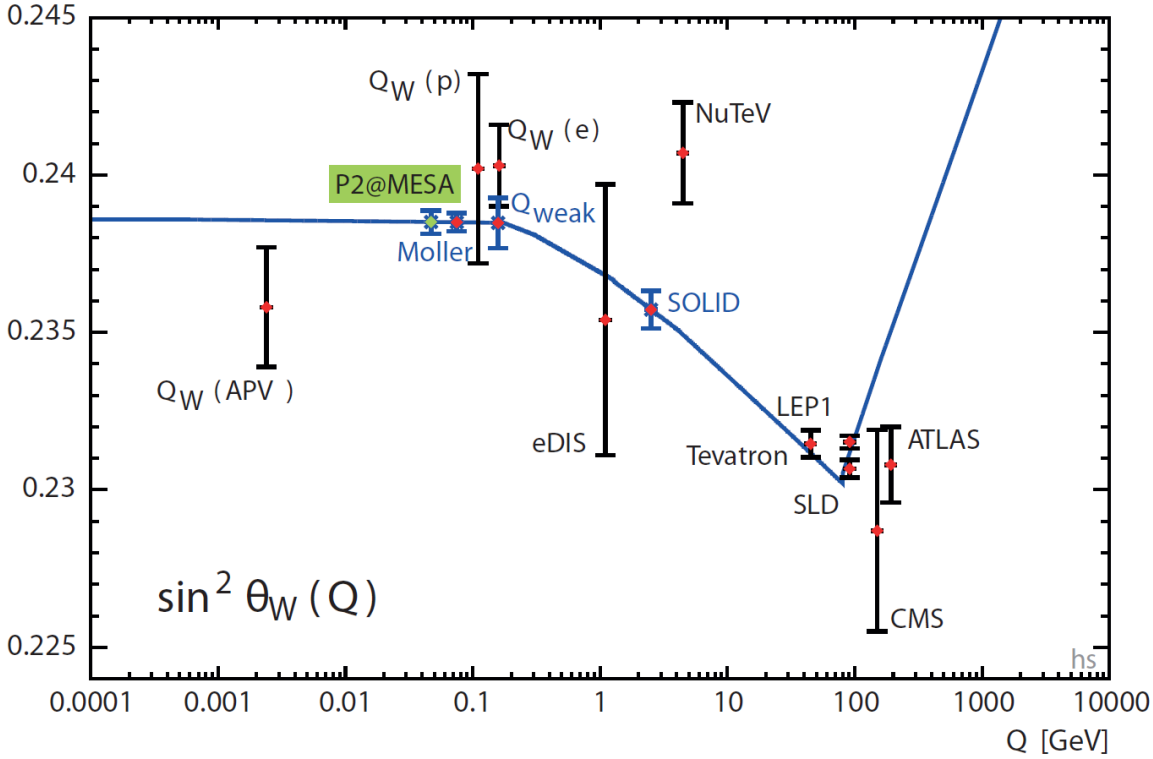

Figure 2.4: Scale dependence of the weak mixing angle in the $\overline{\text{MS}}$ renormalization scheme along with selected published measurements [22, 24, 26, 29, 25] and proposed measurements [30, 31, 32]. Reproduced from [30].

The Q_{weak} experiment's full data set will provide the most precise measurement of the running of $\sin^2\theta_W$ to date. This is due in part to the statistical and systematic experimental precision and partly due to the relative ease with which the asymmetry measurement may be interpreted in terms of the weak mixing angle, as discussed in Section 2.2.1. The Q_{weak} measurement, a semi-leptonic measurement, serves as a complementary probe of physics beyond the SM to the E-158 experiment [26], a purely leptonic measurement. The two experiments, at similarl values of Q^2, have different signatures for various models of physics beyond the SM.

2.3.2 Parity-Violating Physics Beyond the Standard Model

As a high-precision test of standard model parameters, the Q_{weak} experiment is sensitive to certain types of new parity-violating physics. Some well motivated examples of such physics include new supersymmetric (SUSY) particles, leptoquarks, or new Z' gauge boson. Figure 2.5 shows the effects these new physics would produce in both the Q_{weak} experiment and E-158 [26] at SLAC.

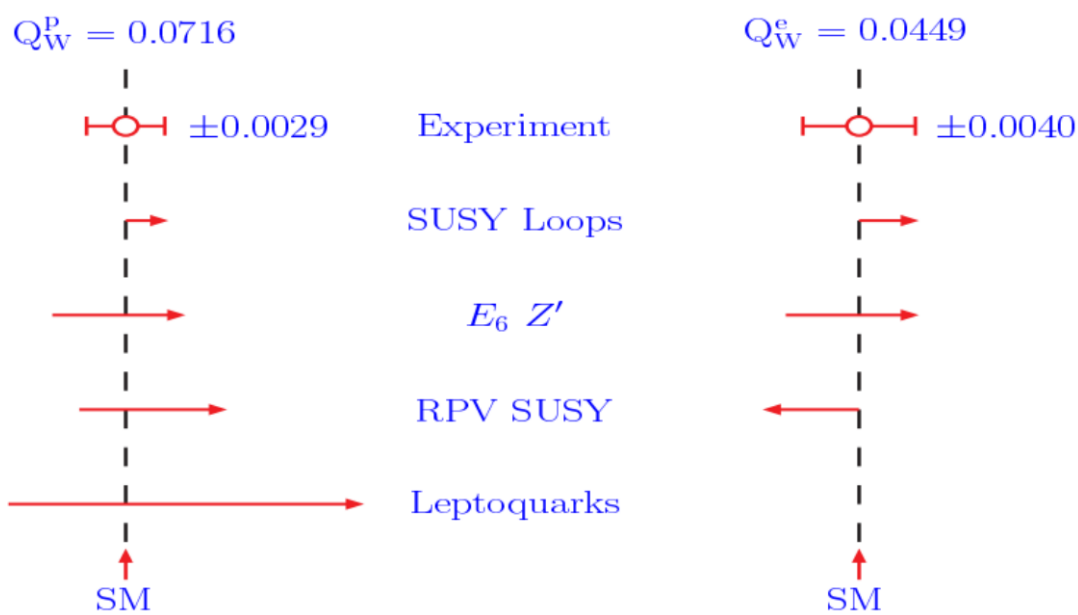

Figure 2.5: Comparison of predicted experimental precision with deviations from SM predictions due to various types of new physics. Reproduced from [27]. Note that the predicted value of Q_W^p has been updated since the publication of [27] due to improvements in electroweak loop corrections.

In order to quantify the sensitivity to physics beyond the SM, we follow the example of Erler, Kurylov and Ramsey-Musolf [27] and construct the PV Lagrangian for axial-electron vector-quark interactions with the new term:

$$\mathcal{L}^{PV} = \mathcal{L}^{\mathrm{PV}}_{\mathrm{SM}} + \mathcal{L}^{\mathrm{PV}}_{\mathrm{NEW}}. \tag{2.27}$$

At sufficiently low values of Q^2, we can treat these pieces as four-point contact interactions. The effective PV Lagrangians are:

$$\mathcal{L}^{\mathrm{PV}}_{\mathrm{SM}} = -\frac{G_F}{\sqrt{2}}\bar{u}_e\gamma_\mu\gamma^5 u_e \sum_q C_{1q}\bar{u}_q\gamma^\mu u_q, \tag{2.28}$$

$$\mathcal{L}^{\mathrm{PV}}_{\mathrm{NEW}} = \frac{g^2}{4\Lambda^2}\bar{u}_e\gamma_\mu\gamma^5 u_e \sum_q h^q_V\bar{u}_q\gamma^\mu u_q \tag{2.29}$$

where g, Λ and h^q_V are the coupling constant, mass scale and effective coefficients associated with the new physics. Assuming Q_{weak} returns the SM value of Q^p_{W} with an uncertainty δQ^p_W, we can place a limit on the mass scale of the new PV physics:

$$\frac{\Lambda}{g} \approx \left(2\sqrt{2}G_F\delta Q^p_W\right)^{-1/2}. \tag{2.30}$$

If one were to take $g = h^q_V = 1$ (as in Figure 2.6) and Q_{weak} reaches a precision of 4%, this corresponds to a roughly 2.3 TeV mass reach, excluding new PV physics below this mass to a 95% confidence level. There currently exists a controversy within the community with regard to what value to use for the coupling constant g [33, 34].

2.4 Elastic Electron-Carbon Scattering

We now move on to discuss the theory behind another measurement made using the Q_{weak} apparatus: the elastic electron-carbon scattering beam-normal single-spin asymmetry (BNSSA). This is an asymmetry that arises from a transversely polarized beam scattering from an unpolarized target. This asymmetry is an observable of the two-photon exchange (TPE) interactions [36]. An accurate measurement of this observable is required to cor-

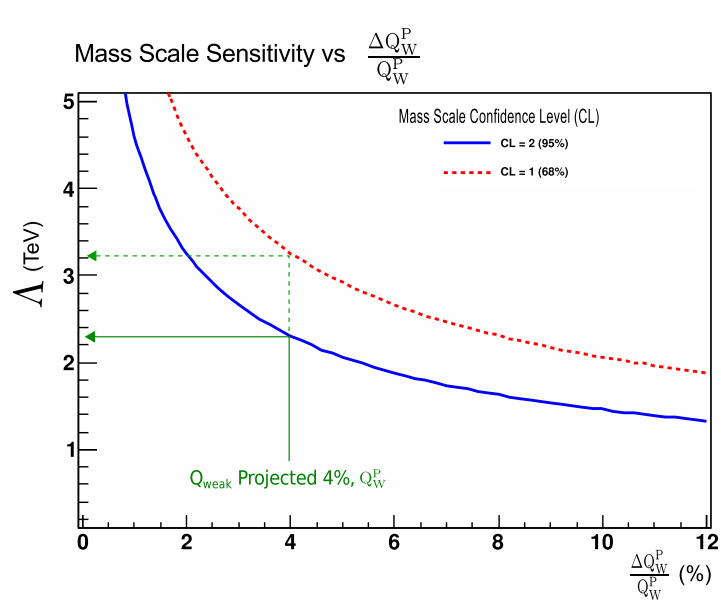

Figure 2.6: Mass scale (Λ) for new parity violating physics as a function of the precision of a measurement of the proton's weak charge. The solid (dotted) curves show the 95% (68%) CL. Reproduced from [35].

rect its effects on precision PVES experiments. Additionally, an accurate understanding of BNSSA observables is required for scattering predictions beyond the Born approximation.

2.4.1 Born Approximation for Electron-Nucleus Scattering

In this section, we discuss elastic electron-carbon nuclear scattering, $e(k) + C(p) \to e(k') + C(p')$. The tree-level, one-photon-exchange (OPE) Feynman diagram of this process, depicted in Figure 2.7, has traditionally been a good approximation of this process within a few percent. The kinematics of this scattering, shown in Figure 2.8, are identical to the more general case discussed in Section 2.1 with the addition of the electron's polarization vector, **S**.

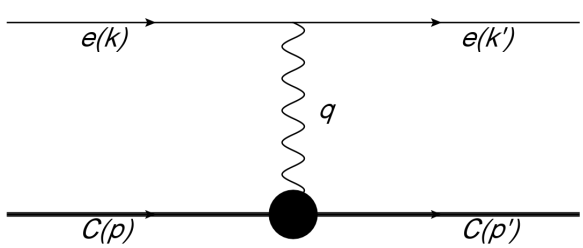

Figure 2.7: The tree-level elastic scattering of an electron from a carbon nucleus.

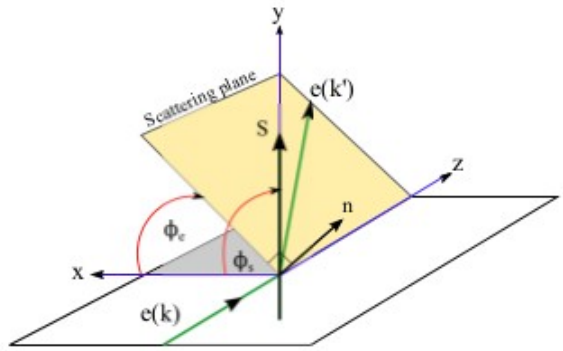

Figure 2.8: Kinematics of an electron with vertical polarization (**S**) scattering from a nucleus. The initial (final) momentum of the electron is k ($k^{'}$). The angle ϕ_e (ϕ_s) refers to the azimuthal angle of the scattered electron (initial polarization) defined from beam left. The scattering plane's normal vector, $\hat{\mathbf{n}}$, is defined below eq. (2.33). Reproduced from [37].

The differential scattering cross section for this process in the Born approximation is:

$$\frac{d\sigma}{d\Omega} = \left(\frac{d\sigma}{d\Omega}\right)_{\text{Mott}} \left|F(q^2)\right|^2 \tag{2.31}$$

where the Mott cross section is given by

$$\left(\frac{d\sigma}{d\Omega}\right)_{\text{Mott}} = \left(\frac{\alpha\hbar c Z}{2E}\right)^2 \frac{\cos^2\theta/2}{\sin^4\theta/2}\frac{E^{'}}{E}, \tag{2.32}$$

where $E^{'}/E = 1/\left(1 + 2(E/m_C)\sin^2\theta/2\right)$, and Z is the charge of the nucleus in elementary units, and m_C is the mass of the nucleus. In eqs. (2.31) and (2.32), the Mott cross section refers to the scattering cross section derived assuming two spinless point particles interacting under the Coulomb force, while the form factor, $\left|F(q^2)\right|^2$, represents the deviations from this assumption due to finite charge distribution. Corrections to this approximation due to higher-order (in α) diagrams are suppressed by the additional vertex factors and generally contribute little to the measured cross section.

2.4.2 Transverse Asymmetry from TPE

It has long been known that scattering asymmetries arise from spin-orbital coupling in electron-nucleus scattering [38, 39]. In the case of transverse polarized electrons scattering

from unpolarized nuclei, we observe BNSSA to have an azimuthal dependence:

$$B(\phi_e) = B_n \mathbf{S} \cdot \hat{\mathbf{n}} = B_n |S| \sin(\phi_e - \phi_s), \tag{2.33}$$

where $\hat{\mathbf{n}} = \frac{\mathbf{k}\times\mathbf{k}'}{|\mathbf{k}\times\mathbf{k}'|}$ is the unit vector perpendicular to the scattering plane and B_n is the analyzing power (known as the Sherman function in low-energy Mott scattering).

This analyzing power can only arise when there is a non-zero imaginary part of the scattering amplitude. However, in the OPE approximation discussed in the previous section, this imaginary part of the scattering amplitude is identically zero. The TPE processes which generate the BNSSA are shown in Figure 2.9. At leading order, the BNSSA asymmetry is the result of interference from the one- and two-photon exchange processes and has the form [40]:

$$B_n = \frac{2\mathrm{Im}\mathcal{M}^*_{\gamma\gamma}\mathcal{M}_\gamma}{|\mathcal{M}_\gamma|^2} \tag{2.34}$$

where $\mathcal{M}_\gamma$ and $\mathcal{M}_{\gamma\gamma}$ represents the one- and two-photon exchange processes, respectively.

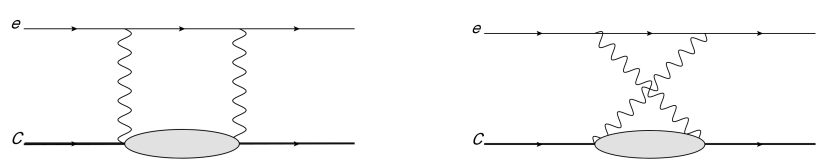

Figure 2.9: The two-photon exchange diagrams that lead to the observed BNSSA in electron carbon scattering. The gray ovals indicate all possible elastic and excited intermediate states that must be summed over to calculate the amplitude.

The imaginary part of the two photon exchange for electron-nucleus scattering is calculated to be [41]

$$\mathrm{Im}\mathcal{M}_{\gamma\gamma} = \frac{e^4}{(2\pi)^3} \int \frac{d^3\vec{k}_1}{2E_1} \frac{1}{Q_1^2 Q_2^2} l_{\mu\nu} W^{\mu\nu}(\omega, Q_1^2, Q_2^2), \tag{2.35}$$

where the explicitly on-shell ($E_1 = \sqrt{{\mathbf{k}_1}^2 - {m_e}^2}$) leptonic tensor is given by

$$l_{\mu\nu} = \bar{u}_e(k')\gamma_\mu \left[\not{k}_1 + m_e\right] \gamma_\nu u_e(k) \tag{2.36}$$

and the nuclear tensor ($W^{\mu\nu}$) is a function of the invariant mass, ω, of the intermediate nuclear state and the incoming(outgoing) virtual photon four momentum-transfer, $Q^2_{1(2)}$.

The calculation required in eq. (2.35) can be completed using various simplifying assumptions and several fitting parameters [41, 42]. In the case of the proton, similar calculations have been carried out under a wide variety of assumptions [43, 40, 44, 45]. The calculations for scattering from the proton and from spin-0 nuclei (such as ^{12}C) show a high degree of model dependence; their predictions can vary by as much as a factor of 4. However, these calculations share several features, primary among them is that the inelastic intermediate states contribute far more to the transverse asymmetry than elastic intermediate states [41]. Additionally, there is a common prediction of linear scaling with respect to $Q = \sqrt{Q^2}$. Using the results provided by Gorchtein and Horowitz [41], one predicts a scaling of the BNSSA in elastic electron-nucleus scattering to be:

$$B_n \approx B_0 \frac{A}{Z} \sqrt{Q^2} \tag{2.37}$$

where A is the atomic mass number of the nucleus, Z is its electric charge, and B_0 is simply a scaling factor in typical units of ppm/(GeV/c).

2.5 Previous Measurements and Motivation: BNSSA on Carbon

In the new millennium, at Jefferson Lab, there have been many precision measurements of asymmetries from semi-leptonic scattering. In particular, there have been several measurements of BNSSA on both the proton and composite nuclei [46, 47, 48]. As these measurements have been made, the theory has grown accordingly. However, neither experiment nor theory is mature at this point. As can be seen in Figure 2.10, there remain discrepancies in scaling with both Q and in terms of proton number Z. Interestingly however, the results of a PV deep inelastic scattering (DIS) experiment on a deuterium target at higher momentum-transfer ($Q^2 \in [1.0, 1.9]$ (GeV/c)^2) [49] measured a transverse asymmetry that agreed with the predictions for elastic scattering on the proton.

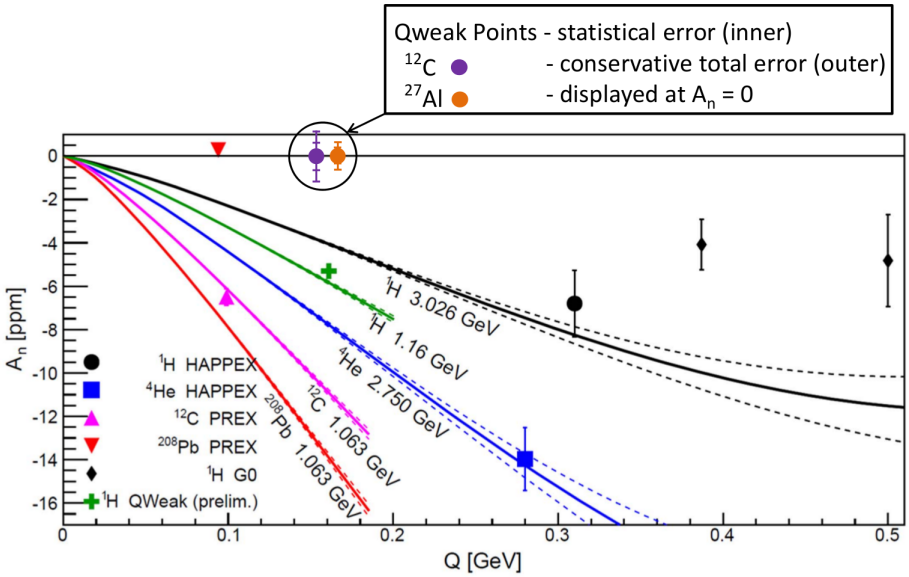

Figure 2.10: Measurements of BNSSA in various nuclei [46, 47, 48] (including preliminary Q_{weak} results on the proton [37]) compared to the predictions [41]. The measured ^{208}Pb data show extreme disagreement with theory while the results from the G0 experiment [48] disagree at larger Q^2. Also shown is the expected precision of the intermediate nuclear results from measurements performed using the Q_{weak} apparatus (centered at zero). Reproduced from [50].

Because the Q_{weak} experiment was designed to perform asymmetry measurements with precision on the order of 10^{-8}, it was relatively easy to take measurements of BNSSA, $\mathcal{O}(10^{-6})$, quickly. As such, a program was developed to measure the BNSSA from ^{1}H, ^{12}C, and ^{27}Al. These results would aid in understanding scattering beyond the Born approximation by directly accessing information about the imaginary part of the TPE amplitude. The carbon measurement, in combination with the measurements from the PREx experiment[51], would provide an excellent constraint on the Q scaling, and particularly the angular portion thereof, due to the similar beam energy of the two results. Unfortunately, as is discussed in Chapters 5 and 6, the transverse asymmetry measured on carbon was not due solely to elastic scattering. It also contained scattering asymmetries from excited states of the carbon nucleus. There is no accepted theory for predicting the asymmetry of these states, nor are there any published experimental results available for scattering asymmetries from these states. In these circumstances, the result presented at the end of this thesis is not as cleanly interpretable as was initially expected.

Chapter 3

The Q_{weak} Experimental Apparatus

The Q_{weak} experiment (E08-016) [52] was performed at the Thomas Jefferson National Accelerator Facility (JLab) in Experimental Hall C from July 2010 through May 2012. The world's first dedicated measurement of the proton's weak charge, Q_W^p, was performed by measuring the parity-violating (PV) asymmetry in elastic electron-proton scattering. An entirely new experimental apparatus [53] was designed and constructed in Hall C to measure this asymmetry. A rendering of this apparatus can be seen in Figure 3.1. Typical experimental parameters, such as beam current and energy, scattering kinematics and detector acceptance are given in Table 3.1. This chapter will provide a general overview of the experimental method and detailed information about important subsystems of the Q_{weak} apparatus.

Parameter	Value
Incident Beam Energy	1.16 GeV
Beam Polarization	89%
Beam Current	180 μA
Target Length	34.4 cm
Nominal Scattering Angle	7.9°
θ - Acceptance	5.8° - 11.6°
ϕ - Acceptance	49% of 2π
Solid Angle	43 msr
Acceptance Averaged Q^2	0.025 (GeV/c)^2
Event Rate (per octant)	6.5 GHz (0.8 GHz)
Full Current Production Running	$\sim$ 2400 hours

Table 3.1: Basic parameters for Q_{weak} production running.

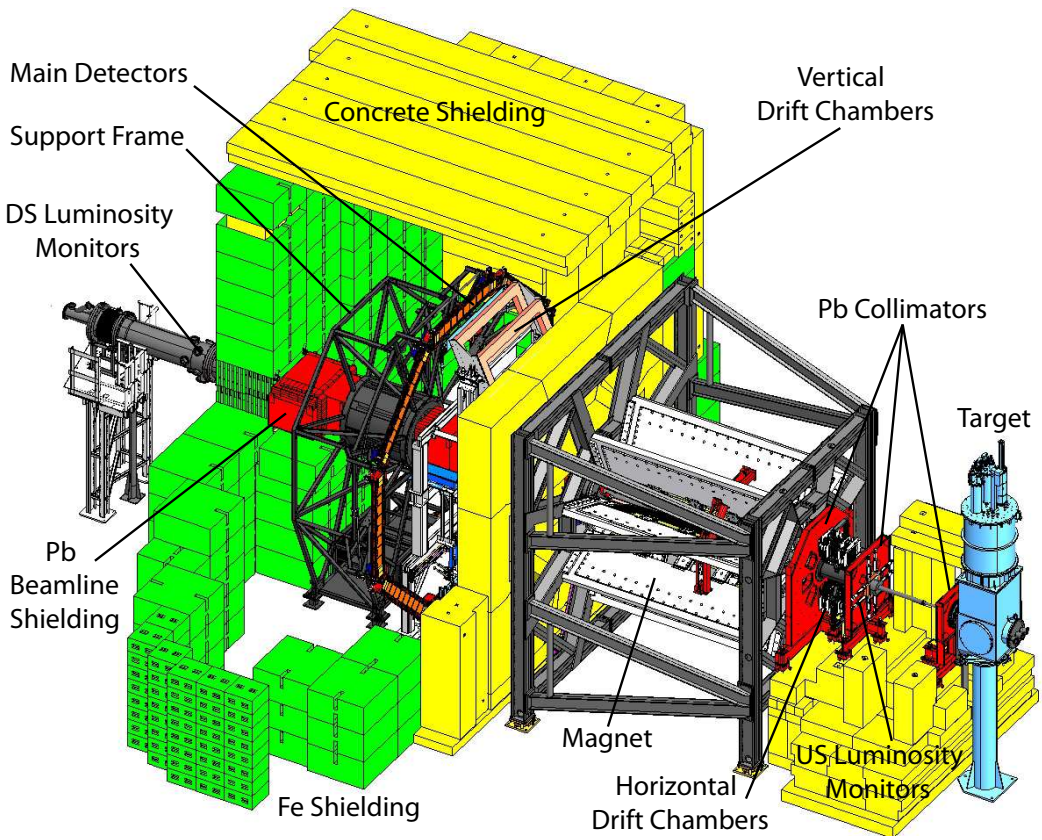

Figure 3.1: CAD schematic of the Q_{weak} apparatus. The beam entered the target from the lower right of the figure. After scattering, electrons passed through the collimators, magnetic field and shielding to hit the main detectors inside the shielded region (shown in a cutaway in the center left of the figure). Reproduced from [53].

3.1 Experiment Overview

The main PV experiment used a high-current beam of longitudinally polarized electrons incident upon a liquid hydrogen (LH_2) target. The scattered electrons passed through a series of three collimators into the field of the Q_{weak} toroidal spectrometer magnet (QTor) that focused elastically scattered electrons onto eight symmetrically placed quartz Čerenkov main detectors (MDs). The electron beam's helicity, defined as the projection of its spin $\mathbf{S}$ onto it's momentum $\mathbf{p}$,

$$h = \frac{\mathbf{S} \cdot \mathbf{p}}{|\mathbf{S}|\,|\mathbf{p}|}, \tag{3.1}$$

was flipped at a rate of 960 Hz. The helicity states were chosen pseudo-randomly and had a *quartet* structure. Once the first state (+ or -) was chosen, the remaining states

were automatically determined, giving two possible patterns: (+,-,-,+) or (-,+,+,-). This pseudo-random, quartet pattern was designed to minimize the experimental sensitivity to linear drifts as well as noise from target boiling. The PV asymmetry was computed for each quartet by integrating the measured signal from the Čerenkov detectors over periods of stable beam helicity and computing the relative difference between states with positive and negative helicity.

The asymmetry of a quartet was defined as

$$A_{raw} = \frac{Y_+ - Y_-}{Y_+ + Y_-}, \tag{3.2}$$

Where $Y_{+(-)}$ was the integrated signal during the positive(negative) helicity states, normalized for measured beam current. This raw asymmetry was related to the physics asymmetry, A_{ep}, by the equation

$$A_{raw} = P\left(\frac{1-\sum_{b=1}^{4} f_b}{R} A_{ep} + \sum_{b=1,3,4} f_b A_b\right) + A_{beam} + A_{BB} + A_T + A_L + A_{PS}. \tag{3.3}$$

The terms in this equation represent:

- $f_b = Y_b/Y$ - fractional contributions of background b to the integrated signal
  - $b = 1$ - aluminum target windows
  - $b = 2$ - beamline background (BB)
  - $b = 3$ - QTor Transport Channel Neutral Background (QTCNB)
  - $b = 4$ - inelastic scattering background
- A_b - the asymmetry of each background
- A_{beam} - false asymmetry due to helicity-correlated (HC) beam properties
- A_T - false asymmetry from signal leakage of residual transverse polarization
- A_L - asymmetry offset due to non-linear detector response
- A_{PS} - detector bias due to secondary scattering asymmetries in detector preradiators

- P - the beam's longitudinal polarization
- R - several corrections due to detector acceptance and radiative effects

The calculation of these quantities will be covered in detail in Chapter 4.

The Q_{weak} experiment had two data-taking modes distinguished by beam current and detector readout procedure. The first, known as *production* mode, was performed at high beam current, $I_{beam} > 50\mu$A, and the detector signals were integrated over each constant-helicity window. This method was how the large majority of the data were taken, including the various transverse asymmetry measurements. The second type of data taking was known as *event* mode. These data were taken at low beam currents, $I_{beam} \in$ [100 pA, 100 nA], and were primarily used to determine the experimental kinematics and observe signals from certain backgrounds. During event-mode data taking, tracking detectors (detailed in Section 3.12) were inserted into the scattering acceptance. Additionally, the photomultiplier tube (PMT) bases on the MD bars were changed and the electronics and data acquisition (DAQ) software were altered to allow the recording of hits by individual electrons incident on the various detectors. Data read-out in event mode was triggered when a selected event definition was met.

The data taken with this apparatus were broken into distinct temporal periods:

- Run 0: Jul 2010 - Jan 2011
- Run I: Feb 2011 - May 2011
- Run II: Nov 2011 - May 2012

Each run period was assigned its own independent blinding factor with a value, $|b| < 60$ ppb, to offset the raw, quartet-level asymmetry as:

$$A_{raw}^{blind} = \frac{Y_+ - Y_-}{Y_+ + Y_-} + b.$$

These run periods could then be independently analyzed and un-blinded when the analysis was sufficiently mature. The Run 0 data, roughly 4% of the total data set, were unblinded and published in 2013 [21]. This dissertation will discuss the blinded analysis of A_{ep} as

measured in Run II in Chapter 4. The Run I data set is currently being analyzed alongside the Run II data and both will be unblinded simultaneously in the near future. The transverse measurement on carbon, which was not blinded, took place during Run II and is discussed in Chapter 5.

All of the production-mode data were organized into segments of approximately 6 minutes, called *runlets*. Data were taken in groups of approximately 10 runlets, called *runs*. Every eight hours or so the helicity of the beam was reversed using an insertable half-wave plate (IHWP) in the injector's laser table (described in the next section). These groups of runs were referred to as *slugs*. Roughly every month, the helicity was also reversed by altering the injector's Wein filters, producing a data set known as a *Wien*. In total, 10 Wiens were taken. The combined data set comprised approximately 1.5×10^9 quartets.

The remainder of this chapter is dedicated to discussing, in varying degrees of detail, the systems necessary to perform the Q_{weak} experiment and the ancillary measurements. The discussion follows the form of and draws heavily from Allison *et al.* [53].

3.2 Polarized Electron Source

The generation of polarized electron beams at JLab was a well developed process by the time of the Q_{weak} experiment. Circularly polarized laser light was incident on a prepared photo-cathode. The photoelectric effect produced free electrons that, through conservation of angular momentum, had a known spin. The electrons were then accelerated away from the surface of the photo-cathode via an electrostatic field. A schematic of the polarized source is shown in Figure 3.2.

The Hall C polarized beam began with a laser pulsed at a rate of 499 MHz. The laser radiation passed through several optical steering elements and a linear polarization filter, giving the light a vertical polarization. Shortly beyond this, an insertable half-wave plate (IHWP) was used for slow polarization reversal of the laser. This element changed the sign of the experimental asymmetry roughly every 8 hours by flipping the laser polarization without changing the sign of any electronic signals of the helicity (such as the Pockels cell voltage). The laser light then passed through the Pockels cell, which circularly polarized

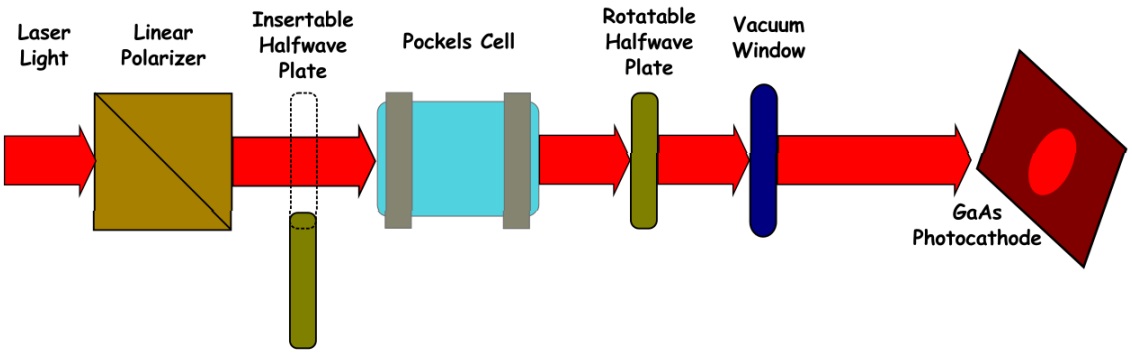

Figure 3.2: Schematic of the CEBAF beam generation. Photon polarization was controlled via the linear polarizer, insertable half-wave plate (IHWP) and Pockels Cell. Additional optical elements are not shown. Reproduced from [54].

the light to varying degrees dependent upon the voltage applied. Flipping the voltage at a rate of 960.15 Hz provided the fast helicity control for the Q_{weak} experiment.

The circularly polarized light then impinged on a p-doped GaAs/GaAsP wafer producing polarized electrons. The electrons were steered into a section of beamline where Wien filters and a solenoid defined the polarization of the electrons over all possible orientations [55]. The Wien filters were used as an additional source of slow helicity reversal, sensitive to different parameters from the laser table IHWP and Pockels cell, roughly once a month. Additionally, these elements could be used to set the polarization such that, when the electrons reached the target, their polarization was completely transverse, allowing the measurement of various transverse asymmetries.

The Q_{weak} experiment proved the most demanding experiment to date for the JLab polarized source. The Q_{weak} collaboration and the JLab Center for Injector Studies group performed many detailed calibrations to ensure that the helicity-correlated beam asymmetries (HCBAs) were minimized. This work resulted in beam position monitors (BPMs) measuring the smallest recorded HC differences ($\leq$ 20 nm) downstream of the photo-cathode. Details of the optimization of the polarized source pertinent to Q_{weak} are discussed in [56].

3.3 Accelerator

After being produced, the polarized electrons were accelerated to $\sim$ 60 MeV in the injector beamline before being fed into the main accelerator. The accelerator at the time of the

Q_{weak} experiment (shown in Figure 3.3), consisted of 2 linear accelerators (linacs) and 2 sets of recirculating arcs. The primary device for accelerating electrons in both the injector and the linacs is the superconducting radio-frequency (SRF) cavity [57]. Each cavity consisted of 5 SRF cells manufactured at JLab out of pure niobium. The cavities were grouped as 8 units that shared cryogenic cooling, known as a *cryomodule*. Each linac used 20 cryomodules to accelerate electrons up to 548 MeV. The beam could pass through the linac pair up to 5 times before being diverted into the experimental hall, allowing energies up to 6 GeV[1].

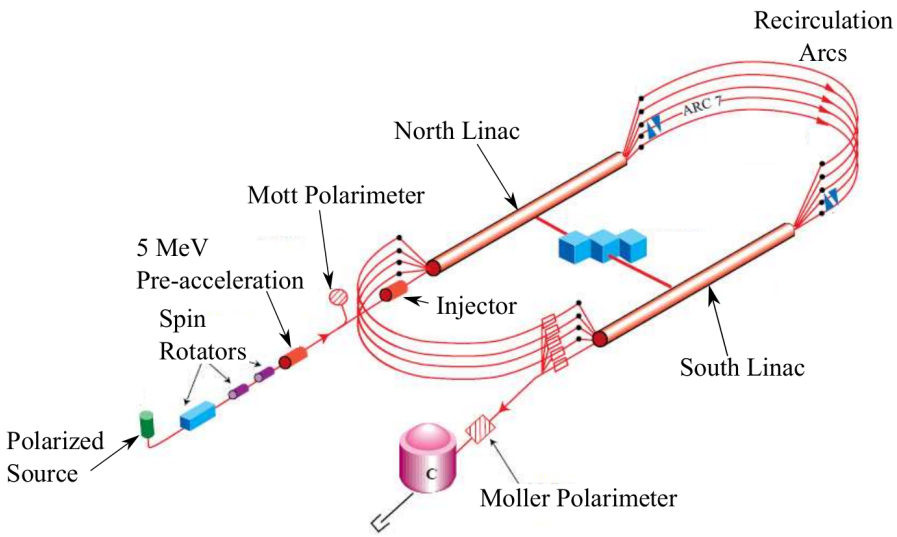

Figure 3.3: A schematic of the Continuous Electron Beam Accelerator Facility (CEBAF) as it was during the Q_{weak} experiment. Polarized electrons were generated in the injector, accelerated in the linear accelerators (linacs) and circulated in the arcs until the desired energy is achieved at which point the beam was extracted and delivered to the experimental halls. Reproduced from [58].

Once the electrons left the injector, they were relativistic to the point that their speed was approximately independent of energy. Thus the high-energy and low-energy electrons could stay in phase with respect to the SRF cavity frequency, allowing for simultaneous acceleration of high and low energy electrons. At the end of each linac, the electrons with different momenta were steered into the appropriate recirculating arc. At the end of the arc, the electrons were steered with a set of dipoles into the next linac. After a set number of circuits to reach the desired energy, RF separators deflected the beam into the appropriate

[1]After the conclusion of Q_{weak} data taking, the CEBAF undertook an extensive upgrade program: increasing the number of cryomodules per linac and building an additional recirculating arc to produce energies of almost 12 GeV and building an additional experimental hall.

hall. The accelerator could deliver maximum energy beam to all 3 experimental halls simultaneously. The Q_{weak} experiment ran almost exclusively with 1-pass beam with an energy of 1.16 GeV. Additional systematic checks and ancillary measurements were made with 3-pass beam (3.3 GeV), low energy (877 MeV) 1-pass beam, and 3-pass beam at 1.16 GeV.

3.4 Polarimetry

The Q_{weak} experiment needed precision polarimetry for two reasons. First, the measurement of the beam polarization was expected to be the largest source of systematic uncertainty in the Q_{weak} measurement. Second, polarimeters were used to ensure that there was negligible transverse polarization in the beam when it reached the target. Prior to the experiment, the Hall C Møller polarimeter [59] had provided polarization measurements with a precision $\lessapprox$ 1.5% for many years. However, Møller measurements were invasive, meaning they interfered with the beam so that it could not be delivered in usable form to an experiment. Additionally, Møller measurements could only be performed at relatively low current, $I_{beam} \approx 2\ \mu$A, which could have introduced an error due to current-dependence in the polarization. Thus, the Hall C Compton Polarimeter was commissioned during the Q_{weak} experiment. Capable of non-invasive measurements at the full Q_{weak} beam current of 180 μA, the Compton polarimeter measured the absolute polarization with a statistical precision better than 1% per hour. In addition to these polarimeters in the experimental hall, the CEBAF injector maintained a Mott polarimeter. Previously, this polarimeter was used to calibrate the Hall polarimeters. During the Q_{weak} experiment, this polarimeter was only used to verify that there was no residual transverse polarization in the beam for production data taking and to determine the degree of transverse polarization during the transverse running. The two Hall C polarimeters are discussed below while the Mott polarimeter, which the author worked on, is discussed in detail in Appendix A.

3.4.1 Møller Polarimeter

The Hall C Møller polarimeter measured the spin-dependent asymmetry in elastic $e + e \rightarrow e + e$ scattering. The polarization-dependent Møller cross section is

$$\frac{d\sigma}{d\Omega} = \sigma_0 \left[1 + P_b^{\parallel} P_t^{\parallel} A_{zz}(\theta_{CM})\right] \tag{3.4}$$

where σ_0 is the unpolarized cross section, $P_b^{\parallel}$ is the electron beam's longitudinal polarization, $P_t^{\parallel}$ is the target electron's polarization, θ_{CM} is the scattering angle in the center-of-mass frame and $A_{zz}(\theta_{CM})$ is the longitudinal spin-dependent analyzing power.

The Møller polarimeter, shown schematically in Figure 3.4, used a superconducting solenoid with a field strength of 3.5 T (above the saturation strength of 2.2 T) to polarize a 1 μm thick pure iron target along the positive beam axis. The scattered incident electron and recoiling target electron were detected in coincidence by a pair of lead-glass calorimeters. Coincidence detection virtually eliminated the Mott scattering background. The acceptance was defined by a series of collimators centered around $\theta_{CM} = 90°$ in order to maximize the analyzing power. The largest sources of uncertainty for this polarimeter comes from scattering from unpolarized non-valence electrons and the intrinsic momentum distribution of the bound electrons (the Levchuck effect) [60]. In addition, one must extrapolate from low beam currents at which the Møller polarimeter operates to the high current of Q_{weak}.

This polarimeter was used throughout the experiment to measure the beam's polarization, typically two or three times a week. In addition, this polarimeter was used in combination with the Mott polarimeter in the injector to ensure there was no residual transverse polarization. More information on the Møller polarimeter can be found in reference [61].

3.4.2 Compton Polarimeter

The Hall C Compton polarimeter was designed to provide continuous, non-invasive polarization monitoring during the running of the Q_{weak} experiment. This polarimeter measured the scattering asymmetry between beam helicity states in the $\vec{e} + \vec{\gamma} \rightarrow e + \gamma$ process. The

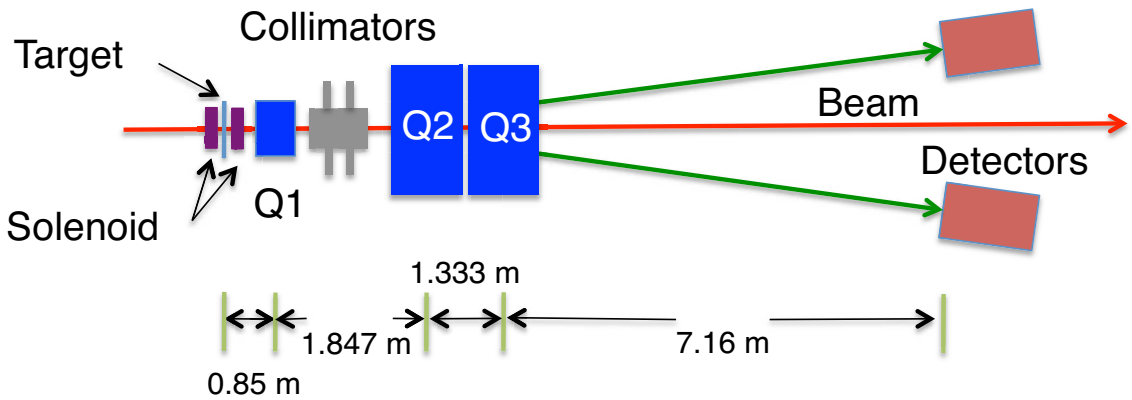

Figure 3.4: Layout of the Hall C Møller polarimeter. The second quadrupole magnet (Q2) was not used during Q_{weak}, but was installed in preparation for the 12 GeV upgrade at CEBAF. Reproduced from [53].

Compton scattering cross section for polarized photons and electrons is

$$\frac{d\sigma}{dxd\phi} = \sigma_0 \left(1 - P_\gamma \left[P_e^{\parallel} A^{\parallel}(x,y) + P_e^{\perp} A^{\perp}(x,y)\cos\phi\right]\right) \tag{3.5}$$

where σ_0 is the unpolarized cross section, P_γ is the polarization of the photon, $P_e^{\parallel}$ is the electron's longitudinal polarization, $P_e^{\perp}$ is the electron's transverse polarization, ϕ is the azimuthal scattering angle of the outgoing photon (relative to the electron's transverse polarization), $A^{\parallel(\perp)}$ is the longitudinal(transverse) analyzing power, and x and y are dimensionless scattering parameters describing the kinematics in the electron's rest frame [62].

The Compton polarimeter, shown schematically in Figure 3.5, operated by steering the electron beam out of the main beamline and into a laser cavity. This steering induced a transverse polarization in the beam that was removed when the beam was steered back into the beamline. In the laser cavity, the electrons scattered from circularly polarized photons from a 10 W green laser (λ = 532 nm). Both the back-scattered photon and the scattered electron were recorded with specially designed detectors. The remainder of the beam was steered back into the main beamline and towards the target. The dipole magnet immediately after the laser cavity also acted as a spectrometer, separating out the scattered electrons and steering them towards the electron detector. It should be noted that the analysis of the photon detector data has proven difficult [63, 64, 65] and the only

measurements discussed in this dissertation were made using the electron detector. The Møller and Compton polarimeters were cross-calibrated once during low-current running to verify that there was little shift ($\leq 0.5\%$) in polarization due to increased beam current.

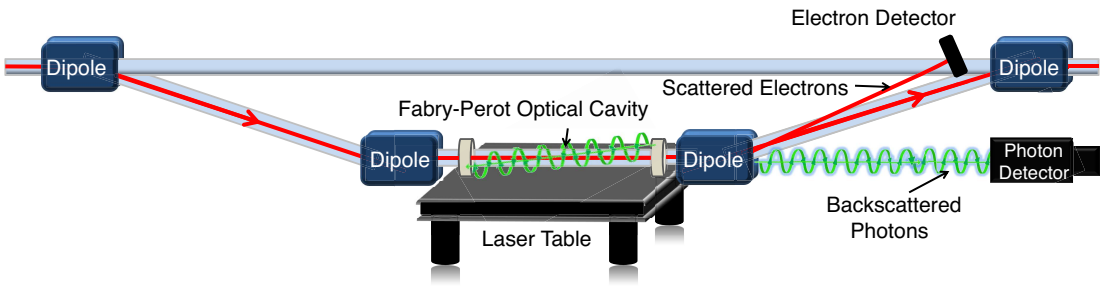

Figure 3.5: A schematic of the Hall C Compton polarimeter. The electron beam was steered into a region where it interacted with a laser. Scattering events were recorded using both photon and electron detectors. The primary beam exited the scattering region and resumed its original course to the target. Reproduced from [53].

3.5 Beam Parameter Monitoring

With a measurement of this precision, minimization and correction of helicity-correlated beam asymmetries (HCBAs) was a primary concern. For this reason, beam properties such as current, energy, position, and angle were constantly monitored using instruments from just downstream of the photo-cathode up to the Q_{weak} target. These properties were all fed into a fast feedback (FFB) system used to suppress HCBAs by an order of magnitude [66]. The FFB system used steering magnets and an SRF cavity to adjust the beam parameters toward stable values. False asymmetries due to HCBAs were removed during analysis as discussed in Section 4.2 of this dissertation.

3.5.1 Beam Position Monitors

A total of 47 BPMs were used to determine the horizontal and vertical position of the beam throughout the accelerator. The beam position monitors were composed of antennae located inside the beam pipe and arranged parallel to and azimuthally symmetrically about the beam [67]. The signal produced in each antenna was inversely proportional to the distance between the beam and the antenna, the combined signals of the four antennae allowed for

determination of beam position in the x and y directions with a typical resolution of roughly 1 μm [37]. By combining measurements of several different BPMs, one could calculate both the position and the angle of the beam at an arbitrary point in the beamline. This was done in order to determine the beam position at the target with a resolution of 1.72 μm and angle at the target with a resolution of 0.13 μrad during Run II [37]. The HC differences of these four parameters ($\Delta X, \Delta Y, \Delta X^{'}, \Delta Y^{'}$) were recorded for each quartet.

3.5.2 Beam Energy Measurements

The absolute beam energy, E, was measured using the Hall C beam arc as a spectrometer. Wire scanners that measured beam position and angle [68] were inserted just before and just after the arc. The eight 3 m long dipoles in the arc were energized while the remaining magnetic beamline elements (quadrupoles and corrector magnets) were left off. The electron momentum was then calculated to be

$$p = \frac{e}{\Theta} \int Bdl \tag{3.6}$$

where Θ is the bend angle and $\int Bdl$ is the integral of the magnetic field over the electron's path. This produced an energy measurement with a relative precision precision of $\delta E/E \sim 10^{-3}$. A full description of this method can be found in reference [69].

The above energy measurement was invasive to the Q_{weak} measurement and gave no information on HC differences in energy, ΔE. This quantity was calculated by measuring the HC beam position difference measured by BPM3C12 at the point of the Hall C arc with maximum beam dispersion. However, this monitor was also sensitive to position and angle changes. Thus, relative energy differences were calculated by correcting for these sensitivities using the formula

$$\frac{\Delta E}{E} = \frac{1}{M_{15}} \Delta X_{3C12} - \frac{M_{11}}{M_{15}} \Delta X - \frac{M_{12}}{M_{15}} \Delta X^{'}. \tag{3.7}$$

Above, ΔX_{3C12} is the HC x-position difference measured in BPM3C12 and M_{11}, M_{12} and M_{15} are the beam transport matrix elements describing the beam's propagation from the

Hall C arc to the target. A full description of the method of calculating the HC energy difference can be found in reference [70].

3.5.3 Beam Current Monitors

Accurate determination of helicity-correlated changes in beam current, I, was very important to the Q_{weak} experiment. In addition to the FFB system, which altered the Pockels cell voltage to suppress HC beam current differences (ΔI), the Čerenkov MD yields were normalized to the beam current integrated over the stable helicity window. The experiment used six RF cavity beam current monitors (BCMs) for continuous, high-precision monitoring of the relative beam current. These BCMs were composed of cylindrical, stainless steel cavities tuned to the fundamental frequency of the CEBAF, 1497 MHz = 3 $\times$ 499 MHz, which produced a resonant response linearly proportional to the beam current. At the beginning of Q_{weak}, only two BCMs (BCM01 and BCM02) were in use. During Run I, four more BCMs (BCM05-BCM08) were commissioned.

These BCMs were did not provide absolute measurements of the beam current and required calibration. Absolute beam current measurements were made using the Hall C Unser monitor [71] and the injector Faraday cups [72]. These absolute measurements were unsuited for the purpose of charge normalization. The Unser monitor was very noisy (0.1%) while the Faraday cups intercepted and stopped the beam before it went to the accelerator.

3.5.4 Beam Modulation

Measuring the detector response to changes in beam parameters could be accomplished using either natural beam parameter shifts,"jitter," or by intentionally modulating beam parameters. During typical beam conditions, parameters experienced minimal jitter by design and any single property of the beam was not guaranteed to vary independently of others. Intentional and independent modulation of the various beam parameters with amplitudes greater than natural jitter allowed for a more accurate determination of detector sensitivities [63].

The modulation hardware consisted of four pairs of inductive copper coils: two each for horizontal and vertical modulation [73]. Energizing these coils would result in a known

change in the beam position and direction. For beam energy modulation, a signal was sent to a SRF cavity in the south linac, resulting in small changes to the energy of the electron beam. The coil currents and SRF cavity voltage were driven by a 16 bit waveform generator. The drive signals were also recorded in the Q_{weak} data stream to be used for the calculation of the sensitivity to driven motion. Corrections using this method are not currently available for Run II but will be used for the final Q_{weak} results.

3.6 Liquid Hydrogen Target

The primary target material for Q_{weak} was liquid hydrogen (LH_2). The LH_2 target cell was designed using computational fluid dynamics to operate with 55 l of LH_2 at -20 $\pm$ 0.02] K at a pressure of 207-241 kPa. The target cell had a conical shape and measured 34.4 cm in length (3.9% radiation lengths) with aluminum entrance and exit windows. These windows were the largest source of background signal. The 1.16 GeV electron beam could deposit up to 2.1 kW in the target depending on the beam current, which necessitated a high-power heat exchanger. The target was designed to provide maximum flow and cooling across the aluminum windows to prevent melting. Such a high-power beam could not only burn through the target windows but also cause boiling within the target. Therefore, the beam was uniformly rastered across a 4 mm $\times$ 4 mm square on the target's upstream face. This induced motion of the beam inserted an additional 46 ppm systematic uncertainty in the measured asymmetry for each runlet, which was small when compared to a statistical width of $\sim$ 230 ppm.

3.7 Solid Targets

The target used for measuring the transverse asymmetry on carbon is one of two dozen solid targets used during the Q_{weak} experiment for a variety of purposes. These solid targets were placed in 3 arrays consisting of aluminum target "ladders" attached to the main LH_2 target apparatus. All the solid targets were 25 mm $\times$ 25 mm squares in the transverse dimensions but differed in thickness. The target apparatus was capable of moving horizontally and vertically to place any of these targets into the path of the beam. Two of the arrays were

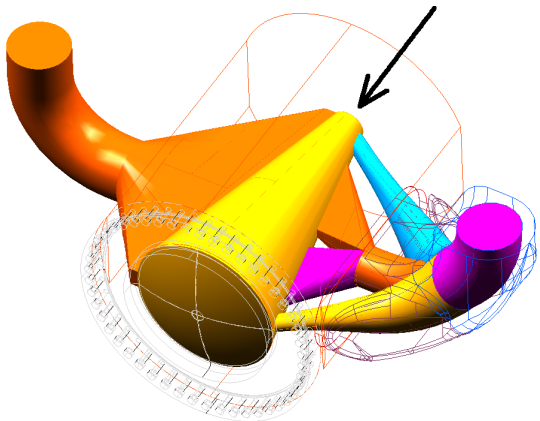

Figure 3.6: A schematic of the liquid hydrogen Q_{weak} target. The target windows and housing are transparent. The beam enters from the upper right. Reproduced from [74].

held in the same z-planes as the two LH_2 target windows. These target ladders included several aluminum targets used to estimate the asymmetry arising due to the LH_2 target windows, as will be discussed in Chapter 4.

The two carbon targets used in this experiment were both graphite wafers composed of 99.95% pure ^{12}C. The target in the upstream target ladder had an areal density 0.1692 g/cm^2, corresponding to a radiation length of $x_0 = 0.397\%$. The downstream target, used for the transverse asymmetry measurement, had an areal density of 0.7030 g/cm^2 ($x_0 = 1.648\%$). In addition to the transverse asymmetry measurement, both carbon targets were also used in systematic studies related to the target window background.

3.8 Collimation and Shielding

After scattering from one of the targets, the electrons were selected through collimation and the use of the QTor magnet so that only elastically scattered electrons reached the main detectors. The main collimation system (see Figure 3.7) consisted of three lead-antimony (95.5% Pb, 4.5% Sb) collimators each with eight apertures that allowed scattered electrons to pass into the eight octants. The first collimator, a cleanup collimator, was 15.2 cm thick and located 74 cm downstream of the target. In the center of this collimator was a water-cooled tungsten plug designed to stop electrons with small scattering angles ($\theta \in [0.75°, 4.0°]$) and serve as the end cap of the beamline leading to the Hall C beam

dump.

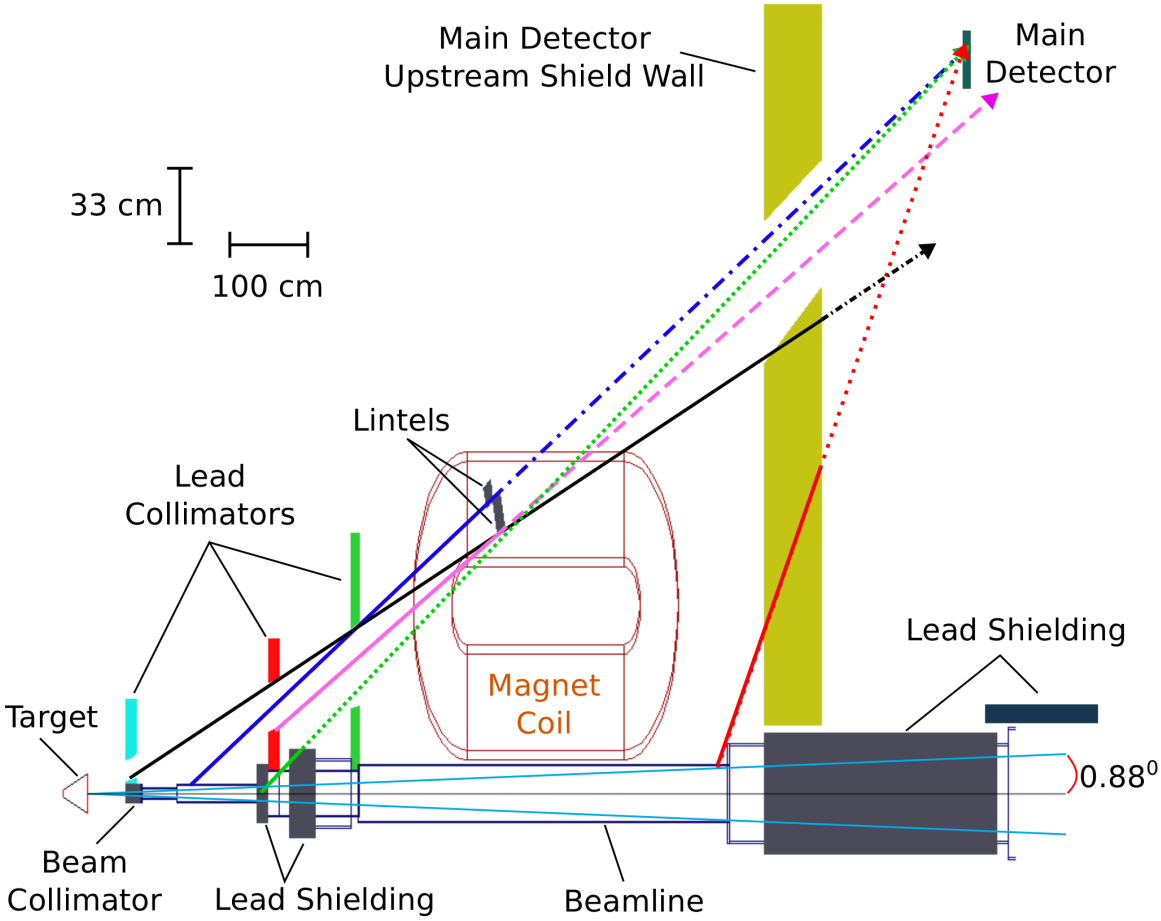

Figure 3.7: A simplified cross section view of the Q_{weak} apparatus. The solid lines indicate possible MD background sources that are intercepted by the various shielding and collimating elements, at which point the path forward is represented by a dotted line. Reproduced from [53].

The second collimator, centered 2.72 m downstream of the LH_2 target, was 15 cm thick. Its downstream face provided the defining acceptance for scattered electrons. Electrons that scattered from the upstream end of the target had an angular acceptance of $\theta \in [5.8°, 10.2°]$ while electrons scattering from the downstream end of the target had a range $\theta \in [6.6°, 11.6°]$. The final cleanup collimator was 3.82 m downstream of the target, just upstream of the QTor magnet.

As can be seen in Figure 3.7, there was a great deal of shielding put in place for this experiment. The design philosophy for this shielding was "two bounces." Shielding was positioned so that particles other than the elastically scattered electrons from the target

would need at least two bounces to hit a main detector. The shielding elements included a concrete hut built around the detectors, lintels placed in the QTor magnet blocking line-of-sight from the target and tungsten plug to the MD bars, and lead shielding around the beamline in the detector hut. However, there was still a small amount of signal that came from neutral particles hitting the detectors. The primary mechanisms for this background were scraping on the shielding of the detector hut and secondary scattering from other apparatus elements in the detector hut. The analysis of this QTor transport channel neutral background (QTCNB) is described in detail in Section 4.9.

3.9 QTor Magnet

The Q_{weak} Toroidal (QTor) magnetic spectrometer focused elastically scattered electrons that passed through the collimator system onto eight rectangular fused silica detectors. The QTor magnet consisted of eight copper coils placed symmetrically about the beam axis. The magnet, centered 6.5 m downstream of the target, deflected the elastically scattered electrons roughly 10° radially outward. Most of the neutral particle flux was thus directed into the shielding wall. Additionally, events with significant energy loss such as electrons from $e + p \rightarrow e + \Delta$ scattering and Møller scattering were swept away from the detector. However, there was some residual signal from $p \rightarrow \Delta$ production observed. Figure 3.8 shows the simulated envelope in which the elastically scattered electrons travel through the collimators and QTor magnet.

In the case of scattering from carbon and aluminum, nuclear excitations comprised a significant fraction of the MD signal. The spectrometer did not adequately separate these events, which lose little energy $\mathcal{O}(1 - 10 \text{ MeV})$, from the elastic signal. The treatment of nuclear excitations in the carbon measurement is discussed in Chapter 5.

3.10 Main Detectors

Q_{weak} utilized an array of eight Čerenkov main detectors (MDs). Each detector consisted of two 100 cm × 18 cm × 1.25 cm bars, joined lengthwise for a total length of 2 meters with UV-transparent glue (SES-406). Each bar was made of highly polished Spectrosil

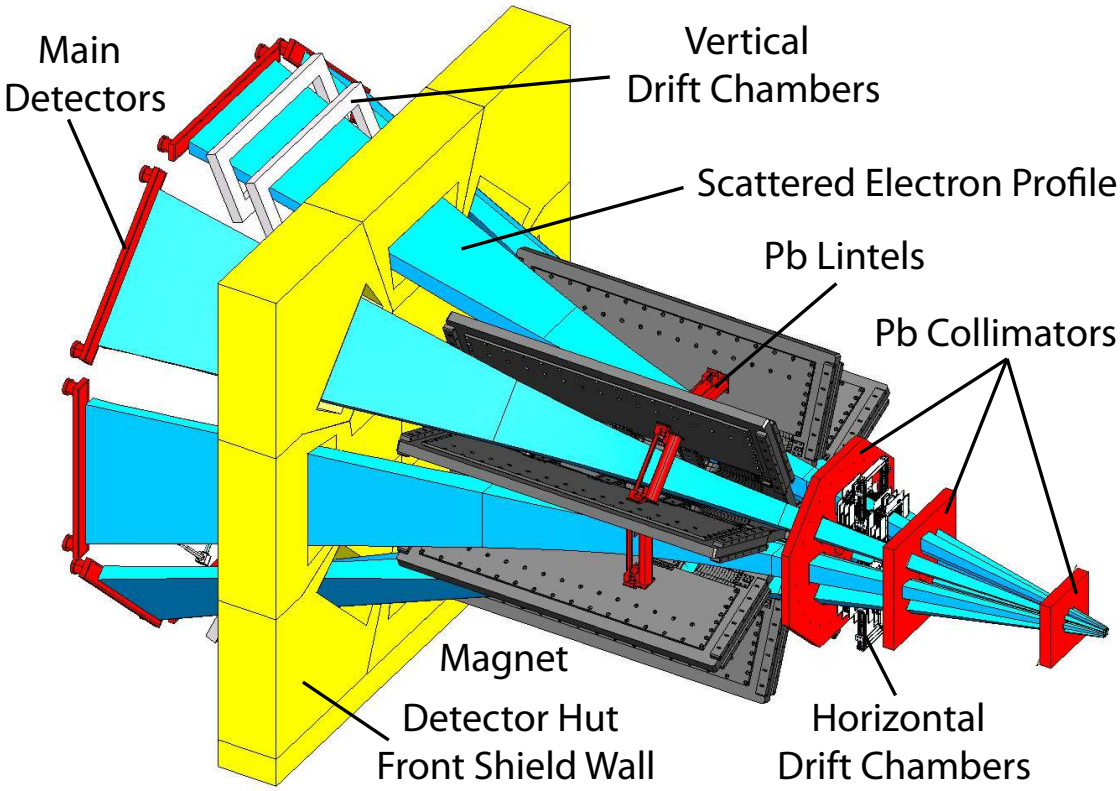

Figure 3.8: The acceptance of elastically scattered electrons, defined by the collimators and QTor, is shown in light blue. Detectors that formed part of the tracking system (the vertical and horizontal drift chambers) are also displayed. Reproduced from [53].

2000, an artificially fused silica material referred to within the collaboration as "quartz." This material was chosen for its radiation-hardness and low luminescence, which decreased sensitivity to "soft" backgrounds. A photomultiplier tube (PMT) was glued onto a quartz lightguide at each end of each detector to measure the Čerenkov light produced in the bar. Figure 3.9 shows MD 7 and MD 8 during installation.

The eight detectors were arranged symmetrically about the beam axis at a radial distance of approximately 335 cm. The MDs and attached PMTs were numbered and identified according to the system indicated in Figure 3.10. They were each secured to an aluminum support structure known as the "Ferris Wheel." Fine radial adjustments occurred after initial surveys to ensure a high degree of azimuthal symmetry. This symmetry was important for suppression of false signals from parity-conserving processes. To suppress soft backgrounds and enhance the signal, 2 cm thick lead preradiators were installed on the front face of each bar. This increased the detector yield by a factor of 7 and improved the

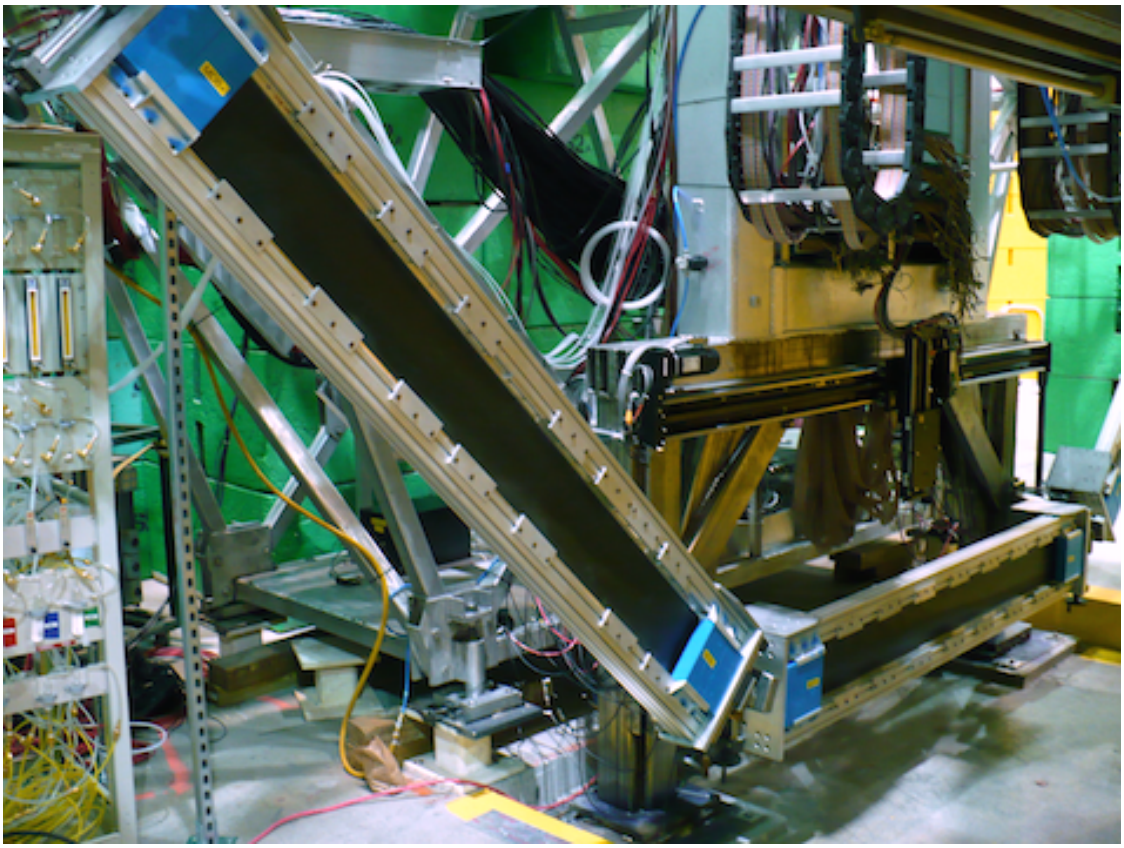

Figure 3.9: Main detectors 7 and 8 prior to the installation of the lead preradiators. The black rectangles indicate the light-tight covering on each MD bar. The blue squares at either end of the bar are lead shielding of the PMTs and lightguides. Reproduced from [53].

signal-to-background ratio by a factor of 20. However, secondary Mott scattering within the lead preradiators induced a detector asymmetry between the signals in the + and - PMTs, leading to an unforeseen systematic effect. This effect will be discussed in Section 4.7.

3.11 Background Detectors

In addition to the MD bars, a number of detector systems were built to monitor the status of various parts of the experiment. These detectors were divided into two groups based on their placement. The first group consisted of three detectors placed inside the detector hut to measure any diffuse background present in the region containing the MDs. The detectors inside the detector hut were constructed of components identical to those used in the MD bars but placed outside of the primary scattering envelope. The second group

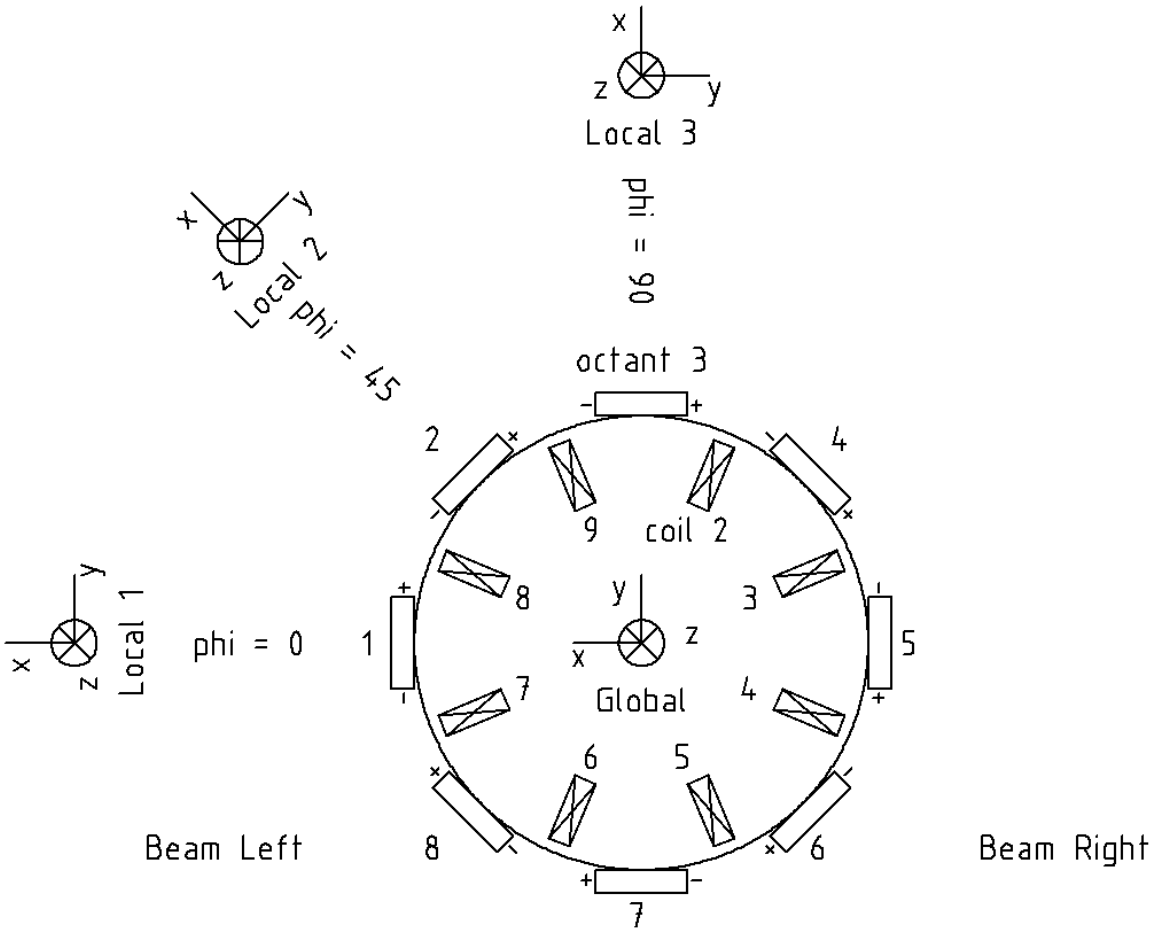

Figure 3.10: Global and local MD coordinate system definition. In each octant, the PMT in the local positive(negative) y direction is called the +(-) PMT.

of detectors was placed outside of the detector hut in positions close to the beamline to measure fluctuations in the luminosity of the experiment and general beam stability.

The detector hut was a highly shielded environment. However, the intensity of the beam and the complexity of the structure of the apparatus meant that there was a non-negligible signal from secondary and tertiary scattering events. To determine the size of these backgrounds, detectors were placed in the vicinity of the MD bars but outside of the path of elastically scattered primary electrons. The largest of these detectors was known as main detector 9. This detector was a MD bar, identical in construction to the eight

primary MDs. During Run I, MD 9 was placed horizontally on top of the beamline shielding downstream of the MD support structure. During Run II, MD 9 was moved to octant 5 in a vertical orientation downstream, radially outward and centered slightly below MD 5. The other two detectors in the detector hut were known as PMTLTG and PMTONL. Both detectors used a PMT identical to those used in the MDs. PMTONL was a bare PMT while PMTLTG included a quartz lightguide identical to those used in the MDs. These detectors were sealed inside light-tight boxes. During Run 0 and the beginning of Run I, PMTONL and PMTLTG were located in the same z plane as the MD bars. PMTONL was between MD 5 and MD 6 while PMTLTG was between MD 1 and MD 8. During March 2011 (partway through Run I), both were moved to octant 3, approximately 1.5 meters behind and slightly below MD3. The positions of the PMTONL and PMTLTG detectors are shown in Figure 3.11.

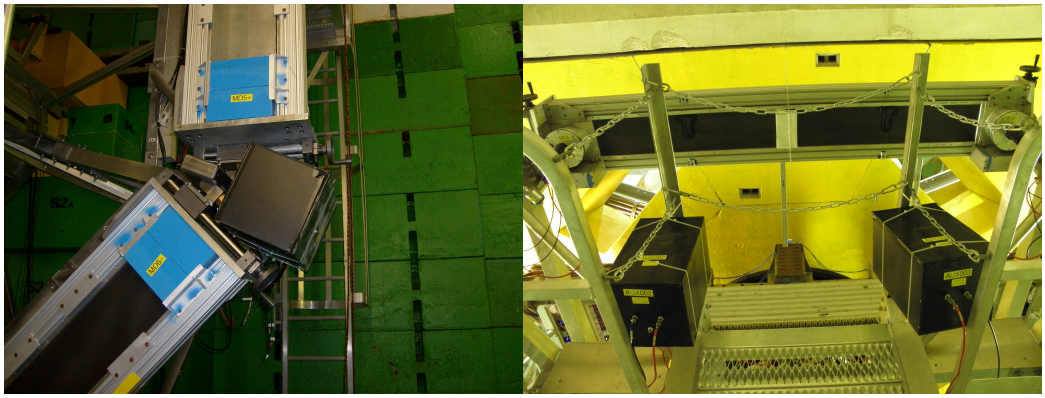

Figure 3.11: Left: PMTONL detector in its first position,between MD 5 and MD 6, viewed from directly upstream . PMTLTG was placed in the same position on the opposing side between MD 8 and MD 1. Right: PMTONL (left) and PMTLTG (right) in their final location. The picture also shows a view of the topmost main detector, MD 3, looking upstream toward the back of the shielding wall.

The other groups of background detectors were *luminosity monitors* (lumis). These two sets of detectors were placed at very forward angles where the scattering rate was large but the predicted PV asymmetry was very small. Since the physics asymmetry was heavily suppressed in these detectors, any observed asymmetry indicated a systematic error to be addressed in the PV asymmetry analysis. The first set of luminosity monitors consisted of four detectors arranged symmetrically on the upstream face of the defining (second)

collimator. The detectors, known as the *upstream lumis* (denoted USLumi and shown in Figure 3.12) were placed next to the apertures leading to octants one, three, five and seven. The USLumi detectors were made from 4 cm $\times$ 2 cm $\times$ 27 cm quartz bars with a 2 cm $\times$ 2 cm $\times$ 35 cm quartz lightguide attached to each end leading to a PMT. These detectors were designed to measure Møller scattering at $\leq 5^\circ$ and serve as a target density monitor. Large density fluctuations in the target would lead to detectable changes in the MD yield. In practice, the USLumis were used by the collaboration to identify a significant background asymmetry resulting from the beam interacting with the tungsten plug. This precipitated the move of the aforementioned background detectors to their later configurations where they would be more sensitive to the same background asymmetry. Together, these background detectors and the USLumis helped provide a correction for this "beamline background," which will be discussed in Section 4.3.

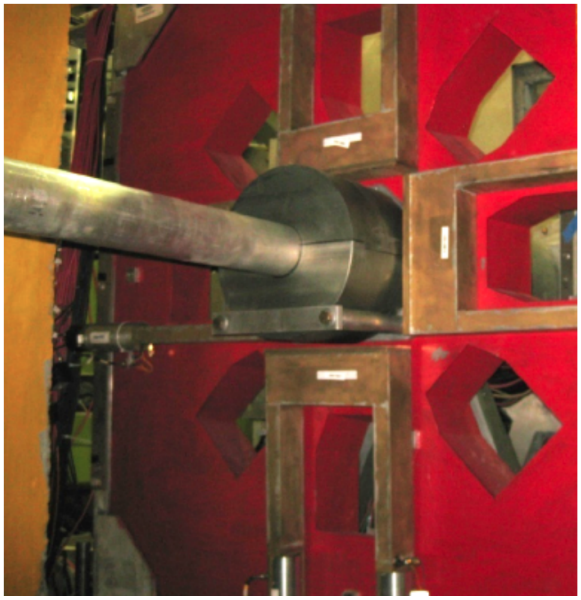

Figure 3.12: The upstream luminosity monitors (USLumis) as installed on the upstream face of the definining collimator. Note that they were designed to avoid signals from events that passed through the first collimator's acceptance.

The second set of luminosity monitors was placed downstream of the main detector shielding hut, approximately 17 m downstream of the target. These detectors, comprised of eight 4 cm $\times$ 3 cm $\times$ 1.3 cm pieces of quartz arranged symmetrically in the same octant pattern as the MDs, measured scattering at $\sim 0.5^\circ$. The light from the detectors traveled

through 34 cm long air-core light guides to the same type of PMTs used in the USLumi detectors. They were primarily designed to act as a null asymmetry monitor. They were very sensitive to helicity-correlated changes in the beam, and provided a set of azimuthally symmetric monitors independent of the main detectors on which various algorithms could be tested. The design and installation of the luminosity monitors is covered in greater depth in Chapter 4 of reference [75].

3.12 Tracking System

The Q_{weak} experiment required an accurate knowledge of kinematic variables in order to extract Q^p_{W} from eq. (2.21). For this purpose there were additional sets of detectors used during certain event-mode runs. Immediately after the second collimator, there were two pairs of horizontal drift chambers (HDCs), each pair placed in opposite octants. The entire HDC apparatus could be rotated about the beam axis to examine each of the four octant pairs. Each HDC consisted of 6 planes of wires and the HDC pair in each octant was separated by 0.4 m along the beam path. The result of these paired HDCs was a position resolution of 200 μm and a scattering angle determination to within 0.6 mrad[76]. In order to ensure the appropriate averaging over the acceptance of the main detector, after traveling through the QTor magnetic field, there was a set of vertical drift chambers (VDCs). These detectors were also placed in opposite octants on a rotating frame, just upstream of the main detectors. In addition, there was a set of trigger scintillators placed just upstream of the main detectors (downstream of the VDCs) in the octants being studied. The scintillators provided a trigger for the electronics during event-mode running. The combination of these detectors allowed for track reconstruction of the scattered electron path. The tracking system not only provided a value for the acceptance-averaged Q^2, these data were also used to identify certain background events and provide rate information. The whole tracking system could be retracted radially inward from the scattered electron path during production running.

3.12.1 Horizontal Drift Chambers

Five HDCs were constructed with the fifth one serving as a spare. One pair of HDCs constituted a package, and the two packages were mounted on two arms, fixed 180° apart. The packages were positioned between the second and third collimators, upstream of the QTor magnet. The arms were mounted on a central hub which rotated, allowing coverage of all eight octants. The arms were positioned and retracted manually.

The drift chambers consisted of two aluminum-mylar cathode planes with an array of parallel sense and field wires, and used a gas mixture of 65% argon - 35% ethane. When an electron passed through the chamber, the gas was ionized and the ionization electrons were pulled towards the grounded sense wires. The signal was amplified via an avalanche, each ion causing more ionization as it moved through the gas. The analog signal was converted to a logic signal by a discriminator and was ultimately sent to a time-to-digital converter (TDC). A full description of the HDCs is presented in reference [76].

3.12.2 Vertical Drift Chambers

As above, five VDCs were built with the fifth serving as a spare. They were arranged into pairs, separated by 30 cm, in opposing octants. The VDCs operated using the same technology as the HDCs with some slight differences. The gas composition was an even mixture of argon and ethane and the geometry was expanded in order to cover the electron envelope in the detector hut. These detectors were also placed on a rotating system capable of covering all eight octants. The VDCs were withdrawn radially inward during high-current running. In addition to being used in Q^2 measurements and track reconstruction, the VDCs were instrumental in determining the signal response to the scattered beam profile on the MD bars. Figure 3.13 shows the hit map on the main detector based on reconstructed tracks using the VDC data. A full description of the VDCs is the subject of Chapter 4 of reference [77].

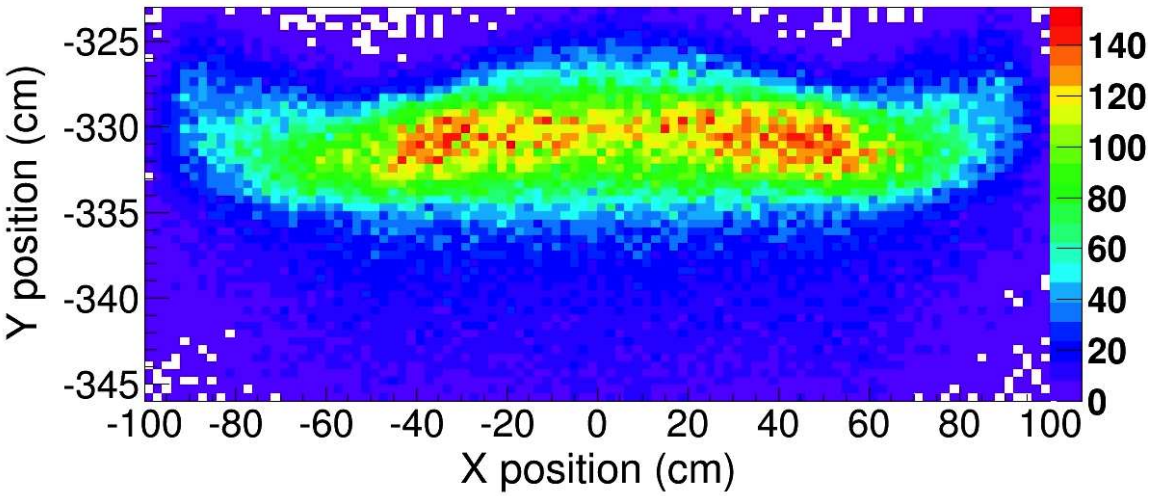

Figure 3.13: Rate profile projected to the MD plane using track reconstruction software based on VDC signals. Note the "moustache" shape that was characteristic of the acceptance and QTor magnet. Reproduced from [53].

3.12.3 Trigger Scintillators

Plastic trigger scintillators (TSs) were placed immediately downstream of the VDCs to provide fast timing triggers for data read-out during event-mode data taking. Each TS was approximately 218 cm $\times$ 30 cm $\times$ 1 cm and made of Bicron BC-408 plastic. Lucite light guides were used to connect the TS bar PMTs. The signals were discriminated with a CAEN N842 8-channel constant fraction discriminator in conjunction with a CAEN V706 16-channel hardware meantime module. During Q_{weak} the discriminator was configured with a large (150 ns) output width, which defined the minimum double-pulse resolution for this detector. The TS detectors were centrally important to study the QTor transport channel neutral backgrounds as discussed in Section 4.9. For a complete description of the commissioning of the trigger scintillator, see Chapter 4 of reference [78].

3.13 Data Acquisition

The data acquisition (DAQ) system had two modes, one for the high-current, production-mode data and another for the low-current, event-mode data. During production running, the signal from each of the main detector PMTs was integrated, digitized, and read out using

specialized low-noise analog-to-digital converters (ADCs). The data trigger was the MPS signal, generated by the helicity control board, ensuring readout over periods of constant helicity. In event mode, the trigger was user configurable; it could be set to read out when an individual detector or group of detectors was hit. For track reconstruction data, the trigger was usually from PMT coincidence in a TS. However, the data discussed in Section 4.9, were triggered by MD PMT signals.

The raw data collection was handled by the CEBAF Online Data Acquisition (CODA) system. CODA communicated with various readout controllers (ROCs) that processed the electronics signals During production running, the ROCs were read out during the 70 μs hold-off period at the beginning of the new helicity state. In event mode-running, a prescaler was used to limit the readout rate to $\leq$ 2 kHZ to minimize computer deadtime. A prescale vale of 0 meant that every event was read out. A prescale value of 9 meant only every tenth event was recorded. Raw data were stored on the Jefferson Lab computer cluster (the `ifarm`). Each runlet had about 2 GB of raw data. Real time analysis was conducted using a combination of a Q_{weak} specific analyzer and various `ROOT`-derived [79] programs for specific tasks. After initial analysis, results were stored in a number of SQL databases for further examination.

Chapter 4

Q_{weak} Analysis Method and Procedures

The goal of the Q_{weak} experiment is to determine the weak charge of the proton, Q_W^p, by measuring the parity-violating asymmetry (A_{ep}) in elastic $\vec{e}p$ scattering. This chapter describes the analysis that went into extracting this asymmetry from the experimentally measured asymmetry (A_{raw}) for the Run II data set. This chapter includes a discussion of the raw asymmetry measurement, including data quality, systematic errors and polarization measurements. Following these corrections, the physics backgrounds will be covered, with particular emphasis on the work the author has done to constrain the QTor transport channel neutral background (the $b = 3$ term in eq. 3.3). Finally, an up-to-date, blinded calculation of the Run II PVES asymmetry will be shown.

4.1 Raw Asymmetry Measurement

The reader will recall the formula that relates the measured asymmetry to the elastic asymmetry accounting for all systematic effects, eq. (3.3):

$$A_{raw} = P\left(\frac{1-\sum_{b=1}^{4} f_b}{R} A_{ep} + \sum_{b=1,3,4} f_b A_b\right) + A_{beam} + A_{BB} + A_T + A_L + A_{PS}. \quad (4.1)$$

The first step towards determining A_{ep} accurately is ensuring the quality of the measurement made by the apparatus, A_{raw}. The asymmetry calculations performed during the Q_{weak} experiment began at the quartet level and were combined into larger groupings. The helicity states within a quartet follow a pattern of (+,-,-,+) or (-,+,+,-). For each quartet,

the asymmetry in each PMT, k, was calculated according to

$$A_{raw}^{k} = \pm \frac{(Y_1^k + Y_4^k) - (Y_2^k + Y_3^k)}{Y_1^k + Y_4^k + Y_2^k + Y_3^k}. \tag{4.2}$$

Here, Y_i^k refers to the charge-normalized, pedestal-subtracted integrated yield for each of the four blocks of constant helicity in a quartet and the sign is determined by the first helicity state signal in the quartet.

To limit the chance of a biased analysis, the main detector PMT asymmetries were blinded. Blinding was achieved by adding a constant undisclosed offset to every asymmetry at the quartet level. The blinding offset was between -60 and +60 ppb. The blinding offset followed the sign of the measured asymmetry due to the induced sign changes from the polarized source and accelerator configuration (summarized in Table 4.1). The systematic uncertainty of A_{raw} associated with this offset was

$$\delta A_{msr}(\text{blind}) = \frac{120}{\sqrt{12}} \text{ ppb} \approx 34.6 \text{ ppb}, \tag{4.3}$$

where the factor $1/\sqrt{12}$ accounts for the variance of the uniform probabilities distribution over which the blinding factor was selected.

In order to combine the asymmetry measurements of all eight MDs, a simple arithmetic mean was used:

$$A_{raw} = \frac{\sum_k^{16} A_{raw}^k}{16} \tag{4.4}$$

where the sum is carried out over all 16 MD PMTs for every quartet. These quartet-level data were subject to a number of data quality cuts during the initial analysis and translation of recorded detector electronics signals. The most straightforward event rejections corresponded to data for which the DAQ system reported a hardware error. Event cuts were also defined in software for individual detector and beam monitor channels. For example, a basic lower limit for beam current monitors was implemented at 100 μA during LH_2 data-taking, below which the current measurements (necessary for normalization) were unreliable. There were loose upper and lower tolerances in place on detector yields and BPMs as well, serving

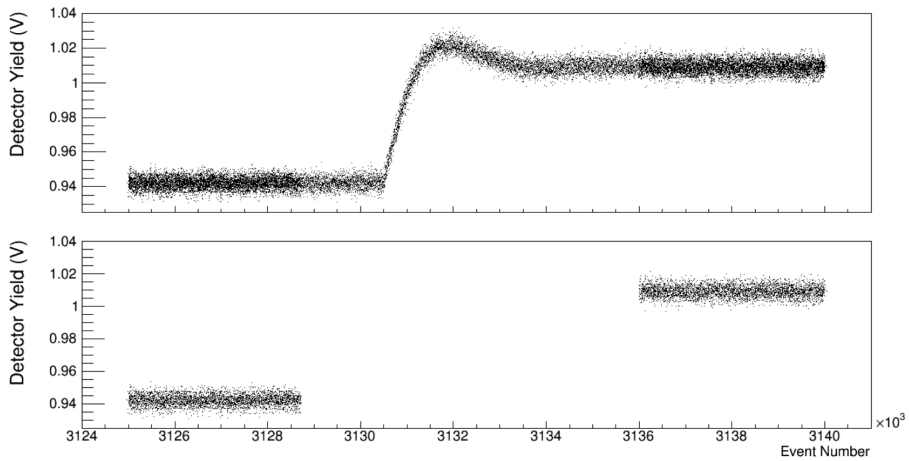

Figure 4.1: The top figure shows a period of data ($\approx$ 7 seconds) prior to the application of beam stability cuts. The bottom figure shows the same data set after the cuts were applied. The observed instability was the result of an erratic beam modulation cycle (see Chapter 3.5.4) during a run on an aluminum target.

as redundant checks on the status of the PMT hardware and electronics.

In addition to the limits listed above, stability cuts were performed by the analysis engine. Figure 4.1 gives an example of how these stability cuts were used to cut out periods of rapidly changing detector signals. Along with BCMs and BPMs, two main detector variables were used for stability cuts: the summed PMT yields of MD 1 (beam left) and MD 7 (beam down). These channels were chosen for their sensitivity to beam excursions and position differences. The DAQ hardware errors cut out about 1% of the data, while the additional cuts affected $< 0.1\%$ of the data [35].

Beyond these analysis engine cuts, Q_{weak} collaborators and subsystem experts made cuts at the runlet level. These cuts were only used to ensure the apparatus was functioning properly and that the data were taken with the experiment in the appropriate configuration (target, energy, *et cetera*).

4.1.1 Main Detector Widths

The smallest time period over which average asymmetries were formed was the runlet. The variance of such a distribution of quartet asymmetries is given by:

$$\sigma^2 = \frac{1}{N}\sum_{i=0}^{N}(A_i - \langle A \rangle)^2 \tag{4.5}$$

where N is the number of quartets with measured asymmetry A_i and average asymmetry $\langle A \rangle$. The standard deviation, σ, was a quantity that was used to determine the status of the experiment throughout its running. Assuming that the main detector yield was dominated by elastic *ep* events, the runlet MD width was expected to be dominated by counting statistics. The predicted runlet asymmetry width in these conditions and at beam current I was calculated to be [74]:

$$\sigma^{\text{pred.}} = \sqrt{\frac{180\ \mu\text{A}}{I}} \times 217\ \text{ppm}. \tag{4.6}$$

The factor of 217 ppm was determined through calculation of the number of quartets measured in a runlet combined with the rate of elastically scattered electrons hitting the bars [78] and the resolution of the preradiated bars [74]. Widths significantly higher than the predicted value indicated that a source of noise in addition to statistics was present. As will be shown later in this chapter, asymmetry widths were reduced by regression against beam parameters and corrected for beamline background effects, indicating that these techniques were effective at removing noise from the measurement.

4.1.2 Averaging Asymmetry Measurements and Sign Corrections

As discussed in Section 3.1, the Q_{weak} experiment had a number of different time scales important to this analysis. Many of these periods were defined by accelerator configuration changes that flipped the sign of the asymmetry measured by the apparatus. Inserting or removing the IHWP (see Section 3.2) denoted the beginning and end of each *slug*. Run II consisted of 182 different slugs (slugs 137-321), each approximately eight hours in length. Double Wien flips were performed approximately once per month and defined *Wien* periods.

Sign Flip Source	State	Sign Correction
IHWP	In	-1
	Out	+1
Wien	Left	-1
	Right	+1
3-Pass	Yes	-1
	No	+1

Table 4.1: Description of sign reversals in the experiment and their effect on the measured asymmetry. For a particular configuration, the measured asymmetry would have its sign multiplied by the product of the three appropriate values from the rightmost column before combining at timescales above a slug.

Run II was comprised of Wiens 6-10. An additional sign flip was induced during parts of Run II as a result of $g-2$ precession in the accelerator. In these periods, the electron beam circulated the accelerator three times (referred to as 3-pass beam) as opposed to only once (1-pass). The energy delivered to the hall was the same but the electron spin was rotated 180° compared to 1-pass beam. Table 4.1 summarizes how these three reversal methods reversed the sign of the measured asymmetry. Unless otherwise stated, asymmetries quoted throughout this work are sign-corrected. Within the Q_{weak} collaboration, asymmetry measurements that needed no sign correction were denoted as *Out* measurements while those that did require a sign change were referred to as *In* measurements. This convention was based on the sign change associated with the IHWP.

Measuring the physics asymmetry over periods smaller than a slug was done by a weighted average of runlets [80]:

$$\langle A \rangle = \frac{\sum_j A_j/\sigma_j^2}{\sum_j 1/\sigma_j^2}, \tag{4.7}$$

where A_j is the asymmetry of runlet j and σ_j^2 is its variance. If the average is performed over longer periods, one will eventually encounter a sign reversal of the asymmetry. In practice, the Q_{weak} experiment formed two asymmetries for these time scales: A_{NULL}, which did not correct for sign reversals, and A_{PHYS}, which did. The null asymmetry should be consistent with zero as the sign-flipped asymmetry measurements should be equal and opposite. It is calculated simply using eq. (4.7). The physics asymmetry makes use of the sign corrections

in Table 4.1 to slightly modify the calculation:

$$A_{PHYS} = \frac{\sum_j s_j A_j / \sigma_j^2}{\sum_j 1/\sigma_j^2}, \tag{4.8}$$

where s_j is the sign correction of runlet j. Note that both eq. 4.7 and 4.8 can be summed over larger units than runlets (i.e. runs, slugs, Wiens). Figure 4.2 shows the slug-averaged asymmetries for both Out and In sign corrections over Run II. Figure 4.3 shows the sign-corrected and null asymmetry for all slugs over Run II. Performing the appropriate fits to the sign-corrected data yields the first quantity of interest,

$$A_{raw} = [-164.5 \pm 7.4] \text{ ppb}, \tag{4.9}$$

the uncorrected MD asymmetry from the Run II dataset.

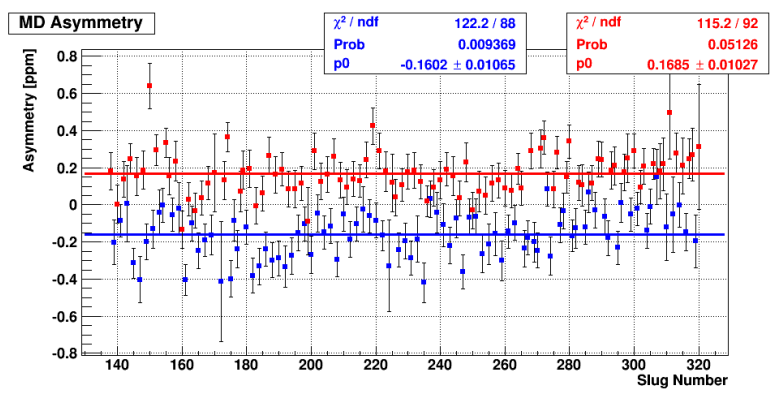

Figure 4.2: Uncorrected MD asymmetries averaged at the slug level. Blue(red) data and fit are Out(In) measurements.

The result in eq. (4.9) gives the purely statistical precision of the Q_{weak} measurement in Run II. However, some of the systematic corrections discussed in the coming sections (particularly linear regression, beamline backgrounds, and polarization) must be applied on timescales of a slug or smaller due to changing experimental conditions. As such, an intermediate variable is constructed:

$$A_C = \frac{A_{raw} - A_{beam} - A_{BB}}{P}, \tag{4.10}$$

where A_C is the MD asymmetry corrected for HC beam properties (A_{beam}), the beamline

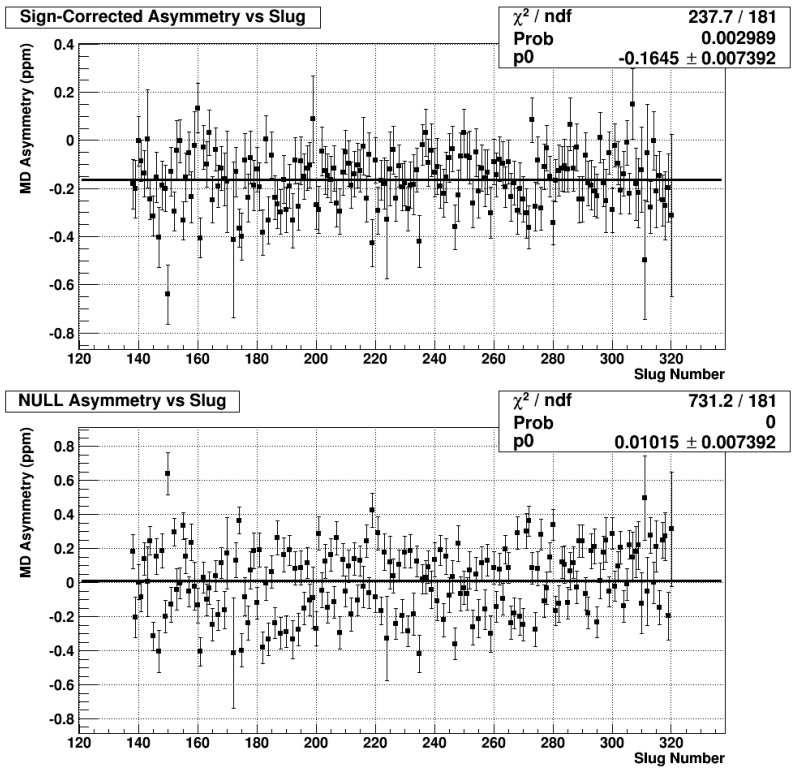

Figure 4.3: Uncorrected MD asymmetries averaged at the slug level. The top(bottom) plot shows the sign corrected(null) asymmetry Note that the null asymmetry has an exceptionally high χ^2/ndf due to the fact that it is fitting two distributions (In and Out) with a single constant.

background (A_{BB}) and the polarization P. These corrections injected some small systematic uncertainty in a way that was non-trivial to separate from the experimental statistics. In this work, the error on A_C will be quoted as statistical (even though it contained these "hidden" systematic uncertainties) and additional systematic uncertainties will be quoted separately.

4.2 Linear Regression

Under ideal circumstances, the beam position and intensity would be independent of the beam's helicity state. However, helicity-correlated (HC) changes in the beam properties changed the flux of scattered electrons observed in a given detector, giving rise to a measured asymmetry in the detector that was not due to a scattered electron's polarized interactions in the target. This type of asymmetry was referred to as a false asymmetry. The

Beam Parameter	Goal	Run II Average
ΔX [nm]	< 2	-2.11 ± 0.06
ΔY [nm]	< 2	0.60 ± 0.06
$\Delta X'$ [nrad]	< 30	-0.06 ± 0.007
$\Delta Y'$ [nrad]	< 30	-0.05 ± 0.007
ΔE [ppm]	< 1	-0.18 ± 0.00001
A_q [ppm]	< 0.1	0.014 ± 0.001

Table 4.2: Design goals [82] compared to observed HC beam parameter differences measured over Run II.

Q_{weak} experiment took great care to ensure that the HC beam properties were very well constrained as is shown in Table 4.2. The errors quoted in this table were calculated using:

$$\text{error}(\Delta\chi_i) = \frac{\text{resolution}(\chi_i)}{\sqrt{N}} \tag{4.11}$$

where N is the number of quartets over Run II, and the resolutions for beam parameters, χ_i, are discussed in Section 3.5 and references [37, 81].

Even within the small bounds achieved, it was found that the measured asymmetry in the MDs depended upon these beam parameter differences. These beam parameter sensitivities were corrected with *linear regression*. The linear regression analysis for Q_{weak} was performed using a stand-alone `C++` analysis engine [35]. The regression algorithm calculated the sensitivities for any given set of detectors (dependent variables) with respect to a set of beam parameter data (independent variables). A number of *regression schemes* using different independent variable sets were tested and will be discussed in Section 4.2.1. The regression algorithm was based upon a multivariate least-squares analysis [83]. This analysis extracted the correlation matrix elements that corresponded to detector sensitivities for each runlet. These sensitivities were then used to correct the detector asymmetry for each quartet in the runlet. The correction for detector k with respect to beam parameter χ_i took the form

$$A^k_{beam} = \sum_{i=1}^{n} \frac{\partial A^k_{raw}}{\partial \chi_i} \Delta\chi_i, \tag{4.12}$$

where the partial derivative represents the sensitivity of the detector asymmetry to the beam

parameter and the HC parameter difference is $\Delta\chi_i$. Figure 4.4 shows an example of the correlation between the MD 5 asymmetry and the HC horizontal beam position difference calculated for a single slug.

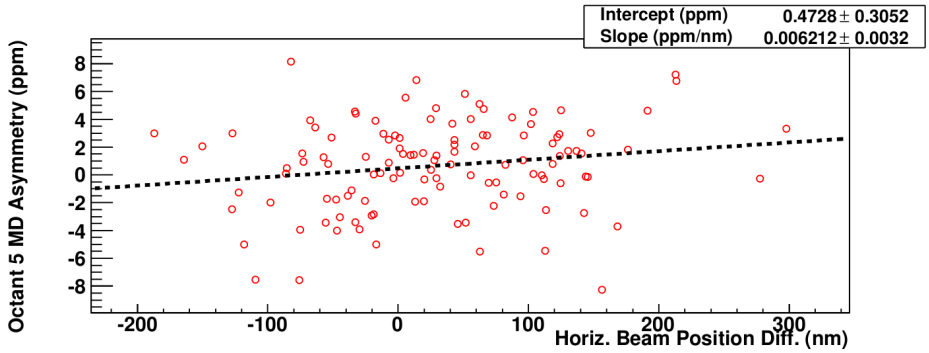

Figure 4.4: Asymmetry measured in MD5 plotted against the horizontal beam position difference (ΔX). Data shown are runlets comprising a single slug. Reproduced from [74].

The regressed data generally showed improved statistical properties after the removal of these false asymmetries. Figure 4.5 shows how the MD asymmetry *widths* at the runlet level were improved, moving closer to agreement with eq. (4.6), after regression. Figure 4.6 compares the physics asymmetries for raw and regressed data at the slug level. One can see that the quality of the fits is improved after regression. However, as mentioned previously, there is a small amount of systematic error associated with this process.

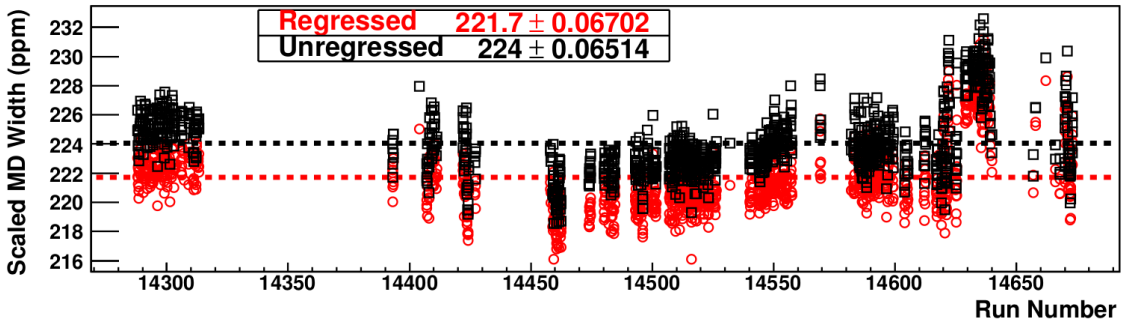

Figure 4.5: Current-scaled MD asymmetry widths for Wien 7. Regressed data are in better agreement with predictions from eq. (4.6) indicating that systematic noise was removed from these data. Reproduced from [74].

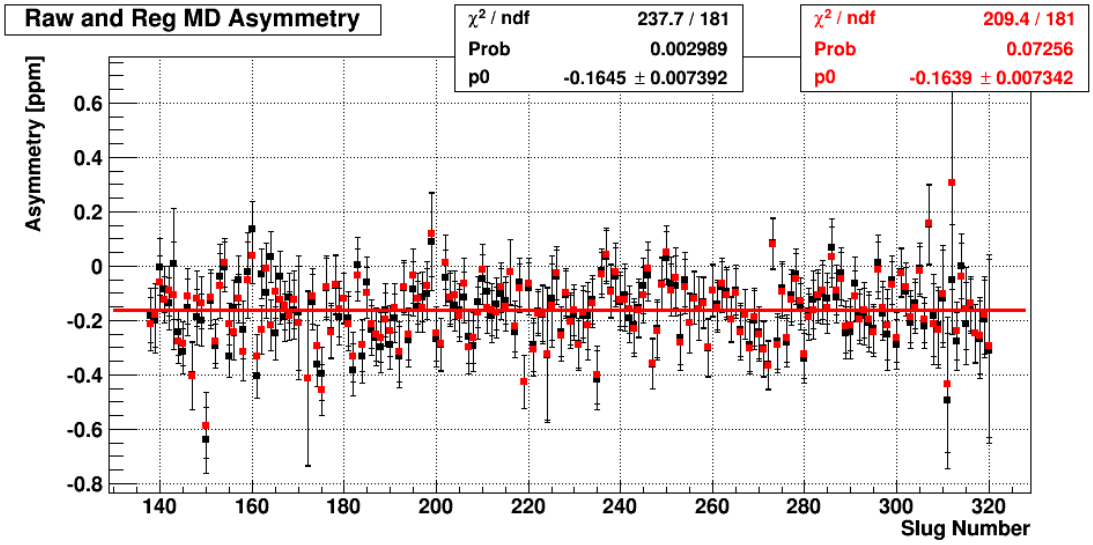

Figure 4.6: Raw (black) and regressed (red) physics asymmetries for each slug in Run II. Note the improved χ^2/ndf on the regressed fit to a constant.

4.2.1 Regression Scheme Dependence

Choosing the set of beam parameters and associated beam monitors against which the detector asymmetries were regressed was a source of concern for the experiment because there was the potential to introduce unforeseen systematic errors. Finding a set of completely independent beam monitors that spanned the parameter space was not practical for this analysis due to the fact that several parameters (particularly beam energy and horizontal position and angle) were highly correlated. In addition, these correlations changed over time due to different conditions in the accelerator.

In order to determine the effects of using different sets of independent variables in the regression engine, several different schemes were investigated. Table 4.3 displays the independent variables used in each regression scheme that was examined. The results in this work used `set10` regression. This choice was based upon the need to correct for clear residual charge-asymmetry correlations that existed in the data. This could not be accomplished effectively with the same beam monitors used to normalize the detector yields without inducing a strong bias [74]. Additionally, this regression scheme provided the best fits to data for both physics and null asymmetries. The systematic error associated with the regression scheme was taken to be the largest point-to-point spread in the measured

Scheme	Position/Angle	Energy	Charge
`std`	Target	Calculated	-
`5+1`	Target	Calculated	Standard
`set3`	Target	3C12X	Standard
`set4`	Target	Calculated	BCM5
`set7`	3H09b/3H04	3C12X	-
`set8`	3H09b/3H04	3C12X	Standard
`set10`	Target	Calculated	BCM6
`set11`	Target	3C12X	-

Table 4.3: A selection of regression schemes used by the Q_{weak} experiment. Each regression scheme is defined by the beam monitors it used. The "Target" position and angle monitors refer to the calculated variables discussed in Section 3.5.1. "Calculated" energy is defined in eq. (3.7). The "Standard" charge definition is covered in Section 3.5.3. These schemes were selected because they were the only ones tested that reduced the MD asymmetry width appreciably.

	NULL			PHYS			
Scheme	Asym [ppb]	Error [ppb]		Asym [ppb]	Error [ppb]	χ^2/ndf	Prob.
`raw`	10.153	7.392		-164.520	7.392	1.313	0.003
`std`	13.771	7.343		-163.826	7.343	1.177	0.070
`5+1`	14.058	7.344		-163.891	7.344	1.189	0.066
`set3`	14.363	7.345		-163.878	7.345	1.192	0.065
`set4`	14.970	7.342		-163.951	7.342	1.184	0.068
`set7`	13.329	7.346		-163.521	7.346	1.175	0.071
`set8`	13.883	7.344		-163.971	7.344	1.190	0.066
`set10`	14.570	7.342		-163.947	7.342	1.157	0.073
`set11`	13.481	7.645		-164.192	7.645	1.180	0.070

Table 4.4: Blinded null and physics asymmetries for Run II. The values shown are the results of plotting all slug-averaged asymmetries and then fitting with a constant as is shown in Figure 4.3.

asymmetry between the different regression schemes. Table 4.4 shows the asymmetry results and fitting information for each regression scheme.

Using the regressed data shown in Figure 4.6, one can calculate the regressed asymmetry over Run II:

$$A_{reg} = \langle A_{raw} - A_{beam} \rangle = [-163.9 \pm 7.3(\text{stat.}) \pm 0.8(\text{syst.})] \text{ ppb.} \tag{4.13}$$

where 0.8 ppb is the regression scheme dependence uncertainty.

4.3 Beamline Background

The beamline background (BB) refers to events that enter the detectors after scattering on beamline elements downstream of the target. Extensive studies were performed [56] that showed the primary source of these scatterings was the tungsten beam collimator located in the center of the first lead collimator. Additionally, the asymmetry of this background was found not to be due to physics (i.e. the beam's polarization-dependent interactions in the target) but rather behaved like the HCBAs corrected by regression. It was later found that the BB asymmetry was in fact caused by HC asymmetries in the beam's "halo," as will be shown below. This background was referred to as a "soft" background, composed largely of low-energy particles incident on the MDs and was highly suppressed by the lead preradiator [78].

This background was discovered early in the running of the experiment through examination of the USLumi asymmetries. These detectors were designed to measure luminosity fluctuations and were predicted to observe no significant helicity-correlated asymmetry. However, it was found that these detectors measured an asymmetry on the order of 1-10 ppm, which is much larger than the physics asymmetry. Since it was determined that this wasn't due to a competing physics asymmetry, but was rather an aspect of the geometry of the apparatus and HC beam properties, its asymmetry was treated as a correction to A_{raw} comparable to linear regression rather than a "true" background. This justifies the presence of A_{BB} in eq. (4.1) and eq. (4.10). The fractional yield of these events was not corrected through this "second regression" and therefore appears as the f_2 term in eq. (4.1).

4.3.1 Blocked-Octant Data

The BB fractional yield, f_2, was measured in a series of dedicated runs. The relevant data were taken using a pair of 2.54 cm thick tungsten shutters. These remotely-insertable shutters were used to cover the upstream collimator's acceptance in octants 1 and 5, as is shown in Figure 4.7. This prevented any elastically scattered electrons from passing directly into these MDs. Any signal in MD 1 or MD 5 with the shutters inserted was therefore attributed to the beamline background. The fractional yield was defined to be

the ratio of the average yield of the two blocked detectors over the average of the unblocked detectors,

$$f_2 = \frac{(Y_1 + Y_5)/2}{(Y_2 + Y_3 + Y_4 + Y_6 + Y_7 + Y_8)/6}, \tag{4.14}$$

where Y_i is the measured yield in MD i.

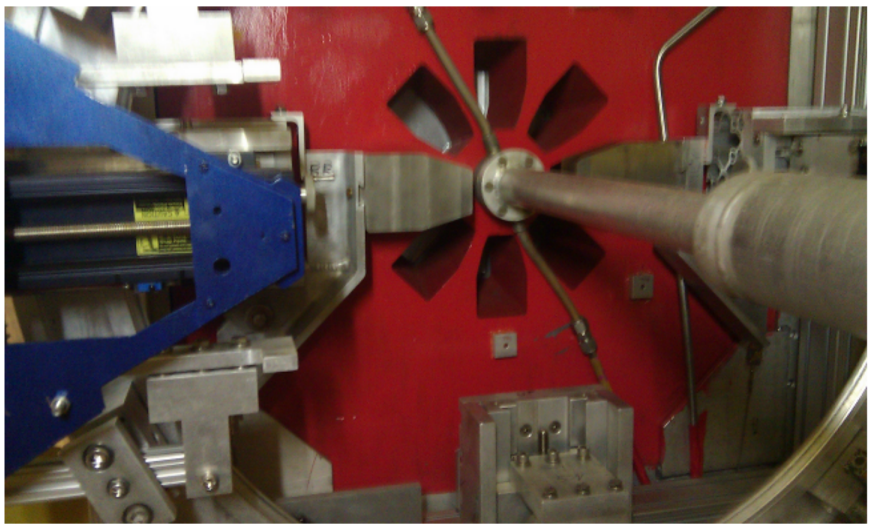

Figure 4.7: The tungsten shutters used for beamline background measurements covered the apertures for octants 1 and 5. The tungsten plug is located in the center of the two shutters.

These data were taken during good and bad halo conditions. The beam halo was defined as those components of the beam greater than 5 mm from the beam center and was measured with dedicated monitors [84]. When there was a particularly large halo, there was a larger amount of electrons interacting with the tungsten plug and therefore a larger amount of beamline background. The HC asymmetry of the beam halo was found to be the source of the beamline background asymmetry. The yield fraction quoted below is simply the average of the good and bad halo condition measurements [56]:

$$f_2 = 0.193\% \pm 0.064\%. \tag{4.15}$$

The error (1/3 of the central value) was used because it encompassed the worst possible beam halo conditions.

4.3.2 Beamline Background Asymmetry Correction

The correction for the BB asymmetry was handled in a manner similar to the helicity-correlated beam parameter false asymmetries. The asymmetry in the upstream luminosity monitors was found to be highly correlated with the asymmetry measured in the main detectors. Since the USLumi detectors were largely insensitive to physics asymmetries (by virtue of their very low angular acceptance), this correlation represented a method of determining BB false asymmetry in the MDs. A simple linear model was adopted to remove this background:

$$A_{BB} = \frac{\partial A_{reg}^{MD}}{\partial A_{reg}^{US}} \langle A_{reg}^{US} \rangle \tag{4.16}$$

where $\langle A_{reg}^{US} \rangle$ is the regressed asymmetry from the upstream luminosity monitors averaged over a slug. The correlation

$$\frac{\partial A_{reg}^{MD}}{\partial A_{reg}^{US}} = [4.72 \pm 1.21] \text{ ppb/ppm}, \tag{4.17}$$

was determined over the entirety of Run II and then applied to each slug. Figure 4.8 shows the data used to calculate this quantity with a simple linear fit.

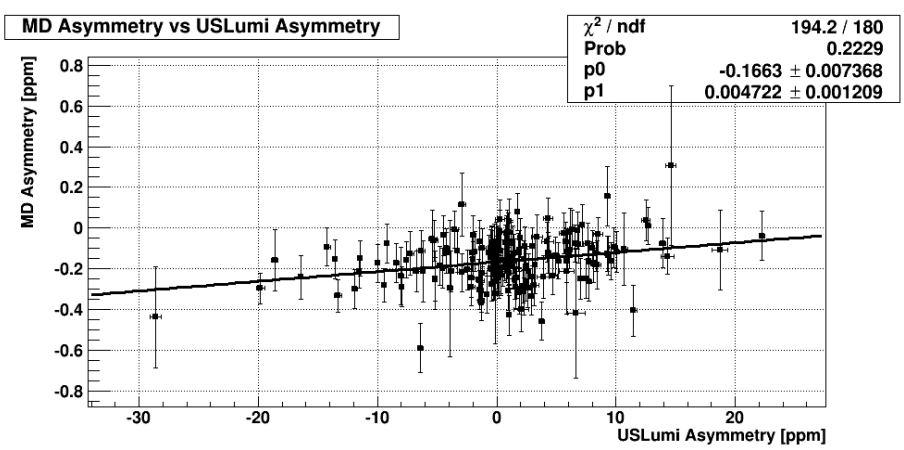

Figure 4.8: MD asymmetry versus USLumi asymmetry for all slugs in Run II. The slope calculated here (p1) is used to remove the BB contribution to the MD asymmetry.

After applying this correction, the data had a null asymmetry consistent with zero, $[5.2 \pm 7.4]$ ppb. This improvement over the raw null asymmetry, $[10.2 \pm 7.4]$ ppb, is shown

in Figure 4.9. The physics asymmetry post BB-correction was calculated to be:

$$A_{reg+BB} = \langle A_{raw} - A_{beam} - A_{BB} \rangle = [-166.4 \pm 7.3(\text{stat.}) \pm 1.0(\text{syst.})] \text{ ppb.} \tag{4.18}$$

as is shown in Figure 4.10. The slight increase of the systematic error compared to eq.(4.13) is due to the uncertainty associated with the calculation of the slope between the MD and USLumi asymmetries.

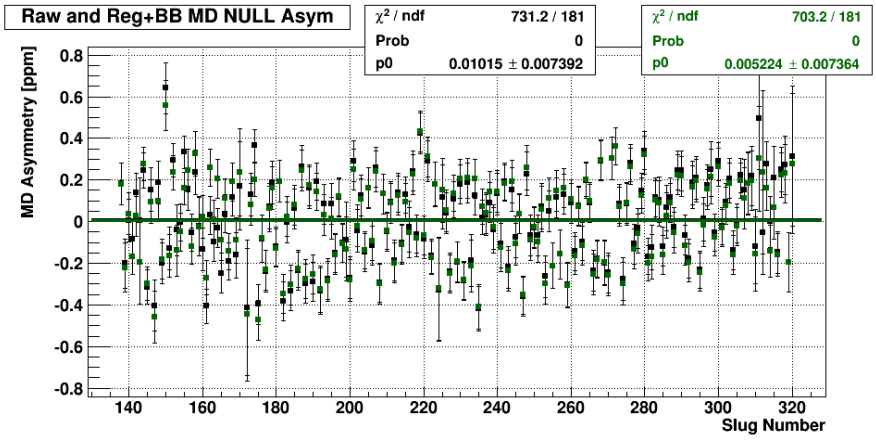

Figure 4.9: Raw (black) and Regressed+BB-corrected (green) null asymmetries for each slug in Run II. Note that the null fits are consistent with zero in the case of the BB corrected data.

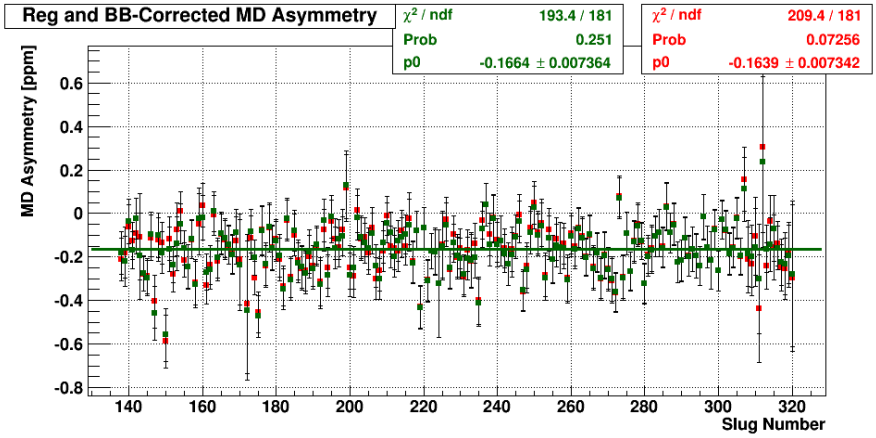

Figure 4.10: Regressed (red) and Regressed+BB-corrected (green) physics asymmetries for each slug in Run II.

4.4 Polarization

The Run II polarization was extracted from a combination of Møller polarimeter and Compton polarimeter measurements. The two polarimeters agreed well, as is shown in Figure 4.11. The Møller measurements in the figure are combined measurements shown with statistical(inner) and systematic(outer) error bars. The Compton polarimeter data points shown represent an average of roughly 30 hours of data taking. Møller measurements were always taken immediately before and after any changes to the polarized source which may have affected the polarization. In particular, it was expected that there would be a different polarization when the laser was focused on a different portion of the GaAs photocathode or the photocathode was replaced.

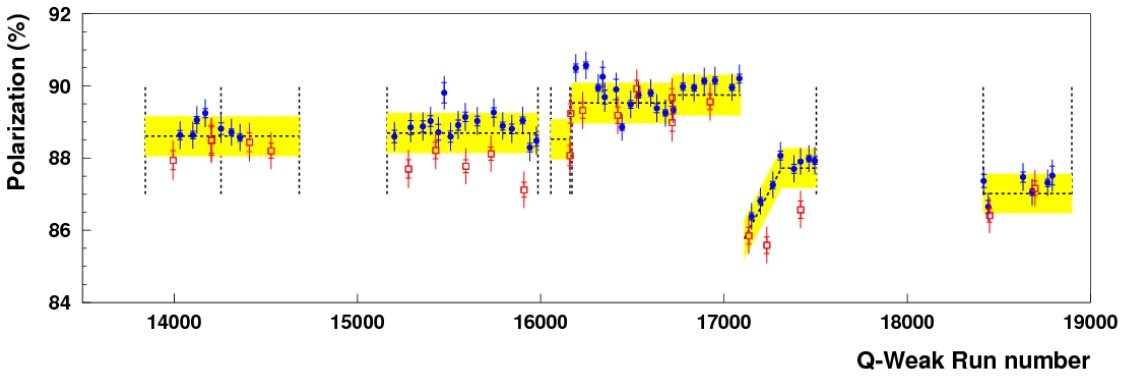

Figure 4.11: Compton (blue circles) and Møller (red squares) polarization measurements made throughout Run II plotted against Q_{weak} run number. Errors shown are statistical and systematic added in quadrature. The black lines with yellow bands represent the mean and uncertainty of the combined polarization measurements of both polarimeters over the stable periods. The portion with linearly increasing polarization after run 17000 is due to changing quantum efficiency at the photo-cathode. Reproduced from [85].

Each period of constant polarization is quoted to a relative precision of 0.62% [85]. Since the polarization could differ significantly between these stable periods, the polarization correction was applied to the asymmetry at the slug level. Each slug, once regressed and corrected for BB asymmetries, was then corrected for the polarization during that period.

As discussed in eq. (4.10), the polarization-corrected asymmetry is averaged over all slugs:

$$\langle A_C \rangle = \left\langle \frac{A_{raw} - A_{beam} - A_{BB}}{P} \right\rangle = [-187.7 \pm 8.3(\text{stat.}) \pm 1.7(\text{syst.})] \text{ ppb.} \tag{4.19}$$

The inflation of the statistical error is simply due to the polarization scaling while the increase in the systematic error is due to polarization scaling as well as the systematic uncertainty of the polarization measurement. The polarization-corrected data (A_C) are shown in Figure 4.12. Both the statistical and systematic errors are increased due to the uncertainty of the polarization measurement. The weighted-average polarization for Run II, which will be used for additional corrections, was calculated to be

$$\langle P \rangle = 0.889 \pm 0.006. \tag{4.20}$$

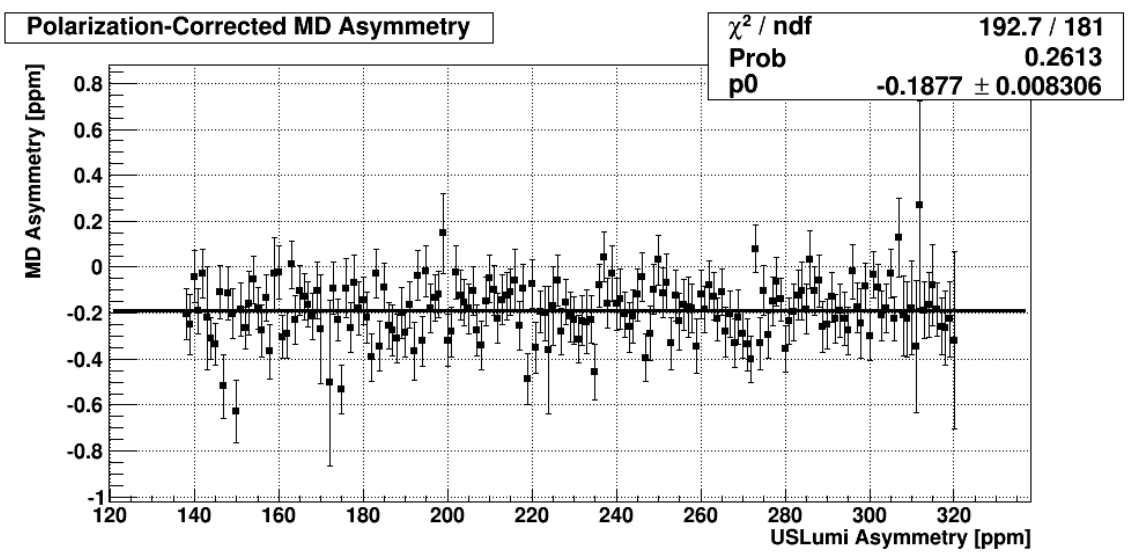

Figure 4.12: Polarization-corrected MD asymmetries for all slugs in Run II.

4.5 PMT Non-linearity

The correction A_L in eq. (4.1) accounted for any potential false asymmetry due to non-linearity in the MD PMT response. Since the current-mode PMTs were designed to function properly for beam currents of 1 - 180 μA, the correction was expected to be zero.

This assumption was bounded within 1.0% by bench tests of the MD PMTs and readout electronics [86]. Assuming the physics asymmetry is found to match the SM prediction, one assigns an error bar of 2.3 ppb to this correction. Thus one obtained

$$A_L = 0 \pm 2.3 \text{ ppb} \tag{4.21}$$

This correction was assumed to be constant over the course of Run II.

4.6 Transverse Asymmetry Leakage

A_T was the false asymmetry arising from residual transverse polarization of the nominally longitudinal polarized electron beam. This parity-conserving asymmetry (B_n) was measured to be $B_n = -4.8 \pm 0.6$ ppm in dedicated studies where the beam polarization was set fully transverse [37]. The transverse asymmetry exhibited an azimuthal dependence for transverse electron polarization:

$$B_n(\phi) = B\cos(\phi + \phi_0) + C, \tag{4.22}$$

where B is the amplitude of the azimuthal asymmetry generated by B_n, ϕ is the azimuthal angle defined from beam-left (octant 1) and ϕ_0 is an azimuthal phase offset. The important quantity for Q_{weak} is the constant C which represents the "transverse leakage" asymmetry that exists as a result of imperfections in the azimuthal symmetry of the eight MDs. The transverse leakage was measured to be[37]:

$$C = [11.7 \pm 40.8] \text{ ppb} \tag{4.23}$$

for a *fully* transverse beam polarization. The leakage factors obtained from simulations based on survey results for the main detector misalignment agreed with the results from these dedicated studies.

The residual transverse polarization during longitudinal running was estimated by examining the residual dipole amplitude present in PV asymmetry measurements, approximately

50 ppb or 1% of the fully transverse asymmetry. Finally, the azimuthal symmetry breaking was measured by determining the differences in asymmetries between opposing octants. While the asymmetry was consistent with zero, the errors on this measurement meant that there was still potential symmetry breaking. The combined effect of the residual transverse polarization and azimuthal symmetry breaking lead to an associated correction [37]:

$$A_T = 0 \pm 0.5 \text{ ppb}. \tag{4.24}$$

4.7 Preradiator Scattering and the PMT Double Difference

An interesting and unforeseen systematic effect was discovered in the discrepancy of the asymmetry measured by the two PMTs at opposite ends of each MD bar, referred as positive and negative PMTs based on the local y coordinate. The placement of these PMTs on every MD bar is shown in Figure 3.10. The difference between the regressed asymmetry measured on positive and negative PMTs, referred as the PMT *double-difference* (DD), is large relative to the physics asymmetry:

$$A_{\text{PMT-DD}} = A^{+}_{reg} - A^{-}_{reg} = [-296 \pm 11] \text{ ppb}. \tag{4.25}$$

This effect is observed to be consistent in all eight octants as is shown in Figure 4.13. In a data set during Run 0 where only four MD bars had preradiators, those four bars observed a non-zero PMT-DD while the four bare bars reported a PMT-DD consistent with zero. This indicated that the source of the PMT-DD was the preradiators.

The mechanism for generating the PMT-DD was later identified as the transverse scattering asymmetry of transversely polarized electrons from lead nuclei in the preradiators. The electrons scattered from the experimental target acquired a transverse polarization component through spin precession in the QTor magnetic field as is shown in Figure 4.14. The polarization direction relative to the direction of motion could be calculated with the

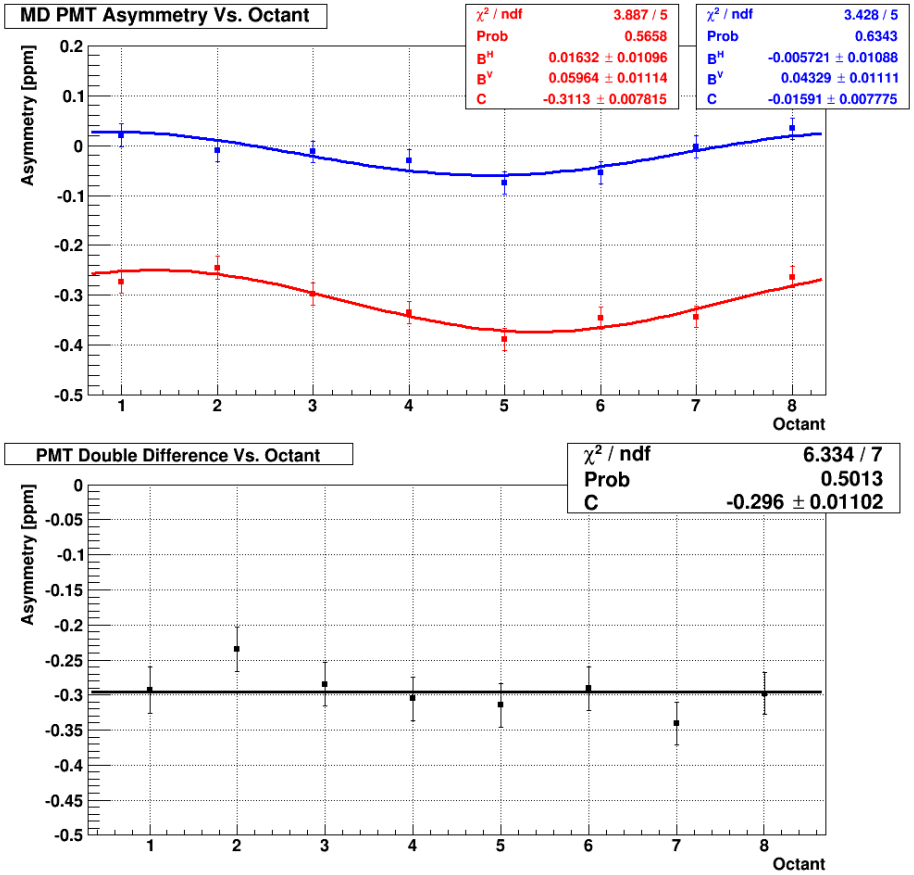

Figure 4.13: Top: The asymmetry measured by the positive PMT (blue) and negative PMT (red) in each octant over Run II. The octant dependence of the asymmetry in this plot was due to residual transverse polarization as discussed in Section 4.6. Bottom: The PMT-DD, eq. (4.25), measured in each octant.

relation [87]:

$$\Delta\phi_P = \frac{E}{0.44065 \text{ GeV}}\Delta\theta. \tag{4.26}$$

where E is the electron's energy, $\Delta\phi_P$ is the change in orientation of the component of the electron's polarization in the dispersion plane and $\Delta\theta$ is the electron's bend angle. Thus, electrons that began with a longitudinal polarization of $P = 0.889 \pm 0.006$ and underwent a bend of $\Delta\theta = 14.3° \pm 1.6°$ in QTor's field reached the preradiator with a transverse polarization component of

$$P_\perp = 0.541 \pm 0.053 \tag{4.27}$$

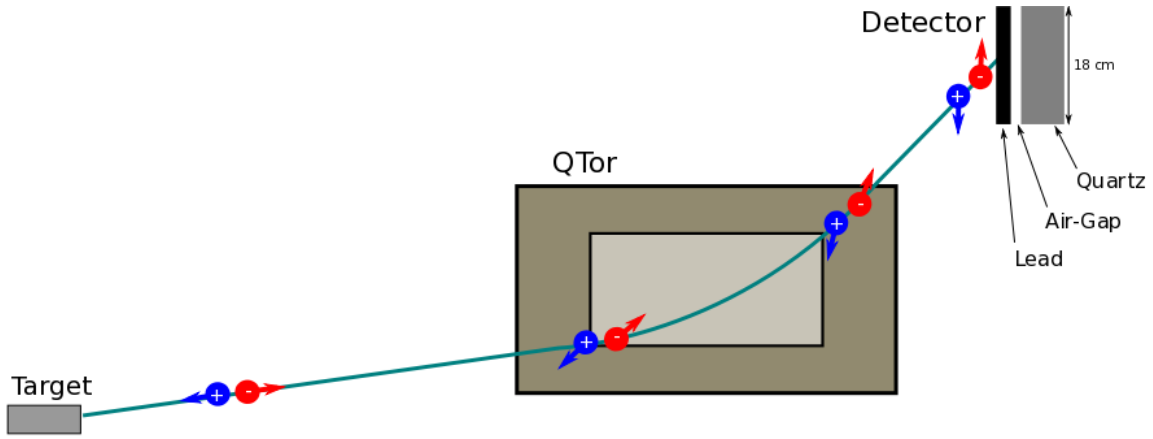

Figure 4.14: The spin of the scattered electrons precesses from purely longitudinal to include a transverse component. Note that the drawing is not to scale and the angles are not exact. Reproduced from [50].

where the additional uncertainty is due to the distribution of angles at which electrons enter and exit the QTor magnetic field.

Mott scattering in the lead of the preradiator carried an analyzing power. Thus when the transversely polarized electrons left the preradiator bar, the electrons preferentially exited the bar with some new, asymmetric position and angle distribution, and when the polarization was flipped, so was this distribution. The PMTs at each end of the MD bar had different sensitivity, to electrons depending upon the position and angle at which they entered the bar. Electrons that entered closer to one PMT than the other or facing towards a PMT produced a larger signal in that PMT than its counterpart. The position dependence of the MD 5 PMTs is shown in Figure 4.15. The asymmetric hit distributions coupled with the individual PMT sensitivities to produce the observed PMT-DD.

Assuming that the MDs were perfectly symmetric (i.e. the per-quartet yield in each PMT is identical), the PMT-DD would not bias the physics asymmetry, which was calculated from the average of positive and negative PMTs. In order to determine the degree of asymmetry and therefore potential bias, studies have been undertaken to characterize the MD bars. Additionally, `GEANT4` simulations have been performed to reproduce the size of the observed PMT-DD. Since many scatterings may occur and there is a large angular acceptance with a heavily convoluted position and angle dependence in the detectors, these

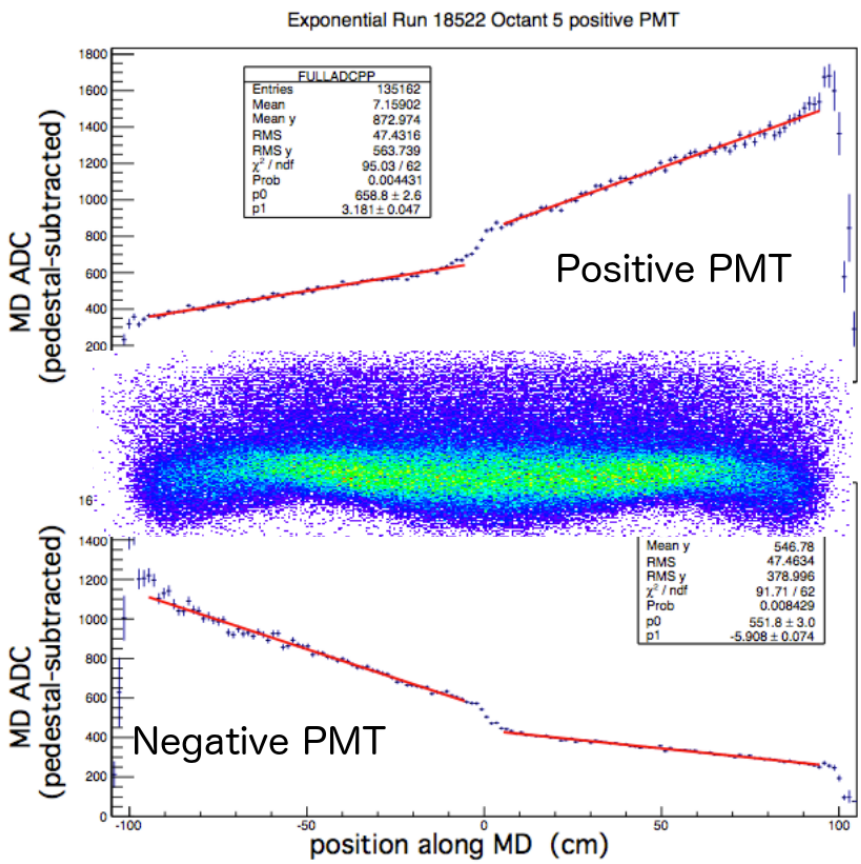

Figure 4.15: Top: The MD 5 positive PMT response as a function of the reconstructed track position on the MD bar during tracking run 18522. The discontinuity was caused by the glue joint connecting the two halves of the MD quartz. Center: The hit profile on the face of the MD. This would shift slightly for each helicity state due to the transverse scattering asymmetry in the lead preradiator. Bottom: Negative PMT response counterpart to the top plot.

studies are difficult. These studies are still in progress and are the primary outstanding issue in the Q_{weak} analysis. However, it has successfully been demonstrated that the bias cancels to first order and is constrained to [88]

$$A_{\mathrm{PS}} = 0 \pm 10 \text{ ppb}. \tag{4.28}$$

The Q_{weak} collaboration expects this error will be reduced with further study so that the final result is statistically dominated.

4.8 Aluminum Target Window Background

Electrons that scattered from the aluminum target windows were the largest background in the Q_{weak} experiment. Because of this, high-precision determinations of both the Al asymmetry and dilution factors were required. Dedicated measurements were performed using a number of solid Al targets; the majority of production Al data were taken at currents of $\approx 70\mu$A on the 4%-radiation length downstream Al target (Al DS4%).

Determination of the PVES asymmetry of electron-aluminum scattering was performed in the same manner in which A_{ep} was determined; corrections were made for beam polarization, helicity-correlated beam parameters, backgrounds, and radiative effects within the target cell. At the current state of analysis, the asymmetry is measured to be [61]

$$A_1 = [1.506 \pm 0.072] \text{ ppm}. \tag{4.29}$$

The total signal fraction in the MD from the target windows was calculated from dedicated measurements with an evacuated target cell,

$$f_1 = Y_{\mathrm{empty}}/Y_{LH_2}, \tag{4.30}$$

where $Y_{\mathrm{empty}(LH_2)}$ was the empty(full) target MD yield. Y_{empty} was verified through measurements on cold hydrogen gas of varying density. The current estimation for the fractional

yield from the aluminum windows in Run II is [61]:

$$f_1 = 0.0285 \pm 0.0008. \tag{4.31}$$

4.9 $\mathbf{Q_{weak}}$ Transport Channel Neutral Background

During the commissioning of the Q_{weak} apparatus, it was discovered that many of the events ($\approx 10\%$) that produced a signal in the MD bars did not produce an associated signal in the trigger scintillator nor in the tracking detectors. These events were referred to as "soft" or *neutral background* (NB) events. This prompted the installation of the lead preradiators, which greatly improved this signal-to-noise ratio. Later studies found that this background was composed of two distinct components.

The first source of neutral events was the beamline background (BB) events discussed in Section 4.3. Those events produced a signal in the MD via scattering from beamline elements downstream of the target. Some of the scatterings in the tungsten plug, for example, produced neutral particles (γ, π^0, n) that traveled through the collimator opening and into the detectors. Other events scattered on beamline elements within the shielding hut and produced a signal in the MD. Neither of these possibilities produced a signal in the TS.

The second source of neutral events is due to secondary scattering of electrons that pass through the collimators and into the QTor magnetic field. Some of these scattered on collimator or shielding edges or on atoms in the air, producing neutral particles that produced a signal in the MD. Additionally, since the MD had a preradiator and the TS did not, the efficiency of the MD was much greater than the TS. Some small fraction of elastically scattered electrons did not produce a signal in the TS. The total MD signal from these types of events was called the *QTor transport channel neutral background* (QTCNB). Figure 4.16 gives a schematic view of the QTCNB as well as *charged* and *neutral* event definitions. Quantifying this signal fraction (f_3) and the asymmetry (A_3) of the QTCNB was the sole responsibility of the author. In order to achieve this goal, the author built upon and refined the methods described in references [78, 89, 35].

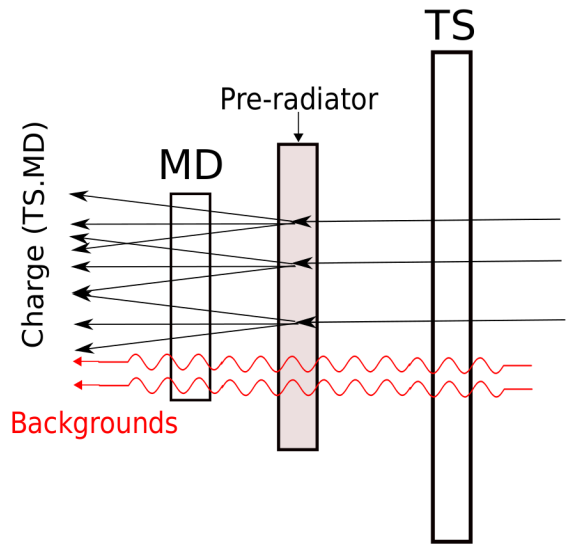

Figure 4.16: Neutral particles (squiggly lines) only generated light in the preradiated MD bars. Charged particles (black lines) typically generated light in both the TS and MD bar. This distinction was the source of the name "neutral" even though some charged particles met the definition for neutral particles.

It was assumed that the two components of the neutral background (BB and QTCNB) were independent and obeyed a simple sum rule,

$$f_n \equiv f_2 + f_3. \tag{4.32}$$

The fraction of the MD signal from all NB events, f_n, is the sum of fractional MD signals from BB (f_2) and QTCNB (f_3) events. Analysis of event-mode data (described in the following section) allowed one to determine f_n directly. Blocked-octant data taking allowed us to determine f_2 as in eq. (4.15). We extracted the QTCNB fraction simply through subtraction:

$$f_3 = f_n - f_2. \tag{4.33}$$

The determination of the PV asymmetry of QTCNB events included in f_3 was accomplished through the use of detailed `GEANT4` simulations, discussed in Section 4.9.4.

4.9.1 Event-Mode Data Set

During production running, there was no way to identify individual events and the quantity measured by the MDs was the integrated yield, (the sum of all light collected by the MD PMTs over the helicity window). Since the neutral events of interest could only be identified in event mode, it was necessary to determine the fraction of the signal from neutral events not just as a ratio of events, but as a ratio of yields in order to determine the impact upon the PV measurement. The event-mode analysis focused on constructing a yield that best represented NB events and then calculating the ratio of this yield to the total event-mode yield.

The analysis of f_n from NB events utilized runs that were triggered by coincidence in the MD PMTs. These events, known to have produced a signal in the MDs, were examined to see if there existed a TS signal consistent with a scattered primary electron. If there was not a TS signal, the events were counted as part of the NB. These data were taken in small run sets throughout both Runs I and II. The runs used for the LH_2 NB measurement are listed in Table 4.5 while the resulting f_n are listed in Table 4.8. A QTor scan was also completed during Run I between run 10544 and 10600. These data showed the dependence of f_n upon the QTor current and will be discussed in the following sections.

4.9.2 Event-Mode Analysis

In order to successfully identify NB events, hit definitions were implemented based on several criteria. First, the *mean time* (`MT`), *PMT time difference* (Δt or `TDC_DIFF`), and *yield* (ADC) variables were defined for our detectors (MD and TS) to be

$$\texttt{MT} = (\texttt{PMT\_LEFT\_TDC} + \texttt{PMT\_RIGHT\_TDC})/2, \tag{4.34}$$

$$\texttt{TDC\_DIFF} = \texttt{PMT\_LEFT\_TDC} - \texttt{PMT\_RIGHT\_TDC}, \tag{4.35}$$

$$\texttt{ADC} = (\texttt{PMT\_LEFT\_ADC} + \texttt{PMT\_RIGHT\_ADC})/2. \tag{4.36}$$

`PMT_LEFT(RIGHT)_TDC[ADC]` refers to the signal from the indicated detector's left(right) PMT TDC[ADC] channel.

Run #	Date	Duration [s]	TS Octants	I_{beam} [nA]	Prescale
10506	2011-03-12	702.2	4 - 8	0	200
10508	2011-03-12	263.3	4 - 8	10	500
10511	2011-03-12	466.7	3 - 7	0	400
10513	2011-03-12	239.0	3 - 7	10	500
10515	2011-03-12	481.8	6 - 2	0	100
10516	2011-03-12	254.8	6 - 2	10	200
10534	2011-03-13	120.6	5 - 1	10	400
10543	2011-03-13	779.8	5 - 1	10	400
10552	2011-03-13	595.6	5 - 1	0	400
10673	2011-03-14	648.7	5 - 1	0	4
13709	2011-11-23	332.5	7 - 3	0	1
13711	2011-11-23	1649.7	7 - 3	10	100
13713	2011-11-23	611.6	7 - 3	50	500
13714	2011-11-23	622.5	7 - 3	100	1000
13717	2011-11-23	451.7	5 - 1	10	80
13718	2011-11-23	436.4	5 - 1	10	200
13720	2011-11-23	207.5	5 - 1	0	40
13721	2011-11-23	301.8	5 - 1	0	1
15027	2012-01-11	694.7	6 - 2	10	80
15028	2012-01-11	723.9	6 - 2	50	400
15034	2012-01-11	538.9	6 - 2	100	800
15122	2012-01-14	555.6	5 - 1	10	64
15123	2012-01-14	527.9	5 - 1	100	700
17608	2012-04-11	140.7	5 - 1	0	0
17627	2012-04-11	563.4	5 - 1	0	0
18487	2012-05-05	717.9	3 - 7	10	80
18524	2012-05-06	36.7	5 - 1	10	0
18525	2012-05-06	26.9	5 - 1	10	0
18526	2012-05-06	4.9	5 - 1	50	0
18527	2012-05-06	24.3	5 - 1	10	0
18578	2012-05-06	379.4	4 - 8	10	60
18579	2012-05-06	360.1	4 - 8	50	300
18580	2012-05-06	343.1	4 - 8	100	600

Table 4.5: List of all runs used in elastic LH_2 NB analysis. Cosmic data (zero beam current) are highlighted in gray. The horizontal line dividing runs 10673 and 13709 represents the end of Run I and beginning of Run II.

These variables had important physical interpretations. `TDC_DIFF` (Δt) was used as an analog for the position of the electron's track(shower) on the TS(MD). This arose simply due to the travel time of the light in the detector. Events with $|$`MD_TDC_DIFF`$| < 20$ channels corresponded to physical positions on the MD bar while those outside this range represented PMT noise. This is due to the effective speed at which Čerenkov light propogated within

the bars as determined by bench tests [78]. Similarly, MT could be used as a restatement of the coincidence criteria on MD and TS hits, events in the TS outside of the accepted mean time window were not from the same electron that triggered the MD readout. The two MD TDC variables can be seen plotted in Fig. 4.17. The ADC value measured the averaged PMT response of the detector, i.e. the amount of light collected from a given detector hit.

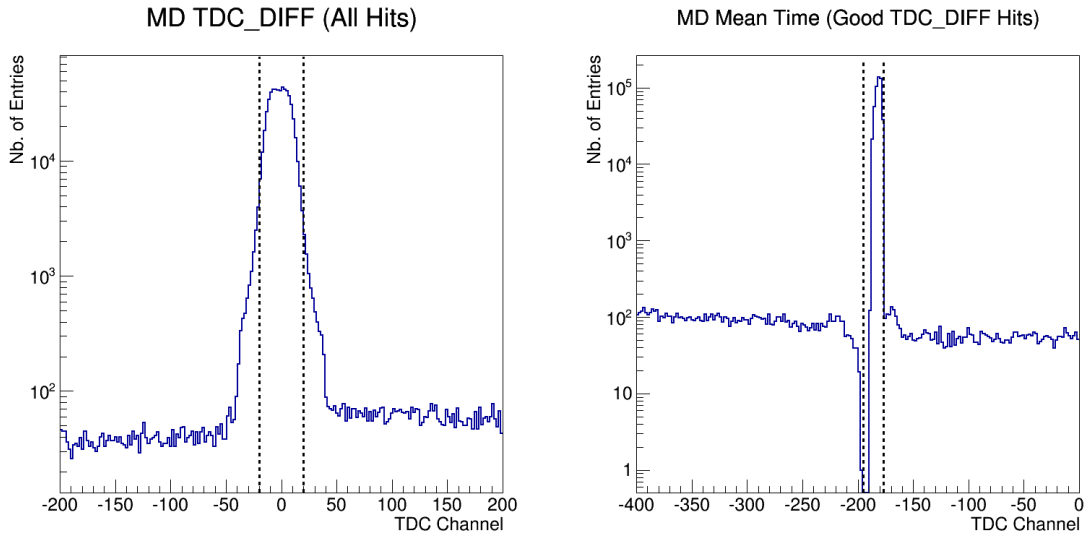

Figure 4.17: Left: MD 6 TDC_DIFF as defined in eq. (4.35) for all events in run 15027. The dashed vertical lines indicate the cuts for good MD hits. Right: The MD 6 MT with the TDC_DIFF cut enforced. The dashed vertical lines indicate the MT cuts for good MD hits. Note the logarithmic scale on both histograms.

With the variables above, hit definitions were constructed for events that correspond to the neutral background. A good MD hit was defined as an event that had a good mean time and physical Δt (as shown in Figure 4.17). A good TS hit was defined as having an ADC value above a threshold of 220 (the reason for this choice is discussed below). The TS ADC spectrum for a run is shown in Figure 4.18. A *charged event* was an event which combined a good MD hit and good TS hit. A *neutral event* was defined as an event with a good MD hit and *no* good TS hit. Histograms of ADC response in the MD for good, charged, and neutral events can be seen in Figure 4.19. The explicit software hit definitions for these and other important event types are shown in Table 4.6.

With the appropriate events in hand, the good and neutral MD ADC spectra (see Figure 4.19) had to be modified so that yield calculations using these spectra more accurately

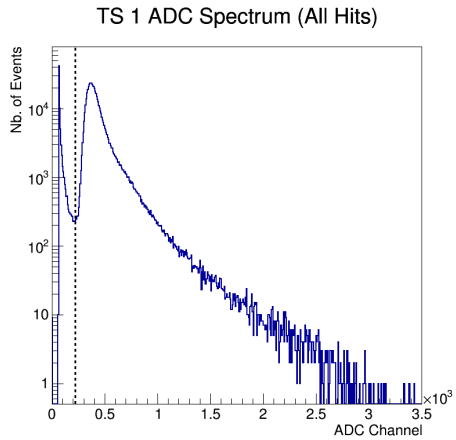

Figure 4.18: The figure shows the ADC data from TS 1, run 15027. This TS was positioned in octant 6 during this run. The dashed line indicates the threshold defining good TS hits.

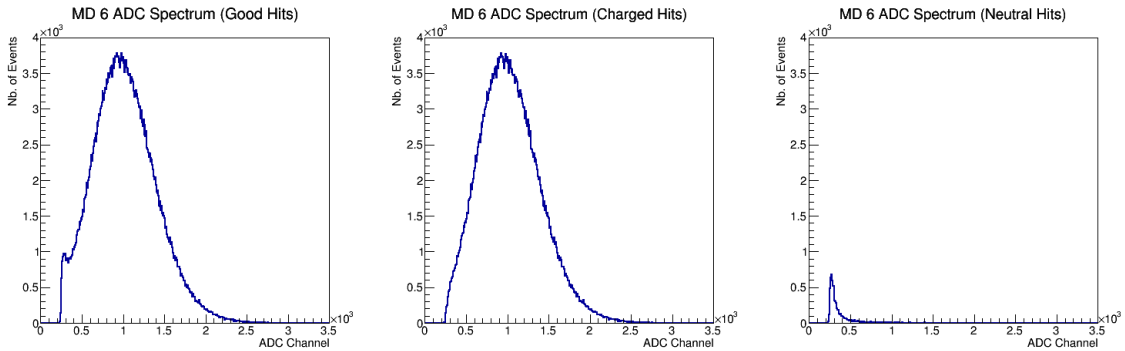

Figure 4.19: Left: MD 6 ADC data for all good MD hits in run 15027. Center: ADC spectrum for charged events. Right: ADC Spectrum for neutral events.

Hit Type	Definition
MD_Good_Hit	(-195 < MD_MT < -177) && |MD_TDC_DIFF| < 20
TS_Good_Hit	TS_ADC > 220
MD_Neutral_Hit	MD_Good_Hit && !TS_Good_Hit
MD_Pedestal_Hit	!MD_Good_Hit && MD_Good_Hit(Opposite Octant)
MD_Rand_Hit	!(-195 < MD_MT < -177) && |MD_TDC_DIFF| < 20
MD_Rand_Neutral_Hit	MD_Rand_Hit && !TS_Good_Hit

Table 4.6: Software hit definitions important for the event mode analysis of the NB signal. The values shown here are discussed in the text.

reflected the integrated yield of current mode. The current-mode yields were pedestal corrected so only the signal above the ADC noise was recorded. In current mode, pedestal measurements were made in dedicated runs without the beam. In the analysis of event-mode data, trigger conditions were exploited to construct a pedestal for each MD of interest

within each run. Pedestal events were defined as those events in an MD which are *not* good hits but were good MD hits in the *opposite octant*. An example pedestal measured in this manner is shown in Figure 4.20. The pedestal value was used to shift the ADC channels for each event in a run according to

$$\texttt{ADC}_{\text{ped. cor.}} = \texttt{ADC} - \langle \texttt{ADC} \rangle_{\text{ped}}, \tag{4.37}$$

where $\langle \texttt{ADC} \rangle_{\text{ped}}$ is the mean ADC channel of the pedestal measurement for a run, and $\texttt{ADC}_{\text{ped. cor.}}$ is the new pedestal corrected ADC value for an event. The subtraction of this pedestal for good events is shown in Figure 4.20.

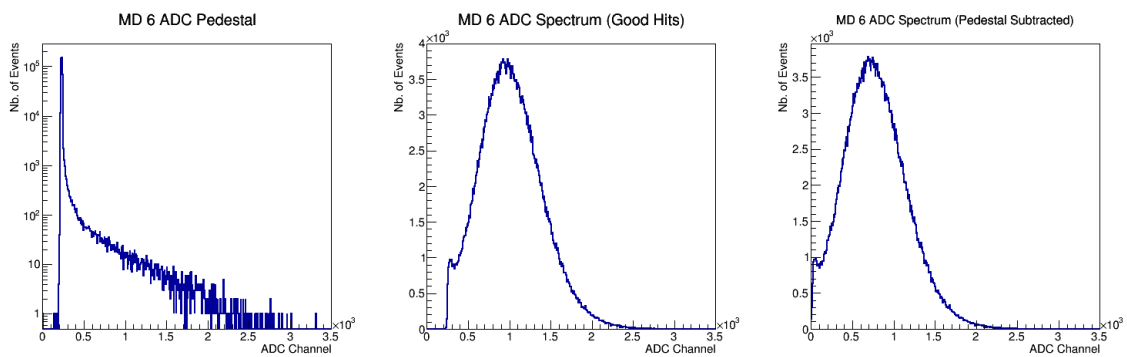

Figure 4.20: Left: The MD 6 ADC signal for the pedestal events as defined in the text and Table 4.6. The peak defines the new zero from which the yield should be measured. Center: Good MD 6 hits as shown in the left histogram of Figure 4.19. Right: The MD 6 ADC spectrum after pedestal subtraction as in eq. (4.37).

Following the pedestal subtraction, the data were corrected for *random* events. These were events due to the MD TDC noise. Randoms were corrected for by constructing a spectrum for MD events that had a good Δt but fell outside the meantime cut. A random spectrum was constructed for both good and neutral MD events following the cuts in Table 4.6. The random spectra were then scaled by the ratio of the width of the good MD hit MT window over the random MT window, a factor $\delta_{\text{rand.}} = 18/382$. The scaled random spectra were subtracted from the appropriate MD spectra as is shown in Figure 4.21. This correction was found to be negligible in the final neutral fraction measurement but was kept for completeness.

From the pedestal- and random-corrected good and neutral MD spectra, shown in

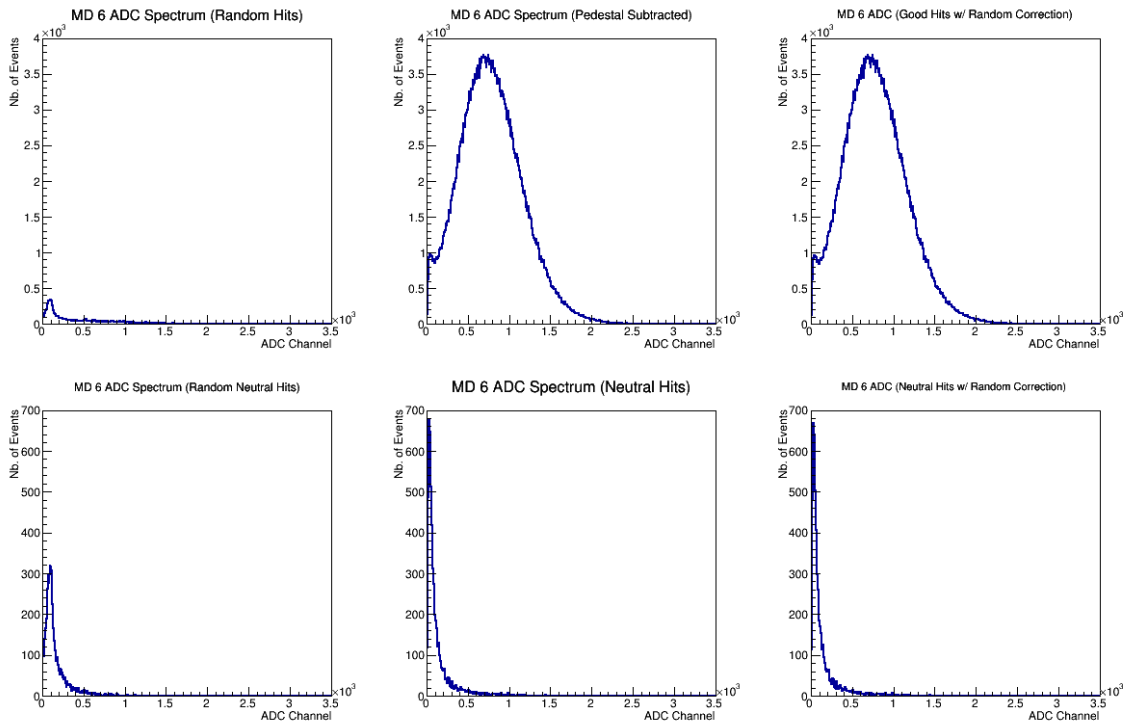

Figure 4.21: This figure details the method of the random event correction for run 15027. In the top left, the total random ADC spectrum for MD 6 is shown. This is scaled by a small factor ($\delta_{\text{rand.}}$) and then subtracted from the spectrum in the top center figure (the same spectrum shown in Figure 4.20). The resulting, random-corrected spectrum is shown in the top right plot. While this is a small change, it is slightly more significant in the case of the neutral spectra, shown on the bottom. Note the difference in scale between the top and bottom histograms.

the right column of Figure 4.21, one could construct a quantity which was comparable to current-mode yields. This event-mode yield was defined as:

$$Y = \sum_{i=1}^{\texttt{nbins}} N_i L_i, \tag{4.38}$$

where the sum is carried over `nbins`, the total number of bins in the spectrum being summed, N_i is the number of events in the bin, and L_i is the central pedestal-corrected ADC channel of the bin. A brief study of bin size found that 350 bins was adequate for the analysis. These yields had associated statistical uncertainties:

$$\delta Y = \left[\sum_i N_i L_i^2 \right]^{1/2} \tag{4.39}$$

The total neutral event fraction was the ratio of the neutral MD yield and good MD yield. The resulting neutral fraction was:

$$f_n = \frac{Y^{neut.}}{Y^{tot}} = \frac{\sum N_i^{neut.} L_i}{\sum N_i^{tot.} L_i}. \tag{4.40}$$

where $N_i^{neut.(tot.)}$ refers to the number of events in the i-th bin of the neutral(total) MD spectrum.

During the analysis of these data, f_n was found to vary with beam current[90]. This behavior was believed to be caused by a constant, beam-independent cosmic-ray neutral signal in the MDs. This signal was more significant at small event rates and became less significant at higher event rates. Since the measurement we needed to correct was taken at currents ~ 3 orders of magnitude larger than the event-mode data, it was necessary to ensure that we accurately represented the NB fraction at those higher currents. An effort was made to correct for this by constructing a scaled yield rate for each run:

$$Y_R = (P + 1)Y/T. \tag{4.41}$$

Here P represents the run's pre-scale value (found in Table 4.5), Y is the yield defined in eq. (4.38), and T is the run's duration. Scaled yield rates were also constructed for beam-off runs (highlighted in grey in Table 4.5). These beam-off values were averaged to create $Y_{R_{cos.}}^{neut.}$ and $Y_{R_{cos.}}^{tot.}$: the neutral and total scaled cosmic yield rate, respectively. These yield rates were used to correct the yield fractions for each run, forming a new neutral fraction measurement:

$$f_n = \frac{Y_R^{neut.} - Y_{R_{cos.}}^{neut.}}{Y_R^{tot.} - Y_{R_{cos.}}^{tot.}}. \tag{4.42}$$

This formula was used to calculate the NB fraction, f_n, quoted in this work. While this method did remove some of the NB fraction's dependence upon beam current, a marginally significant residual dependence was still observed, as demonstrated in Table 4.7.

Using eq. (4.42), f_n was calculated for each active octant for each run in the data set. The results of these calculations are shown in Table 4.8 and Figure 4.22. In the table and figure, one may observe the difference in the neutral fraction recorded by each TS for

I_{beam} [nA]	f_n	δf_n
10	0.285%	0.147%
50	0.240%	0.079%
100	0.183%	0.072%

Table 4.7: The average NB fraction for each beam current at which the event-mode data were taken. The error δf_n is the standard deviation of the measurements.

every run. This was due to the different efficiencies of the two trigger scintillators. This phenomenon had no effect on other aspects of the Q_{weak} measurement. The two octants frequently reported neutral fractions with a relative difference of 50%. This was the largest systematic effect observed in this data. In order to account for it, all averages over neutral fraction measurements were the simple mean (as opposed to a traditional, error-weighted average) and the standard deviation was used as the uncertainty of the averaged value.

Run (in Figure 4.22)	TS 1 f_n[%] (MD)	TS2 f_n [%] (MD)	Average f_n [%]
10508 (1)	0.51 ± 0.07 (4)	0.06 ± 0.05 (8)	0.28 ± 0.32
10513 (2)	0.50 ± 0.06 (3)	0.12 ± 0.07 (7)	0.31 ± 0.27
10516 (3)	0.09 ± 0.04 (6)	0.21 ± 0.03 (2)	0.15 ± 0.09
10534 (4)	0.56 ± 0.03 (5)	0.30 ± 0.03 (1)	0.43 ± 0.18
10543 (5)	0.55 ± 0.01 (5)	0.24 ± 0.01 (1)	0.39 ± 0.22
13711 (6)	0.29 ± 0.00 (7)	0.42 ± 0.01 (3)	0.35 ± 0.09
13713 (7)	0.22 ± 0.01 (7)	0.31 ± 0.01 (3)	0.26 ± 0.07
13714 (8)	0.15 ± 0.01 (7)	0.24 ± 0.01 (3)	0.19 ± 0.06
13717 (9)	0.39 ± 0.01 (5)	0.25 ± 0.01 (1)	0.32 ± 0.10
13718 (10)	0.15 ± 0.02 (5)	0.05 ± 0.01 (1)	0.10 ± 0.07
15027 (11)	0.29 ± 0.01 (6)	0.22 ± 0.01 (2)	0.25 ± 0.05
15028 (12)	0.26 ± 0.01 (6)	0.18 ± 0.01 (2)	0.22 ± 0.05
15034 (13)	0.18 ± 0.01 (6)	0.13 ± 0.01 (2)	0.16 ± 0.04
15122 (14)	0.41 ± 0.01 (5)	0.27 ± 0.01 (1)	0.34 ± 0.10
15123 (15)	0.29 ± 0.01 (5)	0.18 ± 0.01 (1)	0.23 ± 0.08
18487 (16)	0.50 ± 0.01 (3)	0.29 ± 0.01 (7)	0.40 ± 0.15
18524 (17)	0.34 ± 0.00 (5)	0.21 ± 0.00 (1)	0.27 ± 0.09
18525 (18)	0.34 ± 0.00 (5)	0.20 ± 0.00 (1)	0.27 ± 0.09
18526 (19)	0.33 ± 0.00 (5)	0.20 ± 0.00 (1)	0.27 ± 0.10
18527 (20)	0.34 ± 0.00 (5)	0.20 ± 0.00 (1)	0.27 ± 0.10
18578 (21)	0.35 ± 0.01 (4)	0.11 ± 0.01 (8)	0.23 ± 0.17
18579 (22)	0.31 ± 0.01 (4)	0.11 ± 0.01 (8)	0.21 ± 0.15
18580 (23)	0.23 ± 0.01 (4)	0.06 ± 0.01 (8)	0.14 ± 0.12

Table 4.8: This table lists the NB fraction for each octant in each run. The second and third columns are the neutral fractions calculated with eq. (4.42) with purely statistical error. The combined results in the rightmost column are the arithmetic mean of the two previous columns and the error is the standard deviation of the two measurements.

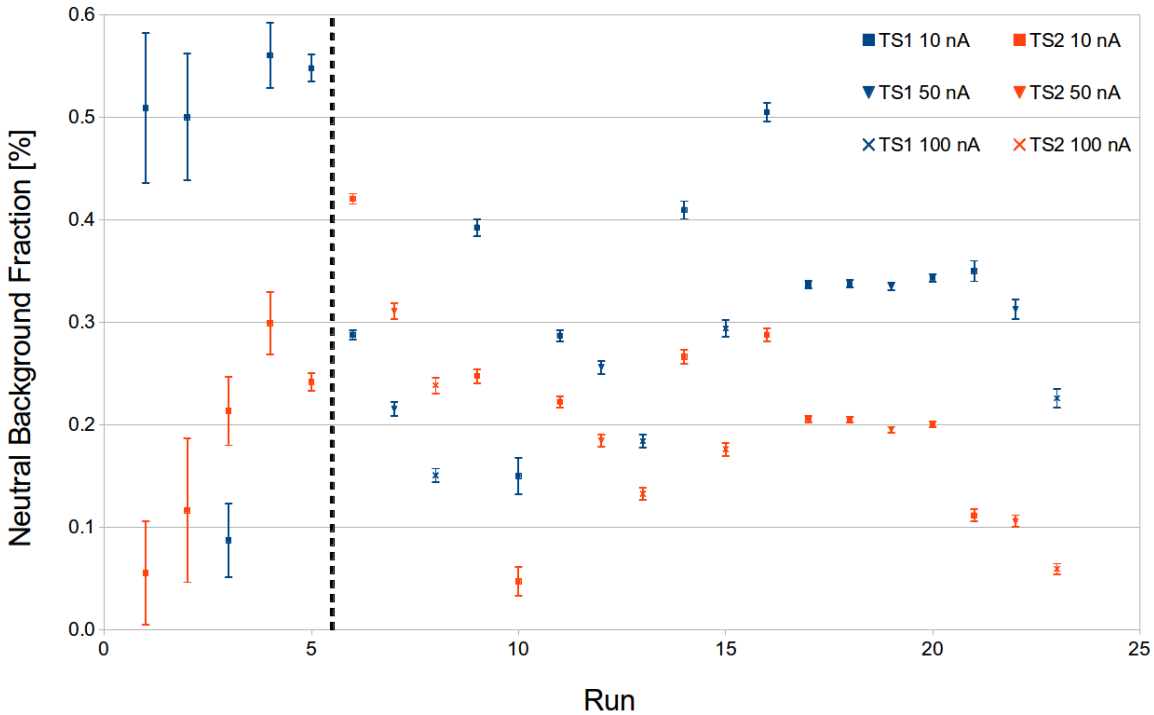

Figure 4.22: Total neutral fraction, f_n, for each octant for all runs in the event mode dataset. This plot clearly illustrates the observed difference between the two trigger scintillators as well as the current dependence.

At this point, the QTCNB fraction could be calculated directly. Averaging f_n over all detectors for Run I resulted in $f_n^{\mathrm{I}} = 0.0031 \pm 0.0020$. Similarly, Run II gave $f_n^{\mathrm{II}} = 0.0025 \pm 0.0010$. Taking values from [56], we see $f_2^{\mathrm{I}} = 0.00190 \pm 0.00040$ and $f_2^{\mathrm{II}} = 0.00193 \pm 0.00064$. Inserting these values into eq. (4.33) resulted in:

$$f_3^{\mathrm{I}} = 0.0012 \pm 0.0020, \tag{4.43}$$

$$f_3^{\mathrm{II}} = 0.0006 \pm 0.0012. \tag{4.44}$$

The large error bars accounted for the large systematic uncertainties due to the TS dependence and the beam-current dependence.

4.9.3 Neutral Background QTor Scan

As mentioned previously, the current of the QTor spectrometer magnet was varied to observe how the magnetic field strength affected f_n. All results of this study are shown in Table

4.9 and Figure 4.23. To see how the absolute current-mode neutral yield varied with QTor current, the neutral yield was defined to be

$$Y_n = f_n Y_{c.m.}, \tag{4.45}$$

where $Y_{c.m.}$ were measured current-mode MD yield values taken from reference [91]. As can be seen in Figure 4.23, the neutral MD yield, Y_n, was independent of QTor current over the majority of QTor currents. This supported the hypotheses of the primary causes of this background, discussed in the preceding sections. The first source, BB events, would be unaffected by QTor current because these tracks did not pass through the magnetic field. The second source, neutral secondaries from scattering on collimators or shielding edges, which is believed to be the primary source of the QTCNB signal, is also independent of the QTor field. The third possible source discussed during the analysis, cosmic backgrounds, also would be independent of QTor.

Run	I_{QTor} [A]	TS 1 f_n [%]	TS 2 f_n [%]	Average f_n
10544	9200	0.62 ± 0.02	0.29 ± 0.01	0.45 ± 0.23
10548	9000	0.57 ± 0.02	0.26 ± 0.01	0.41 ± 0.22
10549	8700	0.69 ± 0.02	0.27 ± 0.01	0.48 ± 0.30
10555	8500	1.24 ± 0.05	0.53 ± 0.03	0.88 ± 0.50
10556	8300	2.01 ± 0.07	0.90 ± 0.05	1.46 ± 0.78
10559	8000	3.09 ± 0.12	1.51 ± 0.09	2.30 ± 1.12
10560	7600	4.39 ± 0.16	2.55 ± 0.15	3.47 ± 1.30
10564	7000	5.71 ± 0.19	3.05 ± 0.15	4.38 ± 1.88
10567	6700	5.78 ± 0.17	2.99 ± 0.13	4.39 ± 1.97
10568	6500	6.47 ± 0.21	2.84 ± 0.15	4.65 ± 2.57
10571	6000	7.57 ± 0.28	3.55 ± 0.21	5.56 ± 2.84
10572	5500	8.82 ± 0.31	4.76 ± 0.24	6.79 ± 2.87
10578	5000	10.57 ± 0.11	5.77 ± 0.09	8.17 ± 3.40
10580	4500	12.34 ± 0.13	6.62 ± 0.10	9.48 ± 4.04
10583	4000	14.07 ± 0.15	7.73 ± 0.12	10.90 ± 4.48
10584	3500	16.09 ± 0.15	9.00 ± 0.12	12.55 ± 5.02
10587	3000	18.64 ± 0.16	10.69 ± 0.14	14.66 ± 5.62
10588	2500	21.29 ± 0.19	13.34 ± 0.17	17.31 ± 5.62
10594	2000	22.75 ± 0.19	15.53 ± 0.18	19.14 ± 5.10
10597	1500	18.34 ± 0.17	13.05 ± 0.15	15.70 ± 3.74
10600	1000	10.10 ± 0.14	7.79 ± 0.13	8.95 ± 1.64

Table 4.9: Results of the QTor current scan. In these runs, TS 1 was placed in front of MD 5 and TS 2 in front of MD 1.

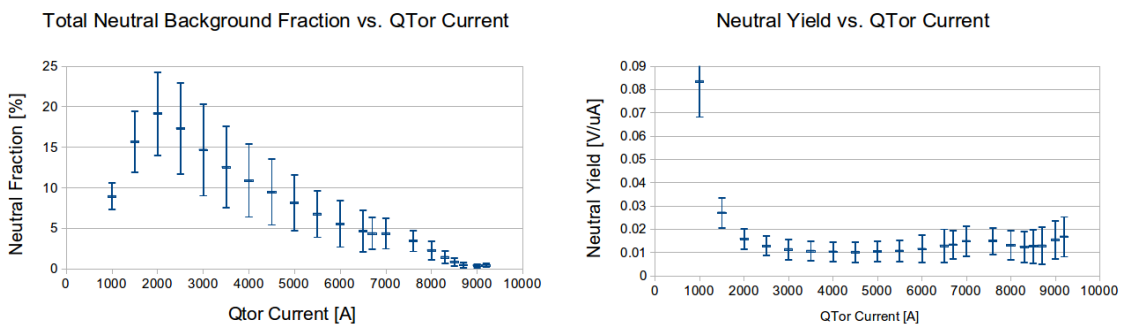

Figure 4.23: Left: Graph indicating the neutral fraction determined from event-mode runs. Values are shown in the rightmost column of Table 4.9. Right: Neutral background yield calculated using eq. (4.45). Recall that during normal data taking the QTor Current was 8900 A.

4.9.4 Neutral Background GEANT4 Simulations

In order to assign an asymmetry to the QTCNB for a given target, a simple process that utilized GEANT4 simulations was implemented. Events were thrown in octant 3 (where the TS is placed in the simulation) into a phase space, Ω, equal to $\theta \in [4°, 13.5°]$, $\phi \in [74°, 106°]$, for all of the relevant event generators for that target. The dominant generators for the LH_2 can be seen in Table 4.12 later in this section. These events were recorded when there was a hit in the MD. In the simulation, a hit was simply a particle passing through a detector's sensitive volume.

In order to accurately replicate data, additional hit definitions, similar to those in Table 4.6, were constructed for these simulated events. The simulation included realistic Čerenkov light propagation and collection in the PMTs. Good MD hits were simply defined to be those events that produced a simulated photo-electron (PE) in the detector PMTs. The additional TDC cuts were unnecessary as the simulation contained no noise on the PMT signals. The simulated TS had no PMTs and therefore good TS events were defined as those that recorded some non-zero energy deposition within the scintillator material. Neutral events were defined as those good MD hits with no corresponding TS hit. The simulation event definitions are shown explicitly in Table 4.10.

For each event generator, i, an average yield (comparable to a current-mode yield within a normalization factor) was constructed, This value is a modification of the well known rate

Hit Type	Definition
MD_Sim_Hit	Cerenkov.PMT.PMTTotalNbOfPEs[3]>0
TS_Sim_Hit	TriggerScintillator.Detector.TotalDepositedEnergy>0
MD_Sim_Neutral_Hit	MD_Hit && !TS_Hit

Table 4.10: Software hit definitions for GEANT4 simulation analysis. PMTTotalNbOfPEs[3] indicates that MD 3 was the detector behind the TS in the simulation. There were no pedestals nor random events within the simulation.

calculation based upon the product of the luminosity $\mathcal{L}$, cross section σ and outgoing solid angle $d\Omega$. The construction of the yield required additional information provided by the simulation about the detector acceptance and response. For a generator i, the yield was defined as

$$Y^i_{sim.} \equiv \int_V \mathcal{L}(x)\sigma^i(x)L(x)\epsilon(x)dV, \tag{4.46}$$

where $L(x)$ is the detector response, in this case the number of PEs measured by the MD 3 PMT, and the acceptance function, $\epsilon(x) = (\#$ of events meeting cuts/$\#$ of events thrown), parameterizes the detector acceptance. All values in the integrand are a function of one or more internal degrees of freedom of the simulation (represented by the vector x) such as position in the target of the initial scattering, energy loss in the target, scattering angle, secondary processes, *et cetera*. The simulation itself provided the numerical integration over the phase space V. These yields were calculated using an estimator of the integral

$$Y^i_{sim.} \approx \mathcal{L}\left\langle \sigma^i L \right\rangle \epsilon\Omega. \tag{4.47}$$

The yields were benchmarked against various data-taking conditions (different target and QTor current) and found to behave appropriately.

Using these simulated yields, one could form predictions of the neutral background fractions from individual processes within the target. This was calculated simply:

$$f^i_{sim.} = \frac{Y^i_{sim.neut.}}{Y^{tot.}_{sim.}}, \tag{4.48}$$

where $Y^{tot.}_{sim.} = \sum_i Y^i_{sim.}$. The total simulated QTCNB was calculated to be the sum of these

individual neutral fractions

$$f_3^{sim.} = \sum_i f_{sim.}^i = 0.00190 \pm 0.00020. \tag{4.49}$$

The quantity in eq. (4.49) is directly comparable to the results shown in eqs. (4.43 - 4.44). A comparison of simulated and observed QTCNB fractions is given in Table 4.11. All simulated results were seen to be compatible with the measured results. The results for individual event generators can be seen in Table 4.12.

Measurement	Data f_n [%]	Simulation f_n [%]
Elastic LH_2 (Run I)	0.12 ± 0.20	0.19 ± 0.02
Elastic LH_2 (Run II)	0.06 ± 0.14	0.19 ± 0.02

Table 4.11: A comparison of measured QTCNB fractions and simulated fractions. All simulations agree with the measured results within errors. The changes made in the simulation to differentiate between Run I and Run II (small geometric changes) produced no discernible shift and so their combined average is what is shown in the right-hand column and eq. (4.49).

To calculate the asymmetry of the QTCNB for a given measurement, we simply performed a weighted average of the asymmetries for each process simulated for that measurement:

$$A_{sim.} = \frac{\sum_i f_{sim.}^i A_i}{f_{sim.}}. \tag{4.50}$$

Table 4.12 shows the significant generators, their contributions to the QTCNB for LH_2 and the associated asymmetry. The resulting QTCNB asymmetry for the Run II data set was calculated to be

$$A_3 = [-0.39 \pm 0.16] \text{ ppm}. \tag{4.51}$$

4.9.5 QTCNB Conclusions

To briefly summarize, the total NB fraction was calculated using event-mode data. This value consisted of both BB events and QTCNB events with an assumed sum rule. Sub-

Event Type	$f^i_{sim.}$ [%]	A_i [ppm]
Elastic LH_2	0.119 ± 0.016	-0.31 ± 0.03 [QwGeant4]
Inelastic $p \to \Delta$	0.026 ± 0.003	-3.02 ± 0.70 [92]
Møller	0.018 ± 0.006	0.001 ± 0.0005 [93]
Elastic (DS Al)	0.009 ± 0.001	2.11 ± 0.11 [94]
Inelastic Rad. (DS Al)	0.003 ± 0.001	2.5 ± 1.3 [94]
Quasi-elastic (DS Al)	0.003 ± 0.001	-0.3 ± 0.3 [94]
Elastic (US Al)	0.006 ± 0.001	2.11 ± 0.11 [94]
Inelastic Rad. (US Al)	0.002 ± 0.001	2.5 ± 1.3 [94]
Quasi-elastic (US Al)	0.001 ± 0.001	-0.3 ± 0.3 [94]

Table 4.12: Simulated QTNCB fractional yields and their associated asymmetries listed according to their importance to the total QTCNB signal.

tracting the BB fraction from the NB fraction yielded the QTCNB fraction in eq. (4.44):

$$f_3^{\mathrm{II}} = 0.0006 \pm 0.0012. \tag{4.52}$$

The large uncertainty was due to systematic differences between the two TSs and the different beam currents at which data were taken. The asymmetry from these events was calculated using `GEANT4` simulations. The asymmetry was due to several different processes within the target, each with a unique PV asymmetry (Table 4.12). The combined weighted-average asymmetry was calculated in eq. (4.51):

$$A_3 = [-0.39 \pm 0.16] \text{ ppm}. \tag{4.53}$$

4.10 Inelastic Scattering Background

The final background came from inelastic scattering events associated with $p \to \Delta(1232)$ production. This PV asymmetry was expected to be roughly 10 times as large as the elastic asymmetry[75]. The experiment typically operated with a QTor current of $\approx$ 8900 A, which maximized the elastic rate relative to backgrounds. However, the integrating mode detectors did not allow the complete separation of the signal from this inelastic background.

`GEANT3` simulations were used to study the fraction of inelastic events in the acceptance [91]. Figure 4.24 shows the results of this study. At the typical QTor current of 8921

A, the inelastic signal fraction is estimated to be

$$f_4 = 0.0002 \pm 0.0002. \tag{4.54}$$

The 100% relative uncertainty is assigned to account for discrepancies between simulation and data. A separate `GEANT4` simulation under development [95] is in agreement with this result and will provide a less conservative uncertainty to the final measurement.

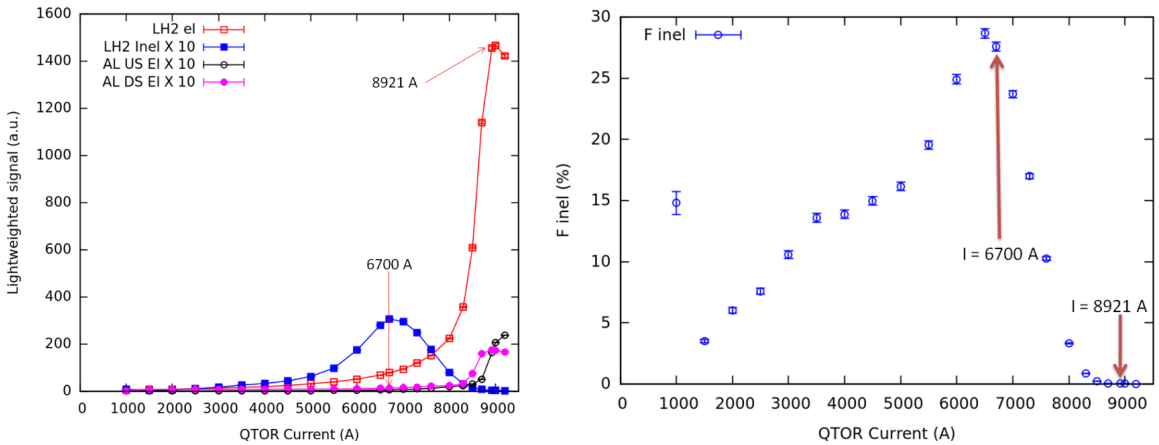

Figure 4.24: Left: Simulated event yields for different scattering processes in the target plotted as a function of QTor current. Note that the units are arbitrary on the Y axis as produced by eq. (4.47) and the inelastic and Al processes are multiplied by a factor of 10 for increased visibility. Right: Simulated inelastic fraction due to $p \to \Delta$ production as a function of QTor current. Reproduced from [96].

To measure the PV asymmetry of this process, production data were taken with the QTor current set to 6700 A. With this magnetic field, the inelastic resonance accounted for approximately 25% of the signal. After the appropriate corrections, the asymmetry was determined to be [75]

$$A_4 = [-3.02 \pm 0.97] \text{ ppm}. \tag{4.55}$$

4.11 Radiative Corrections and Experimental Bias

The final corrections necessary to obtain the tree-level asymmetry were contained in the factor R in eq. (4.1). This term accounted for EM radiative effects, detector bias and acceptance correction, as well as corrections associated with the uncertainty in the momentum

transfer squared Q^2.

The EM radiative corrections relevant to the Q_{weak} experiment were bremsstrahlung photon emission and virtual photon loops as shown in Figure 4.25. Both processes could result in depolarization and energy losses in the incident electron, changing the energy and scattering angle, which produced a measurable change in both Q^2 and asymmetry. To account for these effects, `GEANT3` simulations were conducted with and without these processes turned on as discussed in [81] according to the procedure developed by Mo and Tsai [8] for electron-vertex radiative corrections to the cross section. A factor was calculated that normalized the measured asymmetry (including these radiative effects) to the tree-level asymmetry (without these effects) so that the Q_{weak} results would be easily interpreted. The factor for Run II was found to be:

$$R_{RC} = \frac{A^{sim}_{tree}}{A^{sim}_{Mo-Tsai}} = 1.0101 \pm 0.0007 \tag{4.56}$$

where $A^{sim}_{tree(Mo-Tsai)}$ is the averaged simulated asymmetry given by the tree-level (radiated) event generator.

The detector bias correction, R_{det}, accounted for the fact that the efficiency of light collection in the main detector varied as a function of hit position on the MD bar. `GEANT4` simulations were performed in which the asymmetry was calculated with light-weighting ($A^{sim}_{unbiased}$) and without light-weighting (A^{sim}_{biased}). The size of the correction was computed as the ratio of these two asymmetries [97]:

$$R_{det} = \frac{A^{sim}_{unbiased}}{A^{sim}_{biased}} = 0.9921 \pm 0.0044. \tag{4.57}$$

The Q_{weak} apparatus integrated the signal from scattered electrons with a large range of Q^2 values based on its large angular acceptance. In order to determine the asymmetry and the weak charge of the proton at a single value, an additional "effective kinematics" or "bin centering" correction needed to be performed. This R_{acc} was determined by comparing simulated values for the asymmetry at an average Q^2 and the average asymmetry over the

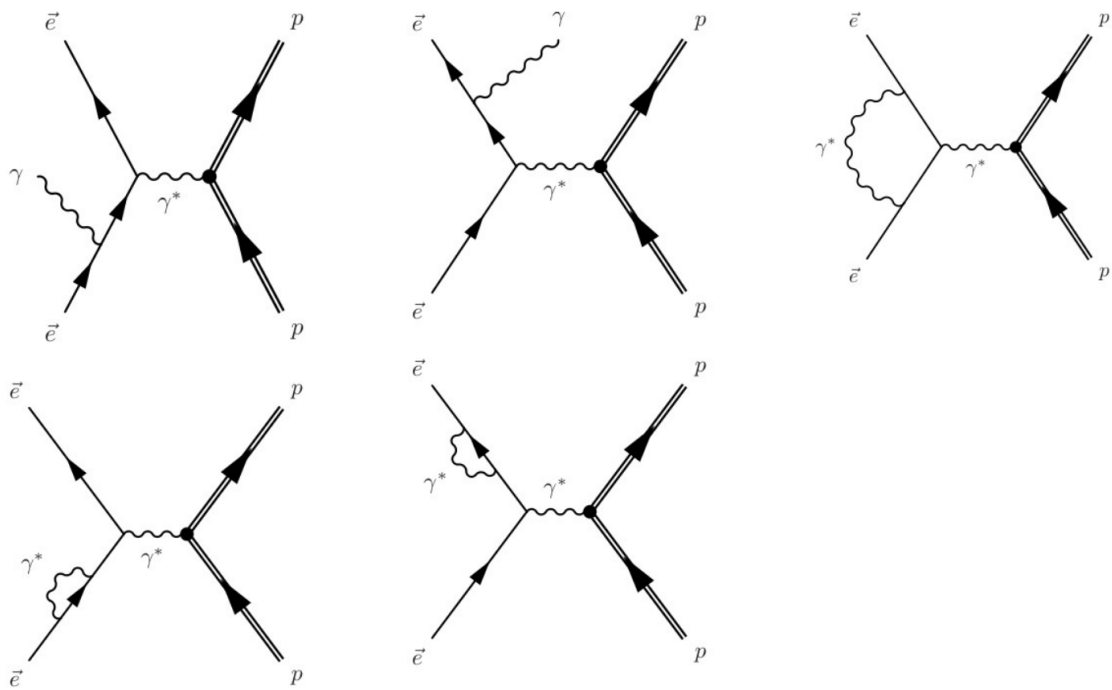

Figure 4.25: Processes which are corrected for in the Q_{weak} experiment using the Mo-Tsai procedure [8].

Q^2 range accepted by the apparatus [98]:

$$R_{acc} = \frac{A(\langle Q^2 \rangle)}{\langle A(Q^2) \rangle} = 0.980 \pm 0.005. \tag{4.58}$$

The final correction, R_{Q^2}, is similar to but distinct from R_{acc}. The experiment was limited in its ability to determine the central Q^2 value precisely. The precision currently stands at $\delta Q^2/\langle Q^2 \rangle = 1.28\%$. Using the same method as was used for the early Q_{weak} result [21] (assumed linear scaling) with an updated Q^2 error, we assign the following correction:

$$R_{Q^2} = 1.000 \pm 0.013.. \tag{4.59}$$

Because all of these corrections were multiplicative, we formed the composite correction:

$$R = R_{RC} \times R_{det} \times R_{acc} \times R_{Q^2} = 0.9770 \pm 0.0207. \tag{4.60}$$

4.12 Kinematics

To determine the four-momentum transfer squared at the scattering vertex, Q^2_{tree}, data collected by the tracking detectors were analyzed by dedicated tracking software built on the algorithms of the HERMES collaboration [99]. The software first identified hits in HDCs and VDCs (see Section 3.12) and reconstructed these hits into track segments. Complete tracks were formed connecting the track segments by applying a 4th-order Runge-Kutta trajectory integration in the magnetic field and then upstream of the HDCs to the target. This allowed the determination of the effective kinematics as the electron left the target.

However, this did not allow for calculation of these kinematics at the interaction vertex directly. Therefore, `GEANT4` simulations with known vertex kinematics were used to generate tracks that were then analyzed using the software above. By comparing the visible kinematic parameters between the tracking data and the simulations, the acceptance-averaged vertex kinematics were extracted [100]. Figure 4.26 shows the comparison in scattering angle between simulation and data calculated using the track reconstruction software and the simulated Q^2 distribution at the scattering vertex. Using this method, the tree-level acceptance-averaged momentum transfer for Run II was determined to be[97]:

$$\langle Q^2 \rangle_{tree} = 0.02455 \pm 0.00031 \text{ (GeV/c)}^2. \tag{4.61}$$

The uncertainty is dominated by the 1.28% relative uncertainty arising from the comparison of simulations and data.

The average incident electron energy at the scattering vertex, E_{tree} was calculated through simulations that accounted for continuous energy loss in the target due to ionization [101]:

$$E_{tree} = \left\langle E_{beam} - \left(\frac{dE}{dz}\right) z \right\rangle = 1.153 \pm 0.003 \text{ GeV}, \tag{4.62}$$

where E_{beam} is the beam energy when entering the target, dE/dz is the energy loss in the target, and z is the distance traveled to the scattering vertex in the target.

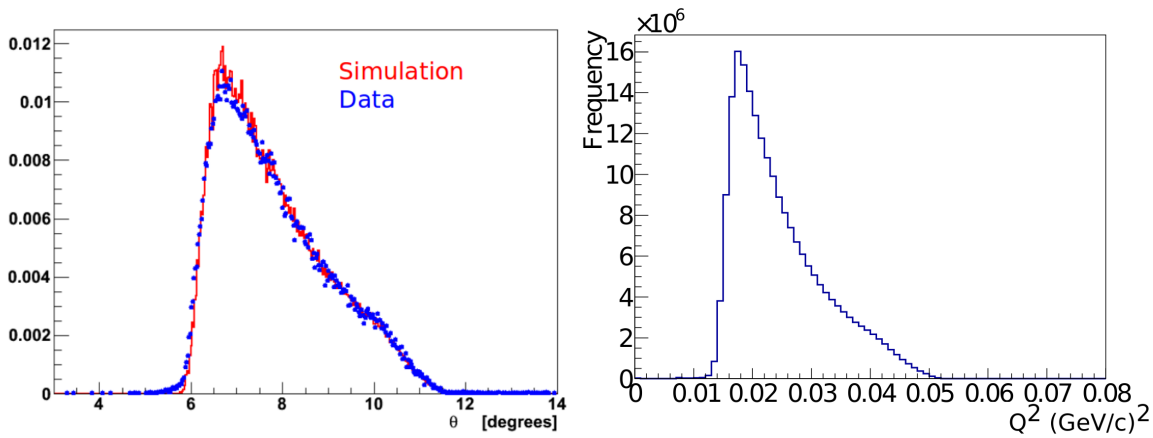

Figure 4.26: Left: The simulation's validity for determining kinematics is shown in this figure of the scattering angle determined by both GEANT4 and data [100]. Right: The distribution of momentum transfer squared Q^2 accepted by the main detectors. The curve comes from a GEANT4 simulation including only hydrogen events.

With these two quantities, the effective scattering angle was calculated according to the equation:

$$\cos\theta_{eff} = \frac{1 - \frac{\langle Q^2\rangle_{tree}}{2E_{tree}^2}\left(1 + \frac{E_{tree}}{m_p}\right)}{1 - \frac{\langle Q^2\rangle_{tree}}{2E_{tree}^2}\frac{E_{tree}}{m_p}} = 0.9906 \pm 0.0001. \tag{4.63}$$

This led to an effective scattering angle:

$$\theta_{eff} = 7.84^\circ \pm 0.05^\circ. \tag{4.64}$$

In the final publication, all of these variables will be calculated using measured values.

4.13 Parity-Violating Asymmetry Measurement

This section will synthesize all of the corrections discussed in this chapter, resulting in the measured parity-violating elastic *ep* scattering asymmetry. We will determine this value by solving eq. (4.1) for A_{ep} with the values shown in Table 4.13.

Beginning with the raw asymmetry - eq. (4.9) - the data were first corrected for systematic effects that varied over short time scales relative to the entire Run II data set. Helicity-correlated beam properties were regressed against at the runlet level - eq. (4.13) -

Name [units]	Value
A_{raw} [ppb]	-164.5 ± 7.4
A_{reg} [ppb]	$-163.9 \pm 7.3(\text{stat.}) \pm 0.8(\text{syst.})$
A_{reg+BB} [ppb]	$-166.4 \pm 7.3(\text{stat.}) \pm 1.0(\text{syst.})$
A_C [ppb]	$-187.7 \pm 8.3(\text{stat.}) \pm 1.7(\text{syst.})$
A_L [ppb]	0 ± 2.3
A_T [ppb]	0 ± 0.5
A_{PS} [ppb]	0 ± 10
P	0.889 ± 0.006
A_{msr} [ppb]	$-187.7 \pm 8.3(\text{stat.}) \pm 11.6(\text{syst.})$
R	0.9770 ± 0.0207
f_1	0.0285 ± 0.0008
A_1 [ppm]	1.506 ± 0.072
f_2	0.00193 ± 0.00064
f_3	0.0006 ± 0.0012
A_3 [ppm]	-0.39 ± 0.16
f_4	0.0002 ± 0.0002
A_4 [ppm]	-3.02 ± 0.97
A_{ep} [ppb]	$-232.2 \pm 8.3(\text{stat.}) \pm 12.9(\text{syst.})$

Table 4.13: Values used in calculating A_{ep}. Note that the blinding offset that affects A_{raw} could generate a substantial shift in the displayed values.

and then beamline background asymmetries were corrected for at the slug level - eq. (4.18). Correcting for polarization, which varied at roughly the slug level, yielded the corrected asymmetry of eq. (4.19):

$$\langle A_C \rangle = [-187.7 \pm 8.3(\text{stat.}) \pm 1.7(\text{syst.})] \text{ ppb.} \tag{4.65}$$

From this point on, we corrected for systematic effects that were consistent over the length of Run II, beginning with PMT non-linearity, transverse polarization leakage, and preradiator scattering. The resulting value was

$$\begin{aligned} A_{msr} &= \langle A_C \rangle - \frac{A_T + A_L + A_{PS}}{\langle P \rangle} \\ &= [-187.7 \pm 8.3(\text{stat.}) \pm 11.6(\text{syst.})] \text{ ppb.} \end{aligned} \tag{4.66}$$

Note that the effects of A_T, A_L and A_{PS} are only on the asymmetry of A_{msr}.

At this point we extract the physical asymmetry of interest, A_{ep}, by solving eq. (4.1)

Source	Contribution to $\delta A_{ep}/A_{ep}$ [%]
Statistics (A_C)	3.61
Regression, BB and P Systematics (A_C)	0.72
Detector Nonlinearity (A_L)	1.12
Transverse leakage (A_T)	0.24
Preradiator Scattering (A_{PS})	4.90
Experimental Bias (R)	2.12
Al Window Yield (f_1)	0.61
Al Window Asymmetry (A_1)	0.94
BB Yield (f_2)	0.07
QTCNB Yield (f_3)	0.08
QTCNB Asymmetry (A_3)	0.04
Inelastic Yield (f_4)	0.24
Inelastic Asymmetry (A_4)	0.08
Total Systematic Uncertainty (A_{ep})	5.63
Total Uncertainty (A_{ep})	6.69

Table 4.14: Size of contributions to the uncertainty of A_{ep} in Run II.

and inserting the intermediate value shown in eq. (4.66). This yields:

$$\begin{aligned} A_{ep} &= \frac{R}{1-\sum_{b=1}^{4} f_b}\left(A_{msr} - \sum_{b=1,3,4} f_b A_b\right) \\ &= \boxed{[-232.2 \pm 8.3(\text{stat.}) \pm 12.9(\text{syst.})]\ \text{ppb}}, \end{aligned} \tag{4.67}$$

Table 4.14 summarizes the individual systematic contributions to the uncertainty of this measurement. Figure 4.27 provides a visualization of the same information. It is clear from both the table and figure that the preradiator scattering systematic uncertainty dominates the measurement's uncertainty The implications of this blinded measurement as well as the plans for improvements are discussed in Chapter 6.

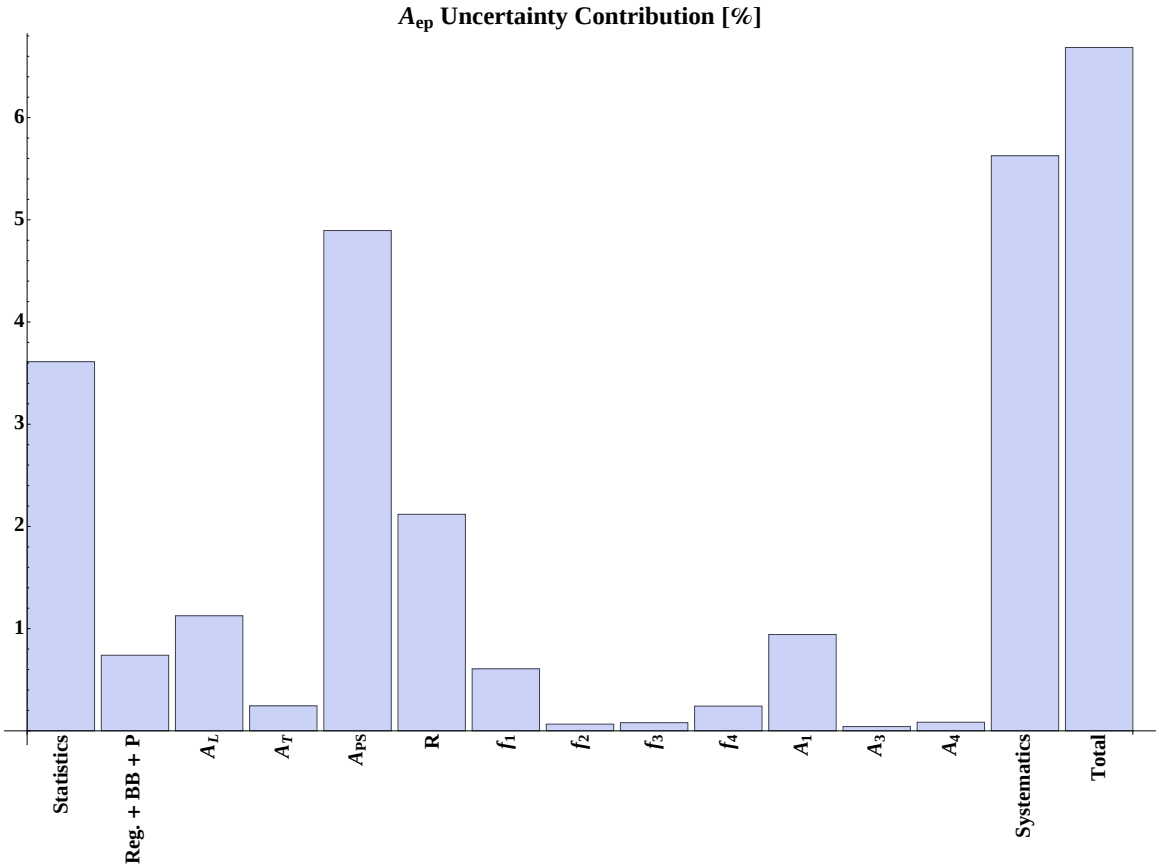

Figure 4.27: Size of contributions to the uncertainty of A_{ep} in Run II.

Chapter 5

Data Taking and Analysis of the Transverse Scattering Asymmetry From Carbon

This chapter begins by covering the conditions under which the transverse asymmetry was measured and the data that were acquired for this measurement. Then the chapter moves on to the raw asymmetry analysis of the carbon data set, followed by the various systematic corrections required for the measurement. The chapter concludes with the reported value of the transverse asymmetry from electrons on the ^{12}C nucleus. This asymmetry is an "effective" asymmetry, including scattering from both the ground state and excited states of the carbon nucleus. There currently exists no experimentally verified method of predicting the transverse asymmetry from these states. This chapter largely follows the structure of Chapter 4. It will focus more heavily on those pieces which differ between the two measurements reported in the dissertation. Note that the author was solely responsible for determining this asymmetry.

5.1 Transverse Data Set

The Q_{weak} transverse program consisted of data taken during two running periods, referred to as *Transverse Run I* (2011-02-08 through 2011-02-10) and *Transverse Run II* (2012-02-18 through 2012-02-20). These transverse data were taken with very similar conditions to the parity-violating (PV) measurements. The primary difference was that the CEBAF injector spin manipulators were used to alter the beam polarization from its usual longitudinal state to a transverse state. Transverse data were taken with the LH_2 target, an aluminum foil

Target	Integrated Beam Charge [Coulomb]	
	Transverse Run I	Transverse Run II
LH_2	8.4	18.9
DS 4% Al	0.5	3.3
DS 1.6% C	-	1.6

Table 5.1: The complete transverse polarization data set measured with the Q_{weak} apparatus. Within each of these data sets various parameters such as polarization orientation, beam current, and QTor magnet current were altered.

QTor Current [A]	Run #	Sign Correction
8900	16144	- 1
	16145	- 1
	16146	+1
	16147	+1
6700	16148	+1
	16149	+1
	16150	- 1
	16151	- 1

Table 5.2: The total transverse carbon run list. Each run lasted approximately 45-50 minutes. The sign corrections correspond to IN (-1) and OUT (+1) IHWP states.

target (DS 4% Al), and the downstream carbon target (DS 1.6% C). Table 5.1 lists all of the transverse measurements made on each target in terms of integrated beam charge. Only the carbon measurements are discussed in the following sections. For discussions of the LH_2 data, see references [37, 102]. The transverse aluminum data analysis is ongoing.

The transverse carbon data set consisted of eight runs, each approximately 45 minutes in length. The beam current was approximately 75 μA throughout. During the transverse carbon measurement, the spin was manipulated in the injector such that electrons that had a *positive* helicity state at the injector photo-cathode were polarized in the *positive* x direction (beam left, towards Octant 1) when the beam arrived at the target in Hall C.[1] Table 5.2 shows the data taken on the carbon target and includes the sign correction convention used to ensure consistency between the two IHWP states.

The data were taken at two QTor currents. These currents were selected based upon the spectrum of *ep* scattering. The higher current, 8900 A, ensured only a very small amount of

[1]While transversely polarized electrons all have zero physical helicity, it is a useful nomenclature. Throughout this chapter, positive helicity refers to those electrons where the spin at the target is oriented along the positive x axis. This definition is consistent with the helicity signal used to perform the asymmetry calculation for each quartet.

inelastic scattering and Møller electrons scattered into the acceptance. The lower current, 6700 A, focused the $\Delta(1232$ MeV) resonance onto the MD to allow asymmetry measurements of that process. This dissertation covers the result of the high-current "elastic" QTor setting measurement. Work on the low current "inelastic" QTor setting measurement is ongoing.

5.1.1 Transverse Carbon Kinematics

The QTor magnet was designed to ensure a clean signal during LH_2 running. The primary backgrounds that were removed using this magnet were $\Delta(1232)$ production from the proton and Møller scattering. Both of these processes resulted in significantly lower energy of the scattered electrons $E - E^{'} > 250MeV$,where $E(E^{'})$ is the incoming(outgoing) electron energy. The energy transfer, $\nu = E - E^{'}$, and angular acceptance functions of the experiment (according to simulation) are shown in Figure 5.1. These acceptance functions are the ratio of hits (events which produce a signal in the simulated PMT photocathode) versus events thrown in each bin of the sampled variable. The rise in $\epsilon(\theta)$ is due to the tapered shape of the defining collimator (see Figure 3.12). The shape of the azimuthal acceptance is dominated by the light collection efficiency (peaks close to either PMT at $\pm 11°$) and small amounts of signal coming through the shielding over the quartz light-guides (tails from $11° - 15°$). The energy transfer acceptance was broad, ≈ 150 MeV. The excited states of ^{12}C, which have energies from 4 to 25 MeV, were therefore accepted by the detectors. Scattering from these states produced a significant portion of the total MD signal, as will be shown below. Because there was no experimentally verified theory predicting the scattering asymmetry from these states at Q_{weak} kinematics, it was decided that the quoted asymmetry *will not* be corrected for scattering from these states. The measured "effective" transverse asymmetry is the weighted average of the contributions from *all* ^{12}C states up to 25 MeV. The states above this point were found to have no significant signal.

Simulation was used to determine the acceptance-averaged values of kinematic quantities of interest to this measurement. Figure 5.2 shows the yield-weighted square of the momentum transfer. In these simulations, events were thrown representing the elastic electron-carbon scattering process and scattering from the excited states of the carbon

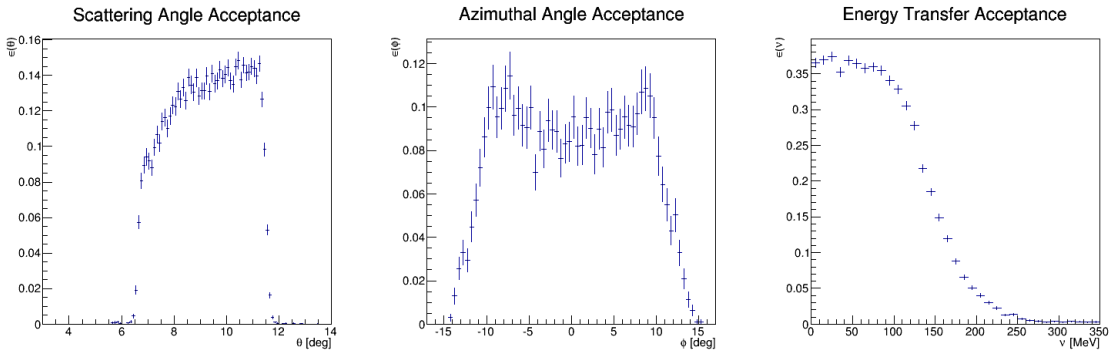

Figure 5.1: Simulated acceptance for events from the carbon target. Each histogram shows the ratio of good MD hits over all events thrown as a function of the indicated scattering parameter. The broad energy acceptance with respect to the ^{12}C excitation energies indicates that there was significant signal from these states.

nucleus. While the detector was unable to distinguish between these different processes during either current mode or event mode, it is worth noting the difference in the shapes and relative sizes of the two curves. At the higher momentum transfer, which corresponded to higher scattering angles, the inelastic portions grew to dominate. When coupled with the angular acceptance shown in Figure 5.1, this clearly demonstrates the large effect that nuclear excited states had on this measurement. The average momentum transfer and standard deviation of each histogram were extracted from the simulation:

$$Q^2(\text{elastic}) = 0.0257 \pm 0.0070 \ (\text{GeV/c})^2 \tag{5.1}$$

$$Q^2(\text{inelastic}) = 0.0300 \pm 0.0090 \ (\text{GeV/c})^2 \tag{5.2}$$

$$Q^2(\text{total}) = 0.0270 \pm 0.0079 \ (\text{GeV/c})^2. \tag{5.3}$$

This total value corresponded to

$$\sqrt{Q^2} = 0.164 \pm 0.024 \ (\text{GeV/c}), \tag{5.4}$$

which will be useful when comparing to theory, as in eq. (2.37). The average scattering angle was calculated in a similar manner to Chapter 4.12 and is found to be:

$$\theta(\text{total}) = 8.08^\circ \pm 1.14^\circ. \tag{5.5}$$

At this time, the tracking mode data on carbon have not been analyzed to extract the parameters of interest. However, the simulation has been shown to be in excellent agreement with data taken during dedicated tracking runs for data on both aluminum and LH_2 data[103].

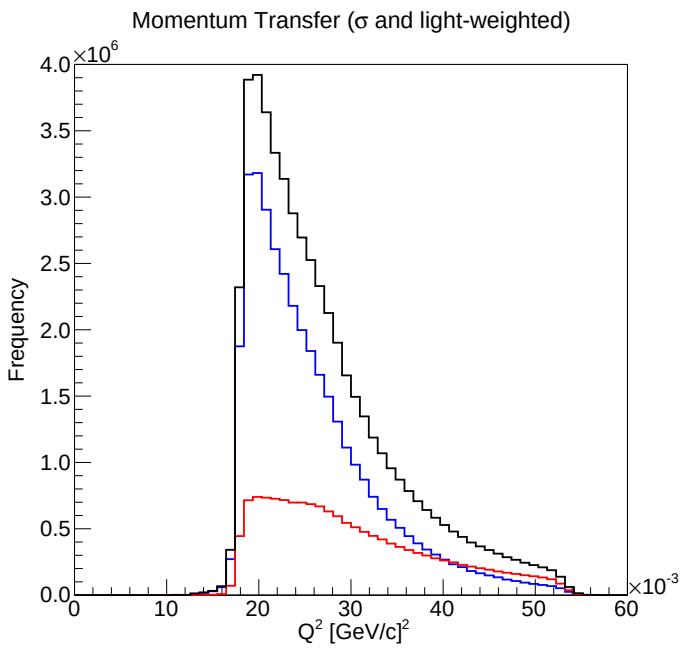

Figure 5.2: Simulated momentum-transfer squared for electrons scattering from carbon target into the detectors. The total signal (black) is the sum of the elastic (blue) and inelastic (red) events.

5.1.2 Polarization

As in the PV measurement, beam polarization needed to be measured precisely in order to effectively measure transverse asymmetries. Both Hall C polarimeters were designed to measure the longitudinal polarization of the electron beam and could not be used to directly measure the transverse polarization. Determination of the transverse polarization was based on several key points. First, the total polarization of the electron beam was constant at each beam spot on the photo-cathode for approximately two weeks [104], much longer than the 6 hour period spent on carbon. Secondly, effects on both polarization magnitude and orientation from passing through the accelerator were also known to a very precise degree [58]. Thus, by knowing the total beam polarization at one point in the beamline, such as the Hall-C Møller polarimeter, and then applying the associated changes

to its orientation, the polarization at the target would still be known to a high precision. The only additional source of error on a polarization measurement made in this manner was that the spin orientation changes performed by the injector spin manipulation system could only constrain the direction of the spin to within a cone of 3° about the desired direction [55]. This corresponded to a 0.07% relative error.

Hall C Møller polarimeter measurements were taken immediately before and after the polarization was rotated, and the measurements were consistent. Using this information, the polarization for a positive helicity state during transverse data taking on carbon was determined to be [85]

$$\mathbf{P} = [0.8852 \pm 0.0028(\text{stat.}) \pm 0.0064(\text{syst.})]\,\hat{\mathbf{i}} \tag{5.6}$$

where $\hat{\mathbf{i}}$ is the unit vector in the x direction and the systematic errors include all those discussed in Section 3.4 as well as the additional uncertainty discussed above.

5.2 Raw Transverse Asymmetry

The method used to measure a transverse asymmetry with the Q_{weak} apparatus differed from the PV measurement primarily in how the asymmetries from individual detectors were *combined*. Asymmetries for individual detectors were calculated on the quartet basis identically to the methods described in Section 4.1. Each main detector's asymmetry was then combined over the entire elastic transverse carbon data set (42 runlets in four runs) as in eq. 4.7. Explicitly,

$$\langle A^j \rangle = \frac{\sum_i s_i A_i^j / {\sigma_i^j}^2}{\sum_i 1/{\sigma_i^j}^2}, \tag{5.7}$$

where A_i^j is the asymmetry measured in detector j in runlet i, σ_i^j is the uncertainty in that measurement and s_i is the sign correction found in Table 5.2.

In the case of the PV measurements, the quantity of interest was the average of all 16 MD PMTs as in eq. (4.4). In the case of transverse measurements, we instead formed the average asymmetry of each bar and then plotted the asymmetry over the eight octants.

With horizontal polarization, the asymmetry varied sinusoidally over the octants as in eq. (**??**). The plotted asymmetries of the eight octants were then fit with a function of the azimuthal angle, ϕ (defined from beam left),

$$A(\phi) = B \sin(\phi - \phi_0) + C, \tag{5.8}$$

where the amplitude, B, phase shift, ϕ_0, and offset C were the fit parameters. The detector asymmetries and the resulting fit are shown in Figure 5.3.

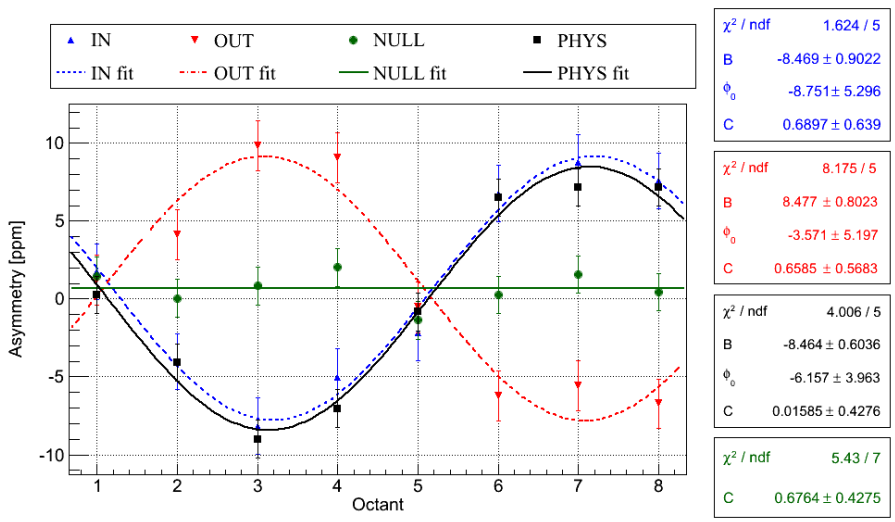

Figure 5.3: Raw MD asymmetries as a function of their surveyed central azimuthal angle for the elastic transverse carbon data set. The fit parameter B is the raw transverse asymmetry we are interested in. Comparison between the two IHWP settings show the appropriate behavior, i.e. equal and opposite asymmetries in each octant.

The amplitude of this fit is the (uncorrected) asymmetry we wish to measure:

$$B_{\text{raw}} = -8.464 \pm 0.604 \text{ ppm}. \tag{5.9}$$

Using this fitting method allowed data from all octants to constrain the fit, even those octants that did not measure any asymmetry. This raw asymmetry was the transverse version of eq. (4.1). It was related to the physics asymmetry of elastic scattering of electrons

from the carbon nucleus, B_n, by the formula

$$(1+\alpha_{\text{det}})\left(\frac{B_{\text{raw}}-B_{\text{beam}}}{\beta_{\text{acc}}}-B_{\text{PS}}\right)=P\left(\frac{1-\sum_i f_i}{R}B_n+\sum_i f_i B_i\right). \tag{5.10}$$

In the above equation, the raw asymmetry is corrected for such things as helicity-correlated beam properties (B_{beam}), false asymmetries from preradiator scattering (B_{PS}), corrections for the detector's azimuthal acceptance (β_{acc}) and non-linearity (α_{det}). The right-hand side contains the systematic corrections for the beam's polarization (P), radiative effects within the target and light-weighting corrections (R), and finally the corrections due to transverse asymmetries (B_i) of backgrounds that comprise some fraction (f_i) of the MD signal. The following sections will describe all of corrections included in the above formula with the ultimate goal of measuring the beam-normal single-spin scattering asymmetry (BNSSA) of electrons from carbon, B_n.

5.3 Linear Regression

In order to remove false asymmetries due to helicity correlated beam properties, linear regression was performed on the detector asymmetries using the method described in Section 4.2. When the regressed detector asymmetries were fit with eq. (5.8), there was a small change in the resulting value of the transverse asymmetry. This is shown in Figure 5.4. The difference between regressed and raw transverse asymmetry was found to be $B_{\text{beam}} = 76$ ppb.

Since the asymmetry measured in each detector was significantly different in a transverse measurement, the effects of regression on each detector were studied. Figure 5.5 shows the effect of regression on the asymmetry of each detector, as well as the effect on the uncertainty (width) of each measurement. The plot on the left indicates $\Delta A^i = A^i_{\text{raw}} - A^i_{\text{reg}}$ for each detector, i. The plot on the right shows the change in each asymmetry's statistical uncertainty, $\Delta\sigma^i = \sigma^i_{\text{raw}} - \sigma^i_{\text{reg}}$. While the the actual correction, ΔA, indicates that octant 7, which measured the full strength of the transverse asymmetry, had a significant shift, it is interesting to note that the width changed very little in both octants 3 and 7. All octants

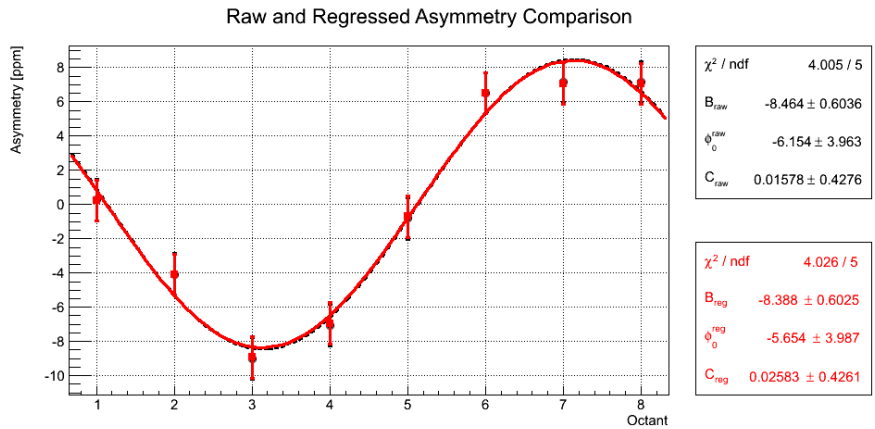

Figure 5.4: Raw (black) and regressed (red) MD asymmetries and accompanying fits.

had a smaller width after regression. This agreed with the expectations discussed in Section 4.2.

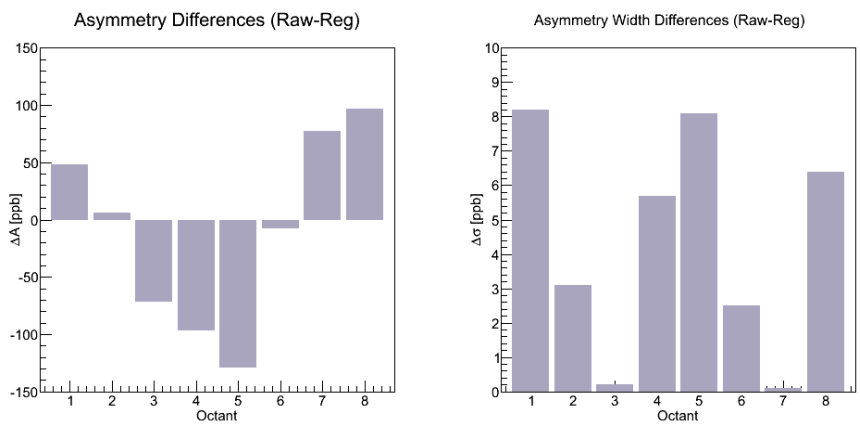

Figure 5.5: Differences between raw and regressed MD asymmetries (left) and widths (right). All asymmetry changes were $\lesssim 1\%$ relative. The widths changed the least in the detectors with the best signal-to-noise ratio (MD 3 and MD 7).

As in the previous chapter, the systematic error associated with regression was estimated by comparison of the results of the various regression schemes. The maximum point-to-point difference between regression schemes was only 2 ppb as is shown in Table 5.3. It was decided that this measurement would use the same regression scheme, `set10`, as the PVES measurement for consistency. This yielded a regressed transverse asymmetry of

$$B_{\text{reg}} = B_{\text{raw}} - B_{\text{beam}} = -8.388 \pm 0.602(\text{stat.}) \pm 0.002(\text{syst.}) \text{ ppm.} \tag{5.11}$$

Scheme	B_n [ppm]
`raw`	-8.464
`std`	-8.388
`5+1`	-8.389
`set3`	-8.389
`set4`	-8.388
`set7`	-8.387
`set8`	-8.388
`set9`	-8.388
`set10`	-8.388
`set11`	-8.388

Table 5.3: Raw and regressed asymmetries for the transverse carbon data set. All shifts due to regression are small compared to the ≈ 600 ppb statistical uncertainty of the measurement.

As observed in the PV case, the statistical uncertainty of the regressed asymmetry was smaller than the raw asymmetry. This was due to a reduction of non-statistical noise in the measurement.

5.4 Fitting Schemes

As shown in Figure 5.3, the transverse asymmetry was determined using a sinusoidal fit to the MD asymmetries. This could have potentially introduced a systematic error based upon the exact parameterization of the fit. In the results quoted above, a fit of the form shown in eq. (5.8) was used. In all appropriate cases, the phase offset parameter was constrained to be $\phi_0 \in [-10, 10]$. The other two parameters were allowed to vary freely.

It was also reasonable to use other fitting approaches for the examination of this data. In these alternative fits, the amplitude was allowed to vary while one or both of ϕ_0 and C were set to be identically zero. Table 5.4 shows a comparison of the results of these fits. All fitting was performed with the standard algorithms provided by CERN's `ROOT` analysis framework[79]. While typically one would choose the fit with the lowest χ^2/ndf, the approach used in this work is to use the three-parameter fit, which made it easier to view any potential systematic effects (visible as significantly large values of ϕ_0 or C). An additional systematic error associated with this fitting selection was included. The

Fit Function $A(\phi)$	B_{reg}	χ^2/ndf
$B\sin(\phi-\phi_0)+C$	-8.388	0.806
$B\sin(\phi-\phi_0)$	-8.389	0.672
$B\sin(\phi)+C$	-8.347	0.987
$B\sin(\phi)$	-8.348	0.847

Table 5.4: Regressed asymmetries determined using different fitting functions. The three-parameter fit (first entry) is the result quoted in this dissertation while the maximum point-to-point difference is quoted as a systematic uncertainty.

additional uncertainty, which was taken to be the largest point-to-point variation in B,

$$\delta B_{\text{fit}} = 0.042\text{ppm}, \tag{5.12}$$

is simply added in quadrature to the systematic error in eq. 5.11. The regressed asymmetry including this systematic error was still statistically dominated:

$$B_{\text{reg}} = -8.388 \pm 0.602(\text{stat.}) \pm 0.042(\text{syst.})\ \text{ppm}. \tag{5.13}$$

5.5 Detector Acceptance Correction

The Čerenkov detectors were designed to cover an azimuthal acceptance of 22° per octant. When an asymmetry has an azimuthal dependence, as in eq. (5.8), one would naturally measure a lower, "average" transverse asymmetry with such large-acceptance detectors. In an idealized scenario for polarization, $\mathbf{P} = \hat{\mathbf{i}}$, and physical analyzing power of B_n, each detector i would measure an average asymmetry

$$A_i = -B_n\langle\sin\phi\rangle, \tag{5.14}$$

where the average is computed over all events that entered the detector. Simulations were performed and the light-weighted value of $\langle\sin\phi\rangle_i$ was determined for each detector. This was compared to the theoretical value at the central angle $\sin\phi_i$ in order to construct the

MD	ϕ_i	$\sin\phi_i$	$\langle\sin\phi\rangle_i$	β_i
1	0	0	-0.0013	-
2	$\pi/4$	$\sqrt{2}/2$	0.6953	0.9833
3	$\pi/2$	1	0.9894	0.9894
4	$3\pi/4$	$\sqrt{2}/2$	0.6976	0.9866
5	π	0	0.0013	-
6	$5\pi/4$	$-\sqrt{2}/2$	-0.6964	0.9849
7	$3\pi/2$	-1	-0.9910	0.9910
8	$7\pi/4$	$-\sqrt{2}/2$	-0.6942	0.9817

Table 5.5: The average value of the azimuthal weighting of each MD from simulation compared to the idealized detectors. The correction β_i is calculated for all octants where it takes a defined value.

necessary acceptance correction

$$\beta_i = \frac{\langle\sin\phi\rangle_i}{\sin\phi_i}. \tag{5.15}$$

Table 5.5 shows the results of these simulations. The corrections were small ($\leq 2\%$) and consistent across the octants. This led to the adoption of a single correction for the entire data set, scaling the fit amplitude by the value:

$$\beta_{\text{acc}} = 0.9862 \pm 0.0036 \tag{5.16}$$

The value quoted above is the average of the values shown in the table and the error is the standard deviation.

5.6 Preradiator Scattering

In the case of longitudinally polarized primary scattering, secondary scattering in the lead MD preradiators caused an additional false asymmetry to be observed in each PMT. This created the PMT *double difference* (PMT-DD) discussed in Section 4.7. While the analyzing power of the lead remains the same, the transverse polarization orientation results in a significantly different set of detector responses and must be corrected in a different manner.

The difference in detector response is clearly illustrated in the case of transverse running on the LH_2 target. Figure 5.6 shows the PMT-DD, which is defined as in eq. (4.25) in each

octant. The PMT-DD for this data set *varied* sharply with octant, contrasting with its stability in the longitudinal data (shown in the lower plot of Figure 4.13). Additionally, the amplitude of the PMT-DD is *larger* in octants 1 and 5 than it is in the longitudinal dataset. There are two reasons that the PMT-DD displayed this behavior.

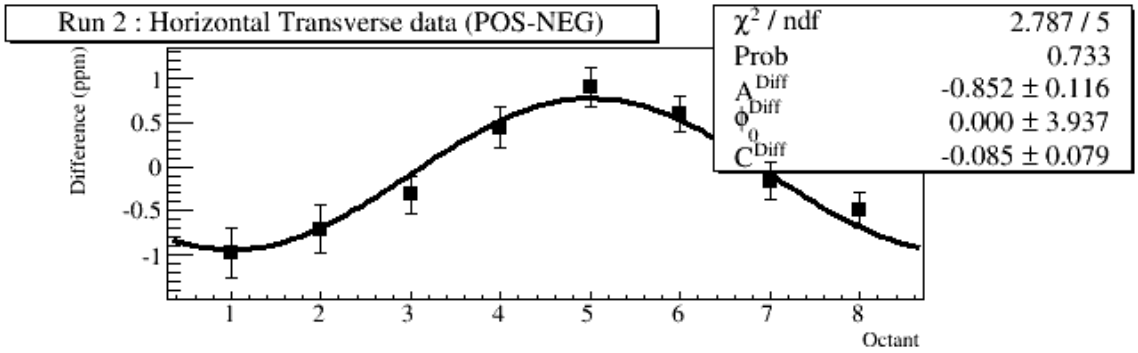

Figure 5.6: The PMT-DD for horizontally polarized electrons during LH_2 running. The double difference is perfectly out of phase when compared to the transverse asymmetry. It is approximately zero where the transverse asymmetry is maximized(octants 3 and 7). Reproduced from [105].

The PMT-DD variance with respect to azimuthal angle was the result of the transverse polarization across the bar (radially) varying in octant. In octants 1 and 5 (9 and 3 o'clock ,respectively), the electrons began with their polarization at fully horizontal and perpendicular to the length of the bar, and precessed through the QTor field, resulting in a slightly reduced transverse polarization when they scattered in the preradiator. Electrons that scattered to octants 3 and 7 (12 and 6 o'clock positions) had spins anti-aligned and aligned with the magnetic field, respectively, and thus did not precess in the field. These electrons arrived with polarization intact and oriented *along* the length of the bar. Thus, the lead's analyzing power did not produce a PMT-DD in these bars. Even-numbered octants accepted electrons with polarization orientations at the bar which were a linear combination of radial and azimuthal components. Thus a PMT-DD with strength between the two limiting cases was measured in these octants.

The reason that MD 1 and MD 5 measured a larger PMT-DD was twofold. First, the transverse asymmetry of the primary scattering (the physics asymmetry we wish to measure) led to a small PMT asymmetry in the bars on the horizontal axis. Second,

the secondary scattering also produced a slightly larger asymmetry due to an increased transverse polarization *at the preradiators* relative to the case where the beam is initially longitudinally polarized. In the case of the PV data, it was shown in eq.(4.27) that the transverse polarization at the preradiator was $P_\perp = 0.541 \pm 0.053$. In the case of the transverse data, the transverse polarization at the preradiator in octant 1 was $P_\perp^C = 0.704 \pm 0.040$.

The PMT-DD was shown in the last chapter to introduce a potential bias to the measurement on the order of 10 ppb. Since the measured PMT-DD was now 3 times larger in octants 1 and 5, this systematic uncertainty was increased by the same factor when applied to the transverse carbon measurement:

$$B_{\text{bias}} = 0 \pm 0.03 \text{ ppm}. \tag{5.17}$$

However, there was another mechanism by which the preradiators could produce a false asymmetry in the detectors. When the polarization was pointed *along* the bar as in octants 3 and 7, the lead's analyzing power produced a helicity-correlated position shift of the hit distribution on the face of the quartz bar. A schematic of such a shift is shown in Figure 5.7. The difference in these two yields over the sum of the two yields is the false asymmetry. Correcting for this systematic error requires two pieces of information: the size of the helicity0correlated position difference in the yield profiles, Δx, and the asymmetry's sensitivity to this helicity-correlated difference $dA/d\Delta x$.

The sensitivity of the MD to local x position shifts was determined by examining the yield profile at the edge of the bars. The simulated yield profile is shown in Figure 5.8. The yield changed for each helicity state due to events moving onto and falling off of the inner and outer edges of the bar. Since the negative x edge had more yield per unit length, this results in a small increase for positive x shifts. The strength of this sensitivity was the difference in the yield per unit length at either bar over the total yield of the bar. This was found to be

$$\frac{dA}{d\Delta x} = 2.3 \pm 0.3 \frac{\text{ppm}}{\mu\text{m}}. \tag{5.18}$$

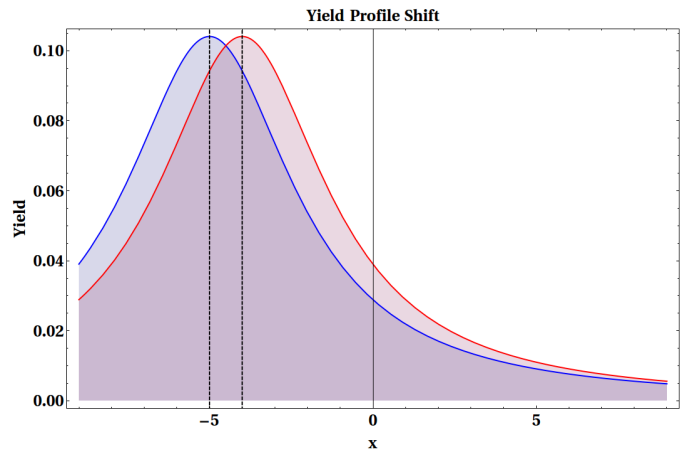

Figure 5.7: Idealized yield profile for positive (red) and negative (blue) helicity states in MD 3 as a function of the local radial coordinate, x. The helicity correlated position shift creates a false asymmetry of the same sign as the physics asymmetry. Interval between dotted black vertical lines indicates Δx. Not to scale.

Studies of the PMT-DD in longitudinal data have shown that the PMT sensitivity to helicity-correlated differences Δy along the bar due to light attenuation was:

$$\frac{dA_{\text{false}}}{d\Delta y} = [0.4 \pm 0.2]\ \frac{\text{ppm}}{\mu\text{m}}. \tag{5.19}$$

The false asymmetry in each PMT is equal and opposite, $A_{\text{false}} = (A_+ - A_-)/2 = 0.148 \pm 0.006$ ppm, as in eq. 4.25. Together these indicate a position shift in the longitudinal data of $\Delta y = 0.37 \pm 19\mu$m. In the case of transverse scattering in octant 3, however, the polarization was larger by a factor of 0.885/0.54 (the ratio of the transverse polarization in octant 3 along the bar versus the transverse polarization across the bar from precession in longitudinal data). Thus, one may calculate the helicity-correlated position difference indicated in Figure 5.7 to be

$$\Delta x = 0.61 \pm 32\mu\text{m}. \tag{5.20}$$

When combined with the calculated helicity-correlated position difference from eq.

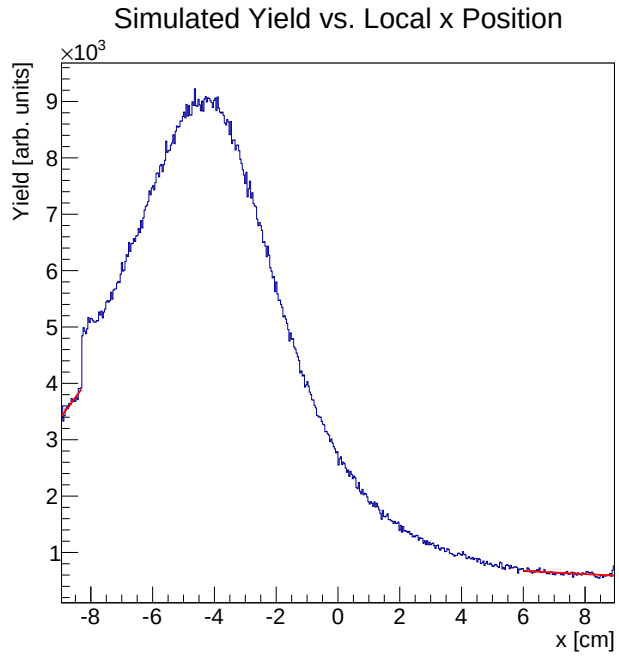

Figure 5.8: The simulated yield profile of MD hits as a function of position across the bar. The drop at ~ -8 cm marks the position of the photocathode edge at the end of the bar.

(5.20), the false asymmetry due to preradiator scattering in MD 3 is found to be

$$B^3_{\text{false}} = [1.40 \pm 0.74] \text{ ppm}. \tag{5.21}$$

This false asymmetry obeyed the same sinusoidal dependence as the physics asymmetry and therefore artificially increased the amplitude of the measured asymmetry, allowing the subtraction shown in (5.10). Including the B_{bias} correction from eq. (5.17), which was negligible, allowed one to write the complete correction for preradiator scattering false asymmetries in the transverse carbon measurement:

$$B_{\text{PS}} = [-1.40 \pm 0.74] \text{ ppm}. \tag{5.22}$$

This was a dominant systematic error in the transverse case as well as the longitudinal measurement. There is an ongoing effort to simulate the effects of scattering in the preradiator in a complete and systematic way. This effort is likely to produce a more accurate estimate of B_{PS}.

5.7 Detector Non-linearity

The final correction featured in the left-hand side of eq. (5.10) corrects for artificial inflation of the asymmetry due to non-linearity in detector response. The detectors were designed to minimize this characteristic and these design attempts were largely successful. The MD PMTs were shown to have a non-linearity of

$$\alpha_{\text{det}} = 0.14\ \% \pm 0.5\ \%. \tag{5.23}$$

when they were bench tested against fast and slowly varying LED signals of varying amplitudes meant to duplicate running at various currents and helicity reversal speeds [106].

5.8 Determining $\mathbf{B}_{\text{msr}}$

The corrections thus far in this chapter have dealt with false asymmetries as opposed to physics within the target. The intermediate variable, which is equal to the left-hand side of eq. (5.10),

$$B_{\text{msr}} = (1 + \alpha_{\text{det}}) \left(\frac{B_{\text{reg}}}{\beta_{\text{acc}}} - B_{PS} \right), \tag{5.24}$$

represents the asymmetry due solely to polarized scattering in the carbon target as measured by the Q_{weak} apparatus. The components of B_{msr} and the uncertainty associated with each piece are summarized in Table 5.6. When these values were entered into eq. (5.24), the result was

$$B_{\text{msr}} = [-7.115 \pm 0.611(\text{stat.}) \pm 0.744(\text{syst.})]\ \text{ppm} \tag{5.25}$$

The largest contribution to the systematic error is due to preradiator scattering, as can be seen in Figure 5.9. The remainder of this chapter will focus on separating the physics of interest in the target (scattering from carbon nuclear states) from backgrounds and

Name	Value	Uncertainty
B_{reg} [ppm]	-8.388	0.602
$\delta B_{\text{reg.}}$[ppm]	-	0.002
δB_{fit} [ppm]	-	0.042
β_{acc}	0.9862	0.0036
B_{PS} [ppm]	-1.40	0.74
α_{det} [%]	0.14	0.50

Table 5.6: Inputs for the calculation of B_{msr} in eq. (5.24). The error quoted for B_{reg} is purely statistical.

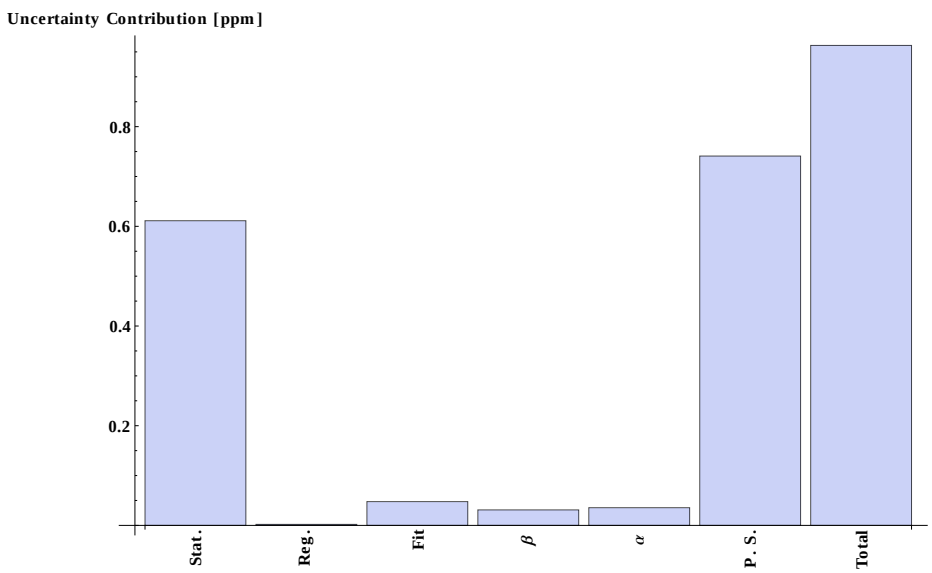

Figure 5.9: The error contributions due to statistics and systematic effects on B_{msr}.

correcting for biases due to radiative effects. In particular the focus will be on the equation

$$B_n = \frac{R}{1 - \sum_i f_i} \left(\frac{B_{\text{msr}}}{P} - \sum_i f_i B_i \right). \tag{5.26}$$

5.9 Radiative Corrections and Experimental Bias

Electromagnetic (EM) radiation within the target caused electrons to lose energy and become depolarized which leads to changes in the measured asymmetry. These effects have been thoroughly studied in the case of LH_2 and Al targets, but have not been examined closely for the case of the carbon target. However, due to the comparatively low precision of the measurement of BNSSA on carbon, one can use the analysis of the LH_2 and Al data

to make order-of-magnitude estimates for the size of these corrections in carbon. As will be demonstrated, this provided enough precision for the current analysis.

The most recent analysis for LH_2 data was shown in Section 4.11. The total experimental bias correction was found to be:

$$R = 0.9770 \pm 0.0207. \tag{5.27}$$

The most recently completed analysis for Al data [61] indicated that this correction was negligible in the case of aluminum. For the carbon measurement, we assign a central value of unity and propose conservative error bars which encompass the LH_2 data and its uncertainty

$$R^C = 1.000 \pm 0.050. \tag{5.28}$$

This error is already below the relative statistical precision, $\delta B_{\mathrm{msr}}/B_{\mathrm{msr}} = 8.6\%$, of the experiment.

5.10 Background Corrections

The most significant systematic corrections that needed to be made to the measurement of the transverse asymmetry from carbon were the physics backgrounds. Some backgrounds, such as the QTor transport channel neutral background, beamline background and the $\Delta(1232)$ resonance, are familiar from the PV LH_2 analysis. In the LH_2 data, the QTCNB and BB corrections were made by using the results of specialized data taking. These measurements were not repeated with the carbon target in place. As such, we made estimates based on the available data and simulations.

In addition to the backgrounds that were familiar from LH_2 case, the nuclear nature of the target (as opposed to a bare nucleon) introduced new effects. The most significant effect is that the scattering electron could excite the nucleus into a higher energy state. As mentioned previously, these excitations contributed a significant signal to the detectors that was impossible to separate from elastic scattering. A literature review revealed that there were no models or data for predicting the transverse scattering asymmetry of electrons

from nuclear excited states. These states are included in the result quoted at the end of this chapter. Their relative contribution is accounted for by empirically based `GEANT4` simulations.

The other significant process introduced by scattering from a nucleus is the contribution of *quasi-elastic* scattering, a process in which the electron scatters elastically from a single nucleon and that nucleon is ejected from the nucleus. In this case, there existed a reasonable method for calculating the asymmetry based on the Q_{weak} collaboration measurement of the transverse asymmetry from the proton. The correction for this background relied on `GEANT4` simulations.

5.10.1 GEANT4 Simulations of Electron Scattering from Carbon

`GEANT4` simulations of events in our apparatus formed a fundamental part of the analysis of the carbon transverse asymmetry. The simulation was used to generate detector rates: the number of events that hit our detectors per second under various conditions. These simulated rates were directly comparable to event-mode data taking. The simulation was also used to generate yields, as shown in eqs. (4.46 - 4.47). These quantities, which were discussed in the last chapter, represented the integrated detector response by simulating the light collection of the PMT photocathodes. The next step in the analysis the fractional yield associated with various processes. These processes include elastic scattering from ^{12}C, scattering from excited states of carbon, quasi-elastic scattering and inelastic $\Delta(1232)$ production.

We begin by discussing the most significant signal, elastic scattering. The differential cross section of electrons scattering elastically from carbon was implemented in the simulation using the formula

$$\left(\frac{d\sigma}{d\Omega}\right)_{\text{Elastic}} = (1+\delta)\left|F(q)\right|^2 \left(\frac{d\sigma}{d\Omega}\right)_{\text{Mott}} \tag{5.29}$$

where the Mott scattering cross-section,

$$\left(\frac{d\sigma}{d\Omega}\right)_{\text{Mott}} = \left(\frac{Z\alpha\hbar c}{2E}\right)^2 \frac{\cos^2(\theta/2)}{\sin^4(\theta/2)} \frac{1}{1+2(E/M)\sin^2(\theta/2)}, \tag{5.30}$$

is the result assuming scattering from a point nucleus with a Coulomb field. The form factor:

$$F(q) = \frac{4\pi^2 R^2 \sin(qR)}{Zeq} \sum_{\nu=1}^{16} a_\nu \frac{(-1)^{\nu+1}}{(\nu\pi)^2 - (qR)^2} \tag{5.31}$$

is an empirically based fit from reference [107]. And lastly, the Schwinger correction is implemented as prescribed in reference [8]:

$$\delta = \frac{-2\alpha}{\pi} \left[\left(\log \frac{E}{\Delta E} - \frac{13}{12} \right) \left(\log \frac{Q^2}{m_e^2} - 1 \right) + \frac{17}{36} + \frac{1}{2} f(\theta) \right] \tag{5.32}$$

with

$$f(\theta) = \log \sin^2(\theta/2) \log \cos^2(\theta/2) + \Phi(-\sin^2(\theta/2)). \tag{5.33}$$

where $\Phi(x)$ is Spence's function [108].

The formula for the elastic differential scattering cross section, eq. (5.29), was benchmarked against published data [109, 110, 111] over the range of Q_{weak}'s accepted momentum transfer. The published form factors agreed with the model within 5.6%. This value was taken as a model uncertainty and applied to all rates and yields calculated using these simulations.

5.10.2 Excited States

The single-particle excited states in the carbon nucleus were treated in an empirically based fashion. Published data form factors were found for all excited states up to 15 MeV and for the giant dipole resonance (GDR) [109, 110, 111, 112, 113, 114, 115, 116, 117, 118]. In the case of the single-particle excited states(where a single nucleon moves to a higher energy orbital within the nuclear potential), the published form factors were simply fit with a Gaussian over the range of momentum transfer, q, at which the data were taken. The results of these fits for the germane excited states are shown in Figure 5.10. The model error associated with these fits was taken to be the greatest relative discrepancy between

the fit and the data within the Q_{weak} acceptance,

$$\sigma_{model} = \left| \frac{|F(q)|^2_{data} - |F(q)|^2_{fit}}{|F(q)|^2_{fit}} \right| . \tag{5.34}$$

The model uncertainty for the excitations of interest for this measurement are shown in Table 5.7. Of those excited states examined only the three lowest lying states and the GDR produced a significant signal in our detectors. This was based on the fact that all other published form factors were a $\leq$1/100 the size of the elastic form factor.

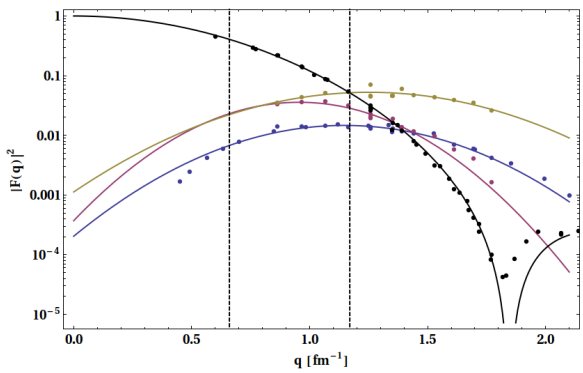

Figure 5.10: Form-factors for the ^{12}C nucleus over the Q_{weak} acceptance (vertical dashed lines). The states shown are: Ground (black), 4.44 MeV (blue), 7.65 MeV (purple) and 9.64 MeV (gold). The data come from references [109, 110, 111]. The black curve is the empirical fit provided in reference [107]. The curves for excited states are simply Gaussian fits to the data.

Excitation Energy [MeV]	Model Error (relative) [%]
4.44	4.4
7.65	18
9.64	8.9
24 (GDR)	17

Table 5.7: The relative uncertainty due to form-factor modeling for those excitations of the ^{12}C nucleus that produce a significant signal in the MDs.

Using the form-factor fits from above, the simulation calculated the cross section for scattering from state j to be:

$$\left(\frac{d\sigma}{d\Omega}\right)_{\mathrm{j}} = (1+\delta^{'})\,|F_j(q)|^2 \left(\frac{d\sigma}{d\Omega}\right)_{\mathrm{Mott}} . \tag{5.35}$$

The Schwinger-like correction for these states, $\delta^{'}$, is calculated as in reference [119]:

$$\delta^{'} = \frac{\alpha}{\pi}\left[\log\left(\frac{\Delta E}{E_i E_f}\right)\left[\log\left(\frac{Q^2}{m_e^2}\right)-1\right]-\frac{1}{2}\log^2\left(\frac{E_i}{E_f}\right)+\frac{13}{6}\log\left(\frac{Q^2}{m_e^2}\right)-\frac{28}{9}\right] \tag{5.36}$$

where $E_{i(f)}$ is the initial(outgoing) electron energy.

The giant dipole resonance was a significant excited state of carbon in which the proton and neutron wave functions oscillate against one another. This resonance was treated as prescribed by [120], scaling the elastic cross section as in:

$$\left(\frac{d\sigma}{d\Omega}\right)_{\mathrm{GD}} = \frac{\Delta_{\mathrm{GD}}}{2}\left(\frac{N}{A}\right)^2\left[\frac{Q^2}{m_C E_{\mathrm{GD}}}+\frac{E_{\mathrm{GD}}}{m_C}\frac{1+\sin^2(\theta/2)}{\cos^2(\theta/2)}\right]\left(\frac{d\sigma}{d\Omega}\right)_{\mathrm{Elastic}}. \tag{5.37}$$

The combined asymmetry from elastic scattering and these excited states is the asymmetry measured by the experiment and analyzed by the author in this work.

5.10.3 Quasi-elastic Scattering and Δ Production

Scattering from carbon with such a large energy acceptance meant that the MDs see significant yields due to *quasi-elastic scattering*. In this process, electrons scatter from *individual* nucleons (typically protons), giving them enough energy to escape the nucleus. The rates and yields for this process were calculated using a generator based on empirical fits by Bosted and Mamyan [121]. At Q_{weak} kinematics, however, the data could vary as much as 40% from the fit [122], which placed a significant model uncertainty upon these calculations. The yield fraction from this process was calculated in simulation to be:

$$f_{\mathrm{QE}} = 0.096 \pm 0.040 \tag{5.38}$$

The asymmetry of this process was taken to be the BNSSA of the proton [37] with additional uncertainties due to the presence of the nuclear medium:

$$B_{\mathrm{QE}} = -5.4 \pm 1.0 \text{ ppm}. \tag{5.39}$$

The simulation indicated that quasi-elastic scattering from neutrons did not form a significant background process, justifying the use of the proton's transverse asymmetry.

Inelastic scattering from individual nucleons, which took the form of $N \rightarrow \Delta$ (1232) production, was also a significant background to the transverse carbon measurement. This process was accounted for by utilizing the same empirically based fit to data which carried the same 40% model uncertainty. Using this fit as the basis of simulations, the yield fraction was found to be

$$f_{\Delta} = 0.045 \pm 0.019. \tag{5.40}$$

The transverse asymmetry of this process was determined from LH_2 data taken at the inelastic QTor setting [102],

$$B_{\Delta} = 43 \pm 16 \text{ ppm}. \tag{5.41}$$

Its uncertainty was already significantly large to account for any nuclear medium effects.

5.10.4 Beamline Background

Unlike the data taken with the LH_2 and Al target, there were no data taken on the carbon target with the tungsten shutters in place. This means that one cannot calculate the beamline background yield fraction in the same manner as was used for the LH_2 data. In light of this lack of data, it was decided to use a conservative estimate based on the downstream aluminum target's blocked octant data. According to a dedicated study [123], the beamline background fraction for the aluminum target during Run II was measured to be

$$f_{\mathrm{BB}}^{\mathrm{Al}} = 0.0069 \pm 0.0006. \tag{5.42}$$

Based upon this, a yield fraction of

$$f_{\mathrm{BB}}^{\mathrm{C}} = 0.01 \pm 0.01. \tag{5.43}$$

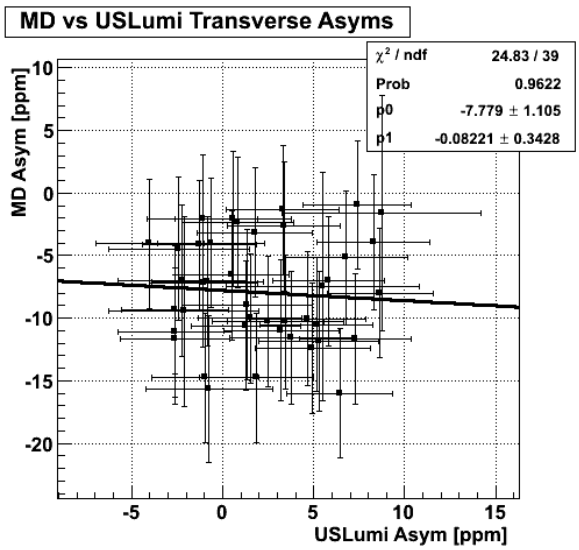

Figure 5.11: Regressed transverse asymmetries in the vertical octants of the MD versus the USLumi. The correlation coefficient of the data is $\rho = 0.022$. The fit slope is consistent with zero and the intercept is consistent with the measured MD transverse asymmetry.

was assigned to cover all reasonable possibilities. As will be shown later, this assumption produced an uncertainty well below statistics.

In the case of the LH_2 data, the asymmetry correction for BB was handled in a manner similar to regression. A correlation was formed between the MD and the USLumi asymmetries and this correlation was corrected. In the case of the transverse asymmetries, however, this is the wrong approach. The transverse asymmetries of the MD and USLumi were uncorrelated as is shown in Figure 5.11. This was consistent with the accepted model of the Q_{weak} beamline background's source: helicity-correlated beam "halo" asymmetries interacting in the tungsten plug and beamline elements downstream of the target. The key point was that these asymmetries did not depend upon the beam's *polarization* but rather on its spatial profile throughout the beamline.

In order to constrain the possibility of a beamline background transverse asymmetry in the carbon measurement, one could look at the dipole measured in the MDs for the LH_2 data. Figure 5.12 shows the average asymmetry for each MD bar over the entirety of Run II. It has been demonstrated that the observed dipole was consistent with residual vertical polarization in the beam [37]. We therefore know that the beamline background transverse asymmetry must be *strictly smaller than* the observed dipole. Moreover, since

the beamline background correction was not shown to vary with Wien filter settings [56], there was little reason to assume that there would be an appreciable dipole phase shift in any beamline background dipole due to the Wien settings required to provide transversely polarized electrons.

The data in Figure 5.12 were fit with a function

$$A(\phi) = B^H \sin\phi + B^V \cos\phi + C. \tag{5.44}$$

The coefficient $B^{H(V)}$ was the amplitude of the transverse asymmetry due to horizontal(vertical) residual polarizations. The constant, C, was consistent with the regressed PV asymmetry in eq. (4.13). We can now state the following:

$$f_{BB}^{\mathrm{LH_2}} B_{BB}^H \leq B^H \tag{5.45}$$

$$\therefore B_{BB}^H \leq \frac{B^H}{f_{BB}^{\mathrm{LH_2}}} \tag{5.46}$$

Taking the maximal allowed value of $B^H = 15$ ppb, and the known value of $f_{BB}^{\mathrm{LH_2}} = 0.00193 \pm 0.00064$, the maximum transverse asymmetry that the beamline background could produce was

$$B_{BB}^H \leq 8 \text{ ppm}. \tag{5.47}$$

Specifically then, $B_{BB} = 0 \pm 8$ ppm.

5.10.5 QTor Transport Channel Neutral Background

The method used to determine the appropriate correction for the QTor Transport Channel Neutral Background in the main LH_2 measurement required two pieces. The first piece was event-mode data taken using the main detector as the triggering detector. There are no such data on the carbon target. The second required piece was a simulation capable of predicting the transverse asymmetry from the target for each interaction possible. There exists no model for the transverse asymmetry from excited states of the nucleus. Thus we

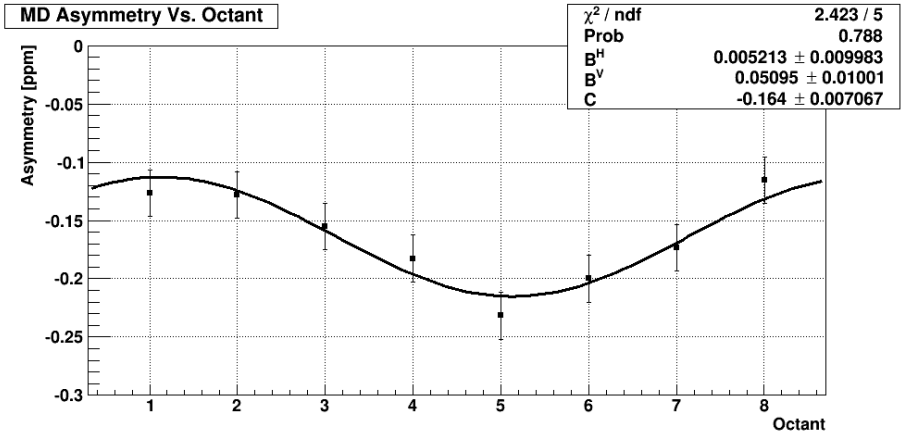

Figure 5.12: The MD asymmetry dipole measured during longitudinally polarized running on the LH_2 target. The fit indicates that it is consistent with residual transverse polarization in the vertical direction.

must find an alternative method.

We again rely on the extant results for LH_2 and Al targets. In the case of the aluminum target, a dedicated study [124] determined that the QTor transport channel neutral background yield fraction was

$$f_{\mathrm{QN}}^{\mathrm{Al}} = 0 \pm 0.004. \tag{5.48}$$

Based upon this, a yield fraction of

$$f_{\mathrm{QN}} = 0.01 \pm 0.01. \tag{5.49}$$

was applied in the case of the carbon target. Once again, the imprecise measurement of this background will be shown to have a small effect on the final transverse asymmetry measurement relative to statistics.

In order to determine an estimate for the QTCNB transverse asymmetry, we considered the cases of LH_2 and Al PV asymmetries. The asymmetry for the neutral signal from the LH_2 target was determined in eq. (4.51) to be

$$A_3 = [-0.39 \pm 0.16] \text{ ppm} \tag{5.50}$$

compared to the measured value of the PVES asymmetry of interest quoted in eq. (4.67)

$$A_{ep} = [-0.23 \pm 0.01] \text{ ppm (blinded)}. \tag{5.51}$$

Similarly, the neutral asymmetry from the DS 4% Al target was determined to be[124]

$$A_3^{\text{Al}} = [1.7 \pm 0.2] \text{ ppm} \tag{5.52}$$

whereas the PV asymmetry was measured to be [61]

$$A_{e\text{Al}} = [1.62 \pm 0.07] \text{ ppm}. \tag{5.53}$$

In both cases shown above, it is observed that the QTCNB asymmetry is consistent with or slightly larger than the physics asymmetry. Thus, a conservative estimate and errors are assigned for the QTCNB transverse asymmetry from the DS 1.6% C target:

$$B_{QN} = [-15 \pm 15]\text{ppm}. \tag{5.54}$$

5.11 Transverse Asymmetry from the Carbon Nucleus

At this point in the chapter, the information has been acquired to calculate the BNSSA of electrons from the carbon nucleus as measured by the Q_{weak} apparatus. We solve eq. (5.26) simply by inserting the values found in Table 5.8. The resulting value is:

$$\boxed{B_n = -11.088 \pm 0.823(\text{stat.}) \pm 1.905(\text{syst.}) \text{ ppm}}$$

This effective asymmetry from the groun- and excited-state scattering asymmetry is a systematically dominated measurement, as can be seen in Figure 5.13. The most significant systematic uncertainty is the due to the fractional signal and asymmetry from inelastic nucleon scattering, f_Δ and B_Δ. Corrections that were simple order-of magnitude estimates based on LH_2 and Al data are all shown to be below statistics.

Parameter	Value
B_{msr} [ppm]	-7.115 ± 0.611 ± 0.744
P	0.8852 ± 0.0067
R	1.000 ± 0.050
f_Q	0.096 ± 0.040
B_Q [ppm]	-5.42 ± 1.00
f_Δ	0.045 ± 0.019
B_Δ [ppm]	43 ± 16
f_{BB}	0.01 ± 0.01
B_{BB} [ppm]	0 ± 8
f_{QN}	0.01 ± 0.01
B_{QN} [ppm]	-15 ± 15

Table 5.8: The values and errors used in the final calculation, eq. (5.26), of the transverse asymmetry of electrons on carbon.

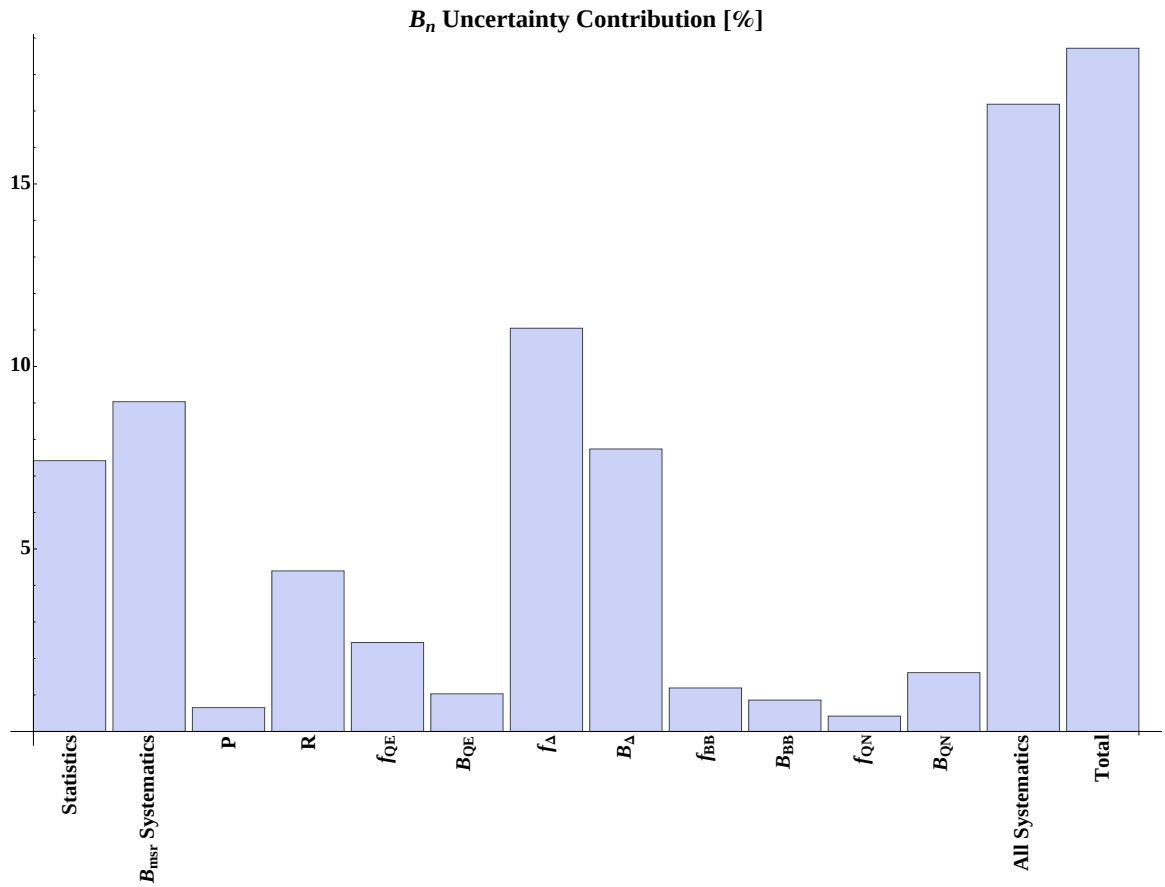

Figure 5.13: The error contributions due to statistics and systematic effects on B_{n}. The uncertainty of the result is systematically dominated by inelastic nucleon scattering.

Chapter 6

Results and Conclusions

In this chapter, we place the results of the previous two chapters in context and discuss their physical implications. We begin by covering the parity-violating asymmetry in elastic electron-proton scattering. This includes preliminary measurements of the proton's weak charge, Q^p_{W} , the quark coupling constants, and weak mixing angle, $\sin^2\theta_W$. The discussion then moves on to the transverse asymmetry measured in electron-carbon scattering. While this measurement is not directly comparable to theory, we indicate its degree of compatibility with published data and theory and how this constrains scattering from nuclear excited states.

6.1 The Weak Charge of the Proton

With the parity-violating electron-proton scattering asymmetry measured by the Q_{weak} experiment during Run II,

$$A_{ep} = [-232.2 \pm 8.3(\text{stat.}) \pm 12.9(\text{syst.})] \text{ ppb (blinded)}, \tag{6.1}$$

one may begin to extract the proton's weak charge. Prior to using the reduced asymmetry fitting method discussed in Section 2.2.1, one must first correct for the parity-violating asymmetry contribution of the two-boson exchange interaction ($\Box_{\gamma Z}$) shown in Figure 6.1. This interaction produces a PV asymmetry with a Q^2 and θ dependence described in references [125, 126] and must be applied to all data used in the fit. At Q_{weak} kinematics, this correction is a $A(\Box_{\gamma Z})$ = [-12.6 ± 0.6] ppb [74].

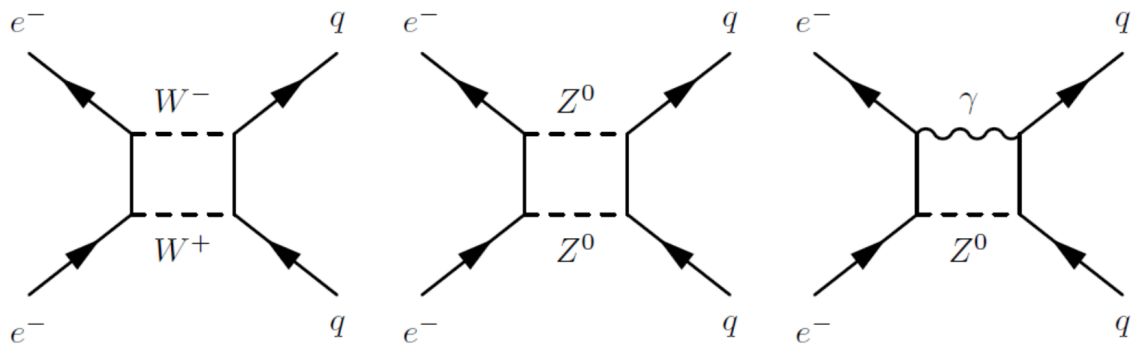

Figure 6.1: Weak and electroweak box diagrams relevant to PVES. The purely weak interactions have known, small contributions to Q_W^p [27] and are accounted for in eq. 6.9. The electroweak diagram has a larger but well calculated correction [125, 126]. Reproduced from [74]

After the correction above, a global fit to corrected PVES data using eq. (2.21),

$$\overline{A_{ep}} = \frac{A_{ep}}{A_0} = Q_W^p + Q^2 B(\theta, Q^2), \tag{6.2}$$

was performed using the method first demonstrated in reference [127]. This fit had five free parameters: the neutral weak quark coupling constants, C_{1u} and C_{1d}, the strange charge radius, ρ_s, and magnetic moment μ_s, and the isovector weak axial form factor $G_A^{Z(T=1)}$ [74]. Fitting using these five parameters was performed over both θ and Q^2 on PVES asymmetry measurements with $Q^2 \leq 1$ (GeV/c)^2 from the SAMPLE[17], PVA4[18], HAPPEX[19] and G0[20] experiments.

Figure 6.2 shows a visualization comparable to Figure 2.2 of the weak charge extraction using the blinded analysis of Run II data. In both of these figures, the plotted data are rotated to the forward angle limit, $\theta = 0$, using the formula [74]:

$$A_{ep}^{data}(\theta = 0, Q^2) = A_{ep}^{data}(\theta, Q^2) - \left[A^{fit}(\theta, Q^2) - A^{fit}(0, Q^2)\right]. \tag{6.3}$$

The data areS then plotted against the forward-angle fit, $A^{fit}(0, Q^2)$. The intercept of this fit is the measured weak charge of the proton:

$$Q_W^p(\text{PVES + Run II}) = 0.070 \pm 0.007 \text{ (blinded)}. \tag{6.4}$$

However with a blinding box of $\pm$ 60 ppb on the raw asymmetry the final Q_{weak} measurement for Run II could range anywhere over $Q_W^p \in [0.047, 0.093]$. Thus it cannot yet be compared to the SM value from eq. (2.23),

$$Q_W^p(\mathrm{SM}) = 0.0712 \pm 0.0009. \tag{6.5}$$

This potential variation in the determination of the proton's weak charge is visualized in Figure 6.3.

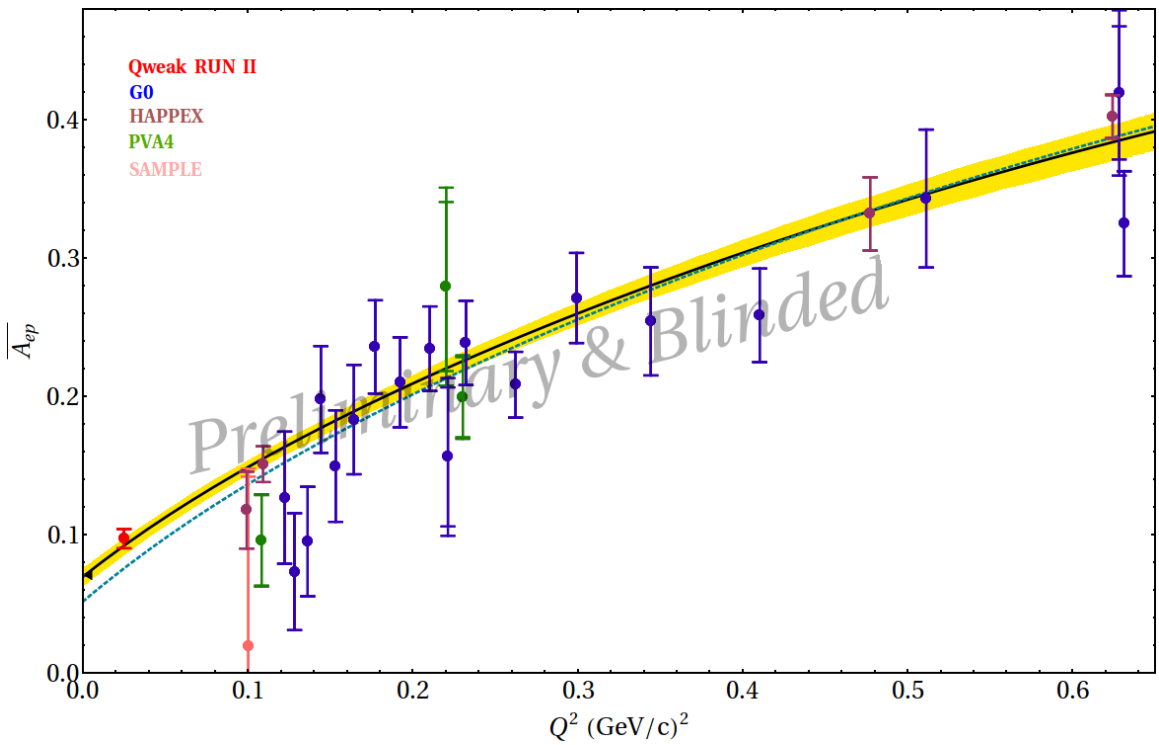

Figure 6.2: Updated version of Figure 2.2 where the Run 0 result has been replaced with the blinded Run II result. The blue dotted line is the fit result without the Q_{weak} data while the black curve and surrounding yellow band is the result with Run II included. While the blinding offset leaves the result uninterpretable, it is clear that the precision and low momentum transfer of the Q_{weak} measurement dominate the position of the intercept and thus the extracted value of Q_W^p.

The values of the neutral weak quark coupling constants returned by the fit are visible as the blue ellipse in Figure 6.4. Additional constraints on these couplings are obtained by combining the results of atomic parity-violation experiments (APV) with the PVES fit results. PVES and APV experiments provide nearly orthogonal constraints on the isovector

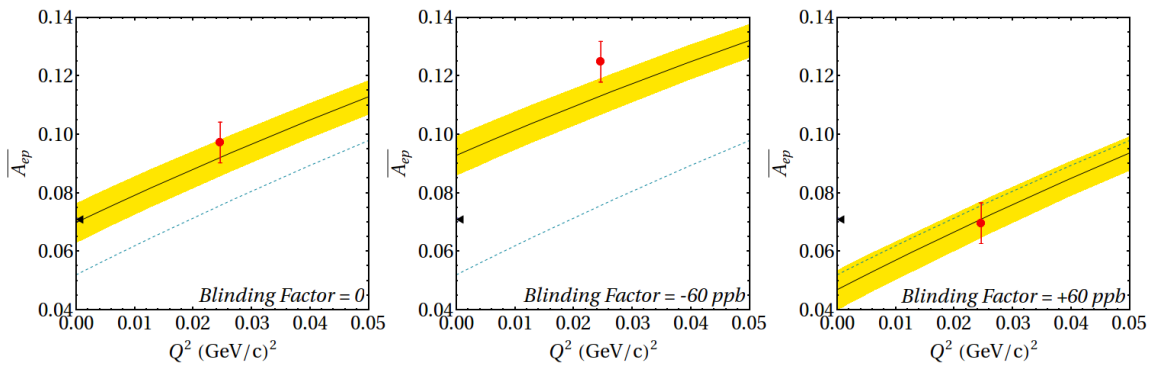

Figure 6.3: Detail of the intercept of the reduced asymmetry for the three cases where the blinding factor is 0, -60 ppb, or +60 ppb from left to right.

$(C_{1u} - C_{1d})$ and isoscalar $(C_{1u} + C_{1d})$ combinations of these couplings, as shown in Figure 2.3. The newest analysis of the ^{133}Cs APV experiment [128], combined with the PVES result above, yields neutral weak vector couplings of

$$C_{1u}(\text{APV + PVES + Run II}) = -0.1864 \pm 0.0032 \text{ (blinded)} \tag{6.6}$$

$$C_{1d}(\text{APV + PVES + Run II}) = 0.3380 \pm 0.0033 \text{ (blinded)} \tag{6.7}$$

and is shown in Figure 6.4 as the red ellipse. Additionally, the neutron's weak charge can be calculated using these experimental values for the quark couplings according to the formula

$$Q_W^n(\text{APV + PVES + Run II}) = -2\,(C_{1u} + 2C_{1d}) = -0.979 \pm 0.007 \text{ (blinded)}. \tag{6.8}$$

In the case of all of these results, the blinding offset means they are not directly comparable to SM predictions despite their apparent agreement.

6.1.1 The Weak Mixing Angle

The SM prediction for the protons weak charge, including all relevant corrections at next-to leading, order can be written as [27]:

$$Q_W^p(\text{SM}) = (\rho_{\text{NC}} + \Delta_e)\left[1 - 4\sin^2\hat{\theta}_W + \Delta_e^{'}\right] + \Box_{WW} + \Box_{ZZ} + \Box_{\gamma Z} \tag{6.9}$$

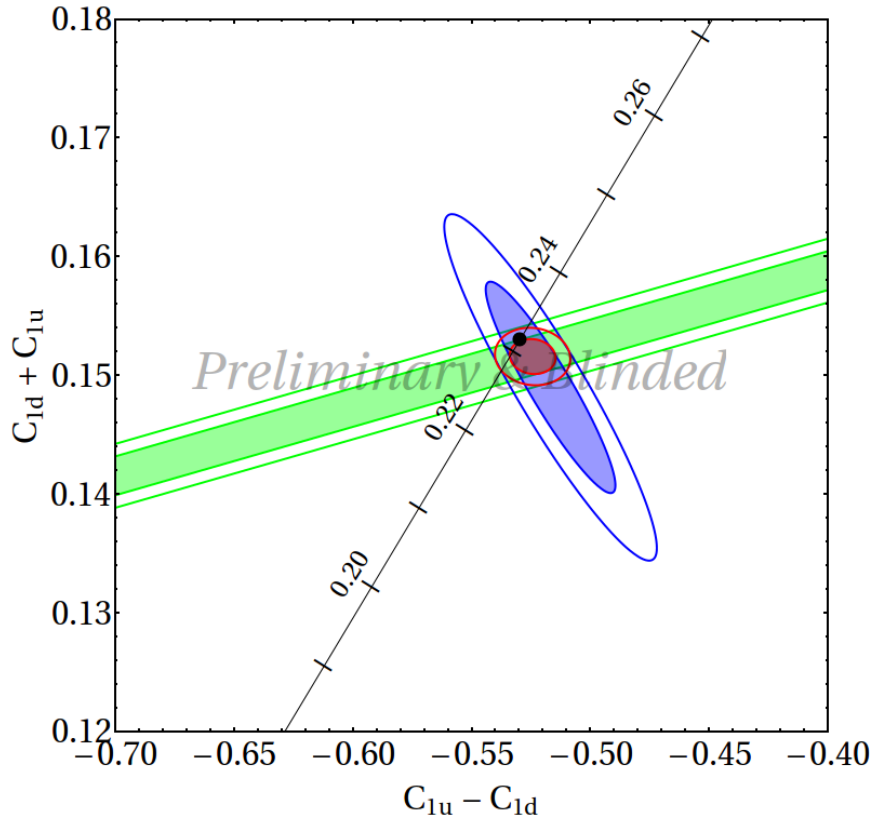

Figure 6.4: Updated version of Figure 2.3 using blinded Run II data. As in the previous figure, the green band indicates results from APV data, the blue ellipse is the result of the global PVES scattering fit, and the red ellipse is the intersection of the two. The inner, shaded area represents the 95% confidence level while the outer border represents the 68% confidence level.

where $\rho_{\rm NC}$ is the renormalization factor between the ratios of charged and neutral current interactions at low energy, Δ_e and $\Delta_e^{'}$ are corrections to the Zee and γee vertex respectively. and the $\Box_{XX}$ terms represent the indicated two-boson exchange contributions. These corrections are summarized in Table 6.1. However, the reported value of the proton's weak charge in eq. (6.4) is already corrected for the $\Box_{\gamma Z}$ diagram. The experimental determination of the weak mixing angle is then calculated to be:

$$\sin^2\theta_W(\text{Run II}) = \frac{1}{4}\left[1 + \Delta_e^{'} + \frac{-Q_W^p(\text{Run II}) + \Box_{WW} + \Box_{ZZ}}{\rho_{\rm NC} + \Delta_e}\right] = 0.238 \pm 0.002 \text{ (blinded)}. \tag{6.10}$$

This result is shown in Figure 6.5 plotted with other measurements of the weak mixing angle over a range of momentum-transfer. Though blinded, the errors indicate that this result

Correction	Value
ρ_{NC}	1.00833
Δ_e	0.00116
$\Delta_e^{'}$	0.00142
$\Box_{WW}$	0.018317
$\Box_{ZZ}$	0.001926
$\Box_{\gamma Z}$	0.0054

Table 6.1: The SM electroweak corrections to the proton's weak charge as defined in the modified minimal subtraction renormalization scheme. All values are taken from reference [27] except for $\Box_{\gamma Z}$, which is taken from reference [126]. The errors are negligible compared to the Q_{weak} experimental errors.

consisting of roughly 2/3 of the Q_{weak} data is the most precise measurement of $\sin^2\theta_W$ at low Q^2 to date.

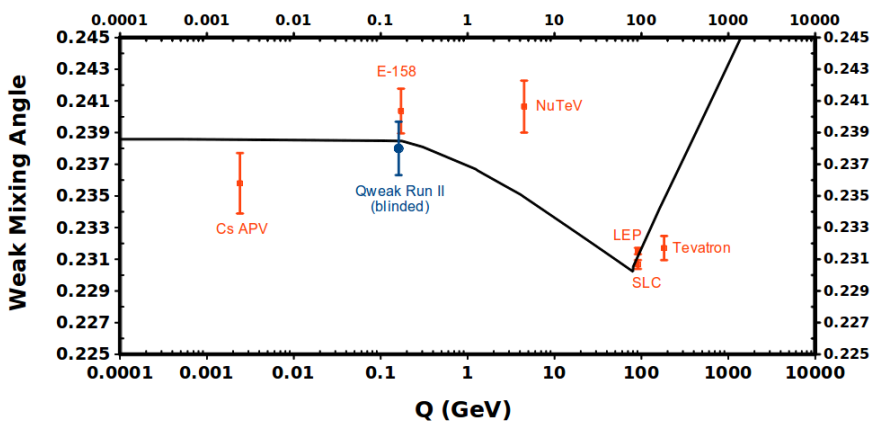

Figure 6.5: Weak mixing angle ($\sin^2\theta_W$) measurements (red) compared to SM prediction[27] (black). The blinded result of Q_{weak} Run II as discussed in this dissertation is shown in blue and is in good agreement with theory.

6.1.2 Q_{weak} Summary

The final result of the Q_{weak} experiment promises to be very interesting. The remaining work is focused on controlling the systematic errors from secondary scattering in the preradiator, utilizing the beam modulation system to determine the appropriate beam correction slopes, and finalizing the background contributions. This work will likely result in a final asymmetry measurement that is statistically dominated. The combined result of all Q_{weak} PVES data will also provide an improved statistical uncertainty. The work on the

Q_{weak} experiment is expected to culminate with the unblinding of Run I and Run II in early Spring of 2017.

6.2 The Transverse Asymmetry of Electron-Carbon Scattering

Because the Q_{weak} experimental apparatus was optimized for scattering from the nucleon, the transverse scattering asymmetry from carbon is not a cleanly interpretable result. The primary difficulty is that a significant, ineluctable background consisting of scattering from excited nuclear states exists in the measured asymmetry. As such, one may only present the results in hand for what they are, the weighted average of asymmetries from elastic and excited-state scattering from ^{12}C:

$$B_n = [-11.1 \pm 2.1] \text{ ppm} = \sum_{i=0}^{N} w_i B_i \tag{6.11}$$

where B_i is the scattering asymmetry from state i and w_i is the fraction of the corrected signal from state i with $i = 0$ being the ground state $i = 1$ being the first excited state and so on. Figure 6.6 shows how this composite result compares to the existing measurements of purely elastic electron-nucleus and electron-proton scattering asymmetries.

The fractional yields, w_i, were determined using the results of `GEANT4` simulations and are shown in Table 6.2. As was mentioned in the previous chapter, only the three lowest excited states and the giant dipole resonance have any significant signal, with the remaining states examined having a combined contribution of $< 1\%$. While there exist no data nor theory to shed light on the inelastic scattering components in Table 6.2, both exist for scattering from the ground state. Using the transverse asymmetry from carbon measured by the PRex experiment [47] (taken at a slightly lower beam energy) and the scaling method denoted in eq. (2.37), one obtains a prediction for the transverse scattering asymmetry from the ground state of carbon at the Q_{weak} kinematics of

$$B_n(\text{predicted}) = [-10.8 \pm 0.3] \text{ ppm}. \tag{6.12}$$

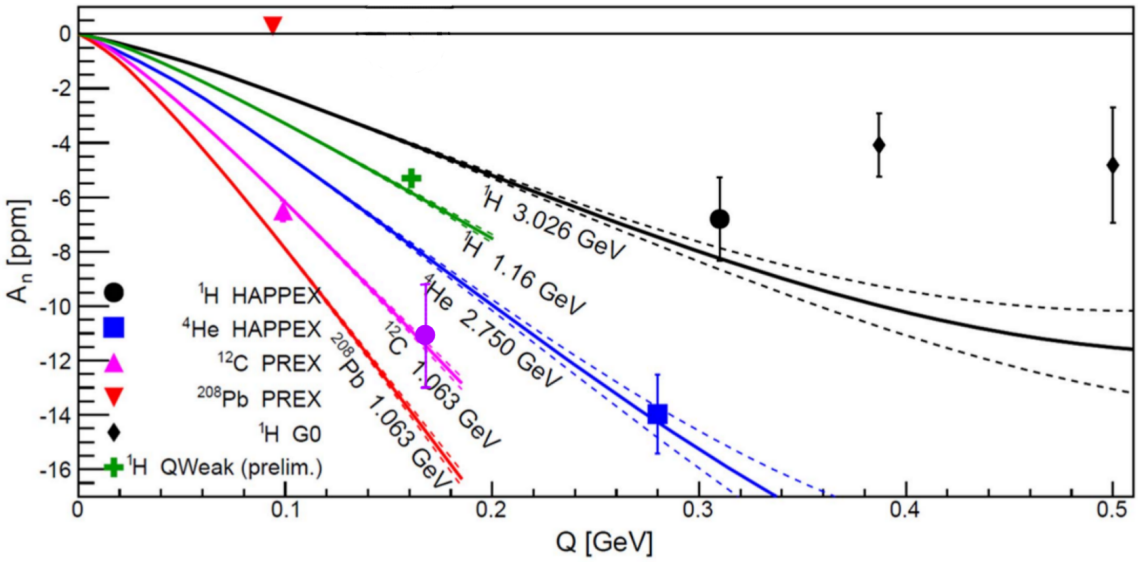

Figure 6.6: Measurements of BNSSA in various nuclei [47, 48, 37] compared to the predictions from [41]. The purple data point is the transverse asymmetry measured on carbon by the Q_{weak} apparatus. Note that this was not taken at the same energy as the line shown for carbon nor was this data point a measurement of a purely elastic signal.

i	E [MeV]	J^P	w_i [%]
0	0 (Ground)	0^+	71.6 ± 7.9
1	4.44	2^+	3.5 ± 0.3
2	7.65	0^+	10.3 ± 2.1
3	9.64	3^-	11.6 ± 1.4
GDR	(24)	(0^+)	$1.9 \pm 0,4$
All others	various	various	≤ 1

Table 6.2: Fractional contributions to the transverse asymmetry from low lying ^{12}C states as determined by `GEANT4` simulations.

It is worth noting that this estimate is indeed commensurate with the experimental value reported in eq. (6.11). This may indicate that the excited states carry roughly the same asymmetry as the elastic case although it is far from conclusive.

6.2.1 Transverse Asymmetry Summary

The measurement of the transverse asymmetry on carbon is nearly mature. The ongoing work on preradiator scattering and the transverse asymmetry measurement from $n \to \Delta(1232 \text{ MeV})$ will serve to improve the precision of the final result. However, this result will only be useful with further experimental and theoretical effort towards under-

standing transverse asymmetries in inelastic scattering. The A1 collaboration has recently used the Mainz Microtron to measure transverse asymmetries from carbon over the same range of momentum transfer as Q_{weak} but has the added benefit of spectrometer detectors that can clearly discern elastic and inelastic events [129].

In general, the study of two-photon interactions through transverse asymmetries is in its infancy. The existing theory is extremely limited and breaks down for large nuclei, momentum transfer and higher angles. There is a paucity of data at energies above traditional Mott scattering (< 10 MeV) and at varying angles and momentum transfer. Yet, the two-photon exchange correction is necessary for many current and future precision scattering experiments. It is my hope that more work is put into this area of research in the future.

Bibliography

[1] Tatsumi Aoyama, Masashi Hayakawa, Toichiro Kinoshita, and Makiko Nio. Tenth-order qed contribution to the electron $g-2$ and an improved value of the fine structure constant. *Phys. Rev. Lett.*, 109:111807, Sep 2012.

[2] S. Chatrchyan, V. Khachatryan, A.M. Sirunyan, et al. Observation of a new boson at a mass of 125 gev with the {CMS} experiment at the {LHC}. *Physics Letters B*, 716(1):30 – 61, 2012.

[3] G. Aad, B. Abbott, J. Abdallah, et al. Combined measurement of the higgs boson mass in pp collisions at $\sqrt{s} = 7$ and 8 tev with the atlas and cms experiments. *Phys. Rev. Lett.*, 114:191803, May 2015.

[4] Y. Fukuda, T. Hayakawa, E. Ichihara, et al. Evidence for oscillation of atmospheric neutrinos. *Phys. Rev. Lett.*, 81:1562–1567, Aug 1998.

[5] K. A. Olive et al. Review of Particle Physics. *Chin. Phys.*, C38:090001, 2014.

[6] Standard model. `https://en.wikipedia.org/wiki/Standard_Model`. Accessed: 2016-07-17.

[7] Steven Weinberg. A model of leptons. *Phys. Rev. Lett.*, 19:1264–1266, Nov 1967.

[8] L. W. Mo and Y. S. Tsai. Radiative corrections to elastic and inelastic ep and up scattering. *Rev. Mod. Phys.*, 41:205–235, Jan 1969.

[9] M. K. Jones, K. A. Aniol, F. T. Baker, et al. G_{E_p}/G_{M_p} ratio by polarization transfer in $\vec{e}p \to e\vec{p}$. *Phys. Rev. Lett.*, 84:1398–1402, Feb 2000.

[10] O. Gayou, K. A. Aniol, T. Averett, et al. Measurement of G_{E_p}/G_{M_p} in $\vec{e}p \rightarrow e\vec{p}$ to $q^2 = 5.6$ gev^2. *Phys. Rev. Lett.*, 88:092301, Feb 2002.

[11] L. Andivahis, P. E. Bosted, A. Lung, et al. Measurements of the electric and magnetic form factors of the proton from q^2=1.75 to 8.83 (gev/ c)^2. *Phys. Rev. D*, 50:5491–5517, Nov 1994.

[12] P. A. M. Guichon and M. Vanderhaeghen. How to reconcile the rosenbluth and the polarization transfer methods in the measurement of the proton form factors. *Phys. Rev. Lett.*, 91:142303, Oct 2003.

[13] J. Arrington, W. Melnitchouk, and J. A. Tjon. Global analysis of proton elastic form factor data with two-photon exchange corrections. *Phys. Rev. C*, 76:035205, Sep 2007.

[14] S. Agostinelli, J. Allison, K. Amako, et al. Geant4 a simulation toolkit. *Nuclear Instruments and Methods in Physics Research Section A: Accelerators, Spectrometers, Detectors and Associated Equipment*, 506(3):250 – 303, 2003.

[15] M.J. Musolf, T.W. Donnelly, J. Dubach, et al. Intermediate-energy semileptonic probes of the hadronic neutral current. *Physics Reports*, 239(1):1 – 178, 1994.

[16] F. J. Ernst, R. G. Sachs, and K. C. Wali. Electromagnetic form factors of the nucleon. *Phys. Rev.*, 119:1105–1114, Aug 1960.

[17] E.J. Beise, M.L. Pitt, and D.T. Spayde. The sample experiment and weak nucleon structure. *Progress in Particle and Nuclear Physics*, 54(1):289 – 350, 2005.

[18] F. E. Maas, P. Achenbach, K. Aulenbacher, et al. Measurement of strange-quark contributions to the nucleon's form factors at $Q^2 = 0.230$ (GeV/c)^2. *Phys. Rev. Lett.*, 93:022002, Jul 2004.

[19] K. A. Aniol, D. S. Armstrong, T. Averett, et al. Parity-violating electroweak asymmetry in $\vec{e}p$ scattering. *Phys. Rev. C*, 69:065501, Jun 2004.

[20] D. Androić, D. S. Armstrong, J. Arvieux, et al. Strange quark contributions to parity-violating asymmetries in the backward angle g0 electron scattering experiment. *Phys. Rev. Lett.*, 104:012001, Jan 2010.

[21] D. Androic, D. S. Armstrong, A. Asaturyan, et al. First determination of the weak charge of the proton. *Phys. Rev. Lett.*, 111:141803, Oct 2013.

[22] S. C. Bennett and C. E. Wieman. Measurement of the $6S \rightarrow 7S$ transition polarizability in atomic cesium and an improved test of the standard model. *Phys. Rev. Lett.*, 82:2484–2487, Mar 1999.

[23] P. Achard, O. Adriani, M. Aguilar-Benitez, et al. Measurement of the running of the electromagnetic coupling at large momentum-transfer at {LEP}. *Physics Letters B*, 623(12):26 – 36, 2005.

[24] G. P. Zeller, K. S. McFarland, T. Adams, et al. Precise determination of electroweak parameters in neutrino-nucleon scattering. *Phys. Rev. Lett.*, 88:091802, Feb 2002.

[25] A. Aktas et al. A Determination of electroweak parameters at HERA. *Phys. Lett.*, B632:35–42, 2006.

[26] P. L. Anthony, R. G. Arnold, C. Arroyo, et al. Precision measurement of the weak mixing angle in møller scattering. *Phys. Rev. Lett.*, 95:081601, Aug 2005.

[27] Jens Erler, Andriy Kurylov, and Michael J. Ramsey-Musolf. Weak charge of the proton and new physics. *Phys. Rev. D*, 68:016006, Jul 2003.

[28] John C. Collins. *Renormalization: An Introduction to Renormalization, the Renormalization Group and the Operator-Product Expansion.* Cambridge University Press, Cambridge, 11 1984.

[29] S. Schael et al. Precision electroweak measurements on the Z resonance. *Phys. Rept.*, 427:257–454, 2006.

[30] Niklaus Berger et al. Measuring the weak mixing angle with the P2 experiment at MESA. In *10th International Workshop on e+e- collisions from Phi to Psi (PHIPSI15) Hefei, Anhui, China, September 23-26, 2015*, 2015.

[31] J. Benesch et al. The MOLLER Experiment: An Ultra-Precise Measurement of the Weak Mixing Angle Using Møller Scattering. 2014.

[32] J. P. Chen, H. Gao, T. K. Hemmick, Z. E. Meziani, and P. A. Souder. A White Paper on SoLID (Solenoidal Large Intensity Device). 2014.

[33] Estia J. Eichten, Kenneth D. Lane, and Michael E. Peskin. New tests for quark and lepton substructure. *Phys. Rev. Lett.*, 50:811–814, Mar 1983.

[34] Jens Erler, Charles J. Horowitz, Sonny Mantry, and Paul A. Souder. Weak polarized electron scattering. *Annual Review of Nuclear and Particle Science*, 64(1):269–298, 2014.

[35] Rakitha S. Beminiwattha. *A Measurement of the Weak Charge of the Proton through Parity Violating Electron Scattering using the Qweak Apparatus: A 21 Percent Result.* PhD thesis, Ohio University, 2013.

[36] Andrei V. Afanasev, Stanley J. Brodsky, Carl E. Carlson, Yu-Chun Chen, and Marc Vanderhaeghen. The Two-photon exchange contribution to elastic electron-nucleon scattering at large momentum transfer. *Phys. Rev.*, D72:013008, 2005.

[37] D. Buddhini P. Waidyawansa. *A 3 Forward Angle Elastic Electron-Proton Scattering Using the Qweak Setup.* PhD thesis, Ohio University, August 2013.

[38] N. F. Mott and H.S.W Massey. *The Theory of Atomic Collisions.* Oxford University Press, 3 edition, 1965.

[39] Noah Sherman and Donald F. Nelson. Determination of electron polarization by means of mott scattering. *Phys. Rev.*, 114:1541–1542, Jun 1959.

[40] L. Diaconescu and M. J. Ramsey-Musolf. Vector analyzing power in elastic electron-proton scattering. *Phys. Rev. C*, 70:054003, Nov 2004.

[41] M. Gorchtein and C. J. Horowitz. Analyzing power in elastic scattering of electrons off a spin-0 target. *Phys. Rev. C*, 77:044606, Apr 2008.

[42] E. D. Cooper and C. J. Horowitz. Vector analyzing power in elastic electron-nucleus scattering. *Phys. Rev. C*, 72:034602, Sep 2005.

[43] B. Pasquini and M. Vanderhaeghen. Resonance estimates for single spin asymmetries in elastic electron-nucleon scattering. *Phys. Rev. C*, 70:045206, Oct 2004.

[44] Andrei V. Afanasev and N.P. Merenkov. Collinear photon exchange in the beam normal polarization asymmetry of elastic electronproton scattering. *Physics Letters B*, 599(12):48 – 54, 2004.

[45] Andrei V. Afanasev and N. P. Merenkov. Large logarithms in the beam normal spin asymmetry of elastic electron-proton scattering. *Phys. Rev. D*, 70:073002, Oct 2004.

[46] S. P. Wells, T. Averett, D. Barkhuff, et al. Measurement of the vector analyzing power in elastic electron-proton scattering as a probe of the double virtual compton amplitude. *Phys. Rev. C*, 63:064001, May 2001.

[47] S. Abrahamyan, A. Acha, A. Afanasev, et al. New measurements of the transverse beam asymmetry for elastic electron scattering from selected nuclei. *Phys. Rev. Lett.*, 109:192501, Nov 2012.

[48] D. S. Armstrong, J. Arvieux, R. Asaturyan, et al. Transverse beam spin asymmetries in forward-angle elastic electron-proton scattering. *Phys. Rev. Lett.*, 99:092301, Aug 2007.

[49] D. Wang et al. Measurement of Parity-Violating Asymmetry in Electron-Deuteron Inelastic Scattering. *Phys. Rev.*, C91(4):045506, 2015.

[50] Kurtis D. Bartlett. Measurement of beam-normal single-spin asymmetries in elastic electron scattering on ^{27}al and ^{12}c. `https://qweak.jlab.org/DocDB/0021/002165/001/kbartlett_April_APS_Meeting_2015_final.pdf`, 2015.

[51] S. Abrahamyan, Z. Ahmed, H. Albataineh, et al. Measurement of the neutron radius of ^{208}Pb through parity violation in electron scattering. *Phys. Rev. Lett.*, 108:112502, Mar 2012.

[52] D. Armstrong, T. Averett, J.D. Bowman, et al. The Q_{weak} experiment: A search for new physics at the tev scale via a measurement of the protons weak charge. Experiment proposal, Thomas Jefferson National Accelerator Facility, 2001.

[53] T. Allison, M. Anderson, D. Androi, et al. The qweak experimental apparatus. *Nuclear Instruments and Methods in Physics Research Section A: Accelerators, Spectrometers, Detectors and Associated Equipment*, 781:105 – 133, 2015.

[54] K. D. Paschke. Controlling helicity-correlated beam asymmetries in a polarized electron source. *The European Physical Journal A*, 32(4):549–553, 2007.

[55] J.M. Grames, P.A. Adderley, J. F. Benesch, et al. Two wien filter spin flipper. In *Particle Accelerator Conference, 2011., Proceedings of the 2011*, pages 862–864, April 2011.

[56] Emmanouil Kargiantoulakis. *A Precision Test of the Standard Model via Parity-Violating Electron Scattering in the Qweak Experiment.* PhD thesis, University of Virginia, December 2015.

[57] Christoph W. Leemann, David R. Douglas, and Geoffrey A. Krafft. The continuous electron beam accelerator facility: Cebaf at the jefferson laboratory. *Annual Review of Nuclear and Particle Science*, 51(1):413–450, 2001.

[58] Joeseph M. Grames. *Measurement of the Weak Polarization Sensitivity to the Beam Orbit of the CEBAF Accelerator.* PhD thesis, University of Illinois at Urbanna-Champaign, 2000.

[59] M. Hauger, A. Honegger, J. Jourdan, et al. A high-precision polarimeter. *Nuclear Instruments and Methods in Physics Research Section A: Accelerators, Spectrometers, Detectors and Associated Equipment*, 462(3):382 – 392, 2001.

[60] L.G. Levchuk. The intra-atomic motion of bound electrons as a possible source of the systematic error in electron beam polarization measurements by means of a mller polarimeter. *Nuclear Instruments and Methods in Physics Research Section A: Accelerators, Spectrometers, Detectors and Associated Equipment*, 345(3):496 – 499, 1994.

[61] Joshua Allen Magee. *A Measurement of the Parity-Violating Asymmetry in Aluminum and its Contribution to a Measurement of the Protons Weak Charge.* PhD thesis, The College of William and Mary, May 2016.

[62] Morris L. Swartz. PHYSICS WITH POLARIZED ELECTRON BEAMS. *Conf. Proc.*, C8708101:83–131, 1987.

[63] Donald Charles Jones. *Measuring the Weak Charge of the Proton via Elastic Electron-Proton Scattering.* PhD thesis, University of Virginia, October 2015.

[64] Juan Carlos Cornejo. *Compton Scattering Polarimetry for the Determination of the Protons Weak Charge Through Measurements of the Parity-Violating Asymmetry of* $^{1}H(e,e)p$. PhD thesis, The College of William & Mary, August 2015.

[65] Amrendra Narayan. *Determination of electron beam polarization using electron detector in Compton polarimeter with less than 1uncertainty.* PhD thesis, Mississippi State University, May 2015.

[66] R. Dickson and V. A. Lebedev. Fast digital feedback system for energy and beam position stabilization. In *Particle Accelerator Conference, 1999. Accelerator Science and Technology., Proceedings of the 1999 IEEE*, 1999.

[67] W. Barry. A general analysis of thin wire pickups for high frequency beam position monitors. *Nuclear Instruments and Methods in Physics Research Section A: Accelerators, Spectrometers, Detectors and Associated Equipment*, 301(3):407 – 416, 1991.

[68] C. Yan, P. Adderley, D. Barker, et al. Superharp a wire scanner with absolute position readout for beam energy measurement at cebaf. *Nuclear Instruments and Methods in Physics Research Section A: Accelerators, Spectrometers, Detectors and Associated Equipment*, 365(2):261 – 267, 1995.

[69] C. Yan, R. Carlini, and D. Neuffer. Beam energy measurement using the hall c beamline (cebaf). In *Particle Accelerator Conference, 1993., Proceedings of the 1993*, pages 2136–2138 vol.3, May 1993.

[70] Nuruzzaman. How beam energy changes will be identified in Q_{weak} . Technical report, Qweak Document, January 2010.

[71] K. B. Unser. Design and preliminary tests of a beam intensity monitor for lep. In *Particle Accelerator Conference, 1989. Accelerator Science and Technology., Proceedings of the 1989 IEEE*, pages 71–73 vol.1, March 1989.

[72] R. Kazimi, B. Dunham, G. A. Krafft, et al. Precision intercomparison of beam current monitors at cebaf. In *Particle Accelerator Conference, 1995., Proceedings of the 1995*, volume 4, pages 2610–2612 vol.4, May 1995.

[73] Joshua Hoskins. *Determination of the Protons Weak Charge via Parity Violating Electron Scattering.* PhD thesis, College of William and Mary, 2015.

[74] Scott J MacEwan. *The Weak Charge of the Proton: A Search for Physics Beyond the Standard Model.* PhD thesis, University of Manitoba, 2015.

[75] John D. Leacock. *Measurign the Weak Charge of the Proton and the Hadronic Parity Violation of the $N \to \Delta$ Transition.* PhD thesis, Virginia Polytechnic Instute and State University, October 2012.

[76] Jie Pan. *Towards a Precision Measurement of Parity Violating e-p Scattering at Low Momentum Transfer.* PhD thesis, The University of Manitoba, 2012.

[77] John Poague Leackey IV. *The First Direct Measurement of the Weak Charge of the Proton.* PhD thesis, Virginia Polytechnic Instute and State University, October 2012.

[78] Katherine E. Myers. *The First Determination of the Proton's Weak Charge Through Parity-Violating Asymmetry Measurements in Elastic e + p and e + Al Scattering.* PhD thesis, The George Washington University, 2012.

[79] Rene Brun and Fons Rademakers. New computing techniques in physics research v root an object oriented data analysis framework. *Nuclear Instruments and Methods in Physics Research Section A: Accelerators, Spectrometers, Detectors and Associated Equipment*, 389(1):81 – 86, 1997.

[80] Louis Lyons. *Statistics for Nuclear and Particle Physicists.* 1986.

[81] Adesh Subedi. Determination of the weak charge of the proton through parity violating asymmetry measurements in the elastic $e + p$ scattering, December 2014.

[82] D. Armstrong, T. Averett, J. Birchall, et al. The Q_{weak} experiment: A search for new physics at the tev scale via a measurement of the protons weak charge. Experiment jeopardy proposal, Thomas Jefferson National Accelerator Facility, 2004.

[83] Philip R Bevington and D Keith Robinson. *Data reduction and error analysis for the physical sciences; 3rd ed.* McGraw-Hill, New York, NY, 2003.

[84] Arne Freyberger and Y. Roblin. Studies of beam halo formation in the 12 gev cebaf design. Technical report, JLab, 2006.

[85] Dave Gaskell. Run 2 final polarizations - updated proposal. `https://qweak.jlab.org/elog/DAQ+%26+Analysis/334`, May 2015.

[86] Rob Mahurin. Description of Q_{weak} pmt linearity tests using the eel126 test stand. Technical report, Qweak Document, June 2013.

[87] D. W. Higinbotham. Electron spin precession at cebaf. *AIP Conference Proceedings*, 1149(1), Aug 2009.

[88] Gregory Smith. Predicting pmt-dd and a_{bias}. `https://qweak.jlab.org/DocDB/0023/002360/001/PredictingPMTDDandAbias_v2.pdf`, 2016.

[89] Rakitha S. Beminiwattha. Main detector neutral background contribution. Technical report, Qweak Document, July 2012.

[90] Martin James McHugh. Current dependence of the neutral fraction. `https://qweak.jlab.org/elog/Analysis+%26+Simulation/1423`, April 2015.

[91] Adesh Subedi. Simulation of qtor scans using qwgeant3. https://qweak.jlab.org/elog/Analysis+%26+Simulation/837, December 2012.

[92] John D. Leacock. Inelastic results. https://qweak.jlab.org/DocDB/0016/001634/003/leacock_2012_05_14_inel.pdf, May 2012.

[93] Mark Pitt. Private communication. 2014.

[94] Katherine E. Mesick. Aluminum asymmetry analysis. https://qweak.jlab.org/DocDB/0021/002142/002/KMesick_AluminumAsymmetry_3.15.pdf, March 2015.

[95] Hend Nuhait and Steven P. Wells. Outline of how f_{b_4} and its error are calculated. https://qweak.jlab.org/elog/Ancillary/253, April 2016.

[96] Fang Guo. *First Determination of the Weak Charge of the Proton.* PhD thesis, Massachusetts Institute of Technology, June 2016.

[97] David Armstrong. q^2 uncertainties - master list. http://dilbert.physics.wm.edu/Physics/125, March 2015.

[98] Mark Pitt. "effective kinematics" and acceptance correction for official wien 0 hydrogen result. https://qweak.jlab.org/elog/Analysis+%26+Simulation/794, October 2012.

[99] Klaus Ackerstaff, A Airapetian, N Akopov, et al. The hermes spectrometer. *Nuclear Instruments and Methods in Physics Research Section A: Accelerators, Spectrometers, Detectors and Associated Equipment*, 417(2):230–265, 1998.

[100] Jie Pan. The tracking analysis in the q-weak experiment. Technical report, Qweak Document, April 2016.

[101] Adesh Subedi. Geant3 based run 2 r_{RC} simulation results. https://qweak.jlab.org/elog/Analysis+%26+Simulation/1449, April 2015.

[102] Nuruzzaman. *Beam Normal Single Spin Asymmetry in Forward Angle Inelastic Electron-Proton Scattering Using the Q_{weak} Apparatus.* PhD thesis, Hampton University, December 2014.

[103] David Armstrong. Tracking/kinematics update may 2016. https://qweak.jlab.org/DocDB/0023/002326/001/Tracking_May2016.pdf, May 2016.

[104] J. Grames, M. Poelker, P. Adderley, et al. Measurements of photocathode operational lifetime at beam currents up to 10 ma using an improved dc high voltage gaas photogun. *AIP Conference Proceedings*, 915(1):1037–1044, 2007.

[105] Buddhini Waidyawansa. Pmt pos neg difference in elastic e+p transverse data. https://qweak.jlab.org/elog/Analysis+%26+Simulation/1300, November 2014.

[106] Scott MacEwan. Md pulsed-led calibrations. https://qweak.jlab.org/elog/Detector/83, April 2014.

[107] H. de Vries, C. W. de Jager, and C. de Vries. Nuclear charge-density-distribution parameters from electron scattering. *Atomic Data and Nuclear Data Tables*, 36:495, 1987.

[108] Spence's function. http://mathworld.wolfram.com/SpencesFunction.html. Accessed: 2016-08-20.

[109] H. L. Crannell and T. A. Griffy. Determination of radiative transition widths of excited states in c^{12}. *Phys. Rev.*, 136:B1580–B1584, Dec 1964.

[110] Hall Crannell. Elastic and inelastic electron scattering from c^{12} and o^{16}. *Phys. Rev.*, 148:1107–1118, Aug 1966.

[111] A. Nakada, Y. Torizuka, and Y. Horikawa. Determination of the deformation in ^{12}C from electron scattering. *Phys. Rev. Lett.*, 27:745–748, Sep 1971.

[112] J. B. Flanz, R. S. Hicks, R. A. Lindgren, et al. Convection currents and spin magnetization in $e2$ transitions of ^{12}C. *Phys. Rev. Lett.*, 41:1642–1645, Dec 1978.

[113] GA Proca and DB Isabelle. Inelastic electron scattering at 180 on 12 c. *Nuclear Physics A*, 109(1):177–200, 1968.

[114] Y Torizuka, M Oyamada, K Nakahara, et al. Electroexcitation of the 10.8-mev (1-; t= 0) level of c 12 and the 7.12-mev (1-; t= 0) level of o 16. *Physical Review Letters*, 22(11):544, 1969.

[115] Y Kawazoe and T Tsukamoto. Calculation of electroexcitation cross sections in c 12 by a continuum shell model. *Physical Review C*, 13(4):1759, 1976.

[116] TW Donnelly, JD Walecka, I Sick, and EB Hughes. Electron excitation of particle-hole states in c 12. *Physical Review Letters*, 21(16):1196, 1968.

[117] JB Flanz, RS Hicks, RA Lindgren, et al. Electron scattering, isospin mixing, and the structure of the 12.71-and 15.11-mev levels in c 12. *Physical Review Letters*, 43(26):1922, 1979.

[118] Y Torizuka, A Yamaguchi, T Terasawa, et al. Excitation of the giant resonance in c 12 by inelastic electron scattering. *Physical Review Letters*, 25(13):874, 1970.

[119] N. T. Meister and T. A. Griffy. Radiative corrections to high-energy inelastic electron scattering. *Phys. Rev.*, 133:B1032–B1036, Feb 1964.

[120] J. Goldemberg, Y. Torizuka, W.C. Barber, and J.D. Walecka. Excitation of the electric dipole giant resonance by inelastic electron scattering at 180. *Nuclear Physics*, 43:242 – 253, 1963.

[121] P. E. Bosted and V. Mamyan. Empirical Fit to electron-nucleus scattering. 2012.

[122] Kurtis Bartlett. Quasi-elastic scattering data comparison with bosted model for qwgeant4. `https://qweak.jlab.org/elog/Analysis+%26+Simulation/1634`, July 2016.

[123] Katherine Mesick. Beamline background dilution for aluminum run 2. `https://qweak.jlab.org/elog/Analysis+%26+Simulation/1439`, April 2015.

[124] Maritn James McHugh. Measurement of the qtor transport channel neutral background. Technical report, Qweak Document, May 2016.

[125] Mikhail Gorchtein, C. J. Horowitz, and Michael J. Ramsey-Musolf. Model-dependence of the γZ dispersion correction to the parity-violating asymmetry in elastic *ep* scattering. *Phys. Rev.*, C84:015502, 2011.

[126] N. L. Hall, P. G. Blunden, W. Melnitchouk, A. W. Thomas, and R. D. Young. Quarkhadron Duality Constraints on Z Box Corrections to Parity-Violating Elastic Scattering. *Phys. Lett.*, B753:221–226, 2016.

[127] R. D. Young, R. D. Carlini, A. W. Thomas, and J. Roche. Testing the standard model by precision measurement of the weak charges of quarks. *Phys. Rev. Lett.*, 99:122003, Sep 2007.

[128] V. A. Dzuba, J. C. Berengut, V. V. Flambaum, and B. Roberts. Revisiting parity nonconservation in cesium. *Phys. Rev. Lett.*, 109:203003, Nov 2012.

[129] Anselm Esser. Measurement of the transverse asymmetry of ^{12}c. `http://www.ectstar.eu/sites/www.ectstar.eu/files/talks/06_AesserTrento.pdf`, 2016.

[130] Gerald G. Ohlsen and P.W. Keaton. Techniques for measurement of spin-1/2 and spin-1 polarization analyzing tensors. *Nuclear Instruments and Methods*, 109(1):41 – 59, 1973.

[131] T. J. Gay and F. B. Dunning. Mott electron polarimetry. *Review of Scientific Instruments*, 63(2):1635–1651, 1992.

[132] M. Steigerwald. Mev mott polarimetry at jefferson lab. *AIP Conference Proceedings*, 570(1):935–942, 2001.

[133] Daniel Moser. Calculating rates. `https://wiki.jlab.org/ciswiki/images/e/ef/Rates.pdf`, 2015.

[134] N. F. Mott. The scattering of fast electrons by atomic nuclei. *Proceedings of the Royal Society of London A: Mathematical, Physical and Engineering Sciences*, 124(794):425–442, 1929.

[135] Xavier Roca-Maza. Mott polarimetry at jlab: Working notes on theory. https://www.dropbox.com/home/Mott%20Team%20Team%20Folder/Theory?preview=mott-theory.pdf, 2015.

[136] Francesc Salvat, Aleksander Jablonski, and Cedric J. Powell. Elsepadirac partial-wave calculation of elastic scattering of electrons and positrons by atoms, positive ions and molecules. *Computer Physics Communications*, 165(2):157 – 190, 2005.

[137] X. Roca-Maza, M. Centelles, F. Salvat, and X. Viñas. Theoretical study of elastic electron scattering off stable and exotic nuclei. *Phys. Rev. C*, 78:044332, Oct 2008.

[138] George Casella, Christian P. Robert, and Martin T. Wells. *Generalized Accept-Reject sampling schemes*, volume Volume 45 of *Lecture Notes–Monograph Series*, pages 342–347. Institute of Mathematical Statistics, Beachwood, Ohio, USA, 2004.

[139] Malvin H. Kalos and Paula A. Whitlock. *Monte Carlo Methods*. WILEY-VCH Verlag GmbH & Co. HGaA, Weinheim, Germany, 2004.

Appendices

Appendix A

CEBAF Injector MeV Mott Polarimeter

This appendix details the work the author has done to improve and quantify the precision of the MeV Mott Polarimeter in the CEBAF injector. This work was part of a group effort aimed at providing a measurement of the electron beam's transverse polarization at the 0.5% level in anticipation of the next generation of parity-violating asymmetry measurements at JLab. This appendix begins with a brief introduction of Mott polarimetry in general, as well as the specifics of the JLab MeV Mott Polarimeter. There will be discussions of the data taken as part of this effort, as well as software and hardware upgrades made to the polarimeter. Then, the extensive work on providing a `GEANT4` simulation of the polarimeter will be covered. A brief comparison of the data and simulation and summary will conclude the chapter.

A.1 Introduction and Motivation

The MeV Mott Polarimeter is located in the Continuous Electron Beam Accelerator Facility (CEBAF) injector at Jefferson Lab (JLab). It is used to measure the transverse polarization of the electron beam in the 2 - 8 MeV energy range before it enters the accelerator and being sent to the experimental halls. The polarimeter (Fig. A.1) measures the elastic scattering asymmetry of electrons incident on the nuclei of a thin target foil. The foils used in the past included gold, silver, and copper, and ranged in thickness from 100-10,000 Å.

The elastically scattered electrons from the target foil pass through an aluminum collimator which sets the scattering angle of $172.6^\circ \pm 0.1^\circ$ with a per quadrant solid angle

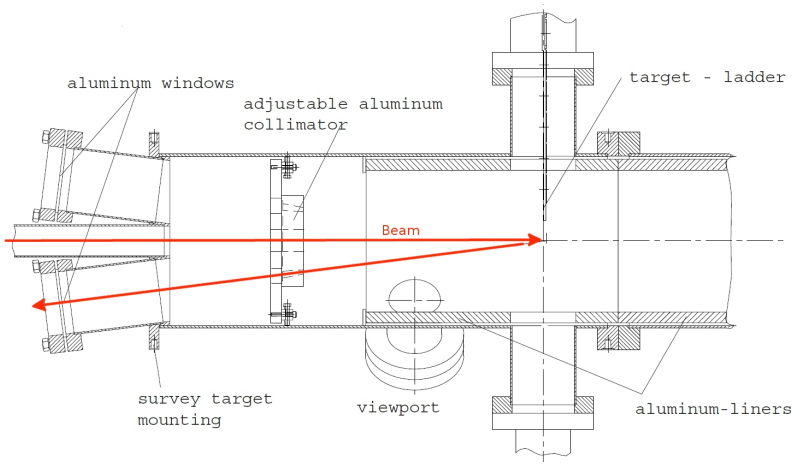

Figure A.1: Cross section of the polarimeter's scattering chamber. A typical event's path toward the DOWN detector is shown in red.

of 0.18 msr. The scattered electrons then pass through the 0.05 mm thick aluminum vacuum window and into one of the four symmetrically placed detector packages. These are referred to as the UP, DOWN, LEFT, and RIGHT detector packages based upon their position relative to the beamline when facing downstream. Each detector package contains two plastic scintillators connected to PMTs for readout: a 1 mm $\times$ 25.4 mm $\times$ 25.4 mm wafer scintillator, the Δ E detector, and a cylindrical 76.2 mm diameter, 63.5 mm long scintillator, the E detector, which functions as a stopping detector and calorimeter with $\approx 3\%$ energy resolution. The data acquisition system utilizes a coincidence trigger of the E and Δ E detectors to filter out any incident neutral particles or particles not coming from the target region. Additional cuts are then applied to the recorded data as described in later sections. The beam polarization changed at a rate of 30 Hz and total polarization asymmetry is calculated using the cross-ratio method [130]. We find the Mott scattering asymmetry due to a vertically polarized beam to be:

$$A_{LR} = \frac{1 - \sqrt{N_L^{\uparrow} N_R^{\downarrow} / N_L^{\downarrow} N_R^{\uparrow}}}{1 + \sqrt{N_L^{\uparrow} N_R^{\downarrow} / N_L^{\downarrow} N_R^{\uparrow}}}, \tag{A.1}$$

Where A_{LR} is the asymmetry and $N_{L(R)}^{\uparrow[\downarrow]}$ is the number of hits which pass all cuts in the LEFT(RIGHT) detector package when the polarization is pointing in the $+y[-y]$ direction.

This asymmetry is proportional to the polarization's vertical component, P_y:

$$A_{LR}(\theta) = S(\theta)P_y \tag{A.2}$$

where $S(\theta)$, known as the Sherman function, is the analyzing power [131]. Similar ratios are constructed to measure the vertical polarization as well. Using this method, the asymmetry is measured with 0.5 % statistical precision in about 5 minutes using a 1 μm Au foil and 1 μA of beam current.

When this polarimeter was commissioned over a decade ago, the total systematic uncertainty was quoted to be 1.1%, dominated by the uncertainty in the theoretical uncertainty in the Sherman function [132]. At that time, the polarimeters in the experimental halls were only precise to the 5% level and all polarization measurements were found to be in agreement. Over the lifetime of the Mott polarimeter, the polarization level of the CEBAF beam has gone from <50% to almost 90%. In addition, the current precision of the hall polarimeters has reached $< 1\%$. At this precision, and assuming the quoted Mott polarimeter accuracy above, a measured polarization discrepancy of 2 - 3 σ has been observed. This discrepancy motivated the recent effort to quantify and reduce the systematic errors of Mott polarimeter measurements to improve the accuracy of the device.

Work done on the Mott Polarimeter in support of this upgrade was focused on two areas. The first was ensuring the cleanest possible measurement of the asymmetry on each foil, primarily by reducing the low-energy background included in the asymmetry measurement, which is shown in Figure A.2. This required taking data on several targets in a variety of systematic studies. Additionally, work was done to improve the data acquisition process and hardware changes were made to improve the signal-to-noise ratio. Secondly, in order to determine the polarization from a measured asymmetry on a foil of finite thickness, one must have excellent knowledge of the Sherman function (the zero target thickness case) and understand how the asymmetry varies with target thickness. Accounting for all these issues required input from theorists and the construction of a `GEANT4` model of the polarimeter based upon this theoretical input as well as careful examination of the techniques used to extrapolate to zero target thickness.

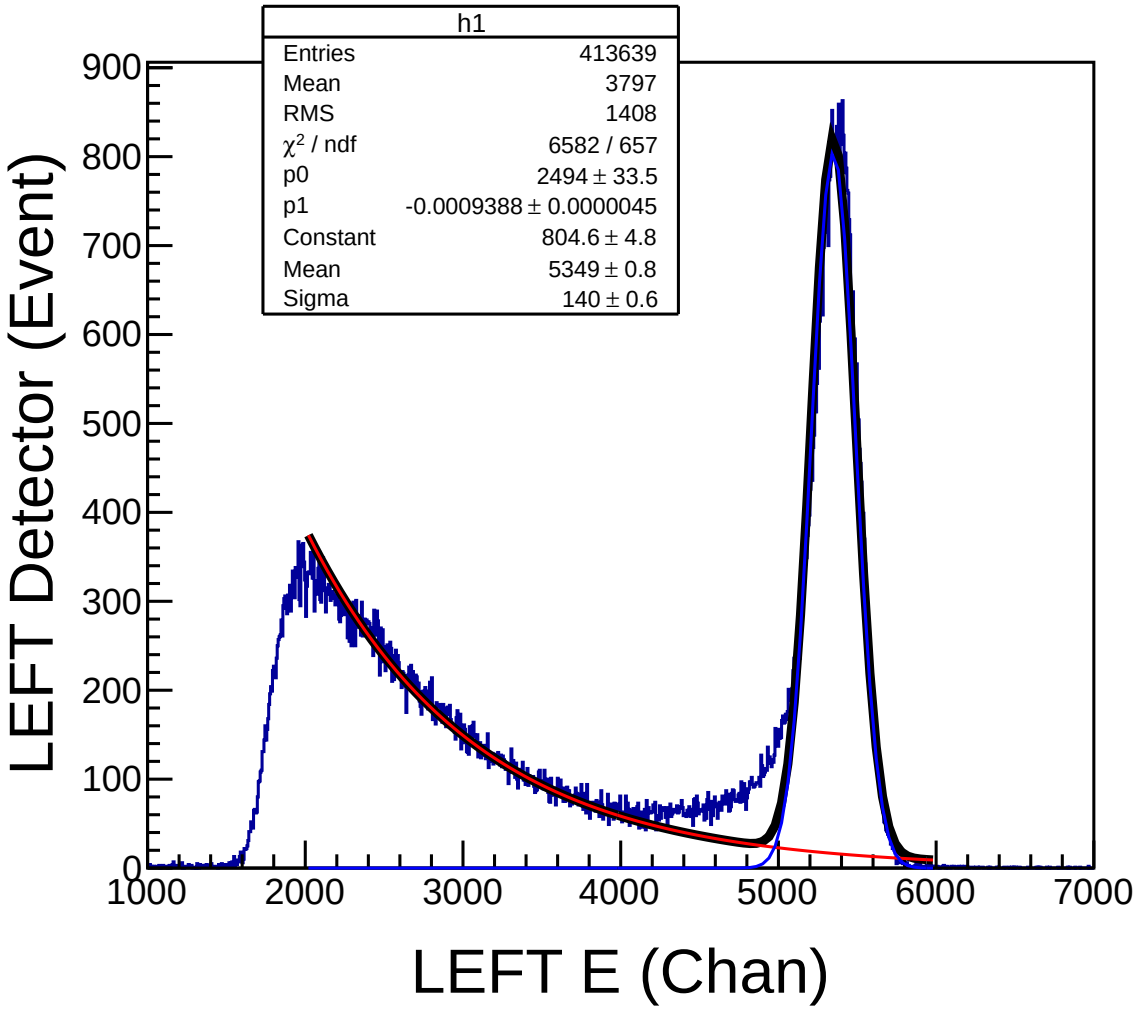

Figure A.2: ADC spectrum seen in the LEFT detector package during a 5 MeV run on 1 μm Au foil. The red exponential fit describes low-energy background while the peak at $\approx$ 5400 ADC channels is the elastic scattering signal. This spectrum represents the data taken with the polarimeter prior to the updates discussed below.

A.2 Polarimeter Design Updates

The first and most pertinent update to the Mott Polarimeter was the utilization of a new fast analog-to-digital converter (FADC) to record the signals from the detectors. When coupled with a low beam-bunch rate (referred to in the JLab community as the rep rate) of 31 MHz - opposed to the traditional JLab operating rep rate of 499 MHz - this allowed clear separation of events recorded in the detector according to the time-of-flight of the electrons.

This separation is shown in Figure A.3. Running at the 499 MHz rep rate meant that events from the dump and the target arrived simultaneously, so there was no possibility of separation.

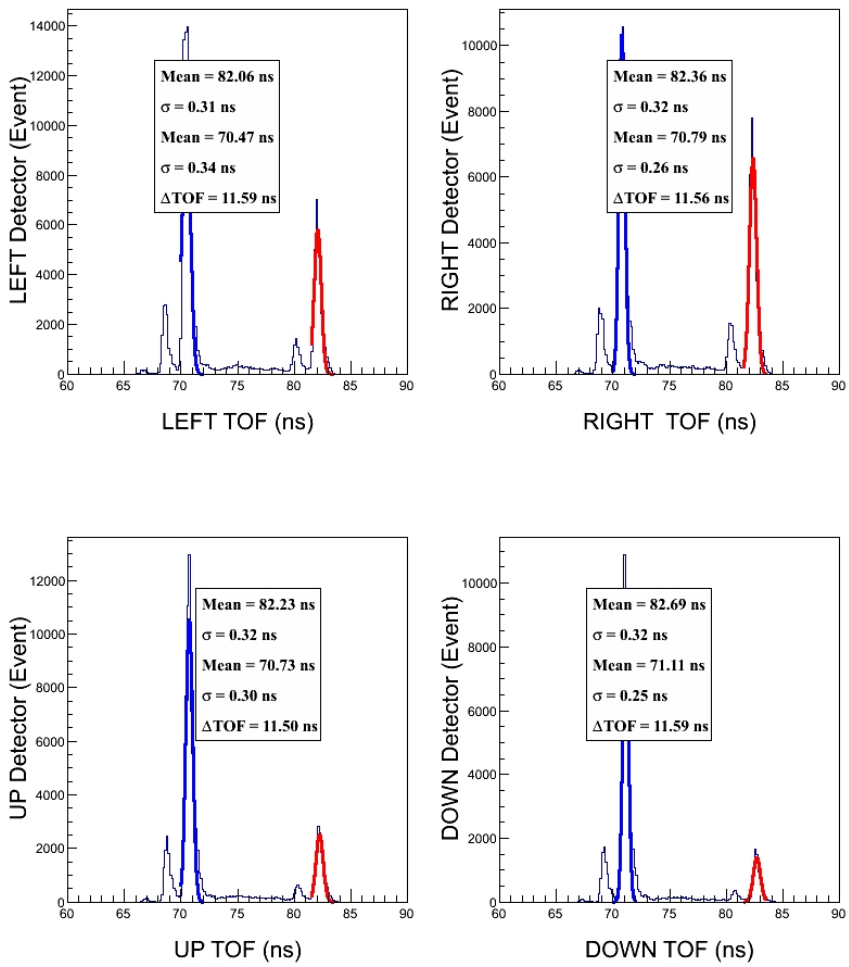

Figure A.3: Time-of-flight separation using 31 MHz bunch rate. Blue events are from the target, red events are from the beam dump ≈ 2 m downstream of the target. This run was taken before the installation of the new beam dump.

In order to reduce the signal from the beam dump when the polarimeter has to be used at the 499 MHz rep rate - thereby eliminating the possibility of time-of-flight separation - a new beryllium and copper dump plate was designed and installed in 2014. The previous dump plate was a 25.4 mm thick aluminum end flange attached to the vacuum chamber of the polarimeter. During runs with thin Au foils, the Al dump produced roughly the

same event rate as the target. The new dump plate, designed with the help of a GEANT4 simulation, consists of 6.35 mm of beryllium backed by 19.05 mm of water-cooled copper. Simulation of backscattering events are shown in Figure A.4. The simulation predicted a four-fold reduction of back-scattered electrons when using the new dump. The additional cooling capacity of this new design also allows for higher beam currents, $\approx 50\mu$A, to be utilized.

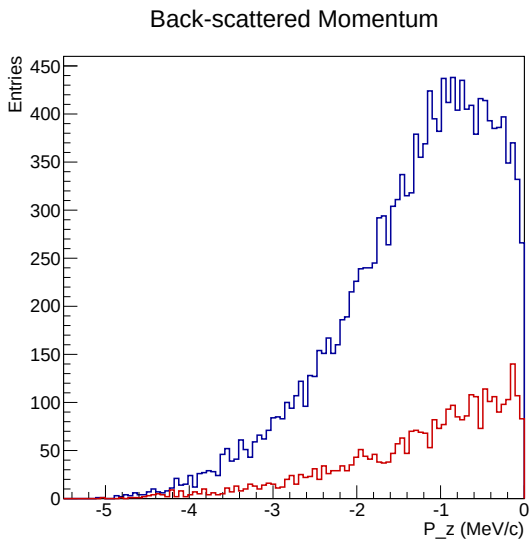

Figure A.4: Comparison of back-scattered momentum spectra from the Al dump and BeCu dump.

A.3 Mott Data Taking

Development and calibration data for the Mott upgrade were taken in two periods, Run 1: January 13-19 2015 and Run 2: October 23-26 2015. During these two runs, the above mentioned upgrades had been put in place. These two sets of data were taken on a set of eight gold foils of varying thickness, shown in Table A.1. Since foil thickness was an essential piece of information for the extrapolation to the single atom scattering case, extra care was taken to measure and document the exact thicknesses of the foils used. The measurements were made using a Hitachi S-4700 field emission scanning electron microscope (FESEM) to view and measure cross sections from samples of the targets, often taken from identical targets in storage. Other targets filling out the 16 available positions on the

Target #	d (nm)	δd (nm)
13	52	6
1	215	13
14	389	22
5	488	29
2	561	37
4	775	43
3	837	49
15	944	78

Table A.1: Selection of the target foils used for target thickness extrapolation data taking in 2015. The uncertainty in the target thickness includes both the uncertainty of the FESEM measurements as well as the manufacturer stated 5% variation between targets within the same batch.

target "ladder" included duplicates, an empty position for examining backgrounds and a scintillating "viewer" target allowing a camera to view the position and profile of the beam at the target position. In both runs, the kinetic energy of the electrons incident upon the Mott was determined to be 4.90 ± 0.15 MeV.

Enough data was accumulated to measure the asymmetry at each target to within 0.1 % statistical error. The data used in the asymmetry calculations was subject to energy cuts in addition to the time-of-flight and coincidence rejection to ensure that only elastic events were included. Between target foil changes runs were taken on one of the 944 nm foils to ensure that stability was maintained. In addition to these measurements for the target thickness extrapolation, there were systematic tests that measured the asymmetry dependence upon such parameters as beam position on target, the beam profile on the target (typically a Gaussian but capable of being de-focused along a given axis), the charge asymmetry, beam current and more. When each of these parameters was varied, the measured asymmetry only differed within statistical fluctuations. This insensitivity was primarily due to the use of the cross-ratio method to calculate the asymmetry, eq. (A.1). In this asymmetry calculation, physical systematics cancel to all orders. As such, a systematic error bar of 0.05% has been assigned to account for total systematic uncertainty of the measurement due to the other parameters.

The main results of the two data-taking periods are shown in Table A.2 and Figure A.5. These two data sets clearly highlight one of the largest challenges confronting the JLab

MeV Mott polarimeter group, namely, determining the dependence of the asymmetry as a function of target thickness in a sound fashion. Throughout the history of Mott scattering experiments, the exact shape of this thickness dependence has never been predicted explicitly and many conventions were utilized [131]. In this work, we utilize a fitting function of the form

$$A(d) = \frac{A_0 + \alpha d}{1 + \beta d}. \tag{A.3}$$

The reason for selecting this form will be discussed in later sections. With the two runs being statistically commensurate, we can combine them into a single effective measurement of the asymmetry as a function of target thickness. Using this combined data, one obtains a fit with parameters

$$A_0 = 43.97\% \pm 0.36\% \tag{A.4}$$

$$\alpha = (1 \pm 6) \times 10^{-3}\ (\mathrm{nm})^{-1} \tag{A.5}$$

$$\beta = (0.28 \pm 0.17) \times 10^{-3}\ (\mathrm{nm})^{-1} \tag{A.6}$$

In order to determine the polarization using this information, one must now make use of the Sherman function as indicated in eq. (A.2).

	Run 1		Run 2		Combined	
d (nm)	A [%]	δA [%]	A [%]	δA [%]	A [%]	δA [%]
52	43.50	0.10	43.36	0.11	43.43	0.07
215	40.96	0.09	40.93	0.11	40.95	0.07
389	39.18	0.10	39.08	0.11	39.13	0.07
488	38.61	0.09	38.60	0.11	38.61	0.07
561	37.25	0.09	37.08	0.11	37.17	0.07
775	35.62	0.09	35.71	0.11	35.67	0.07
837	34.62	0.09	34.83	0.11	34.73	0.07
944	33.77	0.09	33.83	0.11	33.80	0.07

Table A.2: Asymmetry measurements for each foil during each run. The results are typically within 1-2 standard deviations despite the different photocathode used and long interval between measurements. This allows an averaged measurement shown in the final two columns on the right. Errors are combined systematic and statistical measurements.

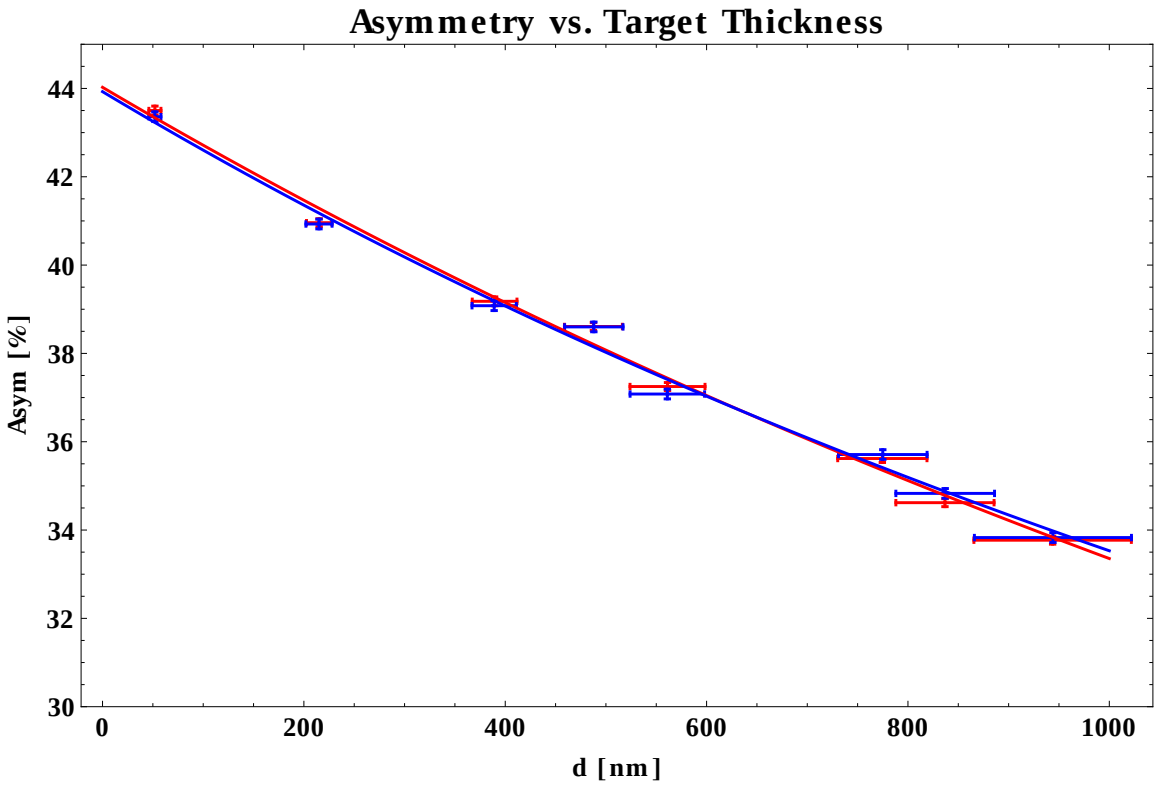

Figure A.5: Mott Run 1 (red) and Run 2 (blue) target foil thickness extrapolations using the fit form shown in eq. (A.3).

A.3.1 Data Rates

Because the Mott polarimeter's beam flipped polarization direction at a rate of 30 Hz, each detector saw a combination of each spin state analogous to an average of the simulated LEFT and RIGHT detectors. Additionally, there were known detector efficiency differences between the four detectors. In order to compare to simulation, data from Mott Run 2 were analyzed and an average rate was constructed from all four detectors. The rate included events that had a coincidence between the E and ΔE detector, and a timing cut to ensure that the electrons were from the target. These rates are shown in Table A.3. The resulting rates were fit with a parabola in order to determine linear and quadratic coefficients. The resulting fit $R^{data}(d) = a_1^{data} d + a_2^{data} d^2$ has coefficients,

$$a_1^{data} = 0.19 \pm 0.01 \text{ Hz}/(\mu\text{A nm}), \tag{A.7}$$

$$a_2^{data} = 70 \pm 17 \ \mu\text{Hz}/(\mu\text{A nm}^2). \tag{A.8}$$

d (nm)	$\mathcal{R}^{\text{data}}$	$\mathcal{R}_1^{\text{fit}}$	$\mathcal{R}_2^{\text{fit}}$
52	9.9±0.1	9.8±0.5	0.19±0.05
215	46.5±0.5	40.3±2.1	3.2±0.8
389	82.6±1.0	73.0±3.7	10.5±2.6
488	97.7±1.0	91.3±4.6	16.5±4.1
561	128.7±1.3	105.2±5.3	21.9±5.4
775	178.3±1.9	145.3±7.4	41.7±10.3
837	209.3±2.2	157.0±8.0	48.7±12.1
944	246.0±2.5	177.0±9.0	61.9±15.3

Table A.3: From left to right, the data, linear fit, and quadratic fit portions. Data and fit taken from[133]. All rates are given in units of Hz/μA.

A.4 Mott Scattering Theory

The theory of Mott scattering [134] describes elastic scattering of a relativistic electron from a nucleus. In the case of polarized Mott scattering, the differential cross section can be written as

$$\frac{d\sigma}{d\Omega}(\theta) = I(\theta)\left(1 + S(\theta)\mathbf{P}\cdot\hat{n}\right) \tag{A.9}$$

where $I(\theta)$ is the spin-independent form of the Mott cross section, $\mathbf{P}$ is the incoming beam's polarization, $S(\theta)$ is the Sherman function and

$$\hat{n} = \frac{\mathbf{p}\times\mathbf{p}'}{|\mathbf{p}\times\mathbf{p}'|} \tag{A.10}$$

where $\mathbf{p}$ ($\mathbf{p}'$) is the incoming (outgoing) momentum of the electron. The spin-independent cross section and the Sherman function are defined as

$$I(\theta) = |f(\theta)|^2 + |g(\theta)|^2 \tag{A.11}$$

$$S(\theta) = i\frac{f(\theta)g^*(\theta) - f^*(\theta)g(\theta)}{|f(\theta)|^2 + |g(\theta)|^2} \tag{A.12}$$

For a vertically polarized beam ($\mathbf{P} = P\hat{y}$), measuring ideal single scattering in the horizontal plane ($\hat{n} = \hat{y}$) we expect to measure an asymmetry,

$$A = \frac{N_L - N_R}{N_L + N_R} = PS(\theta_{sc}) \tag{A.13}$$

where $N_{L(R)}$ is the number of hits in the left(right) detector placed at a scattering angle, θ_{sc}.

Plots of the relevant scattering functions for a selection of typical energies can be seen in Fig. A.6. These plots were generated using the scattering calculations performed by Xavier Roca-Maza [135]. These calculations are based on `ELSEPA` [136] and its refinements [137] and form the basis of Mott scattering physics in the `GEANT4` simulation. The Mott Polarimeter was designed take advantage of the Sherman function's minimum around 172° for 5 MeV electrons.

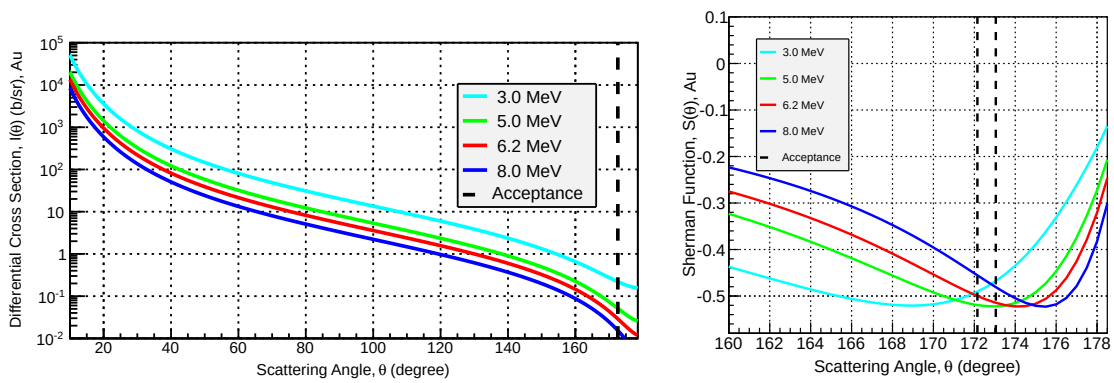

Figure A.6: Mott cross section, $\frac{d\sigma}{d\Omega}$, and analyzing power, $S(\theta)$, as a function of scattering angle. The thick dashed vertical line in both plots indicates the angular acceptance of the polarimeter.

The theory provided by Roca-Maza has been assigned a relative uncertainty of 0.5% based upon the size of higher-order QED contributions and represents ideal scattering from an isolated atom of gold. However, the asymmetry we actually observe depends on several additional parameters. Our physical beam, detectors and finite-thickness targets required averaging over several quantities: θ_{sc}, incident electron energy (E), target thickness (d), azimuthal angle (ϕ) *et cetera*. This produced an "effective" Sherman function, $S_{eff}(\theta, d\Omega, d)$, where $d\Omega$ was the detector acceptance in both angle and energy. The small angular acceptance and typically small energy loss (δE) meant that the experimental parameter of primary importance was the target thickness. The significant target-thickness dependence is clearly shown in Fig. A.5. The extrapolation to zero target thickness combined with the theoretical prediction, with appropriate acceptance averaging, yield the polarization of the

beam

$$P = A_0/\langle S_{\text{theory}}\rangle. \tag{A.14}$$

Including the theoretical errors, we determine the effective Sherman function for the single atom case to be

$$\langle S_{\text{theory}}\rangle = -0.514 \pm 0.003 \tag{A.15}$$

Combined with the fit result for A_0 in eq. (A.4), the polarization was

$$P = 85.5\% \pm 0.9\%. \tag{A.16}$$

While we may make such polarization determinations using fits, we would like to determine the asymmetry at each target thickness from first principles. The target-thickness dependence is suspected to be due to electrons that undergo multiple Mott scatterings within our target. In particular, we hypothesize that the probability of undergoing two Mott scatterings grows with target thickness and that electrons that undergo two or more scatterings carry, on average, a different, smaller analyzing power. The goal of the `GEANT4` simulation is to see if we can reproduce the effective Sherman function using this hypothesis, numerically calculating the effective analyzing power from first principles.

A.4.1 Double Mott Scattering

It is our assumption that the target-thickness dependence of the Mott scattering asymmetry is the result of multiply scattered electrons within the target foil. Simulation of this effect requires us to track the polarization over multiple steps. A Mott-scattered electron carries a new polarization:

$$\mathbf{P}' = \frac{(\mathbf{P}\cdot\mathbf{n} + S(\theta))\,\mathbf{e}_1 + U(\theta)\mathbf{e}_2 + T(\theta)\mathbf{e}_3}{1 + \mathbf{P}\cdot\mathbf{n}\,S(\theta)}, \tag{A.17}$$

where

$$\mathbf{e}_1 = \mathbf{n}, \tag{A.18}$$

$$\mathbf{e}_2 = \mathbf{n} \times \mathbf{P}, \tag{A.19}$$

$$\mathbf{e}_3 = \mathbf{n} \times (\mathbf{P} \times \mathbf{n}), \tag{A.20}$$

and with the spin-transfer functions defined respectively as

$$U(\theta) = \frac{|f(\theta)|^2 - |g(\theta)|^2}{|f(\theta)|^2 + |g(\theta)|^2} \tag{A.21}$$

$$T(\theta) = \frac{f(\theta)g^*(\theta) + f^*(\theta)g(\theta)}{|f(\theta)|^2 + |g(\theta)|^2} \tag{A.22}$$

A.5 Detector Response Simulation

Typical running conditions during the past decade had very few controls in place to reduce the amount of background in the Mott polarimeter. To reduce the impact of this background, stringent energy cuts were applied, which removed a large portion of elastically scattered electrons from the asymmetry calculation as a side-effect. An early goal of the simulation effort was to determine the source of the off-peak events that carry a large Mott asymmetry. An example of this phenomenon is shown in Fig. A.7.

Simulations indicated that the off-peak events that carried a reduced asymmetry consist partly of elastically scattered electrons which lose energy in the collimators, aluminum vacuum windows, ΔE detector and finally, hard bremsstrahlung within the E detector itself. These events mixed with the "low-energy" background shown in Figure A.2 and thus measured a reduced asymmetry. Figure A.8 indicates these effects clearly. The blue peak indicates the simulated detector response given a mono-energetic incident beam. The tail indicates that the detector's recorded energy does not reflect the particle's incident energy perfectly. With more realistic geometry and energy spread (those events shown in red) the simulation begins to show agreement with the shape of the elastic "tail" in the 3.8-4.5 MeV range compared to actual data in black. Thus one may conclude that the drop off in asymmetry shown in Figure A.7 is due to elastic events (carrying the full asymmetry)

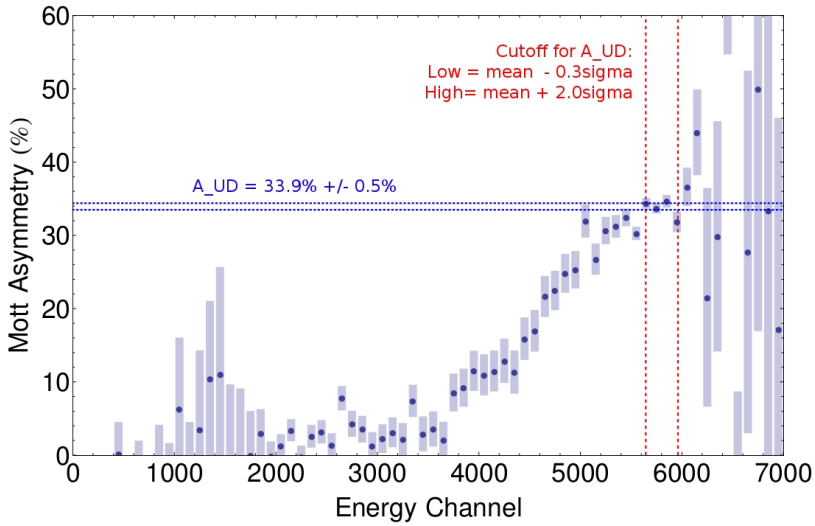

Figure A.7: Mott asymmetry as a function of ADC channel in the E detector. The data outside of the dotted red lines are excluded from the asymmetry calculation. Elastic events carrying the full Mott asymmetry were recorded outside of the elastic window due to energy loss prior to the detector as well as imperfect detector response.

that do not deposit their full energy into the detector, combined with an increasingly large fraction of unpolarized background events as one moves to lower energies.

A.6 Simulating Mott Scattering

To begin our simulation, we must generate electrons in our apparatus to represent certain physical cases. In all of the discussions following, the simulation assumed the electron beam was fully polarized in the positive y direction: $\mathbf{P} = \hat{y}$. The simulated incident electrons had momentum entirely in the z direction: $\mathbf{p} = p\hat{z}$. The beam had a circular, Gaussian profile on the target with a FWHM of 1 mm. All simulations were run with a beam energy of 4.9 MeV and a Gaussian energy spread of 150 keV. The next few sections detail exactly how the simulation recreated a full accounting of elastic scattering within the target so that the simulation could be directly compared to data. In particular, we describe the various methods used to simulate electrons that scatter from exactly one or two nuclei within the target foil before heading towards the detectors. In all of these simulations, the particles undergo realistic energy loss and bremsstrahlung in addition to the indicated number of Mott scattering processes.

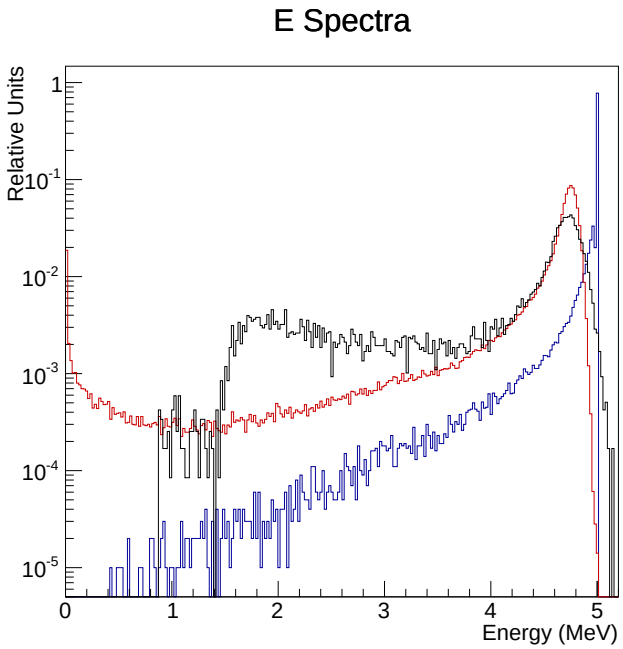

Figure A.8: A comparison of spectra from: simulation of mono-energetic electrons with no beamline elements except the target and detector packages (blue), a simulation with all polarimeter geometry elements between the target and the detectors and an energy spread of 50 keV (red), and actual data with backgrounds separated by a timing cut (black). All histograms are normalized to have unit integrals. Events in simulation are generated at the target scattering vertex and thrown directly towards the detector.

A.6.1 Single Scattering: Rejection Method

The simplest process to simulate was electrons which underwent exactly one, large-angle Mott scattering and then exited the target towards the detectors. To simulate these events, we used the following rejection sampling algorithm [138]:

1. Randomly pick an initial energy (E) and a scattering position ($\mathbf{x}_1$) within the intersection of the beam and the target.

2. Randomly pick a point, $\mathbf{x}_2$, in the acceptance of the primary collimator.

3. Calculate the Mott cross section given these inputs: $\frac{d\sigma}{d\Omega}(\mathbf{x}_1, \mathbf{x}_2)$.

4. Rejection sample against this cross section. If accepted, proceed to generate the event. If rejected, repeat steps 1-3.

Simulations of 10 million events at each target thickness were performed using this algorithm to generate primary electrons. In order to measure the Mott asymmetry from simulations generated in this manner, we simply used eq. (A.13) to get a simulated asymmetry of

$$\varepsilon_1 = \frac{N_{L_1} - N_{R_1}}{N_{L_1} + N_{R_1}} = S(\theta_{sc}) = -0.513 \pm 0.0005. \tag{A.23}$$

The subscript 1 indicates that these simulations represent events which scattered exactly once in the target. As expected, this value was in agreement with the theoretical acceptance-averaged Sherman function for a single atom from eq. (A.15):

$$\langle S_{\text{theory}} \rangle = -0.514 \pm 0.003 \tag{A.24}$$

This indicated that we had indeed simulated single Mott scattering effectively. The results did not change regardless of target thickness simulated, confirming that single scattering alone was not adequate to explain the asymmetry measurements using thick target foils.

A.6.2 Double Scattering: Rejection Method

Double scattering referred to Mott scattering from exactly two distinct nuclei within the target foil. The assumption was that this process became a more important contribution to the detector signal as target thickness increased. The first method used to calculate the effect of double scattering was also a rejection sampling method. To simulate these events, the algorithm was:

1. Randomly pick an initial energy (E) and a scattering position ($\mathbf{x}_1$) within the intersection of the beam and the target.

2. Randomly pick a point, $\mathbf{x}_2$, within the target, such that $|\mathbf{x}_2 - \mathbf{x}_1| \leq D$[1].

3. Calculate $\frac{d\sigma_1}{d\Omega_1}(\mathbf{x}_1, \mathbf{x}_2)$.

4. Randomly pick a point, $\mathbf{x}_3$, in the acceptance the primary collimator.

[1]For these simulations I chose D = 157 μm. This value was selected because it represented the distance over which a 5 MeV electron would lose 0.5 MeV in a gold target. This would have placed the electron outside of the energy cuts used by the experiment. Additionally, varying this parameter showed little effect on the asymmetry calculated

5. Calculate $\frac{d\sigma_2}{d\Omega_2}(\mathbf{x}_2, \mathbf{x}_3)$.

6. Rejection sample against the product of the two cross sections: $\frac{d\sigma_1}{d\Omega_1}\frac{d\sigma_2}{d\Omega_2}$. If accepted, generate electron at $\mathbf{x}_2$ towards $\mathbf{x}_3$ If rejected, repeat steps 1-5.

Simulating 10 million events at each target foil thickness and calculating the asymmetry identically to the single scattering case yielded:

$$\varepsilon_2 = \frac{N_{L_2} - N_{R_2}}{N_{L_2} + N_{R_2}} = -0.011 \pm 0.003 \tag{A.25}$$

The subscript indicated that these events scattered exactly twice. This asymmetry was not directly comparable to theory, but instead represented an effective asymmetry for events which were forced through two scatterings. This asymmetry also did not scale with target thickness. If this value was to be believed as the effective asymmetry for all electrons which scattered twice in the target, the only remaining hurdle was to determine how the *relative rate* of single-scattered electrons (with asymmetry ε_1) and double-scattered electrons (with asymmetry ε_2) changed with target thickness.

A.6.3 Calculating Rates

In order to proceed, we used the simulation to calculate predicted rates in each detector for the two processes of interest because the rate was the simplest quantity with which to compare simulations to data. The rate calculated from a given simulation was a prediction of the number of events that would hit the detector per unit current per unit time, using the assumptions in our simulation. All rates quoted in this appendix have units of Hz/μA.

First, we discuss the general method of rate calculation and show how this leads to a form of the effective Sherman function. The differential rate in our detector from one point ($\mathbf{v}$) in the phase space of single-scattering electrons was:

$$d\mathcal{R}(\mathbf{v}) = \mathcal{L}(\mathbf{v})\sigma(\mathbf{v})\epsilon(\mathbf{v})dv, \tag{A.26}$$

where $\mathcal{L}(\mathbf{v})$ is the luminosity, $\sigma(\mathbf{v})$ is the cross section of the physics of interest and $\epsilon(\mathbf{v})$ is the acceptance function of our detectors (essentially the chance that an event near $\mathbf{v}$ will

be detected). The total rate a detector sees from this process is simply the integral of eq. (A.26):

$$\mathcal{R} = \int_V d\mathcal{R}(\mathbf{v}). \tag{A.27}$$

While $\mathcal{L}(\mathbf{v})$ and $\sigma(\mathbf{v})$ were known quantities, $\epsilon(\mathbf{v})$ was a value obtained solely by simulation. The numerical solutions of eq. (A.27) described in the following sections required a simulation event generator that did not weight by cross section, which the rejection methods of Sections A.6.1 and A.6.2 did. For this purpose, new event generators were designed for single and double scattering as will be discussed in the following sections.

A.6.4 Single Scattering Rate: Reimann Estimator

In order to calculate the rate efficiently, one could not rejection sample as was done in the sections above. The single scattering rate calculations were performed using simulations of 10 million events at each target thickness. These events were generated according to the following algorithm:

1. Randomly pick an initial energy (E) and a scattering position ($\mathbf{x}_1$) within the intersection of the beam and the target.

2. Randomly pick a direction (χ, ψ) from a small solid angle pointing towards either the LEFT or RIGHT detector.

3. Calculate the Mott cross section given these inputs: $\frac{d\sigma}{d\Omega}(\mathbf{x}_1, \chi, \psi)$.

4. Throw electron from $\mathbf{x}_1$ along chosen direction.

For such an event, the phase space vector became $\mathbf{v} = (x, y, z, E, \chi, \psi)$ where (x, y, z) was the position of the scattering vertex, E was the incident energy at the scattering vertex, χ was the scattering angle and ψ was the azimuthal angle and the volume element was $dv = dxdydzdEd\chi d\psi$. The total rate in a detector was then:

$$\mathcal{R} = \int_V \mathcal{L}(\mathbf{v})\sigma(\mathbf{v})\epsilon(\mathbf{v}) \sin\chi dv. \tag{A.28}$$

The integrals over x, y were trivial. Additionally, the dependence of $\sigma(\mathbf{v})$ upon z and E was small enough to ignore. Figure A.9 shows plots of the acceptance function,$\epsilon(\mathbf{v})$, with respect to the different variables of single scattering. As is demonstrated in the figure, the acceptance function's behavior is well characterized solely by its dependence upon scattering angle, χ and azimuthal angle ψ. Thus:

$$\epsilon(\mathbf{v}) \approx \epsilon(\chi, \psi). \tag{A.29}$$

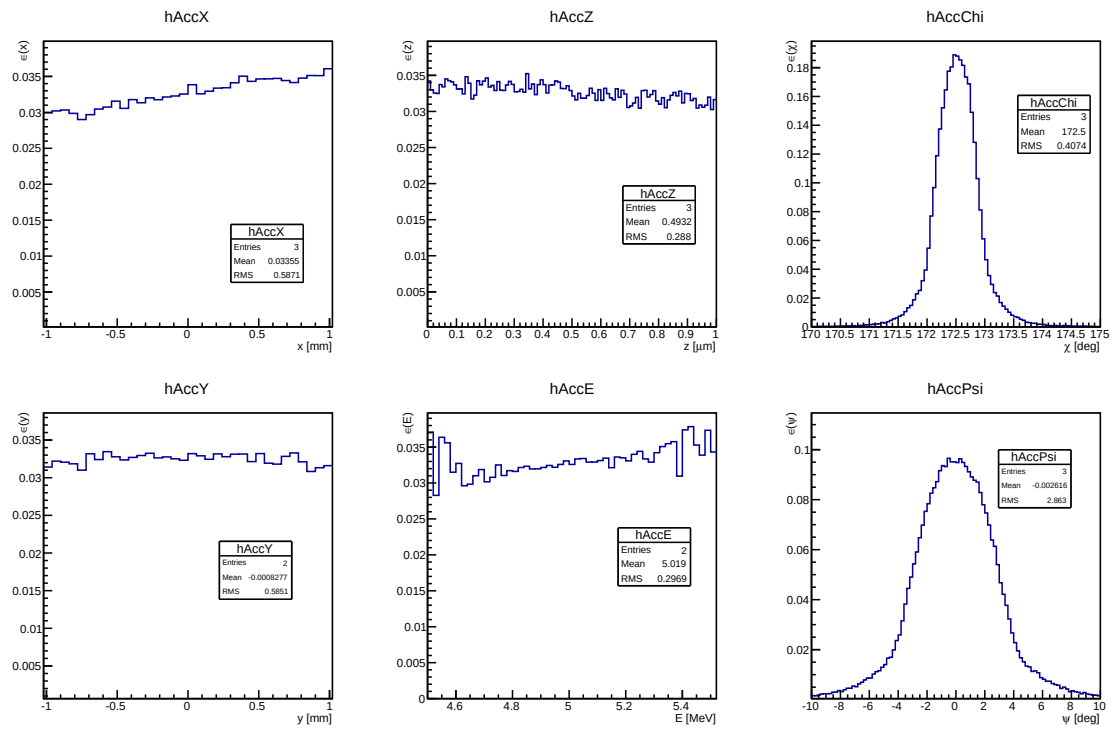

Figure A.9: Simulated acceptance functions for each of the six degrees of freedom in single scattering. Results are from the LEFT detector for 10 million events thrown with a 1μm Au foil. Only $\epsilon(\chi)$ and $\epsilon(\psi)$ show large dependence.

Using these simplifications we obtained a rate:

$$\mathcal{R} = \frac{N_A \rho}{A} N_B d \int_{\psi_{min}}^{\psi_{max}} \int_{\chi_{min}}^{\chi_{max}} \sigma(\chi, \psi) \epsilon(\chi, \psi) \sin\chi d\chi d\psi, \tag{A.30}$$

where N_A is Avogadro's number, ρ is the density of the target foil, A is the atomic weight of the foil material, N_B is the number of electrons per second in 1 μA, and d is the target

thickness. In order to numerically solve eq. (A.30) , we performed a Reimann sum. We divided the 2D integral into $N_\chi \times N_\psi$ bins in χ and ψ of size $\Delta\chi\Delta\psi$. In our case, we used 350 bins for each variable. Then eq. (A.30) could be estimated using

$$\mathcal{R} \approx \frac{N_A \rho}{A} N_B d \sum_{i=1}^{N_\chi} \sum_{j=1}^{N_\psi} \sigma_{ij} \epsilon_{ij} \sin \chi_i \Delta\chi\Delta\psi, \tag{A.31}$$

where σ_{ij} is the average cross section for all events collected in the simulated detector in the ij'th bin and ϵ_{ij} is the acceptance function for the bin. The statistical uncertainty, $\delta\mathcal{R}$, from this method was given by

$$\delta\mathcal{R}^2 = \left(\frac{N_A \rho}{A} N_B d \Delta\chi\Delta\psi\right)^2 \sum_{i=1}^{N_\chi} \sum_{j=1}^{N_\psi} \left(\epsilon_{ij}^2 \delta\sigma_{ij}^2 + \sigma_{ij}^2 \delta\epsilon_{ij}^2\right) \sin^2 \chi_i. \tag{A.32}$$

Figure A.10 shows the binned cross section and acceptance function for a run. Using this method gave the results shown in Table A.4. These results allowed us to make independent predictions of the linear coefficient of the rate

$$a_1^{sim.} = \left\langle \mathcal{R}_1^{sim.}/d \right\rangle = 0.198 \pm 0.001 \text{ Hz}/(\mu\text{A nm}), \tag{A.33}$$

where averaging is carried out over all 18 simulated targets. This result is in good agreement with the fit result in eq. (A.7). The single-scattering asymmetry was calculated similarly from simulated rates as:

$$\varepsilon_1^{rate} = \left\langle \frac{\mathcal{R}_{L_1} - \mathcal{R}_{R_1}}{\mathcal{R}_{L_1} + \mathcal{R}_{R_1}} \right\rangle = -0.513 \pm 0.006. \tag{A.34}$$

The average was again calculated over all 18 targets. These results agreed with theory, shown in eq. (A.15).

A.6.5 Double Scattering Rates: Monte Carlo Estimator

In the case of double scattering, we can't use the Riemann sum method because the phase space is significantly more complicated and the summation needs to be carried out over more dimensions. We turn instead to the idea of Monte Carlo integration using the outputs

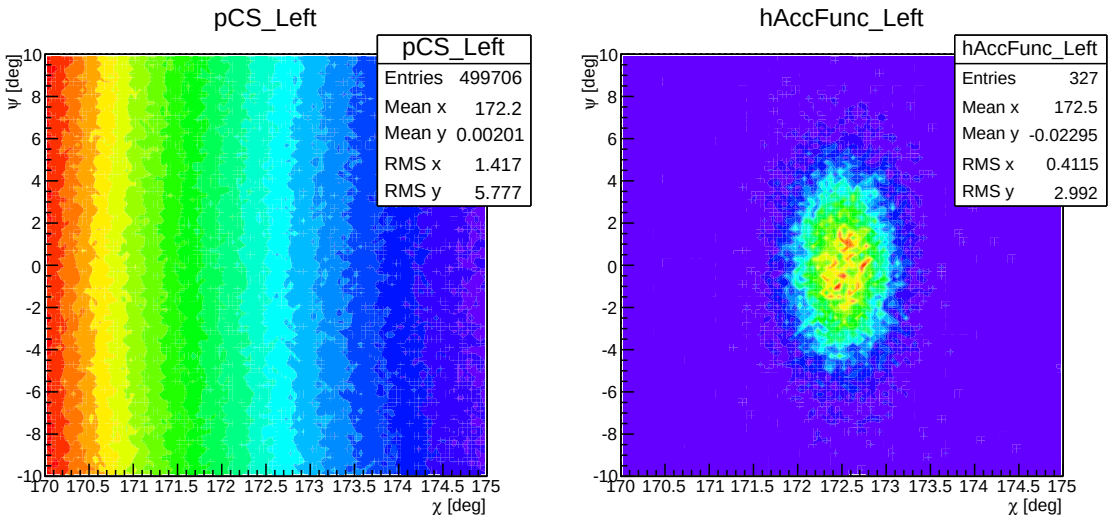

Figure A.10: Left: Simulated average cross section as a function of scattering angle, χ, and azimuthal angle, ψ, for the LEFT detector. Right: Simulated acceptance function, $\epsilon(\chi, \psi)$. Results from a simulation of 1 million events and a 52 nm gold foil.

d [nm]	$\mathcal{R}_{L_1}$ [Hz/μA]	$\mathcal{R}_{R_1}$ [Hz/μA]	$\mathcal{R}_1^{sim.}$ [Hz/μA]
52	5.0±0.1	15.5±0.4	10.3±0.2
100	9.6±0.3	29.8±0.8	19.7±0.4
200	19.3±0.5	59.8±1.7	39.5±0.9
215	20.7±0.6	64.2±1.8	42.5±0.9
300	28.9±0.8	89.7±2.5	59.3±1.3
389	37.5±1.0	116.0±3.2	76.7±1.7
400	38.5±1.1	119.7±3.3	79.1±1.7
488	46.9±1.3	145.5±4.0	96.2±2.1
500	48.2±1.3	149.2±4.2	98.7±2.2
561	54.0±1.5	167.4±4.7	110.7±2.4
600	57.8±1.6	179.2±5.0	118.5±2.6
700	67.4±1.9	209.3±5.8	138.3±3.1
775	74.7±2.1	231.4±6.4	153.0±3.4
800	77.1±2.1	239.2±6.6	158.1±3.5
837	80.6±2.2	249.8±6.9	165.2±3.7
900	86.6±2.4	269.0±7.5	177.8±3.9
944	91.0±2.5	282.2±7.8	186.6±4.1
1000	96.3±2.7	299.5±8.3	197.9±4.4

Table A.4: Rates calculated from single-scattering simulations of 10^7 thrown events. From left to right: Rate in LEFT detector, rate in RIGHT detector, average of the two.

of the `GEANT4` simulation. This method has the advantage of being numerically soluble. However, the integral converged very slowly and we needed generate enormous data sets (10^9 events). These events were generated by the following algorithm:

1. Randomly pick an initial energy (E) and a scattering position ($\mathbf{x}_1$) within the intersection of the beam and the target.

2. Randomly pick a direction (θ, ϕ) uniformly over the unit sphere.

3. Randomly select a distance (ξ) between the primary vertex ($\mathbf{x}_1$) and the edge of the target along the direction from the previous step. This is the secondary scattering vertex (($\mathbf{x}_1$).

4. Randomly pick a direction (χ, ψ) from a small solid angle pointing towards either the LEFT or RIGHT detector.

5. Calculate all relevant quantities: cross sections, Sherman functions, incoming, intermediate and outgoing energy, polarization *et cetera*.

6. Throw electron from $\mathbf{x}_2$ along chosen direction (χ, ψ).

In this case, we considered the rate in pieces associated with each scattering vertex. The rate from the initial scattering at position (x, y, z) and energy prior to entering the target, E, towards the second scattering position along direction (θ, ϕ) was

$$d\mathcal{R}_1(\mathbf{v}) = \mathcal{L}_1(x, y, z, E)\sigma_1(z, E, \theta, \phi) \sin\theta d\theta d\phi. \tag{A.35}$$

The luminosity in an infinitesimal volume about the first scattering vertex was

$$\mathcal{L}_1(\mathbf{v}) = \frac{N_A \rho}{A} \frac{N_B}{(2\pi)^{3/2}\sigma_x \sigma_y \sigma_E} \exp\left[-\frac{x^2}{2\sigma_x^2} - \frac{y^2}{2\sigma_y^2} - \frac{E^2}{2\sigma_E^2}\right] dxdydzdE. \tag{A.36}$$

Similarly the infinitesimal rate a detector saw from the second scattering vertex, a distance, ξ, from the first scattering, towards our detectors at global angles (χ, ψ) was:

$$d\mathcal{R}(\mathbf{v}) = \mathcal{L}_2(x, y, z, E, \theta, \phi, \xi)\sigma_2(z, E, \xi, \theta, \phi, \chi, \psi)\epsilon(\chi, \psi) \sin\chi d\chi d\psi. \tag{A.37}$$

The luminosity at the second scattering vertex due to events from the primary vertex was

$$\mathcal{L}_2(x, y, z, E, \theta, \phi, \xi) = \frac{N_A \rho}{A} d\mathcal{R}_1(\mathbf{v}) \exp(-\xi/\lambda) d\xi. \tag{A.38}$$

where λ characterized of the depth an electron will penetrate in gold. This quantity was calculated to be the mean-free-path due to backscattering:

$$\frac{1}{\lambda} = 2\pi \frac{N_A \rho}{A} \int_{\pi/2}^{\pi} \sigma(E, \theta) \sin\theta d\theta. \tag{A.39}$$

Thus we found

$$\lambda = 183\ \mu\text{m}. \tag{A.40}$$

Since $\lambda \gg d$ we could safely ignore this term in the single scattering case. Testing showed that this term has no effect on the resulting rate calculation. Due to the foil geometry, only a sliver of events scattered at $\approx \pi/2$ ever had appreciable amount of foil to travel through. This factor was included for completeness.

To calculate the rate in a detector due to electrons that Mott scattered exactly twice in the target foil, we defined a function:

$$f(\mathbf{v}) = \exp\left[-\frac{x^2}{2\sigma_x^2} - \frac{y^2}{2\sigma_y^2} - \frac{E^2}{2\sigma_E^2}\right] \exp(-\xi/\lambda)\sigma_1(\mathbf{v})\sigma_2(\mathbf{v})\epsilon(\chi, \psi) \sin\theta \sin\chi. \tag{A.41}$$

This allowed the rate integral to be written as:

$$\mathcal{R}_2 = \left(\frac{N_A \rho}{A}\right)^2 \frac{N_B}{(2\pi)^{3/2}\sigma_x \sigma_y \sigma_E} \int_V f(x, y, z, E, \theta, \phi, \xi, \chi, \psi) dv. \tag{A.42}$$

The `GEANT4` double-scattering simulation sampled the phase space, V, according to the probability density function (PDF):

$$g(\mathbf{v}) = C \exp\left[-\frac{x^2}{2\sigma_x^2} - \frac{y^2}{2\sigma_y^2} - \frac{E^2}{2\sigma_E^2}\right] \sin\theta \sin\chi. \tag{A.43}$$

This represented Gaussian sampling over incoming beam parameters x, y, and E, and uniform outgoing momenta direction sampling over segments of the unit sphere while uniformly sampling all non-explicit variables. The normalization of this PDF was

$$1 = \int_V g(x, y, E, \theta, \chi) dv. \tag{A.44}$$

The integrations over x, y, E, ϕ, ξ, χ, and ψ can be performed trivially, leaving:

$$\frac{1}{C} = (2\pi)^{3/2}\sigma_x\sigma_y\sigma_E\frac{2\pi^2}{9}\left(\cos\frac{\pi}{36} - \cos\frac{\pi}{18}\right) \times I, \tag{A.45}$$

where we defined

$$I = \int_0^d \int_0^\pi \xi_{max}(\theta, z)\sin\theta d\theta dz. \tag{A.46}$$

In the above equation, $\xi_{max}(\theta, z)$ is the distance between the initial scattering vertex, $\mathbf{x_1} = (x, y, z)$, and the edge of the foil or the user-defined maximum, $D = 157\,\mu$m, for those particles traveling at $\theta \approx \pi/2$ (See footnote in Section A.6.2). Thus we defined this integration boundary to be:

$$\xi_{max}(\theta, z) = \begin{cases} \frac{d-z}{\cos\theta}\left[1 - H\left(\frac{d-z}{\cos\theta} - D\right)\right] + DH\left(\frac{d-z}{\cos\theta} - D\right) & \text{if } \theta \leq \pi/2 \\ \frac{-z}{\cos\theta}\left[1 - H\left(\frac{-z}{\cos\theta} - D\right)\right] + DH\left(\frac{-z}{\cos\theta} - D\right) & \text{if } \theta > \pi/2, \end{cases} \tag{A.47}$$

where $H(x)$ is the Heaviside step function. The integral in eq. (A.46) is covered in Section A.9 where it is found that $I = d^2$ regardless of the value of D chosen. Thus eq. A.45 becomes

$$\frac{1}{C} = (2\pi)^{3/2}\sigma_x\sigma_y\sigma_E\frac{2\pi^2}{9}\left(\cos\frac{\pi}{36} - \cos\frac{\pi}{18}\right) d^2. \tag{A.48}$$

Given the definitions above, we can express the rate from double scattering to be

$$\mathcal{R}_2 = \left(\frac{N_A\rho}{A}\right)^2 \frac{N_B}{(2\pi)^{3/2}\sigma_x\sigma_y\sigma_E}\int_V \frac{f(\mathbf{v})}{g(\mathbf{v})}g(\mathbf{v})dv. \tag{A.49}$$

To numerically calculate this integral, we used a Monte Carlo estimator as described in

[139]:

$$\mathcal{R}_2 \approx \frac{1}{n}\left(\frac{N_A\rho}{A}\right)^2 \frac{N_B}{(2\pi)^{3/2}\sigma_x\sigma_y\sigma_E}\sum_i^n \frac{f(\mathbf{v}_i)}{g(\mathbf{v}_i)} \tag{A.50}$$

$$\approx \frac{1}{C}\frac{1}{n}\left(\frac{N_A\rho}{A}\right)^2 \frac{N_B}{(2\pi)^{3/2}\sigma_x\sigma_y\sigma_E}\sum_i^n \sigma_1(\mathbf{v}_i)\sigma_2(\mathbf{v}_i)\epsilon(\chi_i,\psi_i) \tag{A.51}$$

$$\approx \frac{2\pi^2}{9}\left(\cos\frac{\pi}{36}-\cos\frac{\pi}{18}\right) N_B \left(\frac{N_A\rho d}{A}\right)^2 \frac{1}{n}\sum_i^n \sigma_1(\mathbf{v}_i)\sigma_2(\mathbf{v}_i)\epsilon(\chi_i,\psi_i) \tag{A.52}$$

Results calculated with this method are shown in Table A.5.

d [nm]	$\mathcal{R}_{L_2}$ [Hz/μA]	$\mathcal{R}_{R_2}$ [Hz/μA]	$\mathcal{R}_2^{sim.}$ [Hz/μA]
52	0.22±0.02	0.12±0.02	0.17±0.01
100	0.78±0.09	0.36±0.05	0.57±0.05
200	2.92±0.32	1.74±0.23	2.33±0.20
215	3.79±0.48	2.68±0.73	3.24±0.44
300	8.21±0.97	3.59±0.47	5.90±0.54
389	12.94±1.70	5.58±0.78	9.26±0.93
400	11.25±1.37	10.33±1.83	10.79±1.14
488	20.46±3.09	8.79±1.64	14.63±1.75
500	16.64±1.82	10.82±1.57	13.73±1.20
561	29.69±4.17	11.47±1.83	20.58±2.28
600	28.60±4.33	21.27±3.71	24.94±2.85
700	43.84±4.90	26.69±5.93	35.26±3.85
775	40.56±5.58	22.95±3.63	31.76±3.33
800	67.56±8.87	25.98±4.54	46.77±4.98
837	49.58±6.34	31.81±4.86	40.69±4.00
900	67.97±8.44	37.97±7.92	52.97±5.79
944	77.47±10.19	37.28±6.63	57.37±6.08
1000	76.53±9.86	49.38±8.53	62.95±6.52

Table A.5: Rates calculated from double-scattering simulations of 2.5×10^8 thrown events. From left to right: Rate in LEFT detector, rate in RIGHT detector, average of the two.

By simply dividing the average double-scattering rate by the square of the simulated target thickness, we could compare the simulation to the quadratic rate scaling coefficient from the fit to data, eq. (A.8). Such calculation yielded

$$a_2^{sim.} = \left\langle \mathcal{R}_2^{sim.}/d^2 \right\rangle = [62 \pm 15]\ \mu\text{Hz}/(\mu\text{A}\,\text{nm}^2). \tag{A.53}$$

This result was compatible with eq. (A.8). However, constructing a double-scattering

asymmetry analogous to eq. (A.34) proved problematic. While there was no clear thickness dependence, there was significant point-to-point variance, which can be seen in Figure A.11. Performing an average in spite of this large variance yielded:

$$\varepsilon_2^{rate} = \left\langle \frac{\mathcal{R}_{L_2} - \mathcal{R}_{R_2}}{\mathcal{R}_{L_2} + \mathcal{R}_{R_2}} \right\rangle = 0.28 \pm 0.11. \tag{A.54}$$

This result is not consistent with the results of the rejection method in Section A.6.2.

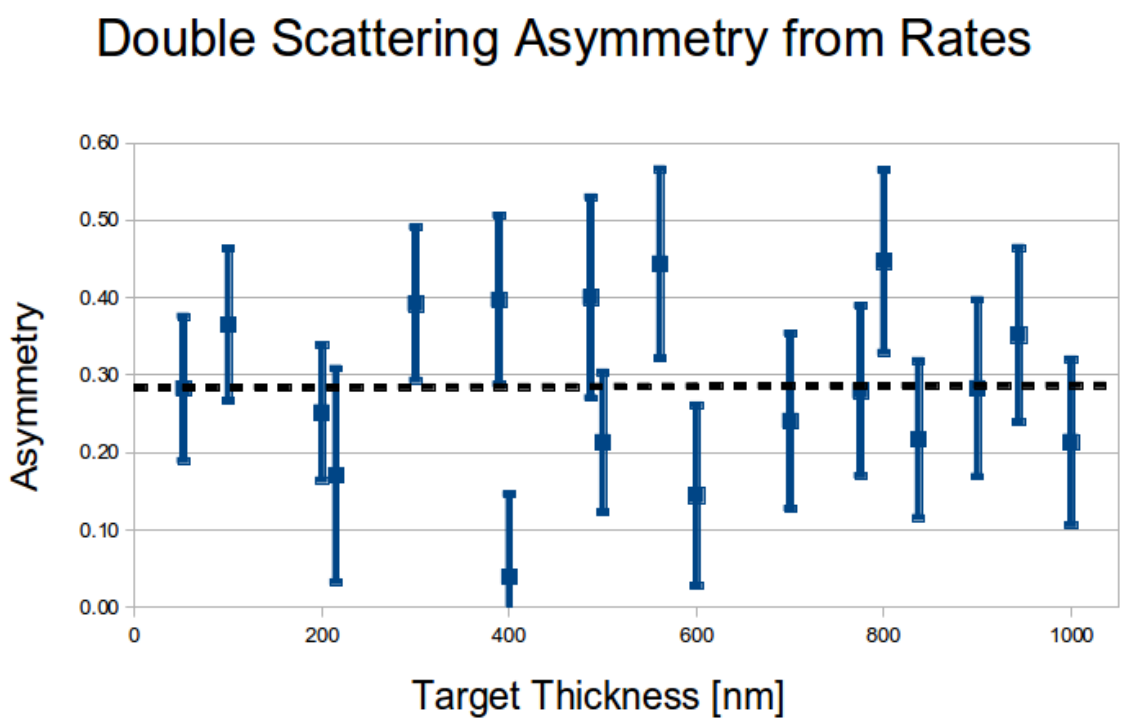

Figure A.11: Asymmetry as calculated in eq. (A.54) from results of 2.5×10^8 event simulation at each target thickness.

A.7 Combined Results

Using the simulated rates for the LEFT and RIGHT detectors for both single and double scattering, one could calculate the combined rate, which should be comparable to data. Such rates were calculated as

$$\mathcal{R}_{tot.}^{sim.} = \frac{1}{2}\left[\mathcal{R}_{L_1} + \mathcal{R}_{R_1} + \mathcal{R}_{L_2} + \mathcal{R}_{R_2}\right]. \tag{A.55}$$

The results of eq. (A.55) can be seen compared to data in Table A.6. Figure A.12 shows the data versus simulation comparison including those simulations performed at intermediate target thicknesses. The black curve is a function calculated from simulation using the results of eqs. (A.33) and (A.53):

$$\mathcal{R}^{pred.}(d) = a_1^{sim.} \cdot d + a_2^{sim.} \cdot d^2 \tag{A.56}$$

Both the table and figure indicate that the simulation is able to reproduce the Mott scattering rate from the target foil accurately. The simulation also clearly indicated that a significant portion of events came from double scattering in the target foil.

d[nm]	$\mathcal{R}^{\text{data}}$[Hz/$\mu$A]	$\mathcal{R}^{\text{sim}}_{\text{tot.}}$[Hz/$\mu$A]
52	9.93±0.09	10.45±0.23
215	46.50±0.48	45.69±1.03
389	82.58±1.04	85.98±1.94
488	97.74±1.00	110.82±2.75
561	128.66±1.32	131.31±3.34
775	178.30±1.86	184.76±4.75
837	209.30±2.15	205.90±5.41
944	246.00±2.53	243.98±7.34

Table A.6: Data rates compared to combined simulated rates.

A combined asymmetry could also be constructed. Defined as:

$$A^{sim.} = \frac{[\mathcal{R}_{L_1} - \mathcal{R}_{R_1}] + [\mathcal{R}_{L_2} - \mathcal{R}_{R_2}]}{[\mathcal{R}_{L_1} + \mathcal{R}_{R_1}] + [\mathcal{R}_{L_2} + \mathcal{R}_{R_2}]}, \tag{A.57}$$

This allowed direct comparison with data as in Table A.7 and Figure A.13. The simulations, which had poor statistics due to the very slowly converging Monte Carlo estimator method, show excellent agreement at the thinner target foils. This does not hold as one moves to thicker target foils although the uncertainty of the target thickness means that almost every target is within statistical agreement with a nearby simulation. This gradual separation can be tied to the relatively large asymmetry for double scattering that was calculating using the rate method in eq. A.54.

Even with the marginal agreement shown above, the simulation rather clearly demonstrated some important phenomena. The results of rate method simulations clearly indi-

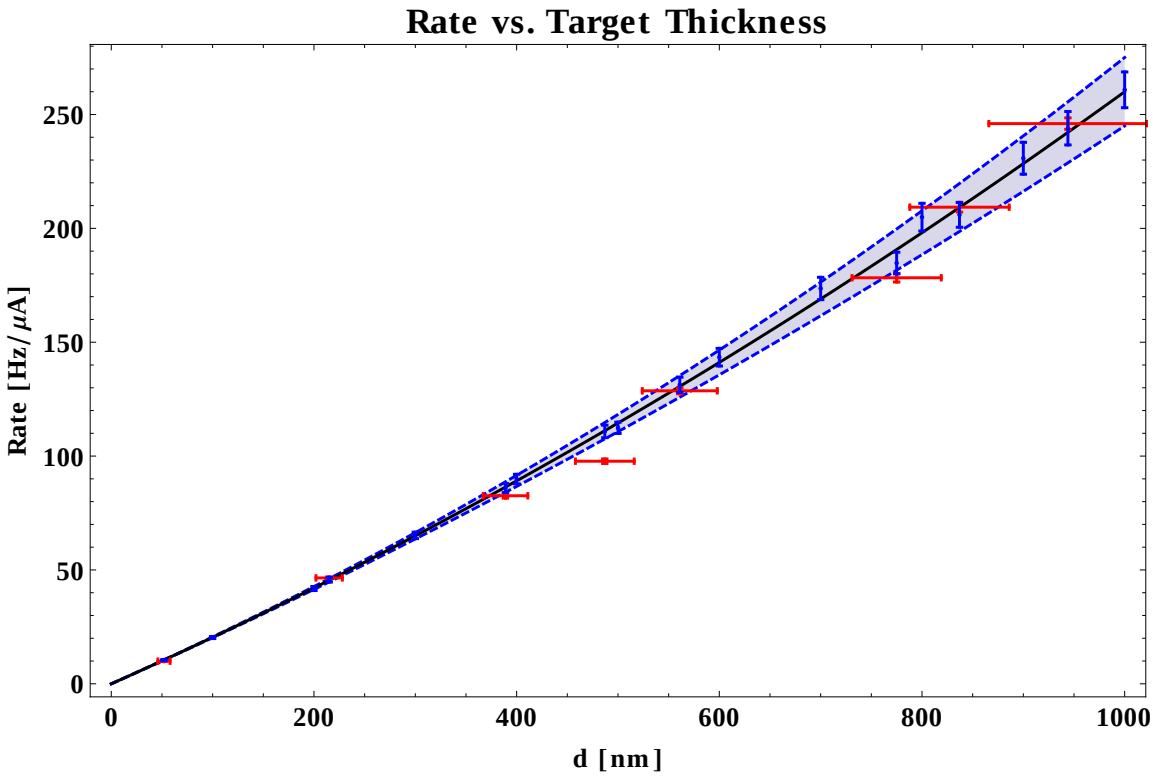

Figure A.12: Combined simulation rates (blue) compared to data rates (red). The values can be seen in Table A.6. The black curve is the analytic simulation prediction from eq. A.56.

d [nm]	A^{data} [%]	$A^{sim.}$ [%]
52	43.43±0.07	43.0±2.2
215	40.96±0.07	39.9±2.2
389	39.18±0.07	35.6±2.1
488	38.61±0.07	33.8±2.3
561	37.25±0.07	31.2±2.4
775	35.62±0.07	32.4±2.4
837	34.62±0.07	31.6±2.4
944	33.77±0.07	26.6±2.7

Table A.7: Asymmetry measured on the target foils compared to simulated asymmetries calculated according to eq. A.57.

cated that the rate of single-scattered electrons scaled linearly with target thickness and the rate of double-scattered electrons scaled quadratically with target thickness. Additionally, both the rejection method and rate method both showed that the asymmetry due to each type of scattering did not vary with target thickness. Combining these observations, we made the following well founded assumptions predicting the rate due to each scattering

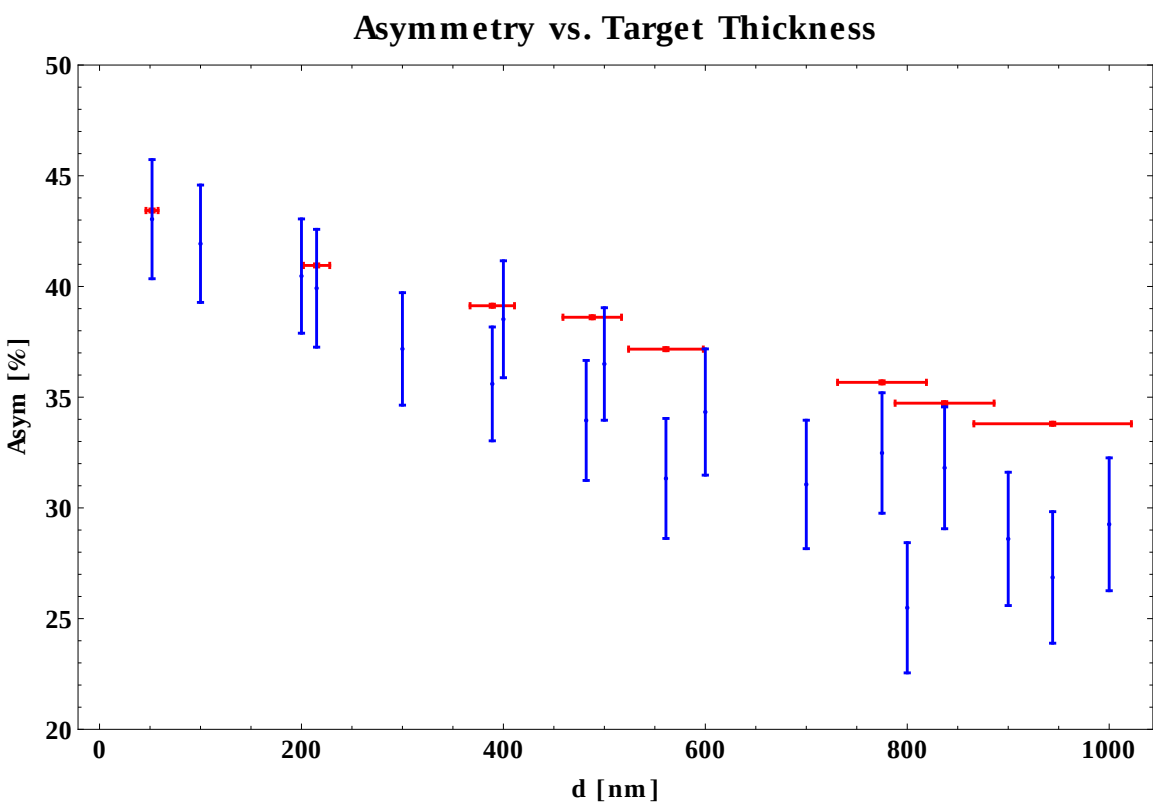

Figure A.13: Simulated asymmetries (blue) compared to data (red).

type in each detector (LEFT or RIGHT) assuming a beam with polarization $\mathbf{P} = P\hat{y}$:

$$\mathcal{R}_{L_1}(d) = a_1^{sim.} d(1 + P\varepsilon_1) \qquad \mathcal{R}_{R_1}(d) = a_1^{sim.} d(1 - P\varepsilon_1)$$

$$\mathcal{R}_{L_2}(d) = a_2^{sim.} d^2(1 + P\varepsilon_2) \qquad \mathcal{R}_{R_2}(d) = a_2^{sim.} d^2(1 - P\varepsilon_2)$$

When inserted into eqs. (A.55 - A.57), these assumptions lead to analytic predictions for the rate and the asymmetry with only one input, the polarization, P. The predicted rate for a given thickness using this method is polarization-independent and was shown in eq. (A.56). The prediction for the asymmetry was calculated to be:

$$A^{pred.}(d) = P\frac{a_1\varepsilon_1 + a_2\varepsilon_2 d}{a_1 + a_2 d}. \tag{A.58}$$

Dividing out the polarization, we have a prediction for the effective Sherman function as a

function of target thickness using only simulation-derived values:

$$\boxed{S_{eff}^{pred.}(d) = \frac{a_1\varepsilon_1 + a_2\varepsilon_2 d}{a_1 + a_2 d}}. \tag{A.59}$$

The uncertainty of these rate and asymmetry prediction formulas are shown in Section A.10.

One remaining question was which effective asymmetry (ε_2) should one use for double-scattering events when making predictions using eq. (A.59). The simulations using the rejection method and rate method produced significantly different values for this quantity while simulation, data and theory agreed rather well on most other points as shown in Table A.8. Recall eq. (A.3), which was fit to the asymmetry data. The resulting fit is directly comparable to eq. (A.58) where:

$$A_0 = P\varepsilon_1 \tag{A.60}$$

$$\alpha = Pa_2\varepsilon_2/a_1 \tag{A.61}$$

$$\beta = a_2/a_1 \tag{A.62}$$

Because the fit value of α from eq. (A.5) was poorly constrained, there is little to be gained attempting to extract ε_2 from eq. (A.61). Thus we must rely upon which prediction best reproduces the data. Figure A.14 shows how well the two options predict data. In both plots the parameters are; $P = 0.855 \pm 0.009$, $a_1 = [0.198 \pm 0.001]$ Hz/(μA nm), $\varepsilon_1 = -0.514 \pm 0.003$, and $a_2 = [62 \pm 15]$ μHz/(μA nm^2). The left plot shows the prediction using the result of the rate calculation and the right plot shows the prediction using the result of the rejection method. The prediction using the rejection method is clearly a better fit to data.

A.8 Conclusions

The CEBAF Injector MeV Mott Polarimeter has been improved significantly as a result of the efforts of the upgrade team. Improvements to the hardware, including the beam dump, have led to reduced background rates. The new time-of-flight information provided by the FADCs at low beam rep rates allows for even better background suppression. Various

	a_1 [Hz/(μA nm)]	a_2 [μHz/(μA nm^2)]	ε_1	ε_2
Theory	-	-	-0.514±0.003	-
Data (Fits)	0.19±0.01	70±17	-	-
Rejection Method (Sim.)	-	-	-0.513±0.001	-0.011±0.003
Rate Method (Sim.)	0.198±0.001	62±15	-0.513±0.006	0.28±0.11

Table A.8: Summary of important parameters regarding single and double scattering events as determined through various methods in this work.

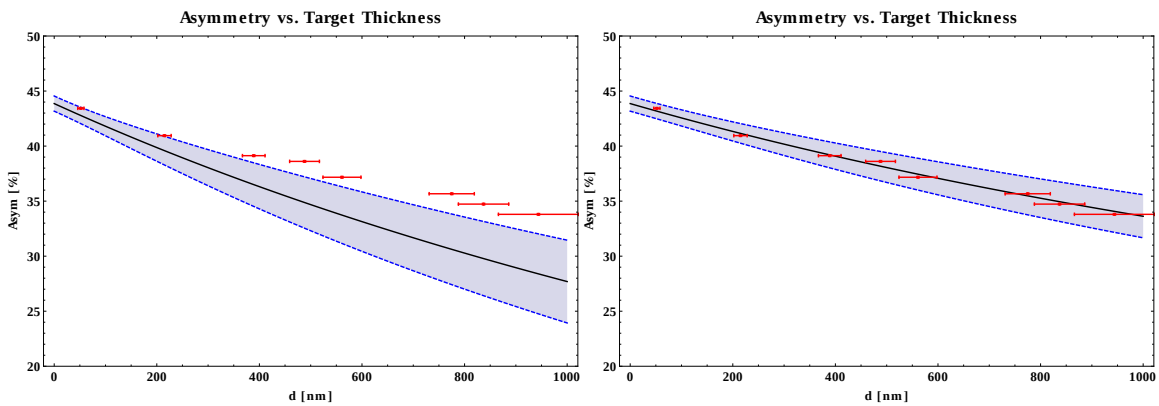

Figure A.14: Left: Prediction using eq. (A.58) with a value $\varepsilon_2 = 0.28 \pm 0.11$ (from rate calculations) compared to data (red). Right: Identical to the previous except with the $\varepsilon_2 = -0.011 \pm 0.003$ (from the rejection method). All other parameters are identical and are discussed in the text.

systematic studies indicated that the physics asymmetry was largely insensitive to those variables examined.

New, more precise theoretical calculations allowed for the construction of a `GEANT4` simulation of the polarimeter as well as cleaner extraction of the polarization from the asymmetry data. This simulation was vital to characterizing the detector response. Additionally the simulation provided an excellent method for describing how the asymmetry varied as a function of the target thickness. The simulation clearly indicated that the observed target-thickness dependence was fully explained by a combination of single- and double-scattering events within the target.

Data taken months apart with the polarimeter during and after the upgrades had excellent agreement. Using this data, the fitting form suggested by the `GEANT4` simulation, and the updated theory, the polarization was measured to be $P = 0.855 \pm 0.009$ the first sub-percent measurement with the polarimeter. Work is continuing on the Mott Polarimeter using the simulation and data-taking improvements with the goal of providing increasingly precise polarization measurements to the CEBAF users.

A.9 Appendix: Normalization Integral

Herein we perform the explicit integration of eq. (A.46):

$$I = \int_0^d \int_0^\pi \xi_{max}(\theta, z) \sin\theta d\theta dz. \tag{A.63}$$

Examining the integral over θ we see

$$\int_0^\pi \xi_{max}(\theta, z) \sin\theta d\theta = (d-z) \int_0^{\alpha_1} \tan\theta d\theta + D \int_{\alpha_1}^{\alpha_2} \sin\theta d\theta + (-z) \int_{\alpha_2}^{\pi} \tan\theta d\theta, \tag{A.64}$$

where $\cos\alpha_1 = (d-z)/D$ with $0 \leq \alpha_1 < \pi/2$ and $\cos\alpha_2 = -z/D$ with $\pi/2 \leq \alpha_2 < \pi$. We then see:

$$(d-z) \int_0^{\alpha_1} \tan\theta d\theta = -(d-z) \log(\frac{d-z}{D}), \tag{A.65}$$

$$D \int_{\alpha_1}^{\alpha_2} \sin\theta d\theta = d, \tag{A.66}$$

$$-z \int_{\alpha_2}^{\pi} \tan\theta d\theta = z \log(\frac{z}{D}), \tag{A.67}$$

$$\therefore \int_0^\pi \xi_{max}(\theta, z) \sin\theta d\theta = d \left[1 - \log(\frac{d-z}{D})\right] + z \left[\log(\frac{d-z}{D}) + \log(\frac{z}{D})\right]. \tag{A.68}$$

Therefore we see

$$I = \int_0^d \left(d \left[1 - \log(\frac{d-z}{D})\right] + z \left[\log(\frac{d-z}{D}) + \log(\frac{z}{D})\right] \right) dz \tag{A.69}$$

$$= d^2 \tag{A.70}$$

regardless of our initial choice of D (so long as it is a physically possible value).

A.10 Appendix: Error Propagation

From eq. (A.56) we obtain an uncertainty:

$$(\delta\mathcal{R}^{pred.})^2 = d^2 \delta {a_1}^2 + d^4 \delta {a_2}^2 + (a_1 + a_2 d)^2 \delta d^2. \tag{A.71}$$

From eq. (A.58) we obtain an uncertainty:

$$
\begin{aligned}
(\delta A^{pred.})^2 = & \left(\frac{A^{pred.}}{P}\right)^2 \delta P^2 \\
& + P^2 \frac{(a_2\varepsilon_1 - a_2\varepsilon_2)^2 d^2}{(a_1 + a_2 d)^4} \delta {a_1}^2 \\
& + P^2 \frac{a_1^2}{(a_1 + a_2 d)^2} \delta {\varepsilon_1}^2 \\
& + P^2 \frac{a_1^2 d^2 (\varepsilon_1 - \varepsilon_2)^2}{(a_1 + a_2 d)^4} \delta {a_2}^2 \\
& + P^2 \frac{a_2^2 d^2}{(a_1 + a_2 d)^2} \delta {\varepsilon_2}^2 \\
& + P^2 \frac{a_1^2 a_2^2 (\varepsilon_1 - \varepsilon_2)^2}{(a_1 + a_2 d)^4} \delta d^2. \qquad \text{(A.72)}
\end{aligned}
$$

Appendix B

Personal Contributions

The work presented in the body of this dissertation is the result of the work of myself as well as my many collaborators. In this section, I clearly delineate those portions of the Q_{weak} experiment that were my sole responsibility as well as those pieces which I contributed significantly as part of a team. In addition to the primary Q_{weak} measurement of the PV asymmetry on LH_2, I led the analysis of the transverse asymmetry of carbon in all aspects. As part of my professional development during my time as a student, I was part of the small team tasked with re-commissioning the JLab MeV Mott Polarimeter. This separate effort and my work on it are described in detail in Appendix A.

B.1 Q_{weak} Contributions

When I joined the Q_{weak} collaboration in late 2010, the installation was nearly complete and the data taking was about to start. Throughout the experimental runs, I was involved in data taking and small analysis tasks while I began my work as part of the group building and maintaining the Q_{weak} `GEANT4` simulation. Some of my contributions to this code included geometric descriptions of beamline elements such as the tungsten plug, implementation of background detectors such as the luminosity monitors and the PMTONL and PMTLTG detectors, building event generators for the ^{12}C target, various small improvements and significant debugging.

After data taking ended in June 2012, I contributed to the long and indeed ongoing task of analysis of the Run I and Run II data sets in various ways. As part of a large team of graduate students, I performed a number of data quality checks, developed and

updated the analysis software used by the collaboration. As part of smaller analysis working groups, I focused on beam corrections by developing new regression schemes and working to implement the beam modulation method of beam corrections, work that is still ongoing.

My `GEANT4` expertise was utilized in a number of ways throughout the years. I performed simulations that helped qualitatively verify the origin of the beamline background in the tungsten plug. I used the simulated background detectors to provide support for the beamline background asymmetry correction method shown in Section 4.3.2. I worked with other working groups such as the aluminum background group and inelastic background group in order to provide them with the simulations needed for their analysis. I've also provided simulation input to the groups working on corrections for preradiator scattering effects for both longitudinal and transverse data sets. I was solely responsible for both the method and calculation of the QTor transport channel neutral background over the entire experiment, including for the various ancillary physics measurements made.

The blinded results from Q_{weak}'s Run II data shown in Chapter 4 and Chapter 6 is my independent analysis representing the currently accepted methodology within the Q_{weak} collaboration. Unless otherwise indicated, all values and corrections were calculated by myself using methods developed by either myself or the collaboration.

B.2 Transverse Carbon Measurements

I was responsible for all aspects of determining the transverse asymmetry from carbon at the elastic QTor setting. This work entailed analysis of event-mode and current-mode data. I developed `GEANT4` simulations that were integral to the study of this process. I also determined the method in which all necessary corrections were calculated and applied to the data.

B.3 Mott Polarimeter Contributions

My work on the Mott Polarimeter was extensive. I participated in all of the data-taking periods of the polarimeter during my tenure. I helped update the data acquisition software, re-wrote analysis software used by the working group and developed the nearly-in-time

analysis method used during data taking. I provided design input on the new BeCu dump. I helped plan and execute systematic tests of various parameters of the polarimeter (beam energy, spot location, spot size, beam bunch rate etc.) which will be essential to the proposed publication. While I was heavily involved in all aspects of the upgrade, I had sole responsibility for the GEANT4 simulation development and utilization.